CRANFIELD UNIVERSITY

GIANROCCO MARINELLI

Wire and Arc Additive Manufacture of tungsten and tantalum

School of Aerospace, Transport and Manufacturing

PhD Thesis
Academic Year: 2017 – 2018

Supervisors
Dr. Supriyo GANGULY
Prof. Stewart WILLIAMS

May 2018

CRANFIELD UNIVERSITY

School of Aerospace, Transport and Manufacturing

PhD Thesis
Academic Year 2017 – 2018

GIANROCCO MARINELLI

Wire and Arc Additive Manufacture of tungsten and tantalum

Supervisors:
Dr. Supriyo GANGULY
Prof. Stewart WILLIAMS
May 2018

This thesis is submitted in partial fulfilment of the requirements for the degree of Doctor of Philosophy. © Cranfield University 2018. All rights reserved. No part of this publication may be reproduced without the written permission of the copyright owner.

Abstract

The advent of the next industrial revolution is clearly represented by the constant maturation of additive manufacturing. Wire + Arc Additive Manufacturing (WAAM) is a novel technique suitable for the deposition of medium to large scale components. This study was focused on investigating the WAAM process for the deposition of refractory metals, such as tungsten and tantalum. Generally, this class of metals is characterised by intrinsic low-temperature brittleness, poor weldability and a high susceptibility to oxidation over a large temperature range. For unalloyed tungsten, the process parameters to produce defect-free autogenous welds were found by varying the shielding gas composition and the welding speed. This represents a fundamental study for the WAAM deposition of tungsten, which has been reported to be markedly influenced by the wire feeding orientation. In particular, wire side feeding produced a large amount of spatter which resulted in an enhanced presence of structural defects within the structure deposited. The occurrence of defects was eliminated when employing wire front feeding. The characteristic microstructure of tungsten was investigated resulting to be composed of two specular arrays of large columnar grains meeting at the centre of the structure. The thermal conductivity and thermal diffusivity of as-deposited and annealed tungsten structures were observed to considerably decrease over the temperature range analysed.

200-mm-long structures in pure tantalum have been also deposited using two wires with different oxygen content. The tantalum structures can be deposited with high integrity and excellent mechanical properties. Superior yield strength was achieved for the WAAM deposited material compared to commercially available tantalum, even though the grains in the WAAM material were larger and had a high aspect ratio. The typical columnar grains of the tantalum deposits were refined into an equiaxed microstructure when additional cold-working was implemented to the deposition process. This led to obtaining a microstructure with an average grain size of 650 μm and completely random texture. Furthermore, two functionally graded structures were produced within the same built using tantalum, molybdenum and tungsten achieving a regular compositional and hardness gradient. The results of this study have shown that WAAM is able to produce refractory metal components with relatively low cost, exploiting the characteristic freedom of 3D printing and the opportunity of obtaining optimised properties, offering a solid alternative manufacture route to powder metallurgy.

Acknowledgements

First of all, I need to assert my immense gratefulness to my family, in particular, to my father and my mother. You have been fundamental for every achievement of my life. Your constant support always pushed me to overcome every obstacle. Whenever I was feeling completely lost, I just needed to promptly speak with you and everything became clear.

My strength is my brother! I feel that I need to apology to you for my physical absence. I really understand how difficult was being separated for so long because I felt exactly what you felt. I am so proud of whom you are and I will never leave you alone anymore!

I should also thank my uncle Pasquale for letting me occupy his own entire house for six months. I wrote most of my thesis within those walls. I need to thank my little cousin Vittoriana because without her support I would have never learnt how to play Mario Kart on the Nintendo Wii.

The complete merit of who I became on both professional and human point of view goes to Prof Stewart Williams, Dr Supriyo Ganguly and Dr Filomeno Martina. I genuinely think that it would not have been possible to find better mentors than they are. Apart from the enormous support when discussing the technical aspects of the research and setting the objectives of my research, their complete dedication and attitude became one of the reasons to wake up being motivated. I have always felt inspired by your way of working and relating to people. I seriously wish to become a person like you. I will never thank you enough.

Every single person of the Welding Engineering and Laser Processing Centre has made me feel part of a large family and each member of this family has been really important for the positive outcome of my research. An immeasurable thank you to Sonia, Goncalo, Wojciech, Leo, Jialuo, Paul, Anthony, Florent, Julio, Eloise, Jan, Xiangfang, Sergio, Michelangelo, Junny, Yash, Kuladeep, Pawel, Uzuma, Zsolt, Francesco, Daniela, Davide, Kwasi, Alex, Philippe, Armando, Philip, and Flemming. Not the least, I would like to thank my second father, Nisar.

I lived with you all so many experiences which will live with me forever. Just to name few of them: the numerous trips around the world, in particular, to Beijing,

Iceland, Montecarlo, Northern Ireland, the never-ending Crossfit training, and the ferocious discussions about French and Italian food.
The help of Steve Pope, Andrew Dyer, Xianwei Liu, Tracey Roberts, Christine Kimpton, Graham Hartwell is also acknowledged. Furthermore, I would like to thanks Michael Porton, David Hancock, Heather Lewtas, Shahin Mehraban, Geoff Shrimpton and Tim Rogers for the possibility to collaborate with you.
I also need to thank Tom and Satnam for all the support, the discussion and fun we had together.
For eight unforgettable years, I have been supported by an amazing person. Without her presence, I would have achieved only a part of what I actually have today. Thank you, Ileana! I also need to thank Nicla, Lella and Nicola for their incommensurable and unconditional affection.
I must reward the massive love that I keep receiving from my life-long friends from Italy. I am amazed by you all every time and I always felt extremely connected with you, even if a lot of kilometres were dividing us, in particular, 2253.082 km. I would never want to lose you as you are the most important people of my life. Thank you, Domenico, Michele, Sergio, Gianvito, Anthony, Antonio, Teresa, Cinzia, Rossella, Roberto, Flavio, Gianni, Candido, Vitoluca, Donato, Mauro, Loredana and many others.
I must admit that the last twelve months of my PhD overlapped with one of the hardest periods of my life. Many different things added pressure on me and made me spent entire night asleep. Going through all this has been possible only because of the presence of one of the most important people in my current life. Thank you, Isabella! In you, I found everything I needed to annihilate the negativity and the worries that were pervading me. You entered in my life in an unexpected way and you completely changed it. You taught me so many things. I will never forget what you have done for me and I hope to immediately support you back.
Thank also to you blonde angel. You flew in the sky just before I left Italy to begin my PhD. I know that you have been constantly giving me an immense. I would like to hug you how I used to do. Thank you, Fedele, you are living inside me!
Finally, I would like to thank everyone who will dedicate time to read this manuscript.

List of Papers

The different chapters of this thesis are written in paper format. Below the list of papers is provided.

Paper A
"Effect of the shielding gas composition and welding speed on autogenous welds of unalloyed tungsten plates", presented in **Chapter 2**.

Paper B
"Process development of Wire + Arc Additive Manufacture for the production of large-scale unalloyed tungsten components", presented in **Chapter 3**.

Paper C
"*Wire + Arc Additive Manufacturing process of unalloyed tungsten components and the correlation between microstructure and thermal properties*", presented in **Chapter 4**.

Paper D
"*Process development, microstructure and mechanical properties of two different unalloyed tantalum wires deposited via Wire + Arc Additive Manufacture*", presented in **Chapter 5**.

Paper E
"*Grain refinement in unalloyed tantalum structure deposited using Wire + Arc Additive Manufacture and vertical cold rolling*", presented in **Chapter 6**.

Paper F
"*Investigation of Wire + Arc Additive Manufacture for the production of functionally graded structures by refractory and its characterisation*", presented in **Chapter 7**.

Table of Contents

1 Introduction **1**

1.1 Research background 1

1.2 Research sponsorship 3

1.2.1 AMAZE project 4

1.2.2 AWE project 4

1.3 Review of previous research 4

1.3.1 Nuclear fusion 4

1.3.2 Physical metallurgy of refractory metals 8

1.3.3 Influence of alloying elements and interstitial elements 10

1.3.4 Oxides of tungsten and tantalum 12

1.3.5 Extraction of tungsten and tantalum 13

1.3.6 Estimation of welding efficiency 14

1.3.7 Additive Manufacturing of refractory metals 15

1.3.7.1 Tungsten 15

1.3.7.2 Tantalum 18

1.3.8 Research gap 19

1.4 Research aim and objectives 20

1.5 Outline of the thesis 21

1.6 Bibliography 24

2 Paper A **31**

2.1 Introduction 32

2.2 Experimental Procedure 35

2.3 Results and Discussion 38

2.3.1 Operative window and bead morphology 38

2.3.2 Humping formation 40

2.3.3 Transient welding state 43

2.3.4 Good weld 44

2.4 Conclusions 46

2.5 Bibliography 47

3 Paper B **51**

3.1 Introduction 52

3.2 Experimental Procedure 55

3.2.1 Weld pool formation and geometrical stabilisation 56

3.2.2 Metal transfer from the wire to the weld pool 57

3.2.3 Deposition of large-scale tungsten wall 59
3.3 Results and Discussion 59
3.3.1 Substrate orientation and clamping system 59
3.3.2 Weld pool formation and geometrical stabilisation 60
3.3.2.1 Autogenous welds 60
3.3.2.2 Stationary arc start 63
3.3.3 Metal transfer from the wire to the weld pool 65
3.3.3.1 Wire side feeding 66
3.3.3.2 Wire front feeding 69
3.3.4 Microstructure 70
3.3.4.1 Microstructure side-fed deposit 70
3.3.4.2 Microstructure front-fed deposit 71
3.3.5 Deposition of large-scale tungsten wall 72
3.4 Conclusions 73
3.5 Bibliography 74

4 Paper C **79**
4.1 Introduction 80
4.2 Experimental Procedure 83
4.3 Results and Discussion 89
4.3.1 Appearance and chemical analysis 89
4.3.2 Microstructure 90
4.3.3 Dilatometry 96
4.3.4 Laser flash analysis 101
4.4 Conclusions 106
4.5 Bibliography 107

5 Paper D **113**
5.1 Introduction 114
5.2 Experimental Procedure 116
5.3 Results and Discussion 120
5.3.1 Chemical analysis 120
5.3.2 Bead Appearance and outer oxide layer 121
5.3.3 WAAM process and geometrical control 122
5.3.4 Porosity 123
5.3.5 Microstructure and banding occurrence 124
5.3.6 Hardness 126
5.3.7 Tensile properties 128
5.3.8 Strain localisation 131
5.3.9 Fractography 132

5.4 Conclusions 133
5.5 Bibliography 134

6 Paper E 139
6.1 Introduction 140
6.2 Experimental Procedure 143
6.3 Results 147
6.3.1 Contour profiles 147
6.3.2 Microstructure 148
6.3.3 Porosity and deformation bands 150
6.3.4 Hardness 152
6.3.5 Texture 154
6.4 Discussion 155
6.4.1 Induced strain and the depth of recrystallisation 156
6.4.1.1 Recrystallisation of unalloyed tantalum 156
6.4.1.2 The relation between hardness and strain 157
6.4.1.3 The relation between hardness and dislocation density 157
6.4.1.4 Effect of the thermal field on the hardness 158
6.4.1.5 Dislocations density and oxygen content 159
6.4.2 Recrystallisation mechanism 160
6.4.3 Porosity 161
6.4.4 Texture 162
6.5 Conclusions 162
6.6 Bibliography 163

7 Paper F 169
7.1 Introduction 170
7.2 Experimental Procedure 173
7.3 Results and Discussion 176
7.3.1 Microstructure 176
7.3.2 Correlation between hardness and chemical composition 179
7.3.3 EDS chemical analysis 181
7.3.3.1 Interface between tantalum and molybdenum 181
7.3.3.2 Molybdenum to tungsten interface 183
7.4 Conclusions 184
7.5 Bibliography 186

8 Conclusion and Future Work 191
8.1 Introduction 191
8.2 Contribution to knowledge 191

8.3 Impact of the research 193
8.3.1 Research aspects of further development 194
8.3.2 Research aspects for further understanding 195
8.4 Impact on future applications of the research 195
8.4.1 Nuclear 196
8.4.2 Defence 197
8.5 WAAM system for refractory metals 197
8.6 Conclusions 198

A Strategies for tungsten deposition 203
A.1 Introduction 203
A.2 Methodology 203
A.2.1 Experimental Set-up 203
A.2.2 Deposition Strategy 1 203
A.2.3 Deposition Strategy 2 204
A.2.4 Deposition Strategy 3 204
A.3 Results 206
A.3.1 Deposition Strategy 1 206
A.3.2 Deposition Strategy 2 207
A.3.3 Deposition Strategy 3 207

B Mechanical Testing and Residual Stresses measurements of tungsten 209
B.1 Introduction 209
B.2 Methodology 209
B.2.1 Experimental Set-up 209
B.2.2 Mechanical Properties 209
B.2.3 Residual Stresses 210
B.3 Results 211
B.3.1 Mechanical Properties 211
B.3.2 Residual Stresses 211

C Development of parameters for tantalum deposition 213
C.1 Introduction 213
C.2 Methodology 213
C.2.1 Experimental Set-up 213
C.2.2 Autogenous welds 213
C.2.3 Single-pass welds 213
C.3 Results 214
C.3.1 Autogenous welds 214
C.3.2 Single-pass welds 215

D Refining tantalum microstructure by using pulsing arc current 217
D.1 Introduction 217
D.2 Methodology 217
D.3 Results 219

E Development of parameters for dissimilar metal deposition 221
E.1 Introduction 221
E.2 Methodology 221
E.2.1 Experimental Set-up 221
E.2.2 Tungsten on Molybdenum 221
E.2.3 Tungsten on Tantalum 222
E.3 Results 223
E.3.1 Tungsten on Molybdenum 223
E.3.2 Tungsten on Tantalum 225

List of Figures

1.1 Map of the main AM processes according to the ISO/ASTM 52900 [1] 2
1.2 Schematic of future AM components in relation to the industrial sectors and the materials 2
1.3 Schematisation of the nuclear fusion reaction 5
1.4 Schematisation of the cross-section of the International Thermonuclear Experimental Reactor 6
1.5 Schematisation of the nuclear reactor first wall (a) and the divertor (b) 7
1.6 Tantalum-tungsten phase diagram [30] 9
1.7 Tungsten-molybdenum phase diagram [31] 10
1.8 Molybdenum-tantalum phase diagram [32] 10
1.9 Pictures of the tungsten cube manufactured by Nie et al. [61], reporting the total dimensions of the deposit 15
1.10 Photograph showing the pure tungsten part fabricated by SLM by Wang et al. [62] 16
1.11 SEM images showing the top surface of tungsten parts fabricated using (a) polyhedral and (b) spherical powders by Wang et al. [62] 16
1.12 Micrographs of polished cross-sections of tungsten deposited (a) without preheating and (b) with baseplate preheating to 400 °C in the work of Iveković et al. [63] 17
1.13 SEM images of the top surface of the different tungsten specimens deposited using SLM in the work of Zhou et al. [64] 18
1.14 SEM pictures of the top surface of as-built tantalum SLM parts from the work of Thijs et al. [66] 19

2.1 Experimental set-up used for the production of the tungsten weldment 35
2.2 Schematic of the planes used to analyse the microstructure of the samples produced. In particular, longitudinal cross-section (a), transversal cross-section (b) and top section (c) 37

2.3 (a) Operative process window respect to SGC and TS; Weld bead morphology of the *Good Weld* (b), *Transient* (c), *Humping* (d) and *No Weld* samples (e) 38
2.4 Longitudinal cross-section (a) and top section (b) of the weld performed using a shielding gas composition of 50% of helium and 1 mm/s of welding speed 41
2.5 Time-resolved images of the weld performed using a shielding gas composition of 50% of helium and 1 mm/s of welding speed 42
2.6 Time-resolved images of the weld performed using a shielding gas composition of 75% of helium and 2 mm/s of welding speed 43
2.7 Time-resolved images of the weld performed using a shielding gas composition of 100% of helium and 1 mm/s of welding speed 44
2.8 Transversal cross-section (a), longitudinal cross-section (b) and top section (c) of the weld performed using an arc gas composition of 100% of helium and 1 mm/s of welding speed 45

3.1 Schematisation of all the components used for the clamping system (a) and the material used for each of them (b) 56
3.2 Set-up used for the development of the WAAM process for unalloyed tungsten when using side feeding (a) and when using front feeding (b) 58
3.3 Time-resolved images of the autogenous weld performed using an arc current of 350 Amperes with a frame time of 5.0 seconds 61
3.4 Time-resolved images of the autogenous weld performed using an arc current of 375 Amperes with a frame time of 5.0 seconds 62
3.5 Time-resolved images of the autogenous weld performed using an arc current of 400 Amperes with a frame time of 5.0 seconds 62
3.6 Time-resolved images of the weld pool evolution under stationary arc for 3.5 seconds 63
3.7 Time-resolved images of the weld pool evolution under stationary arc for 4.0 seconds 64
3.8 Time-resolved images of the weld pool evolution under stationary arc for 4.5 seconds 64

3.9 Time-resolved images of the steady welding process of unalloyed tungsten using an arc current of 400 Amps, a travel speed of 2 mm/s and a stationary arc for 4.0 seconds 65

3.10 Time-resolved images of the deposition performed using side-feeding configuration 66

3.11 Schematisation of different metal particle ejection during the deposition of tungsten using side feeding: ejection from the wire (a-c) and ejection from the weld pool (d-f) 67

3.12 Tungsten linear structure deposited using side feeding (a). Comparison of the wire feeding side (b) of the structure and the opposite one (c) 68

3.13 Time-resolved images of the front-fed deposition process with a time frame of 4.0 seconds 69

3.14 Microstructure of the linear structure deposited using wire side feeding (a). Details of the defects located on the side facing the wire feeder (b-d). Detail of the microstructure at the base of the linear structure (e) 70

3.15 Microstructure of the linear structure deposited using wire front feeding (a). Details of the elongated grains found at the centre of the structure (b, d). Detail of the microstructure of the upper part of the structure (c). Detail of the microstructure at the base of the linear structure (e) 72

3.16 Large-scale unalloyed tungsten linear structure deposited via Wire + Arc Additive Manufacturing process (a-b). Picture of the fracture from the outer surface (c) and SEM picture of the fractured surface (d) 73

4.1 Set-up used for the deposition of the tungsten structure via Wire + Arc Additive Manufacture 84

4.2 Geometry and main dimensions of the coupon used for dilatometry (a) and the coupon used for laser flash analysis (b) 85

4.3 Denomination and location of the coupons (a); Arrangement and extraction plan of the coupon with respect to the deposition direction (b) 86

4.4 Location of the samples within the deposited structure (a). Plane analysed for the *Front View* (b), *Side View* (c) and *Top View* (d) 86

4.5 Large-scale unalloyed tungsten linear structure deposited via Wire + Arc Additive Manufacturing (WAAM) process 89
4.6 Microstructure of the *Front View* of the as-deposited (a) and the annealed structure (b) 91
4.7 Microstructure of the (a) *Top View* and (b) *Side View* of the as-deposited structure 91
4.8 Microstructural detail from the *Top View* showing porosity at the end of the deposition (a); Microstructural details from the *Side View* showing wavy grain boundaries (b) 92
4.9 Reconstructed microstructural schematic for the *Top View* (a), the *Front View* (b) and *Side View* (d). Three-dimensional schematic representing the microstructure of unalloyed tungsten structure produced via WAAM (c) 93
4.10 Schematics of the main heat flow components and of the formation the future gran boundaries for the *Front View* scenario when $T_s \approx$ RT (a), $T_s >$ RT (b) and $T_s >>$RT (c), and for the *Side View* scenario (d) 95
4.11 Typical thermal expansion curves of the tested samples in the as-deposited condition (a) and the annealed condition (b) 97
4.12 The variation of the α_t over temperature for the heating and cooling phase of the as-deposited samples (a) and annealed samples (b) 98
4.13 Grain structure of the base and the side of the cylindrical DIL sample indicated with respect to the expansion direction for the Vert As-Dep samples (a) and the Long As-dep samples (b) 99
4.14 Thermal diffusivity curves against temperate of the tested samples in the as-deposited condition (a) and the annealed condition (b) with the associated error bars 101
4.15 Specific heat capacity curves against temperate of the tested samples in the as-deposited condition (a) and the annealed condition (b) with the associated error bars 103
4.16 Thermal conductivity curves against temperate of the tested samples in the as-deposited condition (a) and the annealed condition (b) with the associated error bars 104

5.1 Set-up used for the development of the WAAM process for unalloyed tantalum 117

5.2 (a) Extraction position and direction of the tensile coupons for each wall; (b) Main dimensions of the tensile coupon used for the tests; (c) Apparatus used for tensile tests and DIC recording 119
5.3 (a) Linear structure made of unalloyed tantalum with the main dimensions; (b) Picture of the two linear structures deposited and studied in this investigation 121
5.4 Detail of the outer surface of the top (a) and the bottom (b) of the tantalum structure; Scanning electron microscope picture of the cross-section of the top (c) and the bottom (c) of the structure 122
5.5 (a) Increment of the layer height against the layer number; (b) Total layer width against the layer number 123
5.6 Optical microscope picture of a section of the Wall1 (a) and Wall2 (b) after polishing 124
5.7 Microstructure of Wall1S (a), Wall1 (b) and Wall2 (c) 125
5.8 Banding between the layers in Wall1 (a) and the band detail at higher magnification (b) 125
5.9 Hardness values of the tantalum Wall1S and Wall2S with respect to the distance from the top of the substrate 128
5.10 Representative stress-strain curves of Substrate (a), Wall1 and Wall2 in the vertical direction (b), Wall1 (c) and Wall2 (d) in the horizontal direction 129
5.11 Strain maps produced with digital image correlation for (a) substrate, (b) vertical coupon Wall 1, (c) horizontal coupon close to the top of the Wall 2 (Wall2H1) and (d) horizontal coupon close to the bottom of Wall 2 (Wall2H2) 131
5.12 Fracture surface of a coupon from Wall 1 (a-b), Wall 2 (c-d) and the substrate (e-f) 133

6.1 Set-up used for the deposition of unalloyed tantalum using the WAAM process 144
6.2 Schematic of the rolling rig used for the application of cold working between each successive layer 145

6.3 Schematic of the manufacturing route used to produce each sample analysed. The name of the samples extracted per each region is also reported 146
6.4 Overlap of the total contour of the cross-section of sample 1R, 2R and 3R 147
6.5 Optical micrograph images of sample 1R (a), 2R (b) and 3R (c). High magnification of the recrystallised top part of sample 3R (d) 148
6.6 Optical micrograph of sample 4R (a). Detail of the microstructure from the recrystallised zone (b) with highlighted grain boundaries (c) and schematisation (d). Detail of the microstructure from the columnar as-deposited region (e) with highlighted grain boundaries (f) and schematisation (g) 150
6.7 Polished cross-sections showing the porosity within the sample 1R (a), the top of the sample 2R (b), the bottom of the sample 2R (c), the top of the sample 3R (d) and the bottom of the sample 3R (e) 151
6.8 Flattened pores found at the top of the sample 2R (a); Microscopic bands across grains in sample 2R (b-d) 151
6.9 Contour maps relative to the Vickers hardness measurements for sample 1R (a), 2R (b) and 3R (c) 153
6.10 EBSD images of the columnar as-deposited region (a) and the recrystallised grains (b) of sample 4R. Legend with regards to colour and orientation (c) 154
6.11 Pole figures and inverse pole figures obtained from EBSD maps for the columnar as-deposited region (a-b) and the recrystallised grains (c-d) of sample 4R 154

7.1 Set-up used for the deposition of refractory metal FGS using the WAAM process 174
7.2 Microstructure of the entire deposited structure (a); Higher magnification micrographs of the tantalum to molybdenum interface (b) and the molybdenum to tungsten interface (c) 176
7.3 Microhardness (black) of the graded alloys overlaid on W (green), Ta (blue) and Mo (red) composition versus the distance from the substrate top 179

7.4 Back-scattered electron images (a)(d) and EDS elemental maps (b-c)(e-f) of the Ta-Mo interface 181
7.5 Back-scattered electron image (a) and EDS elemental maps (b-c) for the FGS between Mo and W; Back-scattered electron image (d) of the FGS between Mo and W and **Table 7.5** with the elemental composition of the local chemical analysis (e) 183

A.1 Substrate orientation with respect to the deposition for Deposition Strategy 1 204
A.2 Substrate orientation with respect to the deposition for Deposition Strategy 2 204
A.3 Model of the clamping system used during the investigation (blue part: tungsten; red parts: copper/tantalum; orange part: copper) 205
A.4 Description of the steps of the new strategy of deposition for tungsten. a) beginning of deposition onto the substrate; b) deposition of few layers of tungsten; c)deposition on top of the wall without substrate 205
A.5 Tungsten wall deposited using the Deposition Strategy 1 206
A.6 Different features found on the cracked features 206
A.7 Tungsten wall deposited using the Deposition Strategy 2 207
A.8 a) Top view of tungsten plate and copper lateral bars; b) Bottom view of tungsten plate and copper lateral bars; c) Top view of tungsten plate and tantalum lateral bars; d) Side view of tungsten plate and tantalum lateral bars 208

B.1 Geometry and main dimensions of the 3-point bending test (a) and the Small punch test (b) 209
B.2 Wire + Arc Additively Manufactured Tungsten Wall deposited on Tungsten substrate a); Microstructure of a Tungsten wall with suggested dimensioned Gauge Volumes b) 210
B.3 Thin slices of tungsten structures cut using electro-discharge machining 211

C.1 Bead appearance of the tantalum autogenous bead-on-plates welds 215
C.2 Bead appearance of the tantalum single layer deposition 215

D.1 Scheme of the waveform of the current during pulsed deposition 217
D.2 Comparison of the microstructure of the tantalum deposited structure using pulsed current 219

E.1 Micrographs of the tungsten single layer depositions onto molybdenum substrate 223
E.2 Micrographs of the tungsten wall onto molybdenum substrate 224
E.3 Micrographs of the fracture located at the fusion boundary of the tungsten wall onto molybdenum substrate 224
E.4 Electron microscope image of the fractured surface between molybdenum substrate and tungsten wall 224
E.5 Micrographs of the tungsten single layer deposition onto tantalum substrate 225
E.6 Micrographs of the tungsten wall onto tantalum substrate 225
E.7 Micrographs of the fracture located at the fusion boundary of the tungsten wall onto tantalum substrate 226
E.8 Electron microscope image of the fractured surface between tantalum substrate and tungsten wall 226

List of Tables

1.1 List of advantages and disadvantages of the main AM processes 3
1.2 Main impurity elements contained in the two types of powders (wt %) used in the work of Wang et al. [62] 17

2.1 Elemental composition (wt %) of tungsten plates (W Plates) 35
2.2 The combinations of welding speed (TS) and shielding gas composition (SGC) used for the study 36
2.3 Average measured voltage for the different shielding gas compositions 39

3.1 Elemental composition (wt%) of tungsten substrate and wire used and of the structure presented in this study 55
3.2 Process parameters used for the autogenous welds of tungsten substrate 57
3.3 Process parameters used for the stationary arc 57
3.4 WAAM process parameters used for the deposition of unalloyed tungsten 58
3.5 Grinding and polishing procedures used for the microstructural preparation 59

4.1 Values of density (ρ), thermal diffusivity (α), thermal conductivity (k), coefficient of linear thermal expansion (CTE) and specific heat capacity (CP) for different manufacturing routes of tungsten components. Please note that every value refers to a temperature of 293 K 82
4.2 Wire + Arc Additive Manufacturing process parameters used for the deposition of unalloyed tungsten 85
4.3 Elemental composition (wt%) of tungsten substrate, wire and wall used in this study 90
4.4 Average density at 293 K for each sample set, the standard deviation of the measurements; the calculated density at 800 K and 1300 K; the density in percentage respect to the theoretical value 102

5.1 Overview of mechanical properties of pure Ta obtained via different manufacturing routes 116

5.2 Summary of the samples produced and their domination 118
5.3 WAAM process parameters used for the deposition of unalloyed tantalum 118
5.4 Grinding and polishing procedure used for the microstructural preparation 119
5.5 Elemental composition (wt%) of tantalum Substrate, Wire1, Wire2, Wall1 and Wall2 120
5.6 The average hardness value of the Substrate, Wall 1 and Wall 2 with the associated standard deviation and the oxygen content in ppm 127
5.7 Statistical study of the distributions of tantalum hardness values 128
5.8 Tensile properties of the Substrate, Wall1 and Wall 2 in both vertical and horizontal direction 129

6.1 Elemental composition (wt%) of tantalum substrate, wire and wall used in this study 143
6.2 WAAM process parameters used for the deposition of unalloyed tantalum 144
6.3 Rolling parameters used for this study 145
6.4 Grinding and polishing procedures used for the microstructural preparation 146

7.1 Elemental composition (wt%) of tungsten wire (W wire), molybdenum wire (Mo wire) and tantalum substrate (Ta sub) 173
7.2 Typical values of thermal conductivity (K), melting point (T_f), the coefficient of thermal expansion (α) and elastic modulus (E) for tungsten, molybdenum and tantalum 174
7.3 Table 7.3: Values for the process parameters excluded from the factorization 175
7.4 Procedure of deposition of the functionally graded structures 175
7.5 The elemental composition of the local chemical analysis 183

A.1 Process parameters used for the Deposition Strategy 1 203
A.2 Process parameters used for the Deposition Strategy 2 204
A.3 Process parameters used for the Deposition Strategy 3 206

C.1 Process parameters for the tantalum autogenous bead-on-plate welds 214

C.2 Process parameters for the tantalum single layer depositions 214

D.1 Process parameters used for the deposition of tantalum using pulsed current 218

E.1 Process parameters used for the tungsten single layer deposition onto molybdenum substrate 222
E.2 Process parameters used for the deposition of tungsten wall onto molybdenum substrate 222
E.3 Process parameters used for the tungsten single layer deposition onto tantalum substrate 222
E.4 Process parameters used for the deposition of tungsten wall onto tantalum substrate 223

List of Equations

2.1 Heat input per unite length 39

4.1 True coefficient of the linear thermal expansion 87
4.2 Specific heat capacity from Laser Flash Analysis 88
4.3 Density from the method of hydrostatic weighing 88
4.4 Temperature-dependent density 88
4.5 Thermal conductivity from Laser Flash Analysis 89

6.1 Dislocation density from Vickers hardness for cold worked tantalum 157

Chapter 1

Introduction

1.1 Research background

The technological progress in all the industrial sectors is always accompanied by the development of advanced materials and innovative ways of manufacturing high-quality components. Novel materials always lead to an improvement in the effectiveness of the applied science already known and, most importantly, open to completely new areas of applications and to modifications of the design of existing components. Furthermore, the improvement of manufacturing routes also plays an important role in lowering production costs and reducing material waste. Thus, research and development focused on improving the knowledge in manufacturing and materials science results to be one of the key aspects of the technological maturation.

One of the most imminent and promising breakthroughs can be definitely represented by the complete integration of Additive Manufacturing (AM) technologies within the manufacturing supply chain. These manufacturing techniques are capable of producing almost any geometry using a layer-by-layer approach starting from a 3D-model. For this reason, complete freedom is obtainable from the design point of view and absolute control over material utilisation can be achieved. Additive Manufacturing can inspire components with geometries and functionalities which were unavailable until now. Moreover, the AM is heavily pushing the complete digitalisation of the manufacturing processes. However, with all the undeniable potential of the AM process, the complete process understanding has not yet been achieved. In fact, at the current development state, there are various limitations with regards to the in-situ monitoring capabilities to ensure repeatable high-quality depositions.

Furthermore, the limited understanding of the melt dynamics under different heat source leads to unpredictable geometrical and microstructural features of the component.

The AM techniques are differentiated by the raw material forms and the nature of the heat source. In particular, the main raw material forms are powder and wire and, the main heat sources are represented by laser, electric arc and electron beam. Each of them is characterised by specific and unique benefits which can be suitable for a specific application.

The concise schematic of **Figure 1.1** provides an overview of the main AM processes according to the standard ISO/ASTM 52900 [1]. Furthermore, **Table 1.1** reports briefly the main advantages of each technique. In order to illustrate the main industrial sectors which will benefit from the implementation of the AM, a comprehensive schematic with regards the main product areas and materials is reported in **Figure 1.2**.

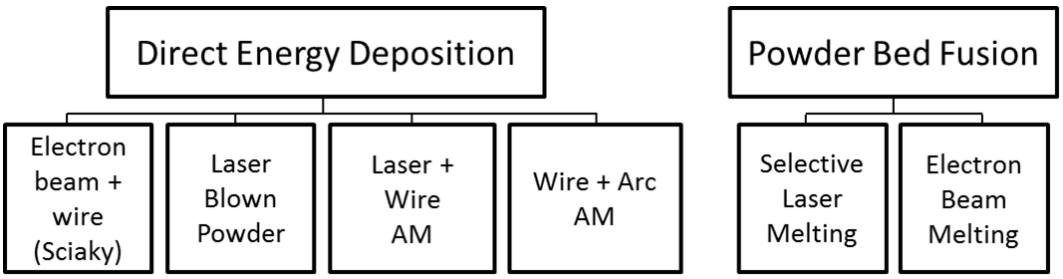

Figure 1.1: Map of the main AM processes according to the ISO/ASTM 52900 [1].

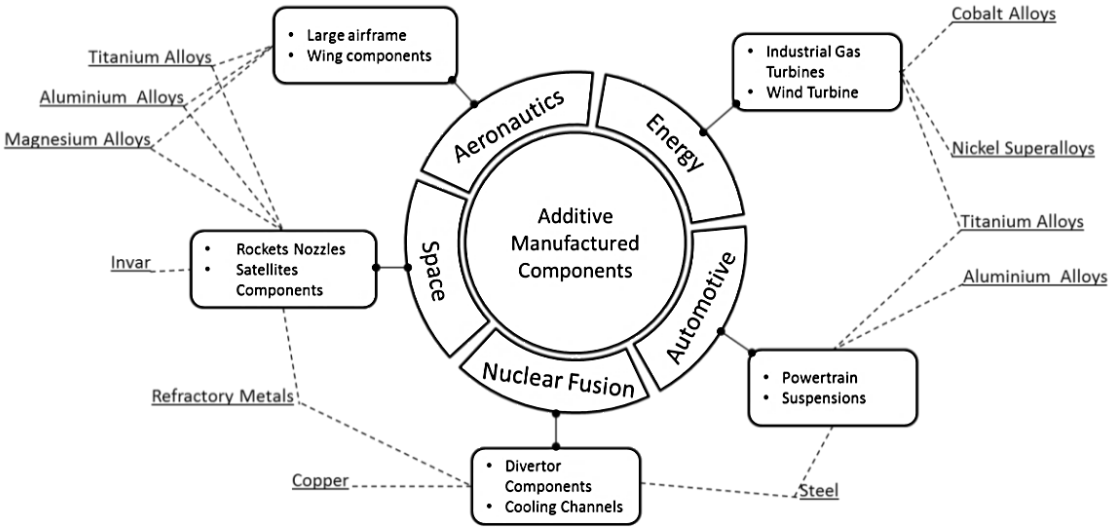

Figure 1.2: Schematic of future AM components in relation to the industrial sectors and the materials.

AM Process	Advantages	Disadvantages
Electron Beam Melting (EBM) [2]	• High geometrical accuracy • High deposition speed • Completely automated • Minimal residual stresses and distortion • Small-scale components	• Limitations in the volumetric build rate • Unrecyclable powder often wasted • Poor Surface finish • Large maintenance • Require Vacuum
Sciaky [3]	• Very high deposition rate • Large-scale components	• Expensive equipment • Large maintenance • Require Vacuum
Selective Laser Melting (SLM) [4]	• As for Electron Beam Melting	• As for Electron Beam Melting but no vacuum or large maintenance required
Laser Blown Powder [5]	• Alloy composition can be continuously varied • High deposition rate • Flexible	• Large columnar grains • Anisotropic mechanical properties • Distortion • High residual stresses • Entrainment of solid clusters into melt-pool • Porosity formation • Limitations on the tool path for complex components • Require Machining
Wire + Arc Additive Manufacturing (WAAM) [6]	• High deposition rate • Inexpensive equipment • Flexible • Large-scale components • Theoretically no size limitations	• As for Blown Powder but no solid clusters and no porosity

Table 1.1: List of advantages and disadvantages of the main AM processes.

1.2 Research sponsorship

This dissertation contains all the findings of two research programmes both aiming to the development of the Wire + Arc Additive Manufacturing (WAAM)

process for refractory metals. In particular, AMAZE project funded by the European Union and a collaborative industry-funded program between Cranfield University and The Atomic Weapons Establishment (AWE). The following sections give a brief description of the two research programmes.

1.2.1 AMAZE project

The AMAZE project ("Additive Manufacturing Aiming Towards Zero Waste and Efficient Production of High-Tech Metal Products") has been an EU-founded research programme which involved 31 organisations, including Cranfield University. The primary goal of the entire project was to produce large defect-free metallic components up to 2 meters in size using additive manufacturing. Cranfield University collaborated on this project with Culham Centre for Fusion Energy (CCFE) to develop the Wire + Arc Additive Manufacturing process for unalloyed tungsten and molybdenum. The raw material was supplied from CCFE. The process development and the characterisation of the deposited materials used have been entirely conducted at Cranfield University, with the valuable support of Swansea University for the measurements of thermal properties.

1.2.2 AWE project

Cranfield University and the Atomic Weapon Establishment (AWE) agreed on developing a research collaboration aiming to lay the foundations of the development and the implementation of the Wire + Arc Additive Manufacturing process for unalloyed tantalum. The duration of the research programme was agreed to be of 24 months. The raw material was supplied from AWE. The process development and the characterisation of the deposited materials used have been entirely conducted at Cranfield University.

1.3 Review of previous research

1.3.1 Nuclear fusion

One of the most researched energy sources to supplant the utilisation of fossil fuel in the near future is the nuclear fusion energy [7]. This technology is based on the production of a large amount of energy in form of electricity by using the heat

from the fusion nuclear reaction controlled and confined within thermo-nuclear reactors [7]. The complete implementation of fusion power is seen as an important step for the energy sector because it can replace the nuclear fission and so decrease the amount of nuclear waste and radioactivity generated.

The nuclear fusion reaction involves two or multiple atoms to combine into a new single and more massive atom releasing energy. This because the total mass of the new atom is appreciably smaller than the sum of the parent atoms so that the difference in mass is transformed in energy.

The most common nuclear fusion reaction is the one that involves the utilisation of hydrogen nuclei, tritium and deuterium (**Figure 1.3**), as parent reactants to form helium nuclei as products of the reaction (**Figure 1.3**). The same reaction constantly occurs on the Sun, where the enormous gravity pushes the lighter helium nuclei together with a high enough force to ignite the reaction.

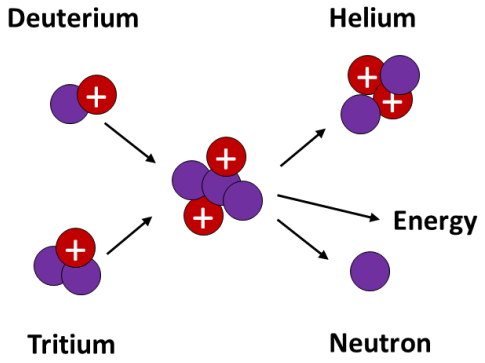

Figure 1.3: Schematisation of the nuclear fusion reaction.

Since the conceptualisation of the possibility to use nuclear fusion reaction as a sustainable source of energy on Earth, multiple design and concepts of fusion reactors have been proposed [7]. Among these, the Tokamak has been chosen as the real candidate for commercialisation [7]. This machine uses strong magnetic fields to confine the nuclear fusion reaction within the middle of a toroidal chamber, which favours the acceleration of the particles for the ignition. The research on this specific design represents the proof of concept for future reactors as DEMO (DEMOnstration Power Station) and ITER (International Thermonuclear Experimental Reactor) (**Figure 1.4**) [7].

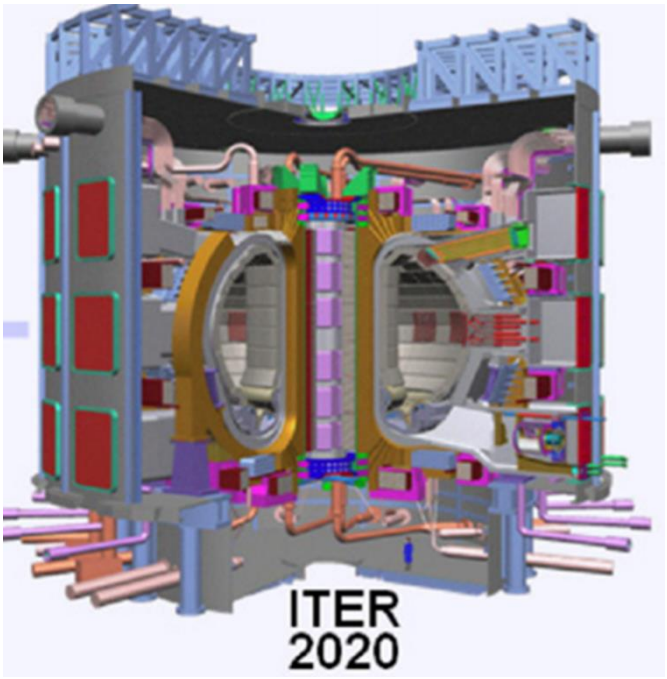

Figure 1.4: Schematisation of the cross-section of the International Thermonuclear Experimental Reactor.

Material selection is a key aspect for the safe implementation of the nuclear fusion technology. High-temperature strength and good thermal conductivity are fundamental properties of the material intended to operate within the reactor [8–11]. Tungsten has been chosen over low-Z materials like carbon and beryllium due to the considerably lower erosion under high-heat fluxes [11,12] and also because of their high melting point, strength at high temperatures, high thermal conductivity and low coefficient of thermal expansion [8,13]. In fact, The ITER organisation has proposed and approved that a full tungsten nuclear divertor will be installed from Day 1 instead of carbon/graphite monoblock [12,14,15].

For these reasons, tungsten and its alloys are considered the ideal candidate as plasma facing material and also structural material [8–11]. In particular, tungsten-based materials will be used for the nuclear divertor and for the nuclear first wall on the reactor [8–11].

The nuclear divertor is one of the high heat flux components of the fusion reactor [10] and its main role is the remove unburnt fuel, eroded particles and other waste in order to keep high the quality of the plasma [16]. **Figure 1.5b** reports a schematisation of one single divertor cassette, which forms the entire

divertor system at the bottom part of the reaction chamber [15], as shown in **Figure 1.5a**. The divertor system has been designed using different modular parts for easier handling and maintenance [16]. Each cassette is approximately 2 metres in height, 5 metres in length and 0.5 metres in width [17] and armours of plasma facing materials are installed on the upper surface. The first wall (**Figure 1.5a**) is the primary wall of the reaction chamber which protects all the other components of the reactor placed behind it [17]. The main role is confinement and protection.

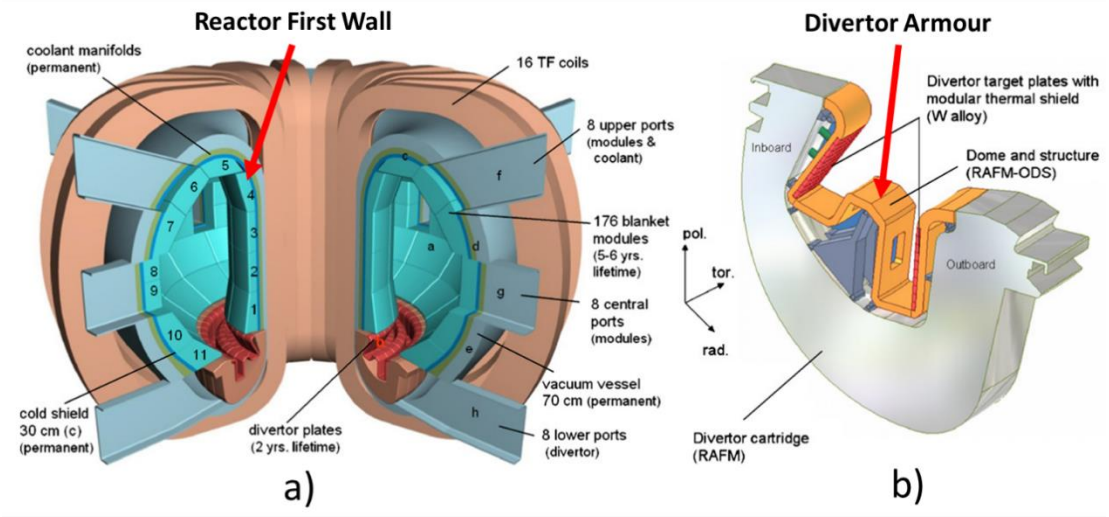

Figure 1.5: Schematisation of the nuclear reactor first wall (a) and the divertor (b).

These components will operate in an aversive environment which will lead to high erosion by incident particles and high heat fluxes from the plasma [8,18]. For the divertor maximum temperatures of around 1700°C instead maximum temperature of around 1000°C will be seen by the first wall components [8].

Tungsten is clearly the candidate material for plasma-facing components in future fusion devices. Tungsten can surely withstand the expected high heat load due to its high melting point, high thermal conductivity, and relatively low thermal expansion. In addition, it is a low-activating element with a high resistance against sputtering and erosion [16,19].

However, the operative window of tungsten components within the nuclear fusion reactor is limited by its brittleness at room temperature [16] and its low fracture toughness [8]. This intrinsic brittleness is mainly due to the high activation energy of the screw dislocations [8].

The needs for a divertor armour material are high crack resistance and compatibility with plasma–wall interaction phenomena [8,18,20]. Instead, a good ductility and toughness over the operational temperature range are needed for the first wall components [8,18,20]. Furthermore, as all the components facing the internal side of the reactor will be actively cooled using helium, the material utilised need to be able to withstand high-temperature gradients and high thermal stresses [18]. The completed implementation of tungsten for these critical components need to ensure a low ductile-to-brittle transition, and enhanced fracture toughness and a high recrystallisation temperature [7].

The main tensile properties and thermal properties of pure tungsten for advanced application in the fusion environment are reported in the studies of Yin et al. [7] and Fukuda et al. [21].

1.3.2 Physical metallurgy of refractory metals

Refractory metals are a class of metals characterised by very high melting points and high densities. They also show a good combination of strength over a large temperature range and high thermal and electrical conductivity [22,23]. The refractory metals are tungsten (W), tantalum (Ta), molybdenum (Mo), niobium (Nb) and rhenium (Re) [23]. All those metals are body-centred cubic (bcc) except rhenium which is hexagonal close-packed (hcp). Tungsten, tantalum and molybdenum solidify along the preferred crystallographic direction <001>, as most of the bcc metals [24].

Refractory metals as tungsten and molybdenum are characterised by a marked ductile-to-brittle temperature transition (DBTT) over a specific temperature range [25]. In particular, below this temperature range, they are brittle instead, their plasticity and ductility increase when they are heated at temperatures above the transition [25,26]. This is mainly due to an enhanced mobility of screw dislocations based on a thermally activated mechanism [25]. The DBTT of tungsten was not exactly determined but it stays in a large range from 150°C to 600°C.

Tungsten usually experiences brittle fractures at room temperature, and only above its DBTT, the failure mechanism experiences a slight change towards a

ductile fracture. The DBTT for tungsten was found to be dependent on grain size, dislocation density, interstitial concentration and the applied strain rate [25,26].

In general, the low fracture toughness, the high ductile-to-brittle-transition temperature and the high recrystallization temperature of tungsten represent the limiting factors for the manufacture of tungsten components.

An effective way to decrease the DBTT of tungsten is by alloying it with rhenium [27,28]. The ductility of tungsten can also be improved by high deformation by cold work, such as cold rolling [27,29]. This increases the dislocation density and activity at lower temperature promoting a ductile deformation mechanism [27]. An additional method is to create multilayers of ductile tungsten foils to create a bulk tungsten composites [27].

The phase diagrams of the alloys formed between tungsten and tantalum, tungsten and molybdenum and tantalum and molybdenum are reported (**Figure 1.6**, **Figure 1.7** and **Figure 1.8**). All of them are binary diagrams and the two components results to be completely miscible and soluble within each other. The diagrams present the melting points of the pure elements on the Y-axis connected by the solidus and the liquidus lines.

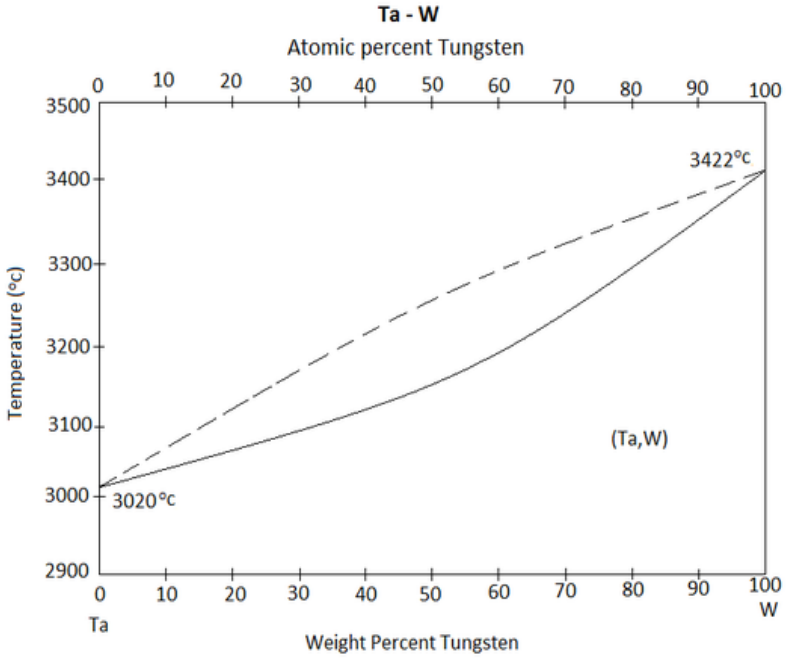

Figure 1.6: Tantalum-tungsten phase diagram [30].

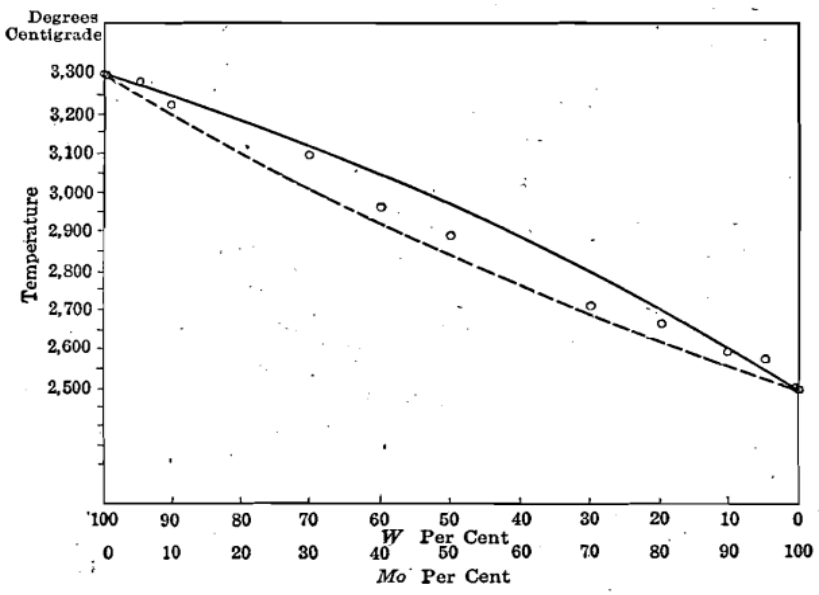

FIG. 3.—EQUILIBRIUM DIAGRAM OF TUNGSTEN AND MOLYBDENUM.

Figure 1.7: Tungsten-molybdenum phase diagram [31].

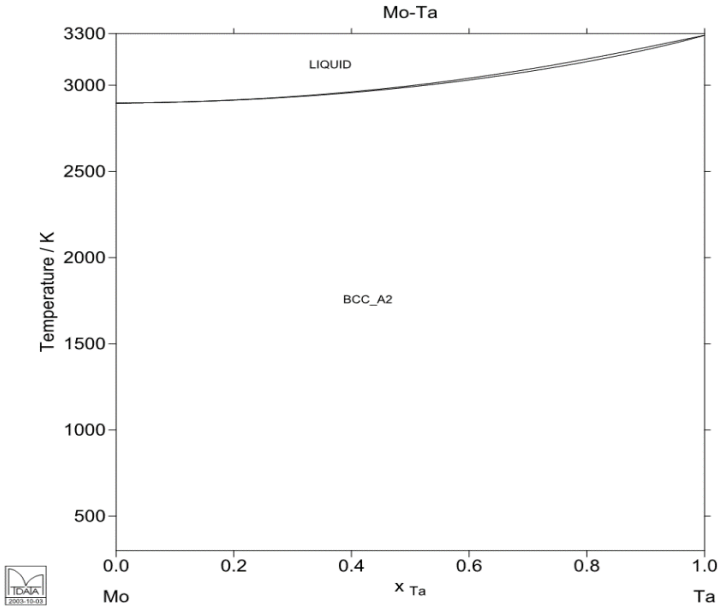

Figure 1.8: Molybdenum-tantalum phase diagram [32].

1.3.3 Influence of alloying elements and interstitial elements

The utilisation of tungsten has been limited by its intrinsic low-temperature brittleness at room temperature [28]. A well-known way of improving the ductility of tungsten is alloying pure tungsten with other elements.

Tungsten-rhenium alloys exhibit a significantly lower ductile-to-brittle transition and improved strength than unalloyed tungsten at high temperatures

[23,33]. Tungsten-rhenium alloys present an improved ductile already with the addition of 1% of rhenium [28]. In particular, for these alloys, the temperature and the strain rate dependence of the yield strength are decreased by alloying with rhenium [28]. These improvements seem to be caused by an increased plastic strain at crack tips as a result of increased dislocation mobilities caused by the presence of rhenium [28].

The improved fabricability and ductility of tungsten-rhenium alloys have been also attributed to the increased solubility of interstitials such as nitrogen, carbon, oxygen and sulphur [23]. Dispersion strengthening and precipitation hardening of tungsten are also considered effective ways to increase the high-temperature strength and creep resistance of tungsten [23].

Alloying of tantalum is usually required to improve the strength at high temperature while preserving good ductility and inertness [23,33]. The most common tantalum-tungsten alloys are Ta-2.5W, Ta-7.5W, and Ta-10W. These alloys combine the corrosion resistance of tantalum and the high strength at elevated temperatures of tungsten [23,33]. Furthermore, alloys with tantalum and niobium (mainly Ta-40Nb alloy) have been characterised by high melting point, high corrosion resistance and good cold processing and they are widely used in chemical and aerospace sectors [34].

Interstitial elements such as carbon, nitrogen and oxygen are likely to deteriorate the properties of tungsten. In particular, carbon, oxygen and nitrogen have a low solubility within tungsten and they tend to increase its brittleness and reduce its fracture toughness [35,36].

They tend to segregate at the grain boundaries promoting the formation of brittle compounds as carbides and oxides [37]. These compounds usually form a thin layer along the grain boundary which initiates the fracture and, also, limits the mobility of the dislocation.

In tungsten, the ductile-to-brittle transition increases as the content of oxygen increases. In particular, a large increase has been seen when comparing tungsten samples with 4 ppm of oxygen and components with 50 ppm of oxygen [38]. The oxygen additions also produced a progressive lowering of the ultimate

tensile strength [38]. For these reasons, oxygen levels should be maintained below 20 ppm to avoid deterioration of the properties [38].

Unlike tungsten, tantalum shows a high solubility for interstitials, which hardly segregate at the grain boundaries. This is one of the main causes of its improved ductility at room temperature respect to tungsten [39,40]. Despite this aspect, the mechanical properties of tantalum are highly influenced by the purity [40–42]. In particular, interstitials such as nitrogen and oxygen have a strong effect on hardness and yield strength. It has been reported about the solid solution hardening due to oxygen as interstitial for vanadium, niobium and tantalum [43]. The effect has been addressed to the misfit between the oxygen and the metal atoms [43].

1.3.4 Oxides of tungsten and tantalum

The oxides of tungsten are numerous and most of them are non-stoichiometric oxides derived as intermediates of the extraction reactions [44,45]. In general, there are three main forms of stoichiometric tungsten oxide and these are tungsten trioxide (WO_3), tungsten dioxide (WO_2) and tungsten pentoxide (W_2O_5) [44,45]. The formation of different oxides prevalently depends on the oxygen partial pressure within the atmosphere [44,45]. Tungsten starts to react with oxygen to form tungsten oxide at a temperature around 400°C, which become significant at a temperature above 600°C [44,46]. The oxidation rate usually follows a logarithmic trend at low temperature and parabolic trend at high temperatures [44,46]. At very high temperature, the oxides become volatile and start to sublimate at a temperature as low as 800°C [44,46].

The formation of these oxide limits the utilisation of tungsten for high-temperature applications within an oxygen-rich atmosphere and for this reason the tungsten components must be coated with protective materials [47].

Tantalum is also a reactive metal and it reacts with oxygen at rates proportional to the temperature. The most common tantalum oxide is the tantalum pentoxide (Ta_2O_5) [48]. This oxide gives to tantalum the characteristic high corrosion resistance as it is not attached by most of the acid solutions [48]. Furthermore, this oxide is characterised by a pronounced polymorphism. In

particular, β-Ta_2O_5 is the low-temperature form, instead, α-Ta_2O_5 is the high-temperature form [49]. The transition is reversible and occurs around 1000°C [49]. The tantalum pentoxide is mainly used for the production of electronic, such as tantalum capacitors, because of its high dielectric constant [50]. Furthermore, this oxide has good thermal and chemical stability [48]. All these characteristics lead tantalum to be optimally utilised for high-temperature applications, even in the atmosphere with a high content of oxygen.

1.3.5 Extraction of tungsten and tantalum

Tungsten is present in several ores on Earth. Among these, wolframite [$(Fe,Mn)WO_4$] and scheelite ($CaWO_4$) are the one commercially mined and extracted. Wolframite accounts for about 70% of the total tungsten resources in the world, and scheelite accounts for about 30%. The countries that produce most of the tungsten are China, United States of America and Russia.

The initial phases of the extraction of tungsten from these ores aim to produce Tungsten (VI) oxide (WO_3) from the wolframite and scheelite by using a series of reactions with alkali and hydrochloric acid (HCl). When WO_3 is produced, it is reacted with carbon or hydrogen to be reduced to the tungsten pure metal powder. The equations of reduction are indicated below:

$$2\ WO_3 + 3\ C \rightarrow 2\ W + 3\ CO_2$$

$$WO_3 + 3\ H_2 \rightarrow W + 3\ H_2O$$

Due to the difficulties in the casting of pure tungsten in ingots, caused by its high melting point, tungsten is produced as a powder which is successively sintered and hot formed during the manufacturing process of tungsten components.

Tantalum is available on Earth in different ores such as tantalite [$(Fe,Mn)Ta_2O_6$], columbite [$(Fe,Mn)Nb_2O_6$] and tapiolite [$(Fe,Mn)(Nb,Ta)_2O_6$]. These ores are prevalently present in Rwanda, Democratic Republic of Congo and Brazil. Refining these ores to produce pure tantalum is a difficult process as it is difficult to separate from niobium. In fact, tantalum and niobium have large similarities with regards their chemical behaviour and radius of the nuclei.

The extraction process begins by leaching the ores with hydrofluoric acid together with sulfuric acid or hydrochloric acid. This forms tantalum pentoxide (Ta_2O_5) which is then reduced to tantalum powder.

1.3.6 Estimation of welding efficiency

The consolidation of the welded material by using any welding techniques available usually depends markedly on the welding parameters [51–56]. In particular, the heat input and the welding speed are the main factors affecting the microstructure of the component [51–56].

The influence of these factors on the microstructure and consolidation of the welded material can be directly measured by extensive testing and measurements, which can be used to build a model for the specific process and material [57–59]. The correct measurement techniques strongly depend on the nature of the heat source, which can be laser, electron beam or electric arc. Although these measurements could give a precise evaluation of the dependence between process parameters and consolidation, reconstruct and ensure the precise welding condition could be challenging.

For welding processes that employ an electric arc as heat source, the heat input depends on different variables as the composition of the shielding gas, shielding gas flow rate, welding current, welding speed and the distance between electrode and workpiece [60].

Fundamental dimensional functions can be also used to estimate the influence of the process parameters on the welded material. In particular, weld pool dimensions and the hardness profile along the welded material can be used as fundamental data to calculate the heat input and the process efficiency.

In fact, it is possible to calculate the volume of melted material by using the weld pool dimensions. Using the specific properties of the metal such as heat capacity and latent heat of fusion, it is possible to calculate the energy required to liquefy the specific volume of the material. Comparing this and the machine heat input, it possible to calculate the efficiency of the welding process for the parameters used. Furthermore, the welded material usually present different values of hardness when compared to the parent metal. For this reason, the weld

pool dimensions can be measured by using the hardness profile along the welded material.

1.3.7 Additive Manufacturing of refractory metals

As already reported in **Figure 1.2**, improvements in the manufacturing route of functional refractory metal components can have a considerable impact on space and nuclear fusion sectors. This is mainly due to the unique high melting point and high density of the refractory metals which allow them to be used in high-temperature applications, as for instance, rocket nozzles or nuclear fusion divertors. Furthermore, the elevated cost of these metals represents one of the biggest drivers for the implementation of cost-effective manufacturing routes. Despite, the constant request for better performing materials and innovative production routes within these sectors, the literature on AM of refractory metals was found to be very scarce. Only few investigations are available, and they entirely refer to the AM processes for unalloyed tungsten and tantalum that employ a laser as the heat source and powder as the feedstock evenly distributed on a deposition bed.

1.3.7.1 Tungsten

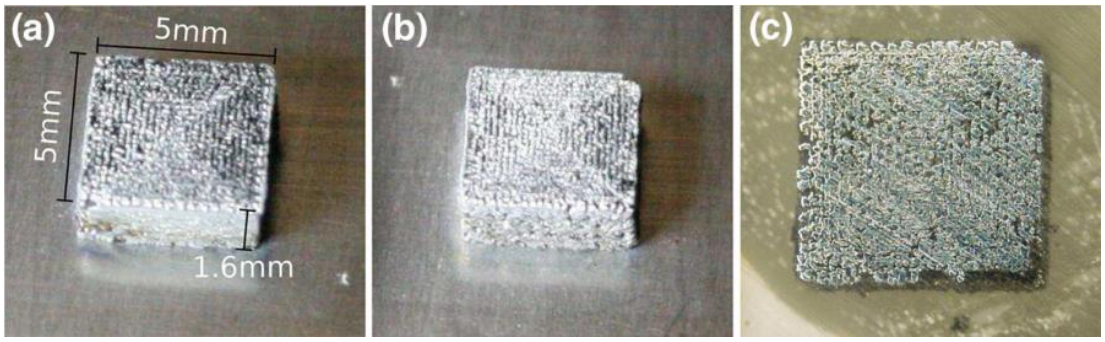

Figure 1.9: Pictures of the tungsten cube manufactured by Nie et al.[61], reporting the total dimensions of the deposit.

Nie et al.[61] produced tungsten cubes using selective laser melting (SLM), which are shown in **Figure 1.9**. The samples were produced with an average layer height of around 15 μm and presented light oxidation, discontinuities and porosity. The study demonstrates a lack of data with regards to the powder composition, oxygen levels during the deposition and the eventual formation of micro-cracks the samples.

Wang et al. [62] claimed to have produced pure tungsten components using SLM achieving densities as close as 96 % of the theoretical density (**Figure 1.10**). They showed that when using polyhedral powder there was a marked occurrence of balling resulting in large defects and pores (**Figure 1.11a**). Contrarily, when using a spherical powder, continuous tracks were achieved although a dense network of micro-cracks and porosity was present (**Figure 1.11b**).

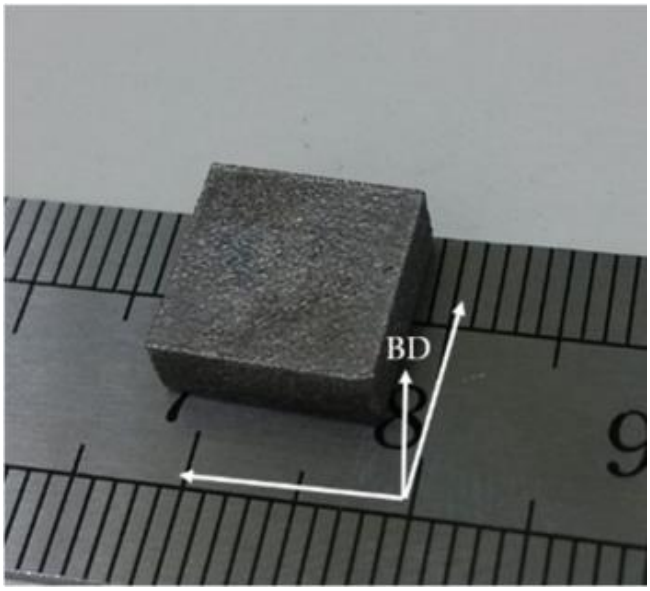

Figure 1.10: Photograph showing the pure tungsten part fabricated by SLM by Wang et al. [62].

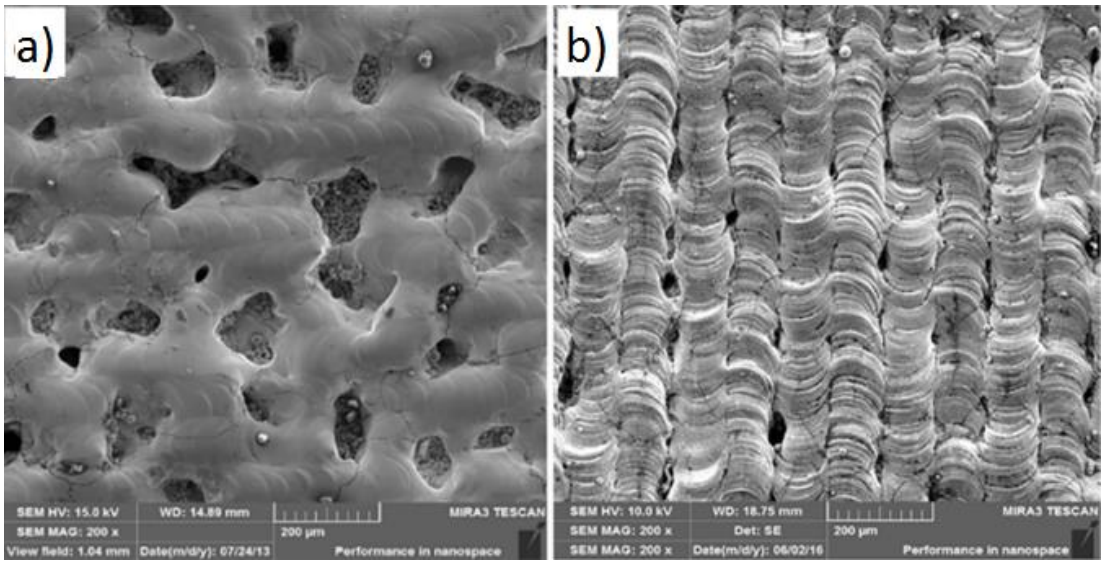

Figure 1.11: SEM images showing the top surface of tungsten parts fabricated using (a) polyhedral and (b) spherical powders by Wang et al. [62].

The oxygen level during the deposition was not indicated. The content in wt.% with regards to the concentration of carbon, oxygen and nitrogen of the powder used in the study of Wang et al. [62] is indicated in **Table 1.2**.

Powder Type	C [wt%]	O [wt%]	N [wt%]
Polyhedral	0.0066	0.021	0.0052
Spherical	0.0083	0.010	0.0018

Table 1.2: Main impurity elements contained in the two types of powders (wt %) used in the work of Wang et al. [62].

The marked occurrence of cracks could be directly caused by the considerable presence of these interstitial elements. In fact, it is well known that carbon, oxygen and nitrogen usually diffused at the grain boundaries (powder surface in this case) and lead to the formation of brittle carbides, oxides and nitrides.

Iveković et al. [63] have also deposited tungsten components using SLM achieving the maximum density of 94.4% of the theoretical density. The networks of cracks showed in **Figure 1.12** have always been found for every parameter used, even after pre-heating of the substrate at 400°C (**Figure 1.12b**). The oxygen level was reported to be kept constant at 150-200 ppm during deposition, but the impurity levels of the powder used were not indicated.

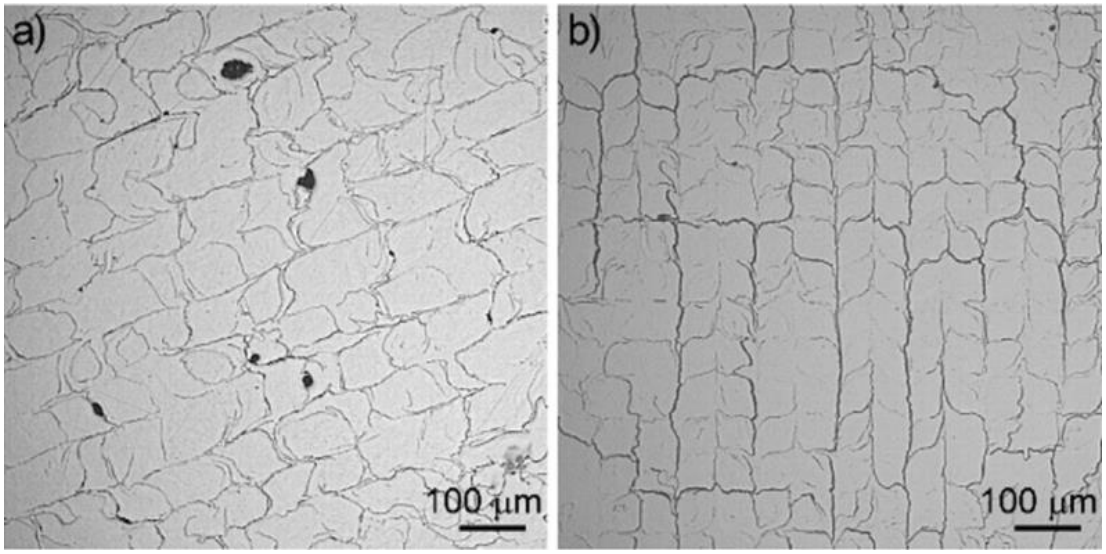

Figure 1.12: Micrographs of polished cross-sections of tungsten deposited (a) without preheating and (b) with baseplate preheating to 400 °C in the work of Iveković et al. [63].

The solidification dynamics for tungsten powder and the relative issues were studied by Zhou et al. [64] using SLM. They found that the high surface tension and viscosity of tungsten induced a relative slow wetting and spreading speeds enhancing the balling phenomena (**Figure 1.13a**). Moreover, cavities and pores with entrapped not melted powder and cracks were also frequently found (**Figure 1.13b-c**). A maximum density of 82.9% of the theoretical density was achieved.

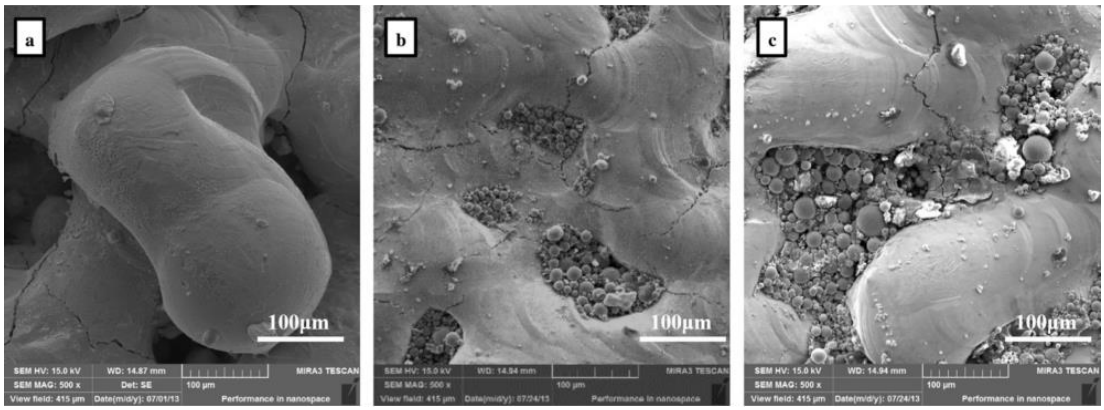

Figure 1.13: SEM images of the top surface of the different tungsten specimens deposited using SLM in the work of Zhou et al. [64].

In general, there are two main problems which greatly affect the integrity of tungsten components produced via SLM: the level of impurities of the powder and the high-thermal shock induced by the laser. Both of these factors increase the likelihood to obtain serious networks of cracks and pores.

1.3.7.2 Tantalum

Zhou et al. [65]. conducted a comprehensive study with regards to the SLM process for unalloyed tantalum, analysing microstructure and mechanical properties of the deposits. Micro-pores and micro-cracks were found within the build when the laser power was not optimised. The authors claim to have improved the hardness and the tensile properties of the deposited tantalum with respect to the wrought material.

However, the powder used for this study was characterised by an oxygen concentration of 0.18 wt%, which is a considerably high level of oxygen. In fact, it is known that oxygen leads to a strengthening effect on tantalum. For this reason, a

large loss in ductility was reported accompanied by a brittle-like fracture, which is absolutely not typical of unalloyed tantalum.

Moreover, Zhou et al. [65] were measuring an average hardness of 450 Hv for the deposited structure, much higher than the hardness of around 90-100 Hv of tantalum components manufactured using traditional manufacturing routes.

In the work of Thijs et al. [66], the SLM process was studied for pure tantalum focusing mainly on the microstructural evolution and mechanical properties. Almost fully-dense (99.6% of the theoretical density) tantalum components were produced (**Figure 1.14**). No cracks and no loss in ductility were registered. Epitaxial grain growth through the layers was observed and led to the formation of large columnar grains and the development of a strong texture. The anisotropy within the microstructure has been seen for the yield strength as well.

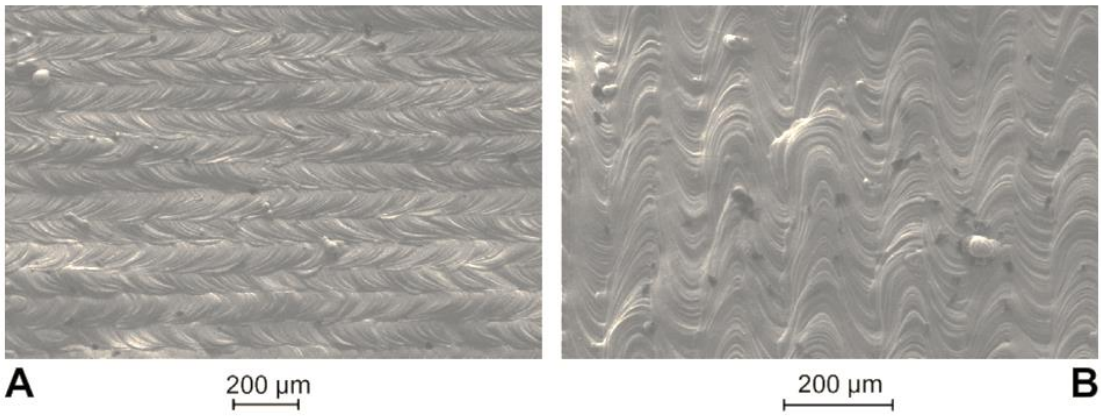

Figure 1.14: SEM pictures of the top surface of as-built tantalum SLM parts from the work of Thijs et al. [66].

Generally, the marked ductility of tantalum at room temperature allows obtaining deposits which are free from internal cracks. A high level of impurities could lead to the formation of cracks because they act as tantalum embrittlement agents.

1.3.8 Research gap

The points indicated below correspond to the research gaps found in the literature related to the development of additive manufacturing processes for the deposition of refractory metals, such as tungsten and tantalum. These gaps

motivated the research presented in this thesis.

- The lack of investigations on the Wire + Arc Additive Manufacturing process for refractory metals revealed a clear knowledge gap with regards the suitable process parameters to use for these materials as well as the requirements for the efficient shielding to prevent oxidation. Furthermore, no data are available on the microstructural development and the properties of both tungsten and tantalum manufactured via WAAM;

- The final application of these metals within the defence and the nuclear section mostly requires the ability to deposit large-scale components using AM. No investigations which aim to the production of sizable parts is currently reported in the literature;

- Generally, up until the most recent research, there is no completely suitable AM process to produce crack-free fully-dense tungsten component, for advanced and critical applications;

- Lastly, no research has been reported to study the feasibility of the production of functionally graded structures involving dissimilar refractory metals when using an AM process.

1.4 Research aim and objectives

The aim of the research presented is to investigate the Wire + Arc Additive Manufacturing process for the deposition of large-scale components in refractory metals, as tungsten and tantalum, in order to develop an alternative manufacturing technique for these metals. The objectives of the research are the following:

- to identify an operative window for the controlled melting of tungsten plates through studying the effect of welding speed and arc gas composition on autogenous bead-on-plate welds;

- to design a suitable deposition strategy for large-scale tungsten components developing appropriate process parameters and clamping system;

- to characterise and understand the variation of the thermal properties of tungsten structures over temperature and their relation with the microstructure;

- to evaluate the relationship between the microstructure and the mechanical properties of tantalum structures deposited via WAAM and compare them with the commercially available tantalum components;

- to assess the effect of cold rolling on the microstructure of tantalum WAAM components, in particular, with regards to its effect on microstructure refinement and texture;

- to design a suitable deposition strategy for the deposition of functionally graded structures with smooth and regular variation in composition and hardness.

1.5 Outline of the thesis

The current dissertation has been structured in a paper format according to the guidelines and requirements given by Cranfield University. The thesis has been structured in a series of distinct chapters, which cover the different objectives of the research work. A brief introduction, a general discussion and a conclusion have been incorporated to improve the readability and the continuity between the chapters.

The introduction has been used to frame the research programme while the discussion section has been used to demonstrate the coherence of the individual chapters and the impact on research and industrial development. Each chapter contains a title, a list of authors, an abstract, an introduction, a methodology and

results and discussion section. Furthermore, the conclusion of each chapter is followed by the list of references used in the correspondent chapter.

This specific structure has been chosen so that each chapter can be submitted for peer-reviewed publication with minimum modification. Furthermore, the thesis format has been chosen based on the fact that limited amount of available literature is currently available. The thesis outline has been structured as follows:

- **Chapter 1** contains a brief introduction to the research background, the project sponsorships and a brief review of existing literature about the additive manufacturing of tantalum and tungsten. Moreover, the research gaps, the research aim and objectives complete the research overview;

- **Chapter 2** contains the results of **Paper A** titled: "*Effect of the shielding gas composition and welding speed on autogenous welds of unalloyed tungsten plates*". It describes the effect of the shielding gas composition and the welding speed on autogenous bead-on-plates welds of unalloyed tungsten plates. An operative working window has been designed based on these fundamental process parameters based on the occurrence of welding defects;

- **Chapter 3** contains the results of **Paper B** titled: "*Process development of Wire + Arc Additive Manufacture for the production of large-scale unalloyed tungsten components*". It describes the process development of Wire + Arc Additive Manufacture for the production of large-scale unalloyed tungsten components. In particular, the process has been optimised with regards to the substrate orientation, with respect to the heat source, and the wire feeding orientation achieving defect-free fully-dense tungsten components;

- **Chapter 4** contains the results of **Paper C** titled: "*Wire + Arc Additive Manufacturing process of unalloyed tungsten components and the correlation*

between microstructure and thermal properties". It is based on the characterisation of the thermal properties and the microstructure of as-deposited and annealed tungsten structures produced via Wire + Arc Additive Manufacture. In particular, the linear coefficient of thermal expansion, the thermal diffusivity and the heat capacity over considerable temperate range have been measured for two orthogonal directions using dilatometry and laser flash analysis under an inert atmosphere;

- **Chapter 5** contains the results of **Paper D** titled: "*Process development, microstructure and mechanical properties of two different unalloyed tantalum wires deposited via Wire + Arc Additive Manufacture*". It describes the process development, the microstructure and the mechanical properties of two different tantalum wires deposited via Wire + Arc Additive Manufacture. An anisotropic microstructure and mechanical properties have been found for the tantalum structure deposited;

- **Chapter 6** contains the results of **Paper E** titled: "*Grain refinement in unalloyed tantalum structure deposited using Wire + Arc Additive Manufacture and vertical cold rolling*". It describes the effect of vertical cold rolling on the grain refinement of tantalum structures deposited using WAAM; Not only a great reduction in size has been achieved but also the refined microstructure presented completely random texture;

- **Chapter 7** contains the results of **Paper F** titled: "*Investigation of Wire + Arc Additive Manufacture for the production of functionally graded structures by refractory and its characterisation*". It reports the results of the feasibility study and the characterisation of multiple functionally graded structures in refractory metals using Wire + Arc Additive Manufacturing. A single structure made out of two functionally graded structures respectively between tantalum and molybdenum and between molybdenum and tungsten has been successfully deposited with a regular gradient in

composition and hardness;

- **Chapter 8** presents an overall discussion about the outcome of the whole research programme. In this chapter, the importance of the entire research programme and the contributions to knowledge are discussed. Moreover, the implications for both research and industrial applications are discussed. This chapter is completed with the main research conclusions.

- The last section includes **Appendices**, which contain additional information to support the research.

1.6 Bibliography

1. INTERNATIONAL STANDARD ISO / ASTM Additive manufacturing — General principles — Terminology. 2015. Available at: DOI:10.1520/ISOASTM52900-15
2. Murr LE., Gaytan SM., Ramirez DA., Martinez E., Hernandez J., Amato KN., et al. Metal Fabrication by Additive Manufacturing Using Laser and Electron Beam Melting Technologies. Journal of Materials Science and Technology. The Chinese Society for Metals; 2012; 28(1): 1–14. Available at: DOI:10.1016/S1005-0302(12)60016-4
3. Stawovy MT. Comparison of LCAC and PM Mo deposited using Sciaky EBAM™. International Journal of Refractory Metals and Hard Materials. Elsevier; 2018; 73(February): 162–167. Available at: DOI:10.1016/j.ijrmhm.2018.02.009
4. Yap CYY., Chua CKK., Dong ZLL., Liu ZHH., Zhang DQQ., Loh LE., et al. Review of selective laser melting: Materials and applications. Applied Physics Reviews. 2015; 2(4). Available at: DOI:10.1063/1.4935926
5. Jones J., Whittaker M., Buckingham R., Johnston R., Bache M., Clark D. Microstructural characterisation of a nickel alloy processed via blown powder direct laser deposition (DLD). Materials and Design. Elsevier Ltd; 2017; 117: 47–57. Available at: DOI:10.1016/j.matdes.2016.12.062
6. Williams SW., Martina F., Addison AC., Ding J., Pardal G., Colegrove P. Wire + Arc Additive Manufacturing. Materials Science and Technology. 2016; 32(7): 641–647. Available at: DOI:10.1179/1743284715Y.0000000073
7. Yin C., Terentyev D., Pardoen T., Bakaeva A., Petrov R., Antusch S., et al. Tensile properties of baseline and advanced tungsten grades for fusion applications. International Journal of Refractory Metals and Hard Materials. 2018; 75(April): 153–162. Available at: DOI:10.1016/j.ijrmhm.2018.04.003
8. Rieth M., Boutard JL., Dudarev SL., Ahlgren T., Antusch S., Baluc N., et al. Review on the EFDA programme on tungsten materials technology and science. Journal

of Nuclear Materials. 2011; 417: 463–467. Available at: DOI:10.1016/j.jnucmat.2011.01.075

9. Pamela J., Bécoulet A., Borba D., Boutard JL., Horton L., Maisonnier D. Efficiency and availability driven R&D issues for DEMO. Fusion Engineering and Design. 2009; 84(2–6): 194–204. Available at: DOI:10.1016/j.fusengdes.2009.02.028
10. Norajitra P., Abdel-Khalik SI., Giancarli LM., Ihli T., Janeschitz G., Malang S., et al. Divertor conceptual designs for a fusion power plant. Fusion Engineering and Design. 2008; 83(7–9): 893–902. Available at: DOI:10.1016/j.fusengdes.2008.05.022
11. Bolt H., Barabash V., Federici G., Linke J., Loarte A., Roth J., et al. Plasma facing and high heat flux materials - Needs for ITER and beyond. Journal of Nuclear Materials. 2002; 307–311: 43–52. Available at: DOI:10.1016/S0022-3115(02)01175-3
12. Kaufmann M., Neu R. Tungsten as first wall material in fusion devices. Fusion Engineering and Design. 2007; 82(5–14): 521–527. Available at: DOI:10.1016/j.fusengdes.2007.03.045
13. Nguyen BN., Henager CH., Overman NR., Kurtz RJ. A multiscale microstructural approach to ductile-phase toughened tungsten for plasma-facing materials. Journal of Nuclear Materials. Elsevier B.V; 2018; 508: 371–384. Available at: DOI:10.1016/j.jnucmat.2018.05.048
14. Pitts RA., Carpentier S., Escourbiac F., Hirai T., Komarov V., Lisgo S., et al. A full tungsten divertor for ITER: Physics issues and design status. Journal of Nuclear Materials. Elsevier B.V.; 2013; 438(SUPPL): S48–S56. Available at: DOI:10.1016/j.jnucmat.2013.01.008
15. Hirai T., Panayotis S., Barabash V., Amzallag C., Escourbiac F., Durocher A., et al. Use of tungsten material for the ITER divertor. Nuclear Materials and Energy. Elsevier Ltd; 2016; 9(2016): 616–622. Available at: DOI:10.1016/j.nme.2016.07.003
16. Norajitra P., Boccaccini L V., Diegele E., Filatov V., Gervash A., Giniyatulin R., et al. Development of a helium-cooled divertor concept: Design-related requirements on materials and fabrication technology. Journal of Nuclear Materials. 2004; 329–333(1–3 PART B): 1594–1598. Available at: DOI:10.1016/j.jnucmat.2004.04.137
17. Ioki K., Barabash V., Cardella A., Elio F., Gohar Y., Janeschitz G., et al. Design and material selection for ITER ® rst wall / blanket , divertor and vacuum vessel. Journal of Nuclear Materials. 1998; 263: 74–84.
18. Hirai T., Pintsuk G., Linke J., Batilliot M. Cracking failure study of ITER-reference tungsten grade under single pulse thermal shock loads at elevated temperatures. Journal of Nuclear Materials. Elsevier B.V.; 2009; 390–391(1): 751–754. Available at: DOI:10.1016/j.jnucmat.2009.01.313
19. Davis JW., Barabash VR., Makhankov A., Plöchl L., Slattery KT. Assessment of tungsten for use in the ITER plasma facing components. Journal of Nuclear

Materials. 1998; 258–263(PART 1 A): 308–312. Available at: DOI:10.1016/S0022-3115(98)00285-2

20. Blagoeva DT., Opschoor J., Van Der Laan JG., Sârbu C., Pintsuk G., Jong M., et al. Development of tungsten and tungsten alloys for DEMO divertor applications via MIM technology. Journal of Nuclear Materials. Elsevier B.V.; 2013; 442(1–3 SUPPL.1): S198–S203. Available at: DOI:10.1016/j.jnucmat.2013.01.004

21. Fukuda M., Hasegawa A., Nogami S. Thermal properties of pure tungsten and its alloys for fusion applications. Fusion Engineering and Design. Elsevier; 2018; 132(March): 1–6. Available at: DOI:10.1016/j.fusengdes.2018.04.117

22. Cole NC., Gilliland RG., Slaughter GM. Weldability of Tungsten and Its Alloys. Welding research supplement. Chicago; 1971; : 419–426.

23. Lassner E., Schubert W. Tungsten Properties, Chemistry, Technology of the Element, Alloys, and Chamical Compounds. 1999.

24. Asta M., Beckermann C., Karma A., Kurz W., Napolitano R., Plapp M., et al. Solidification microstructures and solid-state parallels: Recent developments, future directions. Acta Materialia. Acta Materialia Inc.; 2009; 57(4): 941–971. Available at: DOI:10.1016/j.actamat.2008.10.020

25. Gumbsch P. Brittle fracture and the brittle-to-ductile transition of tungsten. Journal of Nuclear Materials. 2003; 323: 304–312. Available at: DOI:10.1016/j.jnucmat.2003.08.009

26. Gludovatz B., Wurster S., Hoffmann a., Pippan R. Fracture toughness of polycrystalline tungsten alloys. International Journal of Refractory Metals and Hard Materials. Elsevier Ltd; 2010; 28(6): 674–678. Available at: DOI:10.1016/j.ijrmhm.2010.04.007

27. Ren C., Fang ZZ., Koopman M., Butler B., Paramore J., Middlemas S. Methods for improving ductility of tungsten - A review. International Journal of Refractory Metals and Hard Materials. Elsevier; 2018; 75(April): 170–183. Available at: DOI:10.1016/j.ijrmhm.2018.04.012

28. Raffo PL. Yielding and fracture in tungsten and tungsten-rhenium alloys. Journal of the Less-Common Metals. 1969; 17: 133–149. Available at: DOI:10.1016/0022-5088(69)90047-2

29. Reiser J., Wurster S., Hoffmann J., Bonk S., Bonnekoh C., Kiener D., et al. Ductilisation of tungsten (W) through cold-rolling: R-curve behaviour. International Journal of Refractory Metals and Hard Materials. Elsevier Ltd; 2016; 58: 22–33. Available at: DOI:10.1016/j.ijrmhm.2016.03.006

30. WTa Phase Diagram. Available at: https://en.wikipedia.org/wiki/Tantalum-tungsten_alloys (Accessed: 30 September 2018)

31. WMo Phase Diagram. Available at: https://www.911metallurgist.com/determine-melting-points-metals/ (Accessed: 30 September 2018)

32. MoTa Phase Diagram. Available at: http://resource.npl.co.uk/mtdata/phdiagrams/mota.htm (Accessed: 30

September 2018)

33. Wei N., Jia T., Zhang X., Liu T., Zeng Z., Yang X. First-principles study of the phase stability and the mechanical properties of W-Ta and W-Re alloys. AIP Advances. 2014; 4(5). Available at: DOI:10.1063/1.4875024
34. V.I. K., T. PE., M. SE. Tantalum-niobium alloys. 1979.
35. Olson DL., Mishra B., Wenman DW. Welding , Brazing and Joining of Refractory Metals and Alloys. Min. Pro. Exi. Met. Rev. 2001; 22: 1–23. Available at: DOI:10.1080/08827509808962487
36. Scott M., Knowlson P. The welding and brazing of the refractory metals niobium, tantalum, molybdenum and tungsten — a review. Journal of the Less Common Metals. 1963; 5: 205–244. Available at: DOI:10.1016/0022-5088(63)90029-8
37. Lessmann GG., Gold RE. The Varestraint Test for Refractory Metals Modified. Welding research supplement. 1971; (January): 1–8.
38. Stephens JR. Effect of oxygen on Mechanical properties of Tungsten. 1963.
39. Köck W., Paschen P. Tantalum-processing, properties and applications. Jom. 1989; 41(10): 33–39. Available at: DOI:10.1007/BF03220360
40. Bechtold J. Tensile properties of annealed tantalum at low temperatures. Acta Metallurgica. 1955; 3: 249–254. Available at: DOI:10.1016/0001-6160(55)90060-2
41. Cardonne SM., Kumar P., Michaluk CA., Schwartz HD. Tantalum and its alloys. International Journal of Refractory Metals and Hard Materials. 1995; 13(4). Available at: DOI:10.1016/0263-4368(95)94023-R
42. Nemat-Nasser S., J. B. Isaacs., M. Liu. Microstructure of high-Strain, High-Strain-Rate Deformed Tantalum. Acta Materialia. 1998; 46(4): 1307–1325.
43. Spitzig W a., Owen C V., Scott TE. Effects of Oxygen on the mechanical behavior of hydrogenated V, Nb, and Ta. Metallurgical Transactions A. 1986; 17(3): 527–535. Available at: DOI:10.1007/BF02643960
44. Habainy J., Iyengar S., Surreddi KB., Lee Y., Dai Y. Formation of oxide layers on tungsten at low oxygen partial pressures. Journal of Nuclear Materials. Elsevier B.V; 2018; 506: 26–34. Available at: DOI:10.1016/j.jnucmat.2017.12.018
45. Wriedt HA. The O-W (oxygen-tungsten) system. Bulletin of Alloy Phase Diagrams. 1989; 10(4): 368–384. Available at: DOI:10.1007/BF02877593
46. Vesel A., Mozetič M., Balat-Pichelin M. Sequential oxidation and reduction of tungsten/tungsten oxide. Thin Solid Films. 2015; 591: 174–181. Available at: DOI:10.1016/j.tsf.2015.02.019
47. Liu DG., Zheng L., Luo LM., Zan X., Song JP., Xu Q., et al. An overview of oxidation-resistant tungsten alloys for nuclear fusion. Journal of Alloys and Compounds. Elsevier B.V; 2018; 765: 299–312. Available at: DOI:10.1016/j.jallcom.2018.06.202
48. Wang C., Wang F., Han Y. Structural characteristics and outward-inward growth behavior of tantalum oxide coatings on tantalum by micro-arc oxidation. Surface

and Coatings Technology. Elsevier B.V.; 2013; 214: 110–116. Available at: DOI:10.1016/j.surfcoat.2012.09.068

49. Colin JJ., Abadias G., Michel A., Jaouen C. On the origin of the metastable β-Ta phase stabilization in tantalum sputtered thin films. Acta Materialia. 2017; 126: 481–493. Available at: DOI:10.1016/j.actamat.2016.12.030

50. Rouahi A., Challali F., Dakhlaoui I., Vallée C., Salimy S., Jomni F., et al. Structural and dielectric characterization of sputtered Tantalum Titanium Oxide thin films for high temperature capacitor applications. Thin Solid Films. Elsevier B.V.; 2016; 606: 127–132. Available at: DOI:10.1016/j.tsf.2016.03.047

51. Sato YS., Urata M., Kokawa H. Parameters controlling microstructure and hardness during friction-stir welding of precipitation-hardenable aluminum alloy 6063. Metallurgical and Materials Transactions A. 2002; 33(3): 625–635. Available at: DOI:10.1007/s11661-002-0124-3

52. Liu FC., Ma ZY. Influence of tool dimension and welding parameters on microstructure and mechanical properties of friction-stir-welded 6061-T651 aluminum alloy. Metallurgical and Materials Transactions A: Physical Metallurgy and Materials Science. 2008; 39(10): 2378–2388. Available at: DOI:10.1007/s11661-008-9586-2

53. Sharma C., Dwivedi DK., Kumar P. Effect of welding parameters on microstructure and mechanical properties of friction stir welded joints of AA7039 aluminum alloy. Materials and Design. Elsevier Ltd; 2012; 36: 379–390. Available at: DOI:10.1016/j.matdes.2011.10.054

54. Zhang Z., Yang X., Zhang J., Zhou G., Xu X., Zou B. Effect of welding parameters on microstructure and mechanical properties of friction stir spot welded 5052 aluminum alloy. Materials and Design. Elsevier Ltd; 2011; 32(8–9): 4461–4470. Available at: DOI:10.1016/j.matdes.2011.03.058

55. Badisch E., Kirchgaßner M. Influence of welding parameters on microstructure and wear behaviour of a typical NiCrBSi hardfacing alloy reinforced with tungsten carbide. Surface and Coatings Technology. 2008; 202(24): 6016–6022. Available at: DOI:10.1016/j.surfcoat.2008.06.185

56. Kim YG., Fujii H., Tsumura T., Komazaki T., Nakata K. Effect of welding parameters on microstructure in the stir zone of FSW joints of aluminum die casting alloy. Materials Letters. 2006; 60(29–30): 3830–3837. Available at: DOI:10.1016/j.matlet.2006.03.123

57. Giedt WH., Tallerico LN., Fuerschbach PW. GTA welding efficiency: calorimetric and temperature field measurements. Welding Journal. 1989; (January): 1987–1989. Available at: http://aws.org/wj/supplement/WJ_1989_01_s28.pdf

58. Pépe N., Egerland S., Colegrove PA., Yapp D., Leonhartsberger A., Scotti A. Measuring the process efficiency of controlled gas metal arc welding processes. Science and Technology of Welding and Joining. 2011; 16(5): 412–417. Available at: DOI:10.1179/1362171810Y.0000000029

59. Lindgren LE. Finite element modeling and simulation of welding. Part 3:

Efficiency and integration. Journal of Thermal Stresses. 2001; 24(4): 305–334. Available at: DOI:10.1080/01495730151078117

60. Giridharan PK., Murugan N. Optimization of pulsed GTA welding process parameters for the welding of AISI 304L stainless steel sheets. International Journal of Advanced Manufacturing Technology. 2009; 40(5–6): 478–489. Available at: DOI:10.1007/s00170-008-1373-0

61. Nie B., Yang L., Huang H., Bai S., Wan P., Liu J. Femtosecond laser additive manufacturing of iron and tungsten parts. Applied Physics A: Materials Science and Processing. Springer Berlin Heidelberg; 2015; 119(3): 1075–1080. Available at: DOI:10.1007/s00339-015-9070-y

62. Wang D., Yu C., Zhou X., Ma J., Liu W., Shen Z. Dense Pure Tungsten Fabricated by Selective Laser Melting. Applied Sciences. 2017; 7(4): 430. Available at: DOI:10.3390/app7040430

63. Iveković A., Omidvari N., Vrancken B., Lietaert K., Thijs L., Vanmeensel K., et al. Selective laser melting of tungsten and tungsten alloys. International Journal of Refractory Metals and Hard Materials. 2018; 72(December 2017): 27–32. Available at: DOI:10.1016/j.ijrmhm.2017.12.005

64. Zhou X., Liu X., Zhang D., Shen Z., Liu W. Balling phenomena in selective laser melted tungsten. Journal of Materials Processing Technology. Elsevier B.V.; 2015; 222: 33–42. Available at: DOI:10.1016/j.jmatprotec.2015.02.032

65. Zhou L., Yuan T., Li R., Tang J., Wang G., Guo K. Selective laser melting of pure tantalum: Densification, microstructure and mechanical behaviors. Materials Science and Engineering A. 2017; 707(September): 443–451. Available at: DOI:10.1016/j.msea.2017.09.083

66. Thijs L., Montero Sistiaga ML., Wauthle R., Xie Q., Kruth JP., Van Humbeeck J. Strong morphological and crystallographic texture and resulting yield strength anisotropy in selective laser melted tantalum. Acta Materialia. Acta Materialia Inc.; 2013; 61(12): 4657–4668. Available at: DOI:10.1016/j.actamat.2013.04.036

Chapter 2

Paper A

"Effect of the shielding gas composition and welding speed on autogenous welds of unalloyed tungsten plates"

G. Marinelli*, [a], F. Martina*, S. Ganguly*, S. Williams*

*Welding Engineering and Laser Processing Centre (WELPC), Cranfield University, Cranfield, MK43 0AL, United Kingdom

Abstract

Tungsten is characterised by poor weldability and marked brittleness at room temperature. For these reasons, tungsten welds are affected by the evolution of cracks along the weld bead and a pre-heating step is required to reduce the thermal straining. In this study, an operative window has been evaluated to understand the working envelope for such refractory metal when using the tungsten inert gas welding process. This has been achieved by varying the welding speed and the shielding gas composition. In particular, five different gas mixtures have been used, starting from 100% in argon to 100% in helium. The occurrence of humping has been reported when using low-helium gas mixtures and when high welding speeds were used. Furthermore, sound and defects-free autogenous welds have been achieved without pre-heating and using a 100% helium arc. Thus, this study has demonstrated that a helium-rich shielding gas is needed for the welding of thick tungsten plates. Moreover, the low process-induced thermal shock coupled with the purity of the alloy used aided to avoid the occurrence of any crack.

2.1 Introduction

For many years, refractory metals and their alloys have been on the attention of researchers because of their noteworthy properties and practicality [1–3]. These unique aspects led the refractories to be considered valuable materials for severe environment applications, as for example in the nuclear sector [4–6]. Among the refractory metals, tungsten is considered a promising material for its characteristic high melting point, good strength over a large temperature range, high thermal conductivity and low thermal expansion. For these reasons, tungsten has been identified to be one of the most capable to be used as structural and confinement components of nuclear fusion reactors [5]. Moreover, tungsten is considered suitable for aerospace applications including thermionic conversion devices, re-entry vehicles and high-temperature fuel elements [7].

In spite of the high potential of tungsten, one of the biggest challenges for its industrial application is the development of an effective joining technology [8], as unalloyed tungsten generally exhibits limited weldability [9,10]. The main factors that limit the weldability of this metal are the high melting point and density, marked brittleness at low temperature, high reactivity over a wide temperature range, the detrimental effect of impurities and the high residual stresses upon cooling. Thus, processing of tungsten components depends markedly upon the development of welding procedures able to produce sound and reliable joints in order to ensure a robust integrity of large-scale tungsten structure, even in complex configurations.

The high melting point and the high density lead to the necessity of a large amount of heat in order to melt the metal and this could lead to marked grain growth in the heat affected zone (HAZ) [8] and also to a marked depletion of the welding equipment [9]. Most of the general advice with regards to the application of various welding processes for refractory metals have been presented and collected in the review of Scott and Knowlson [9] and the review of Olson et al. [10]. Particularly regarding the application of tungsten inert gas (TIG) welding for unalloyed tungsten, the joining must be performed in a high-purity inert environment and all the surfaces of the material used should be properly cleaned

in order to reduce the probability of failure due to contaminants [9,10]. Furthermore, the components to be joined need to be fixed for minimum restraint and pre-heated, preferably above the ductile-brittle transition temperature (DBTT), in order to overcome the limited plasticity of tungsten [9,10].

The manufacturing routes through which the tungsten components have been manufactured also impact their weldability. In general, it has been reported that parts produced via arc-casting (A-C) claimed a greater fabricability and higher purity when compared to components manufactured via powder metallurgy route (PM) and chemical vapour deposited (CVD) [9,11,12]. Joining tungsten components manufactured via PM and CVD usually leads to the formation of porosity [10]. The manufacturing route mainly influences the composition of the component and so that the level of the interstitial element, the entrapment of gasses and/or low-melting-point elements which lead to the formation of defects [10].

Lessmann and Gold [12] have previously investigated the weldability of unalloyed A-C tungsten and unalloyed PM tungsten sheets using TIG welding and electron beam (EB) welding. Welding speeds between 1.5 mm/s and 20 mm/s have been used in combination with no pre-heating, 250° C pre-heating and 700° C preheating. The plates had a thickness of around 0.9 mm. They reported that the pronouncedly higher thermal shock from the EB welding compared to the TIG welding caused dramatic failures, including cracks transverse to the weld seam and delamination of adjacent base metal [12]. The occurrence of cracks was reported for both the manufacturing routes with the addition of porosity for the PM tungsten sheets. The decreasing of process thermal shock seemed to have a benefit on the welded structure through the weakening of occurrence in cracking. In particular, this phenomenon is evident when using TIG welding coupled with pre-heating at around 700° C [12].

The weldability of tungsten plates produced by A-C, PM and CVD was evaluated using TIG welding in the work of Cole et al. [7]. The welds were performed on 1.5-mm-thick plates in an inert atmosphere using a welding current of 350 Amps, argon as a gaseous mean for the electric arc and a welding speed of

around 4.0 mm/s. Welds on A-C material were free from porosity unlike the welds performed on PM plates which were usually porous, particularly along the fusion line [7]. The cracks were eliminated for single pass welds when using pre-heating at around 150° C and it was reported that this temperature needs to be higher for multi-pass welds.

Additional studies of welding of CVD, PM and vacuum A-C tungsten sheets were reported by Farrell et al. [13]. They performed bead-on-plates welds on 1.5-mm-thick plates using TIG welding in order to examine the occurrence of porosity and cracks. The process employed the utilisation of complete inert atmosphere and pre-heating at about 150° C. Pure argon was used as shielding gas, a welding current between 310 Amps and 350 Amps and a welding speed of around 4.0 mm/s were used. Cracks were observed within the weld bead of PM and vacuum A-C tungsten unlike the CVD tungsten plates, which presented cracks within the HAZ. Their occurrence has been identified as intergranular hot cracks caused by the growth and coalescence of grain-boundary pores [13].

Currently, there is few published research that describes the process development and the weldment characteristics for unalloyed tungsten using TIG welding. These investigations also mainly refer to the welding of thin tungsten plates. Furthermore, no studies have been found to discuss the effect of different gas mixtures as a gaseous mean for the electric arc for tungsten welding.

This study principally aimed to understand the correct process parameters for tungsten welding when using TIG welding process and define an operative window. In general, the intention of this study is to investigate the TIG welding for the production of sound welds of unalloyed tungsten, without using pre-heating. This has been achieved by exploring the relationship between two fundamental welding parameters, welding speed and shielding gas composition, with the weldment morphology. Moreover, an explanation regarding the causes of the welding defects has been discussed and the microstructure of the tungsten welds has been shown.

2.2 Experimental Procedure

The autogenous welds were performed on commercially available unalloyed tungsten plates. Each of the plates was 100.0 mm in length, 90.0 mm in width and 5.0 mm of thickness and they were manufactured via powder metallurgy. The chemical composition of the material used is listed in **Table 2.1.** The surface of the material was ground and rinsed with acetone in order to eliminate surface contamination before welding. Furthermore, high-purity argon and high-purity helium were used as shielding gas.

	W	Mo	Ta	Ti	V	Cr	Fe	C	N	O	K
W Plates	99.99	<0.05	<0.05	<0.05	<0.05	<0.05	<0.05	<10 ppm	<10 ppm	<50 ppm	<10 ppm

Table 2.1: Elemental composition (wt %) of tungsten plates (W Plates).

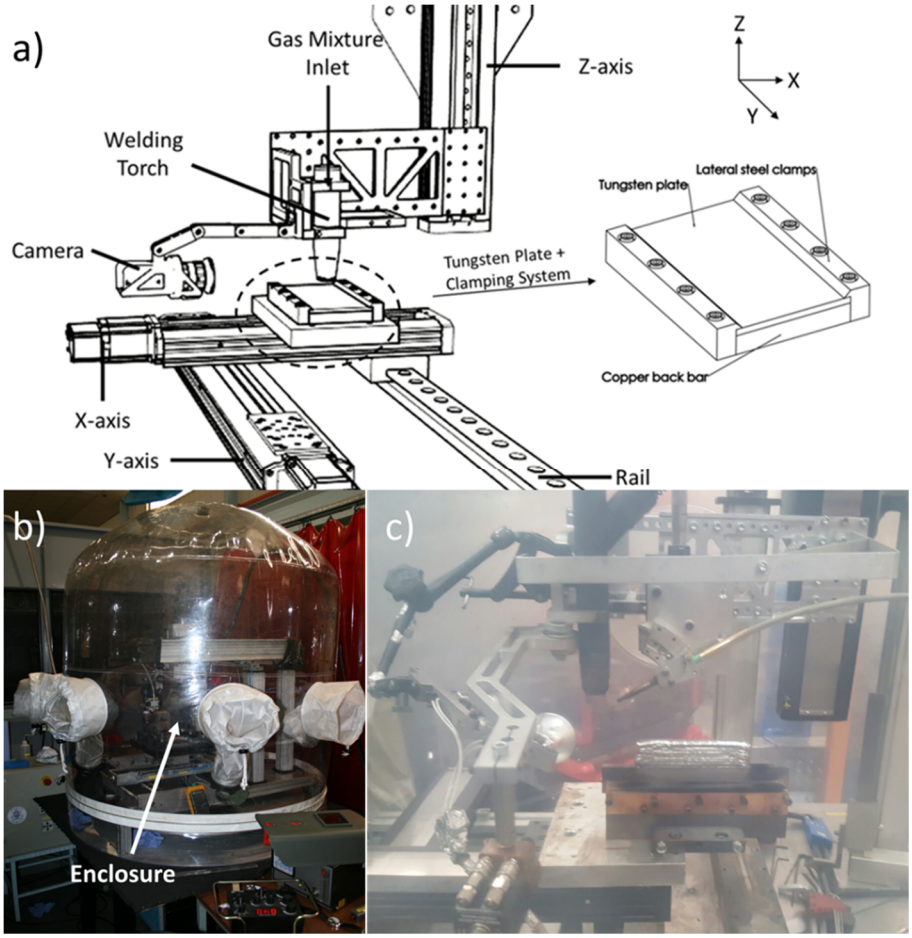

Figure 2.1: (a) Schematisation of the experimental set-up used for the production of the tungsten weldment. Photo of the experimental set-up taken from outside the enclosure (b) and from inside the enclosure (c).

Figure 2.1 shows the layout of the welding apparatus used in this study. In particular, a conventional TIG torch and a power supply were used as welding means. The heat source and the clamping system were attached to three linear motorized high-load stages assembled in XYZ configuration. The tungsten plates were held in position using the clamping system, also shown in **Figure 2.1a.**

A constant vertical force was applied along the long-side of the plates achieved by applying the same torque to every screw of the clamping system. A gas mixing system was used to study the effect of the shielding gas composition on tungsten welding. In particular, two gas channels were used to mix argon and helium in specific proportions. The two gasses were contained in two respective gas cylinders, which were connected to the gas mixer. The outlet of the gas mixer was directly connected to the welding torch. The apparatus was surrounded by a heavy-duty enclosure used to ensure a low level of oxygen when purged with argon.

Sample name	TS [mm/s]	SGC	
		He %	Ar %
1	1	0	100
2	2	0	100
3	4	0	100
4	6	0	100
5	1	25	75
6	2	25	75
7	4	25	75
8	6	25	75
9	1	50	50
10	2	50	50
11	4	50	50
12	6	50	50
13	1	75	25
14	2	75	25
15	4	75	25
16	6	75	25
17	1	100	0
18	2	100	0
19	4	100	0
20	6	100	0

Table 2.2: The combinations of welding speed (TS) and shielding gas composition (SGC) used for the study.

The process was recorded and monitored using a MC500S welding camera, supplied by Redman controls & electronics, for the weld pool development and an AMV 5000 for the arc voltage variations. An experimental plan was developed considering shielding gas composition (SGC) and welding speed (TS) as variables of the process while keeping constant the welding current (I) and equal to 350 Amps. Twenty 80-mm-welds on unalloyed tungsten plates were performed in this study. In particular, four welds have been performed next to each other on the same plate. **Table 2.2** reports the main welding parameters for each weld. In order to reduce the number of variables, some welding parameters were kept constant throughout the experiments. These were:

- Electrode-to-workpiece distance = 3.5 mm;
- Tungsten electrode tip angle = 45°;
- Tungsten electrode diameter = 3.6 mm;
- Torch angle= 90°.

A pre-heating step was not used in this study as it was difficult to integrate a pre-heating mean within the experimental set-up used, preserving the integrity of the manipulation system and of the plastic tent used for the argon confinement. Furthermore, the continuous purging of cold argon would have led to uncontrolled temperature variations of the work piece. Three sections of the weldments were analysed as illustrated in **Figure 2.2.** All the metallographic samples were ground and polished using paper discs of silicon carbide and then etched using the Murakami's reagent in order to study the occurrence of defects, the microstructure and geometrical features of the melt zone.

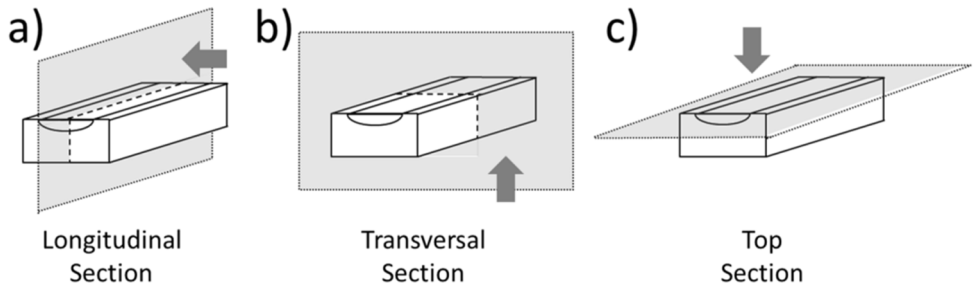

Figure 2.2: Schematic of the planes used to analyse the microstructure of the samples produced. In particular, longitudinal cross-section (a), transversal cross-section (b) and top section (c).

2.3 Results and Discussion

2.3.1 Operative window and bead morphology

Figure 2.3a shows the operative window explored in this study. In particular, one variable was the shielding gas composition (SGC), indicated as a percentage of helium within the mixture, and the other one was the welding speed (TS). The black dots shown in the graph represent the single experiments, according to the set of parameters reported in **Table 2.2.** The boundaries of each region were drawn based on interpolated lines between the testing points.

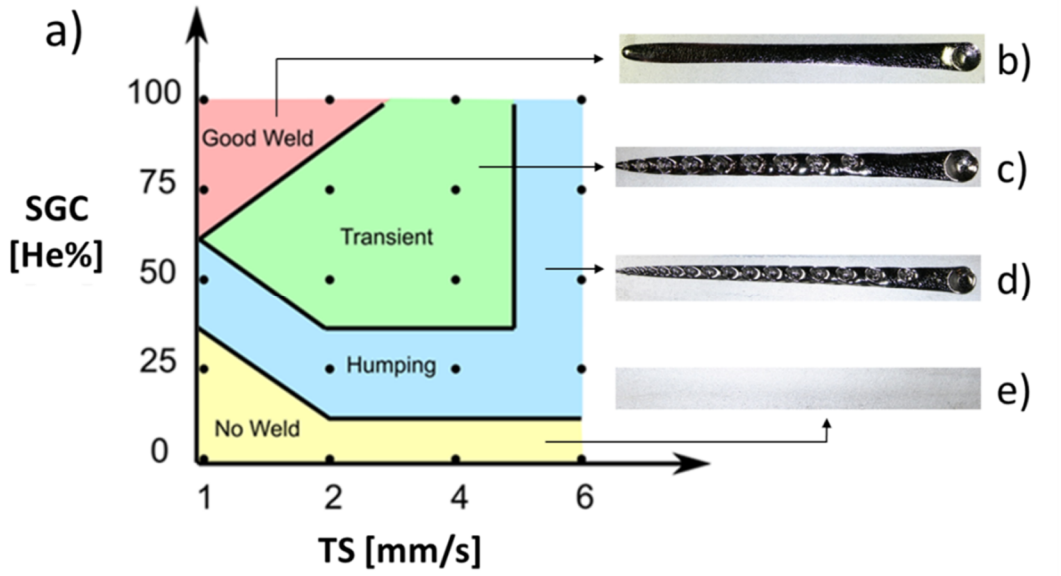

Figure 2.3: (a) Operative process window respect to SGC and TS; Weld bead morphology of the *Good Weld* (b), *Transient* (c), *Humping* (d) and *No Weld* samples (e).

Four main weld bead morphologies have been found for different combinations of TS and SGC. These have been nominated for simplicity: *No Weld* (**Figure 2.3e**), *Humping* (**Figure 2.3d**), *Transient* (**Figure 2.3c**) and *Good Weld* (**Figure 2.3b**). The occurrence of each case has been illustrated as a coloured area within the operative window of **Figure 2.3a.**

In general, the *No Weld* morphology occurred for relatively low-power cases (low helium content) and it was characterised by the absence of clear and visible melted surface. At these particular levels of power, the development of a liquid pool did not occur during the process. Regarding the *Humping* morphology, clear melted surfaces were visible but they were characterised by a periodical

series of crests followed by depressions. A different weld bead morphology has been encountered at relatively medium welding speeds and high content of helium. In particular, the *Transient* case presented a visible transition from the humping regime to a smooth weld within the same weld bead. The humps gradually decrease their periodicity, eventually disappearing into a regular weld profile towards the end of a weld. Confined at a high content of helium, from 75% to 100% in composition, and low welding speed, between 1 mm/s and 2 mm/s, *Good Weld* profiles have been recorded. Noteworthy were the absence of welding defects and the absence of solidification cracks in these welds.

The occurrence of these morphologies has been directly related to the process heat input and the arc characteristics of each specific mixture used. In particular, it is well known that the heat input per unit length for the TIG welding process is proportional to the welding current, the voltage drop of the arc column and the welding speed, according to the following **Eq.(2.1)** [14]:

$$H_{in} = \eta \frac{I*V}{TS} \quad \textbf{(2.1)}$$

Where H_{in} is the heat input per unit length, η is the process efficiency, I the welding current, V the voltage and TS the welding speed. The process efficiency was not measured in this study. The welding speed was directly varied as one of the main parameters of the investigation instead, the voltage was changed depending on the content of helium within the gas mixture. In fact, a helium arc is characterised by an increased arc voltage when compared to an argon arc due to its higher ionization potential [15]. In **Table 2.3**, the values of the average voltage measured during the welding process for each gas mixture are reported and it is possible to see that the voltage increased as the content of helium increased.

SGC [He%]	Voltage [V]
0	14.5
25	16
50	18.5
75	20
100	21.5

Table 2.3: Average measured voltage for the different shielding gas compositions (I=350A).

The shielding gas composition can also affect the total heat flux of the TIG welding process [16,17]. The influence of the gas physical properties on the electric arc characteristics has been already investigated extensively [18]. In particular, helium is characterised by a lower electrical conductivity, a higher specific heat and a higher thermal conductivity with respect to argon [18]. The mixtures of argon and helium have intermediate properties to those of the pure gases [16,18]. Thus, the addition of a helium fraction to the argon increases the thermal conductivity and the arc constriction promoting an increased heat flux and current density to the workpiece [17]. Due to the high melting point and the relatively high thermal conductivity of tungsten, a 100% helium arc and relatively low welding speeds resulted to be essential for the formation and the development of a regular weld pool. Higher welding speeds and lower helium content led to the formation of humping defects mainly due to the reduction in heat input.

The efficiency of each gas mixture could have been estimated correlating the weld pool dimensions or the hardness profile along the weld with the heat input. These data have not been collected as the dimensions of the melted area and of the heat affected zone were changing along the weld leading to a high degree of inconsistency.

2.3.2 Humping formation

Figure 2.4 shows the microstructure of one of the samples produced and characterised by the occurrence of humping defects. In particular, **Figure 2.4a** refers to the longitudinal cross-section and **Figure 2.4b** refers to the top section of the weld bead, as indicated in **Figure 2.2**. When analysing **Figure 2.4a**, it is possible to notice that the average melting depth remained constant along the weld although the occurrence of the humping. The average melting depth and the average humping height resulted to be both equal to 0.7 mm with respect to the top of the plate.

Moreover, the weld width and the humping pitch respectively were found to be constant (**Figure 2.4b**) and equal to 3.8 mm and 6.0 mm. The humping mainly occurred for a low content of helium over the entire range of welding speeds employed and for high welding speed when a higher content of helium was

employed. This means that the heat input was sufficiently high to melt the tungsten plate but the liquid metal was pushed downwards and forced to flow towards the rear of the weld pool, where it prematurely solidified.

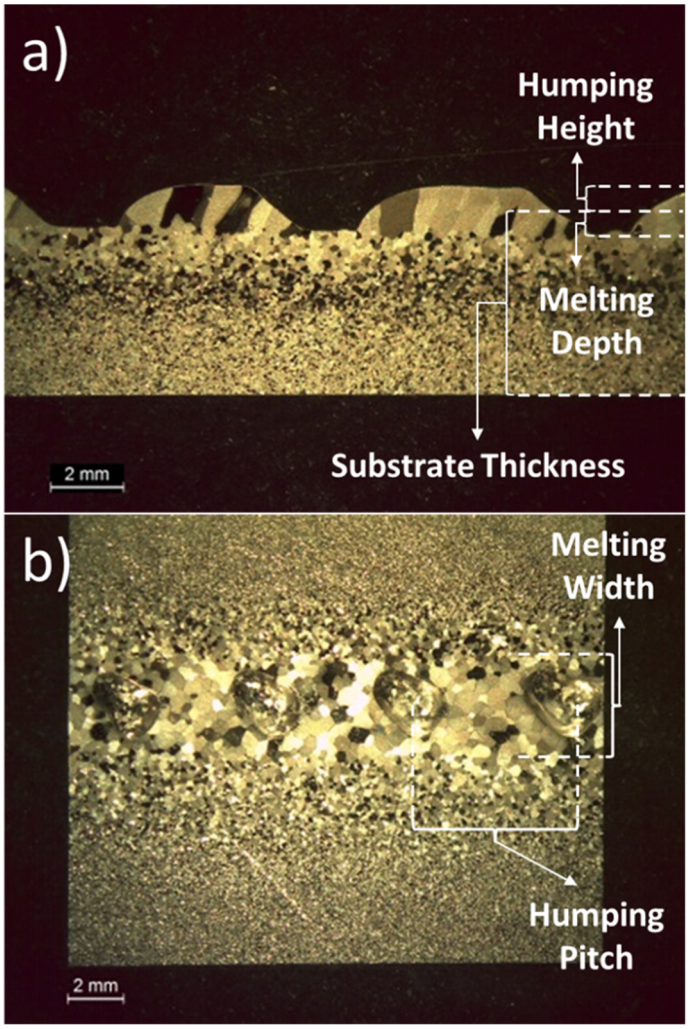

Figure 2.4: Longitudinal cross-section (a) and top section (b) of the weld performed using a shielding gas composition of 50% of helium and 1 mm/s of welding speed.

The constant humping pitch shows that this mechanism occurred regularly along the weld. The occurrence of humping defects have already been reported for high-speed and high-current welds [14,19–21] and it is defined as the occurrence of an alternation of crests (humps) and valleys (undercut) on the top of the weld [22]. In particular, increasing the welding speed beyond a certain critical limit leads to the formation of the humping. This critical speed values decreases as the welding current increases [23]. Furthermore, the composition of the arc gas actually influences the total arc pressure, which contributes to the formation of the

humping defects [23]. Generally, at high currents, the arc pressure causes a marked depression on the weld pool surface [24], forming a thin layer of liquid metal, called gouging region [19]. The humps start to form when the arc pressure extends this region beyond the heat influence of the arc causing a premature solidification of the thin liquid layer [20].

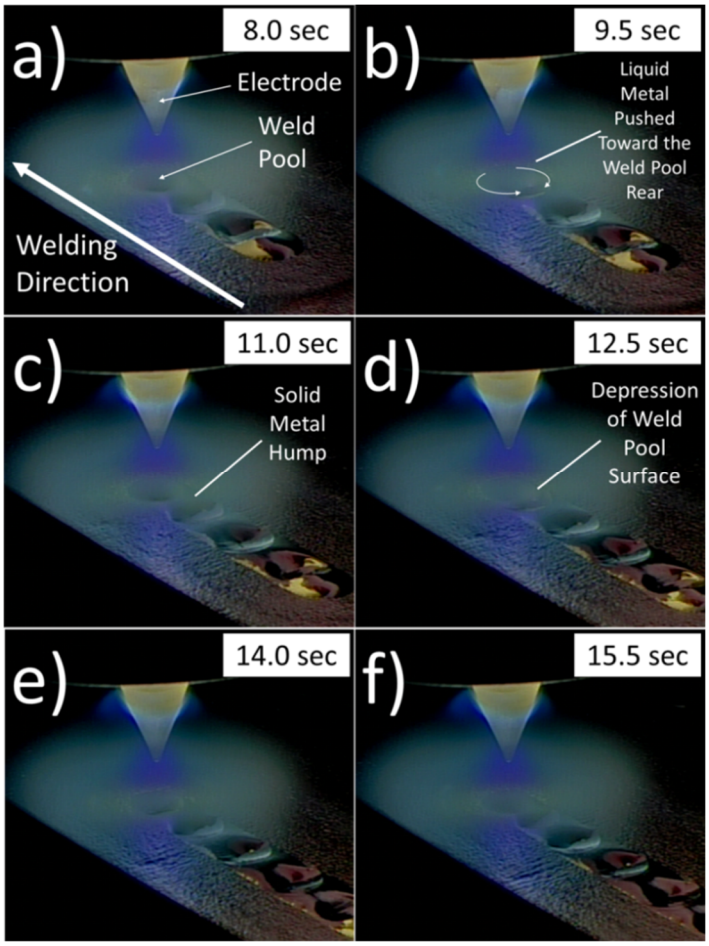

Figure 2.5: Time-resolved images of the weld performed using a shielding gas composition of 50% of helium and 1 mm/s of welding speed.

Figure 2.5 shows a series of time-resolved images of the weld performed using a welding speed of 1 mm/s and a shielding arc composition of 50% of argon and 50% of helium. It is possible to notice the presence of a large depression on the weld pool surface right underneath the arc column in **Figure 2.5a**. Here, the weld pool has been reduced to a thin liquid layer that flows rapidly from the front to the rear of the liquid pool (**Figure 2.5b**) through lateral channels [19]. For these reasons, the liquid experienced an upwards deflection, forming the hump (**Figure 2.5c**) and also, the lateral channels solidified as they were extended to a region

away from the arc column [22]. In this situation, the depression located under the arc column was not filled back with liquid metal and so the undercutting occurred (**Figure 2.5d**) [14,19]. Thus, insufficient welding heat input causes humping as the displaced metal under the arc pressure solidifies before completion of the flow. This effect is enhanced at relatively high arc pressure and high welding speed.

2.3.3 Transient welding state

Figure 2.6 shows the evolution of the weld pool when using 75% of helium within the gas mixture and a welding speed of 2 mm/s. It is possible to see how, starting with the formation of humping (**Figure 2.6a**), the pitch of the humps increased, after 12.0 seconds, as the weld progressed (**Figure 2.6b**). This occurred until a transition to a regular weld profile was obtained (**Figure 2.6c**) specifically toward the end of the weld, where the weld bead was not affected by the presence of any defects. This scenario represents a transient welding state which was mainly caused by three factors: the considerable variation in thermal gradient caused by the decreasing in thermal conductivity of tungsten, the high content of helium and the relatively low travel speed.

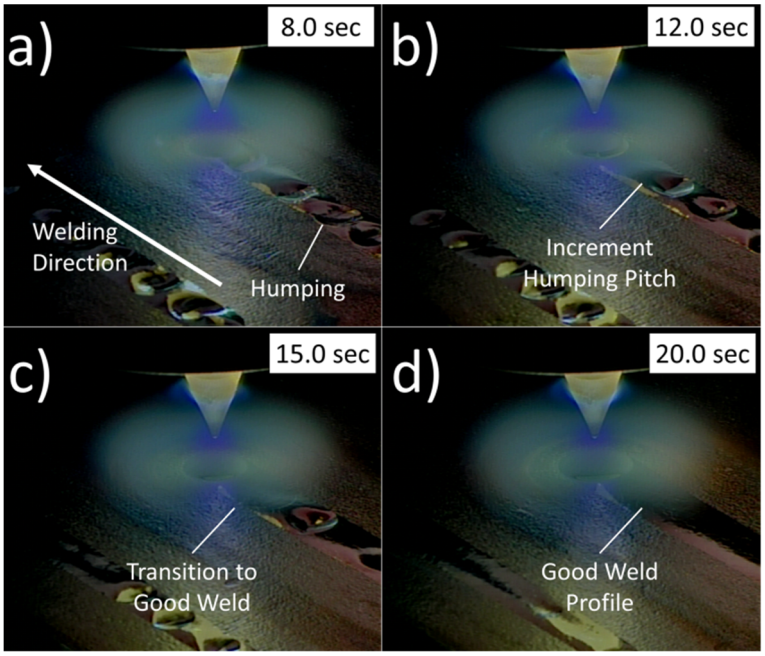

Figure 2.6: Time-resolved images of the weld performed using a shielding gas composition of 75% of helium and 2 mm/s of welding speed.

In particular, it is already known that the thermal conductivity of tungsten decreases when the temperature increases [25–27]. In addition, the shear stress exerted by the helium arc onto the weld pool was previously measured to be smaller than argon and so that resulted to be for the arc pressure. [16,17,28]. Furthermore, it has been already seen that the frequency of the humping decreases for relatively low welding speed, as a result of an increased heat input per unit length [29]. For these reasons, as the weld progressed, the thermal gradient was reduced, due to a constantly decreasing thermal conductivity. This led to an increment with regards to the melting efficiency of the process towards the end of the weld. The larger liquid volume was not completely displaced away from the arc column, as occurred during humping, due to the higher metallostatic pressure and the smaller arc pressure of the 75% helium arc [19,23].

2.3.4 Good weld

In **Figure 2.7** is reported the weld pool evolution over time when 100% helium shielding gas was used with a welding speed of 1 mm/s. It is clear that the weld pool edges were clear and defined since the beginning of the process (**Figure 2.7a**). Furthermore, no occurrence of humping was registered for the entire weld as shown in **Figure 2.7b** and **Figure 2.7c.**

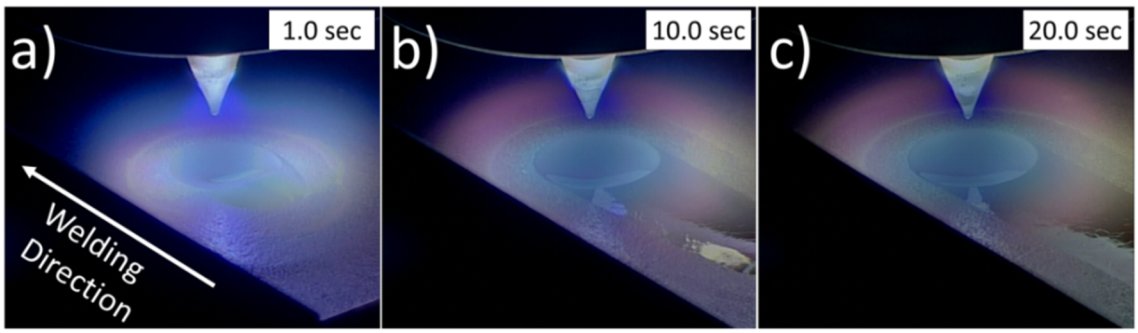

Figure 2.7: Time-resolved images of the weld performed using a shielding gas composition of 100% of helium and 1 mm/s of welding speed.

The microstructure of the *Good Weld* achieved using 100% helium arc and 1 mm/s of welding speed is reported in **Figure 2.8**. In particular, **Figure 2.8a** shows the transversal cross-section, **Figure 2.8b** shows the longitudinal cross-section and **Figure 2.8c** shows the top section (**Figure 2.2**). An average melting depth of 1.45 mm and an average melting width of 6.3 mm were achieved in these

conditions. No clear fusion line has been found at the interface between the melted region and heat affected zone. Thus, a fusion boundary has been chosen according to the sudden change in the grain dimensions and this has been used to measure the average weld width and depth. The melted material seemed to be characterised by numerous elongated grains extending from the bottom toward the top of the weld pool. Each grain possibly nucleated from the smaller parental metal grains and grew epitaxially toward the top of the weld pool.

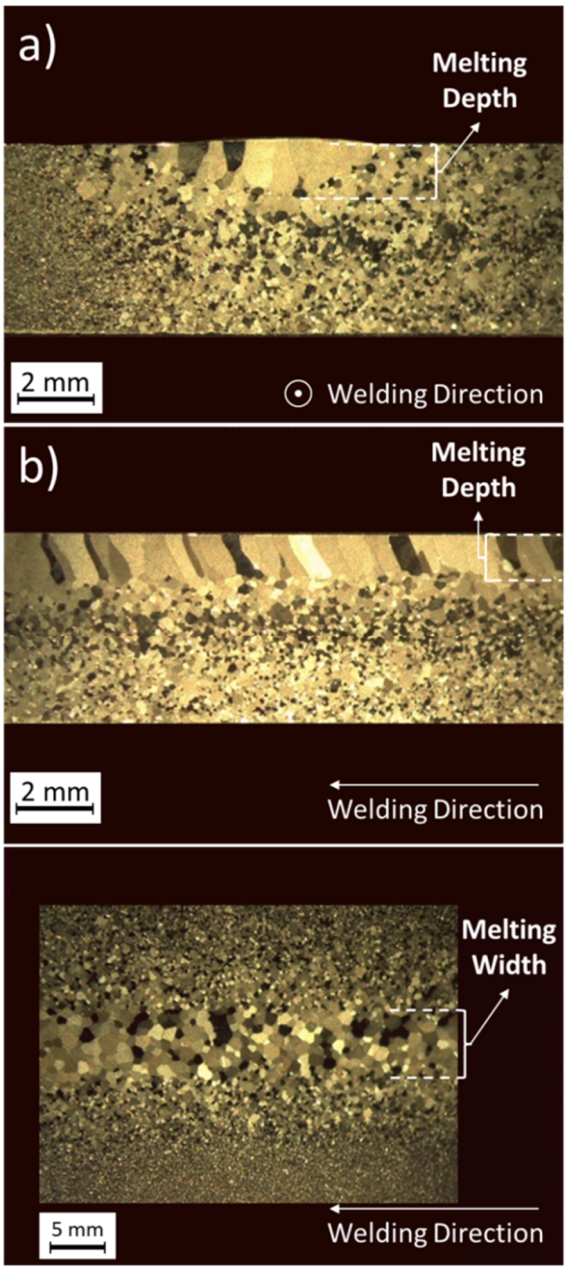

Figure 2.8: Transversal cross-section (a), longitudinal cross-section (b) and top section (c) of the weld performed using a shielding gas composition of 100% of helium and 1 mm/s of welding speed.

It has already been reported that elements like carbon, oxygen and nitrogen tend to increase the brittleness of the welded material mainly due to their limited solubility within tungsten [9,10]. In particular, they tend to segregate at the grain boundaries promoting the formation of brittle compounds as carbides and oxides [30]. Furthermore, the relatively low plasticity and the high modulus of elasticity of tungsten lead to the development of a considerable level of residual stresses, possibly causing the evolution of cracks upon cooling [10]. This is also influenced by the main process parameters as welding speed and heat input. In fact, slower welding speeds and higher heat inputs lead to a reduction of the process-induced thermal shock [10]. Thus, the cracks in tungsten welding are mainly caused by the high level of impurities and high process thermal shock, which causes high levels of strain.

In this study, a great amount of energy has been used to achieve the *Good Weld* condition. For this reason, the absence of cracks for the autogenous weld performed in this study has been directly addressed to the extremely low level of impurities (**Table 2.1**), the limited restraint from the clamping system (**Figure 2.1**) and the relatively low process-induced thermal shock.

2.4 Conclusions

In this research, the influence of the welding speed and the shielding gas composition on the autogenous welds of tungsten plates has been investigated. Furthermore, the occurrence of humping and the transient welding regime have been also discussed referring the arc characteristic and the thermal properties of tungsten. The summary of the main finding is reported below:

- The addition of helium to the shielding gas was necessary in order to achieve effective melting of the 5-mm-thick plates using a welding current of 350 Amps. In particular, a high content of helium is necessary in order to develop a smooth and regular weld pool without any defects, for the welding speeds studied;

- The occurrence of welding defects as humping was reported for high welding speed or low content of helium within the shielding gas. In particular, the humping defects were caused by the arc pressure and the premature solidification of the weld pool rear. The occurrence of this type of defect was associated with low heat input;

- The transient welding state from the humping to the good weld profile has been caused by the overall reduction of the thermal gradient, which is associated with the reduction in thermal conductivity of tungsten with temperature;

- The absence of cracks within the good weld was mainly due to low thermal shock, low level of restraining from the clamping system and the low level of impurities of the tungsten plates.

This research has shown that it is possible to obtain defect-free welds of tungsten plates without the use of pre-heating. The design of a proper heat source is fundamental to preserve the weldments integrity. In particular, a low process thermal shock and a high thermal energy resulted to be required to avoid the occurrence of cracks within tungsten welds. An increased productivity could be achieved by using pre-heating, which will lead to a further reduction of the thermal gradient and thermal shock.

2.5 Bibliography

1. Schubert WD. Aspects of research and development in tungsten and tungsten alloys. Refractory Metals and Hard Materials. 1992; 11(1992): 151–157. Available at: DOI:10.1016/0263-4368(92)90057-9
2. Bolt H., Barabash V., Federici G., Linke J., Loarte A., Roth J., et al. Plasma facing and high heat flux materials - Needs for ITER and beyond. Journal of Nuclear Materials. 2002; 307–311: 43–52. Available at: DOI:10.1016/S0022-3115(02)01175-3
3. Buckman RW. New Applications for Tantalum and Tantalum Alloys. Jom. 2000; (March): 40–41. Available at: DOI:10.1007/s11837-000-0100-6
4. Reiser J., Rieth M., Möslang A., Dafferner B., Hoffmann J., Mrotzek T., et al.

Tungsten foil laminate for structural divertor applications - Joining of tungsten foils. Journal of Nuclear Materials. 2013; 436(1–3): 47–55. Available at: DOI:10.1016/j.jnucmat.2013.01.295

5. Rieth M., Dudarev SL., Gonzalez De Vicente SM., Aktaa J., Ahlgren T., Antusch S., et al. Recent progress in research on tungsten materials for nuclear fusion applications in Europe. Journal of Nuclear Materials. 2013; 432(August 2012): 482–500. Available at: DOI:10.1016/j.jnucmat.2012.08.018
6. Kanpara S., Khirwadkar S., Belsare S., Bhope K., Swamy R., Patil Y., et al. Fabrication of Tungsten & Tungsten Alloy and its High Heat Load Testing for Fusion Applications. Materials Today: Proceedings. Elsevier Ltd; 2016. pp. 3055–3063. Available at: DOI:10.1016/j.matpr.2016.09.020
7. Cole NC., Gilliland RG., Slaughter GM. Weldability of Tungsten and Its Alloys. Welding research supplement. Chicago; 1971; : 419–426.
8. Tabernig B., Reheis N. Joining of Refractory Metals and its Application. 17th Plansee Seminar. 2009. p. GT 12/1-10. Available at: DOI:10.1016/j.ijrmhm.2010.06.008
9. Scott M., Knowlson P. The welding and brazing of the refractory metals niobium, tantalum, molybdenum and tungsten — a review. Journal of the Less Common Metals. 1963; 5: 205–244. Available at: DOI:10.1016/0022-5088(63)90029-8
10. Olson DL., Mishra B., Wenman DW. Welding , Brazing and Joining of Refractory Metals and Alloys. Min. Pro. Exi. Met. Rev. 2001; 22: 1–23. Available at: DOI:10.1080/08827509808962487
11. Moss AR., Richards DT. The Arc-Melting of Niobium, Tantalum, Molybdenum and Tungsten. Journal of the Less Common Metals. 1960; 2: 405–425.
12. Lessmannt GG., Gold RE. WELDABILITY OF TUNGSTEN BASE ALLOYS. 1970.
13. Farrell K., Houston JT., Chumley JW. Hot Cracking in Fusion Welds in Tungsten. 1st International AWS-WRC Brazing Conference. Cleveland; 1970. pp. 132–137.
14. Nguyen TC., Weckman DC., Johnson D a., Kerr HW. High speed fusion weld bead defects. Science and Technology of Welding and Joining. 2006; 11(6): 618–633. Available at: DOI:10.1179/174329306X128464
15. Dong W., Lu S., Li D., Li Y. GTAW liquid pool convections and the weld shape variations under helium gas shielding. International Journal of Heat and Mass Transfer. Elsevier Ltd; 2011; 54(7–8): 1420–1431. Available at: DOI:10.1016/j.ijheatmasstransfer.2010.07.069
16. Murphy AB., Tanaka M., Tashiro S., Sato T., Lowke JJ. A computational investigation of the effectiveness of different shielding gas mixtures for arc welding. Journal of Physics D: Applied Physics. 2009; 42: 115205. Available at: DOI:10.1088/0022-3727/42/11/115205
17. Traidia A., Roger F. A computational investigation of different helium supplying methods for the improvement of GTA welding. Journal of Materials Processing Tech. Elsevier B.V.; 2011; 211(9): 1553–1562. Available at: DOI:10.1016/j.jmatprotec.2011.04.008

18. Tanaka M., Tashiro S., Satoh T., Murphy a. B., Lowke JJ. Influence of shielding gas composition on arc properties in TIG welding. Science and Technology of Welding and Joining. 2008; 13(3): 225–231. Available at: DOI:10.1179/174329308X283929

19. Mendez PF., Mendez PF., Eagar TW., Eagar TW. Penetration and Defect Formation in High-Current Arc Welding. October. 2003; (October): 296–306.

20. Soderstrom E., Mendez P. Humping mechanisms present in high speed welding. Science and Technology of Welding and Joining. 2006; 11(5): 572–579. Available at: DOI:10.1179/174329306X120787

21. Savage WF., Nippes EF., Agusa K. Effect of Arc Force on Defect Formation in GTA Welding. Welding research supplement. 1979; (July): 212–224.

22. Berger P., Hügel H., Hess A., Weber R., Graf T. Understanding of humping based on conservation of volume flow. Physics Procedia. 2011; 12(PART 1): 232–240. Available at: DOI:10.1016/j.phpro.2011.03.030

23. Kumar A., DebRoy T. Toward a Unified Model to Prevent Humping. Welding Journal. 2006; 85(12): 292s–304s.

24. Meng X., Qin G., Zou Z. Investigation of humping defect in high speed gas tungsten arc welding by numerical modelling. Materials and Design. 2016; 94(March): 69–78. Available at: DOI:10.1016/j.matdes.2016.01.019

25. Moreau C., Fargier-Richard P., Saint-Jacques RG., Cielo P. Thermal diffusivity of plasma-sprayed tungsten coatings. Surface and Coatings Technology. 1993; 61(1–3): 67–71. Available at: DOI:10.1016/0257-8972(93)90204-2

26. Lv Y., Song J., Lian Y., Yu Y., Liu X., Zhuang Z. The thermal properties of high purity and fully dense tungsten produced by chemical vapor deposition. Journal of Nuclear Materials. Elsevier B.V.; 2015; 457: 317–323. Available at: DOI:10.1016/j.jnucmat.2014.11.095

27. Niu Y., Zheng X., Ji H., Qi L., Ding C., Chen J., et al. Microstructure and thermal property of tungsten coatings prepared by vacuum plasma spraying technology. Fusion Engineering and Design. Elsevier B.V.; 2010; 85(7–9): 1521–1526. Available at: DOI:10.1016/j.fusengdes.2010.04.032

28. Campbell SW., Galloway a M., Mcpherson N a. Arc pressure and fluid flow during alternating shielding gases. Part 2: arc force determination. Science and Technology of Welding and Joining. 2013; 18(7): 597–602. Available at: DOI:10.1179/1362171813Y.0000000142

29. Wei PS., Chuang KC., Ku JS., Debroy T. Mechanisms of spiking and humping in keyhole welding. IEEE Transactions on Components, Packaging and Manufacturing Technology. 2012; 2(3): 383–394. Available at: DOI:10.1109/TCPMT.2011.2178412

30. Lessmann GG., Gold RE. The Varestraint Test for Refractory Metals Modified. Welding research supplement. 1971; (January): 1–8.

Chapter 3

Paper B

"Process development of Wire + Arc Additive Manufacture for the production of large-scale unalloyed tungsten components"

G. Marinelli*, [a], F. Martina*, S. Ganguly*, S. Williams*

*Welding Engineering and Laser Processing Centre (WELPC), Cranfield University, Cranfield, MK43 0AL, United Kingdom

Abstract

The manufacturing of refractory metal components presents some limitations induced by their characteristic low-temperature brittleness and high susceptibility to oxidation. Refractory metal components are predominantly manufactured via powder metallurgy route. Wire + Arc Additive Manufacture is a promising manufacturing technique able to produce fully-dense parts at relatively low cost, by using high-quality wire as feedstock. In this study, this technique has been used for the production of large-scale tungsten linear structures. The orientation of the substrate and that of the wire feeding have been optimised in order to achieve defect-free deposits produced by fusion. Despite the repetitive thermal cycles, the as-deposited structures were free from internal cracks and the layer dimensions were stable during the entire deposition process. Based on the characterisation and stabilisation of the process, a linear structure with the dimension of 210 x 75 x 12 mm has been successfully produced. This study has demonstrated that Wire + Arc Additive Manufacture can be used to produce large-scale parts in unalloyed tungsten by complete fusion, presenting a potential alternative to the powder metallurgy manufacturing route.

3.1 Introduction

For quite sometimes, the research has been focused on the development of alternative energy generation sources, such as nuclear fusion [1]. In this environment, the material selection is a key point to ensure an optimum service life of the structural components of the reactor. Material with very high mechanical properties, heat resistance and neutron load capacity are required for the manufacture of high-quality components. Refractory metals and their alloys have been on the attention of researchers because of their distinctive physical properties, such as are the very high melting point, high density, and good thermal and electrical conductivity.

Tungsten is one of the candidate materials for high performance and advanced components in the field of innovative high-temperature energy generation and conversion systems [1,2]. In particular, tungsten can be used as plasma facing material in future fusion reactor [1,2]. This is directly related to the attractive physical properties of tungsten. In fact, it is characterised by the highest melting point among the metals, high density, relatively high thermal conductivity at room temperature, low coefficient of thermal expansion, excellent mechanical properties at elevated temperatures, high resistance to sputtering and erosion and low tritium retention [3,4].

Due to their extremely high melting point, refractory metals, in particular tungsten, are generally manufactured via powder metallurgy route and not through melting or casting [5]. The combination of sintering and hot or cold working plays a fundamental role in the powder consolidating and designing of the final structure. The low fracture toughness, the high ductile-to-brittle-transition temperature (DBTT) and the high recrystallization temperature, present also significant challenges for the manufacturing and the structural application of tungsten components [6,7]. Currently, there are three main manufacturing steps that are being studied when referring to tungsten components for the application in a nuclear reactor environment: the actual large-scale production of components, the joining with other components and their efficient repair and maintenance.

One of the most auspicious manufacturing technologies for such advanced alloy can be Additive Manufacturing (AM), which is leading to a new industrial revolution [8,9]. Three-dimensional structures can be promptly deposited starting from 3D-model designs using a layer-by-layer approach [10]. The practical advantages are the cost reduction, the freedom of design and the control of mechanical properties [10]. Numerous researches have already reported the potential of AM techniques for metallic materials, some of them are summarised in [11,12].

The employment of an additive manufacturing process can definitely address some of the manufacturing issues related to tungsten components, possibly open for the development of new designs and approaches. In particular, the tungsten tiles for the divertor can be produced in a more efficient way and their properties can be fine-tuned for the final application. Functionally graded structures produced with AM can lead to a controlled gradient, with regards both composition and properties, which can enhance the structural integrity of the components. Finally, due to the modularity and the extreme flexibility of some AM techniques, the repair and the maintenance of tungsten plasma facing components can be accomplished directly in-situ. This would markedly decrease the costs related to the entire cycle of production of these components.

In the past, tungsten has been reported to exhibit limited weldability [13,14]. Issues for fusion processes mainly are the pronounced cold brittleness, the high melting point and the marked reactivity with environmental gasses over a large range of temperature [15,16]. Fusion processes, as for instance arc welding, would lead to the production of components with a high density of defects, as cracks and pores, and heavy contamination, if not properly shielded [17].

Different studies of AM of tungsten have already been reported which employed laser as the heat source and tungsten powder as the feedstock [18]. The main challenges reported for the selective laser melting (SLM) process for tungsten mainly are the high melting point, the low wettability and the brittleness at low temperature [18]. For these reasons, most of the investigations available in the literature were unable to the achieve fully-dense deposits, avoiding the

predominant occurrence of micro-cracks and pores [19–22]. Tungsten components for nuclear application should be characterised by a density as close as possible to the theoretical density of tungsten, without any defects such as pores or cracks, in order to increase their lifetime under neutron radiation.

In the feasibility study of Nie et al. [19], tungsten cubes were produced using SLM, in particular, using a femtosecond laser as the heat source. The components were characterised by the presence of discontinuities and porosity throughout their volume. Wang et al. [20] reported about the production of pure tungsten components using SLM, achieving density as high as 96% of the theoretical tungsten density. Their study showed that when using polyhedral tungsten powder there was a marked occurrence of balling resulting in large defects and pores while using a spherical powder, continuous tracks were achieved although a dense network of micro-cracks and porosity were present.

Furthermore, Iveković et al. [21] also reported that extensive cracking was observed for tungsten component produced via SLM, even when a pre-heating of the substrate at 400°C was employed. They attributed the occurrence of cracks to thermal stress build-up during the solidification, which is usually rapid for laser processing, and to the presence of interstitial contaminants such as oxygen, nitrogen or carbon. The solidification dynamics of tungsten powder were studied by Zhou et al. [22] during the deposition using SLM. They found that tungsten high surface tension and viscosity induced a relative slow wetting and spreading speeds enhancing the balling phenomena.

Wire-feed technologies are emerging among the vast range of AM technologies mainly because of their ability to produce large-scale components [23,24]. Wire + Arc additive Manufacture (WAAM) is a novel AM process which employs an electric arc as the heat source and high-quality metal wire as the feedstock [25]. WAAM can directly fabricate fully-dense metallic large 3-D near-net-shape components with a much higher deposition rate, in the order of several kg/h, than most other metal additive manufacture processes [23,25]. The WAAM process has been demonstrated to successfully produce large-scale parts in stainless steel [26], Inconel [27], titanium [28] and aluminium [29], achieving even

complex geometries. WAAM is considered to be a technique suitable for the manufacture of large and engineered components because of its high deposition rate, relatively low cost and high flexibility in the design [25,30].

However, there are no reported investigations on the Wire + Arc Additive Manufacturing process of unalloyed tungsten. The main aim of this research is to investigate the WAAM process for unalloyed tungsten. In particular, develop a process which would lead to the production of defect-free fully-dense tungsten components on a large scale. The design of a proper heat source, the study and monitoring of the metal transfer and the characterisation under the microstructural point of view are the main steps of process development discussed. A design-scale structure has also been produced in order to understand the issues related to the scaling up and the implementation of the process as an innovative way to manufacture unalloyed tungsten functional parts.

3.2 Experimental Procedure

Unalloyed tungsten wire with a diameter of 1.0 mm was used for the Wire + Arc Additive Manufacturing process. Unalloyed tungsten plates produced using powder metallurgy route were used as substrates for the deposition. The plates for the initial trials of deposition had dimensions of 80.0 mm in length, 10.0 mm in width and 30.0 mm in height while, the plate used for the deposition of the large tungsten linear structure had dimensions of 210.0 mm in length, 10.0 mm in width and 30.0 mm in height. The surface of the plate was ground and rinsed with acetone prior to deposition in order to remove most of the contaminants. The composition of the materials used and of the linear structures deposited has been reported in **Table 3.1**.

	W	Mo	Ta	Ti	V	Cr	Fe	C	N	O	K
Substrate	99.99	<0.05	<0.05	<0.05	<0.05	<0.05	<0.05	11 ppm	<10 ppm	<50 ppm	<10 ppm
Wire	99.99	<0.05	<0.05	<0.05	<0.05	<0.05	<0.05	33 ppm	<10 ppm	<50 ppm	<10 ppm
Large Wall	99.99	<0.05	<0.05	<0.05	<0.05	<0.05	<0.05	<10 ppm	<10 ppm	<50 ppm	<10 ppm

Table 3.1: Elemental composition (wt.%) of tungsten the substrate and the wire used and of the structures presented in this study.

The study presented can be divided into three main parts with regards to the development of the deposition process. They can be summarised as follows:

- Weld pool formation and geometrical stabilisation;
- Metal transfer from the wire to the weld pool;
- Deposition of large-scale tungsten wall.

All of the experiments were performed using the same clamping system and the same welding apparatus. **Figure 3.1** shows the clamping system used to hold the substrate in the correct position. **Figure 3.1a** shows the complete assembly, indicating each element of the system. The substrate was firmly held by two bars and a lateral force was applied using a series of screws, which were pushing one of the bars. These parts were connected to the main support and two lateral supports which were fixed to the plate connected to the motorised stages. **Figure 3.1b** shows the material of each element of the system. Copper has been chosen as a backing plate and side clamping bars for its intrinsic high thermal conductivity.

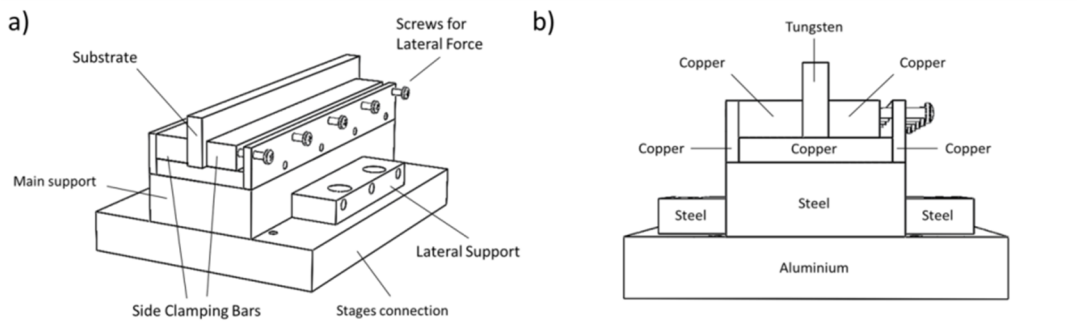

Figure 3.1: Schematisation of all the components used for the clamping system (a) and the material used for each of them (b).

Furthermore, a conventional tungsten inert gas (TIG) welding torch, a power supply and a controlled wire feeder were used for the deposition. The heat source, the wire delivery system and the substrate were attached to three linear motorized high-load stages assembled in XYZ configuration (**Figure 3.2**). The apparatus was completely surrounded by a heavy-duty enclosure used to ensure a low level of oxygen by purging with high-purity argon.

3.2.1 Weld pool formation and geometrical stabilisation

During this stage, the weld pool formation and its geometrical stabilisation were studied, optimising the welding process parameters. In particular,

autogenous welds were performed (without the addition of the wire) in order to obtain the proper parameters to achieve a consistent melting of the tungsten plate. Three autogenous welds of 80.0 mm in length have been performed using the parameters reported in **Table 3.2**. In order to stabilise the thermal flow and, consequently, the weld pool dimensions, a stationary arc was used. In particular, the electric arc was left on and stationary at the beginning of the welding process for different times according to the parameters in **Table 3.3**. This set of experiments were performed using the set-up configuration reported in **Figure 3.2b** but without the addition of wire.

TS [mm/s]	I [A]	Electrode-workpiece Distance [mm]	Electrode angle [°]	Electrode Diameter [mm]	Shielding gas composition [%]	Gas flow rate [L/min]	Oxygen Atmosphere [ppm]
2	350	3.5	45	3.2	100 He	15	≈100
2	375	3.5	45	3.2	100 He	15	≈100
2	400	3.5	45	3.2	100 He	15	≈100

Table 3.2: Process parameters used for the autogenous welds of tungsten substrate.

TS [mm/s]	I [A]	Steady Arc-on [s]	Electrode-workpiece Distance [mm]	Electrode angle [°]	Electrode Diameter [mm]	Shielding gas composition [%]	Gas flow rate [L/min]	Oxygen Atmosphere [ppm]
2	400	3.5	3.5	45	3.2	100 He	15	≈100
2	400	4.0	3.5	45	3.2	100 He	15	≈100
2	400	4.5	3.5	45	3.2	100 He	15	≈100

Table 3.3: Process parameters used for the stationary arc.

3.2.2 Metal transfer from the wire to the weld pool

During this stage, a wire was added to the welding process in order to study the metal transfer to the weld pool. In particular, a study with regards the orientation of wire feeding and its impact on the formation of eventual defects was investigated. The wire feeding orientations used were the side-feeding and the front-feeding approach. The layers were progressively deposited onto the substrate using a single bead. The direction of deposition was always kept constant for each successive layer. Two short walls were deposited using respectively wire side feeding and wire front feeding. **Figure 3.2** shows the layout of the apparatus used for the deposition. The main coordinates are kept constant for both the

schematics reported. **Figure 3.2a** shows the configuration of deposition for the linear structure produced using wire side feeding and **Figure 3.2b** shows the configuration for the wire front feeding approach. The deposition orientation was adapted simply rotating the whole block of clamping and substrate as the wire feeding system was kept fixed. In particular, deposition was performed parallel to the Y-axis for the side feeding and parallel to the X-axis for the front feeding.

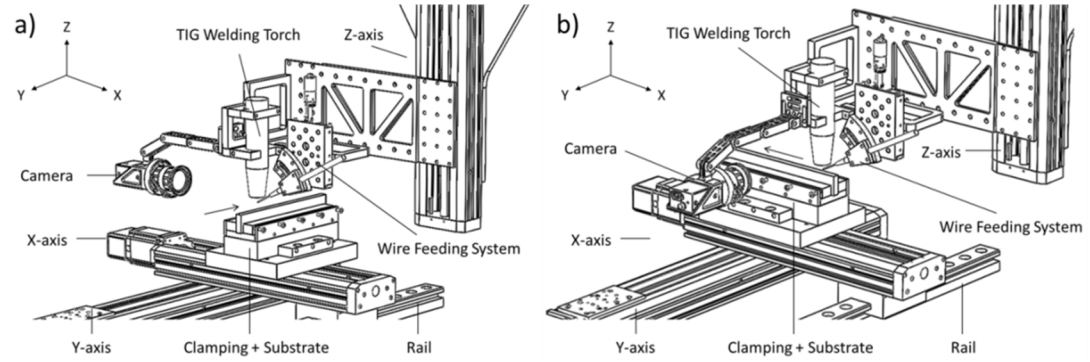

Figure 3.2: Set-up used for the development of the WAAM process for unalloyed tungsten when using side feeding (a) and when using front feeding (b).

In both **Figure 3.2a** and **Figure 3.2b,** the arrow placed close to the substrate represents the movement of the substrate under the torch and wire feeding system so that the actual deposition direction is considered opposite to the arrow. The orientation of the camera was also changed for the two configurations keeping the camera always pointed and focused on the side of the wall. The camera was used to monitor the weld pool dimension and the metal transfer from the wire to the weld pool. The two short walls were produced using the parameters shown in **Table 3.4**. The parameters were kept constant throughout the entire process. The parameters of deposition not shown were kept constant to the values reported in **Table 3.2** and **Table 3.3**.

TS [mm/s]	WFS [mm/s]	I [A]	Steady Arc-on [s]
2	35	400	4.0

Table 3.4: WAAM process parameters used for the deposition of unalloyed tungsten.

The microstructure and the nature of eventual defects were examined using the cross-section perpendicular to the deposition direction for both side-fed and

front-fed sample. The samples were polished using the procedure in **Table 3.5** and Murakami's reagents were used as etching solution for 20 seconds each sample.

Grinding and Polishing means	Time [min]
SiC Paper 240 grid	2
SiC Paper 1200 grid	6
SiC Paper 2500 grid	6
Alpha alumina 0.3 μm suspension	15
Alumina and silica 0.05 μm suspension	15
Colloidal silica 0.02 μm suspension	15

Table 3.5: Grinding and polishing procedures used for the microstructural preparation.

3.2.3 Deposition of large-scale tungsten wall

A large-scale tungsten wall was built using the optimal set-up and parameters developed during the previous phases of the investigation. In particular, the linear structure was produced using the parameters shown in **Table 3.4** and employing the front-feeding configuration. This was performed in order to prove the scalability of the Wire + Arc Additive Manufacturing process. The wall produced was characterised by the dimensions of 120.0 mm in length, 75.0 mm in height and around 12.0 mm in thickness. The parameters were kept constant throughout the entire process and the average layer height was measured to be around 1.25 mm.

3.3 Results and Discussion

3.3.1 Substrate orientation and clamping system

The selection of the substrate orientation with respect to the heat source and the utilisation of a proper clamping system was crucial aspects of the process development. These were chosen based on previous experimental results which were showing consistent substrate cracking caused by the thermal shock and the residual stresses developed during the deposition. Therefore, a specific substrate orientation and clamping system were used in this study in order to prevent the development of lateral cracks and to achieve an even distribution of heat and stresses during the process (**Figure 3.1**). A lateral clamping system was acting on the lower side of the substrate in order to allow the substrate to just be held in position. In this configuration, the upper part of the substrate was left free to thermally expand or contract with regards to its length. In fact, the upper side of

the substrate was not constrained by any colder surrounding metal, therefore, no regions interested by dissimilar thermal shock were in direct contact during the deposition process. Furthermore, this particular orientation of the substrate was simulating a wall-like structure and this aspect made the layer geometry to be more consistent since the beginning of the deposition as the total heatsink was almost unchanged for the entire process.

3.3.2 Weld pool formation and geometrical stabilisation

A complete control of the weld pool dimensions and their preservation for the entire duration of the deposition are required for an accurate prediction of the layers' geometry and to ensure the total stability of the process. Thus, the design of a steady-state thermal flow is needed and it was achieved by studying the interaction of the electric arc with the substrate, without the addition of the wire.

3.3.2.1 Autogenous welds

The time-resolved images of the autogenous welds of the tungsten substrate using the three different arc currents (**Table 3.2**) are reported in **Figure 3.3**, **Figure 3.4** and **Figure 3.5.** A frame time of 5.0 seconds has been used to monitor and characterise the formation and the dimensions of the weld pool**.** In each picture, the electrode tip, the arc column and the substrate are shown. For all three autogenous welds, it is shown that there was melting of the tungsten substrate after 5.0 seconds but no weld pool edges were visible from the side. Clear weld pool edges and a constant weld pool size were achieved after 20.0 seconds when using a welding current of 350 and 375 Amps and after 15.0 seconds, when using a welding current of 400 Amps. This clearly showed that all tests performed were characterised by a transient welding state. In particular, the weld pool dimensions continuously increased from the beginning of the welding process until reaching a constant state. Predictably, the weld pool size, measured at the steady state, increased as the welding current was increased.

The presence of a transient welding state at the beginning of the process is directly related to the transient thermal flow through the volume of the substrate per unit of time. This is caused by the characteristic variation of thermal

conductivity of tungsten. In fact, it is known that the thermal conductivity of tungsten decreases as the temperature increases [31]. At the beginning of the process, the substrate was cold and the material was characterised by a relatively high thermal conductivity. This means that the material was able to efficiently conduct the heat away from the surface facing the arc toward to the bottom of the substrate. The temperature of the material surrounding the weld pool did not rise because of the high-temperature gradient established.

As the process progressed in time, the temperature of the material surrounding the weld pool increased as the system was not connected to an infinite heat sink. This led to a progressive decreasing in thermal conductivity due to the heat accumulation. The heat loss through conduction from the weld pool progressively decreased allowing the weld pool to expand and increase its dimensions.

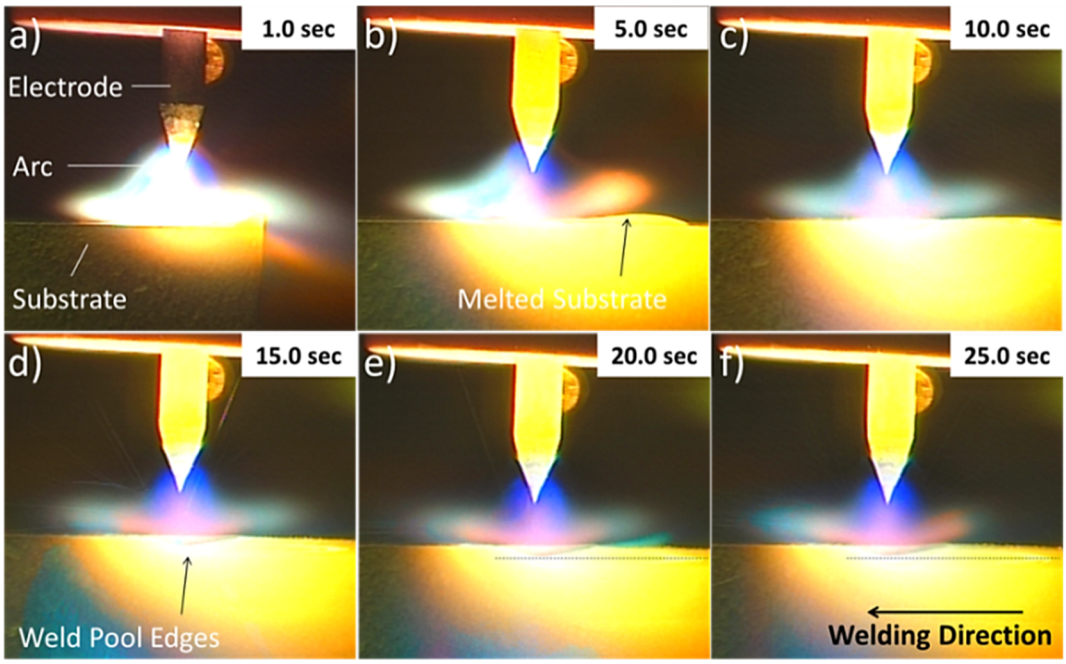

Figure 3.3: Time-resolved images of the autogenous weld performed using an arc current of 350 Amperes with a frame time of 5.0 seconds.

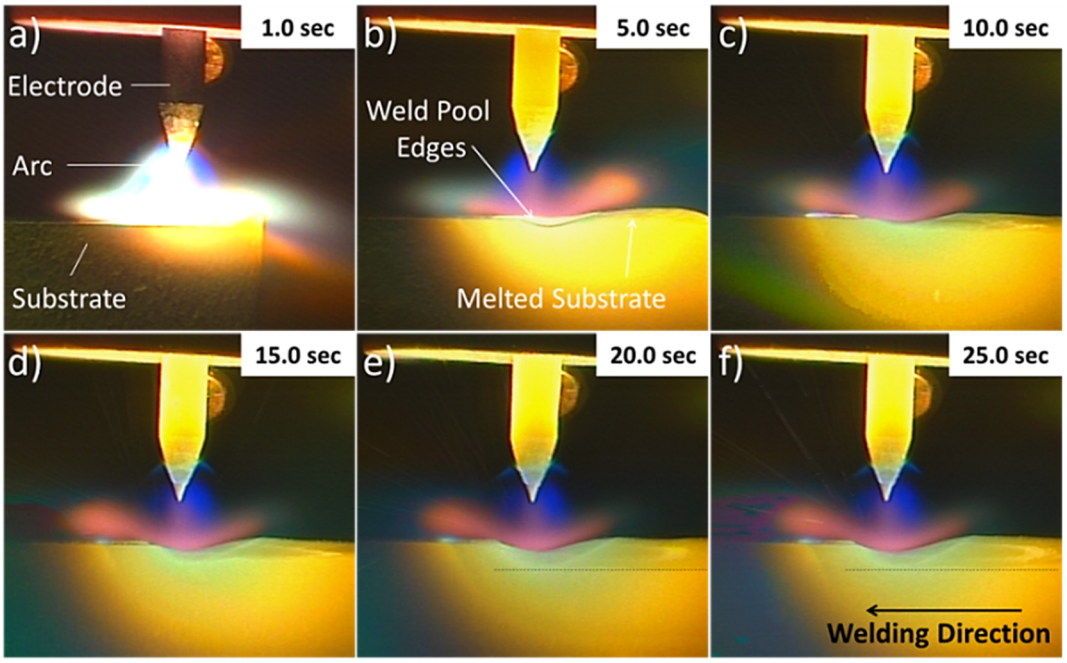

Figure 3.4: Time-resolved images of the autogenous weld performed using an arc current of 375 Amperes with a frame time of 5.0 seconds.

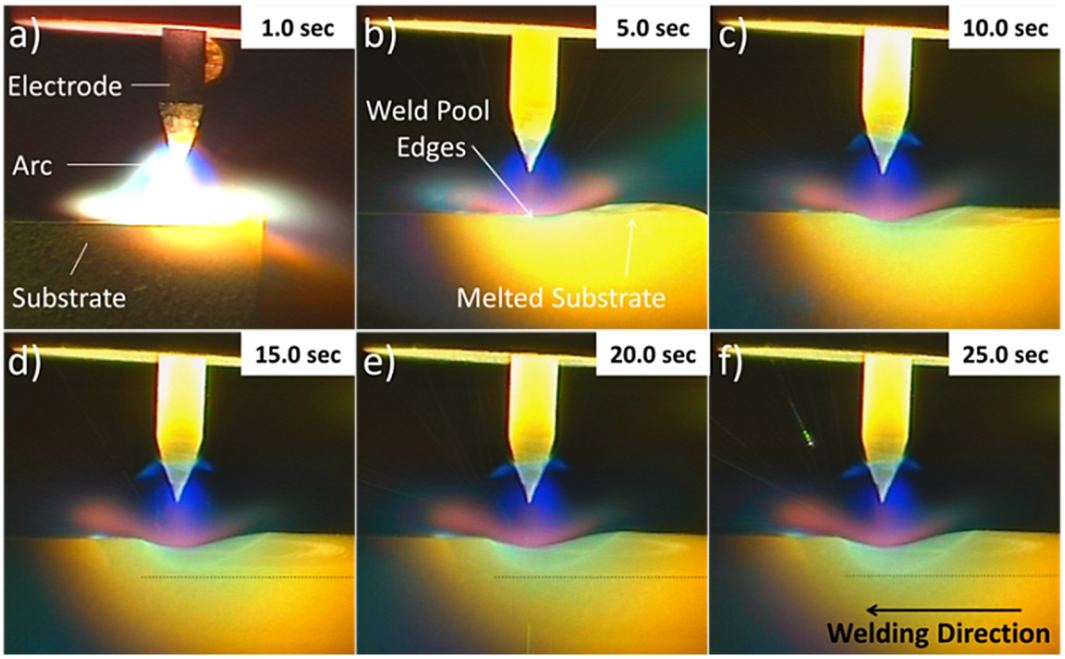

Figure 3.5: Time-resolved images of the autogenous weld performed using an arc current of 400 Amperes with a frame time of 5.0 seconds.

This led to an equilibrium with regards to the heat flow as well as the weld pool dimensions. Regarding the weld pool produced using 400 Amps, as more power was used, the stabilisation of the weld pool dimensions occurred faster when compared to the other two cases. This welding current was chosen for

further investigations due to the larger weld pool dimensions respect with to the other cases. In fact, a shallower weld pool would have been an unfavourable condition for the addition of the wire.

3.3.2.2 Stationary arc start

The achievement of the steady-state heat flow was studied by involving an additional step of weld pool formation and stabilisation. A stationary arc was used at the beginning of each weld for different time durations. The weld pool evolution under stationary arc is reported in **Figure 3.6**, **Figure 3.7** and **Figure 3.8** respectively for 3.5 seconds, 4.0 seconds and 4.5 seconds. All of the time-resolved images present a liquid pool that formed at around 1.0 second from the arc strike and progressively grew in width and in depth until solidification, when the electric arc was turned off. A weld pool depth of 2.45 mm, 2.7 mm and 2.95 mm were achieved respectively for 3.5 seconds, 4.0 seconds and 4.5 seconds stationary arc.

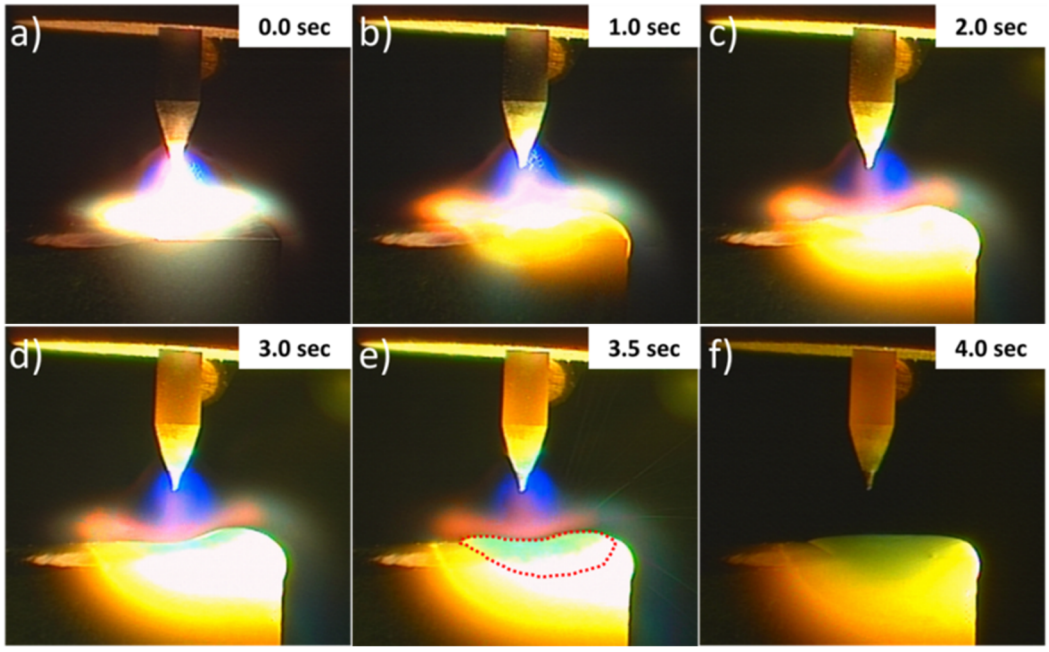

Figure 3.6: Time-resolved images of the weld pool evolution under stationary arc for 3.5 seconds.

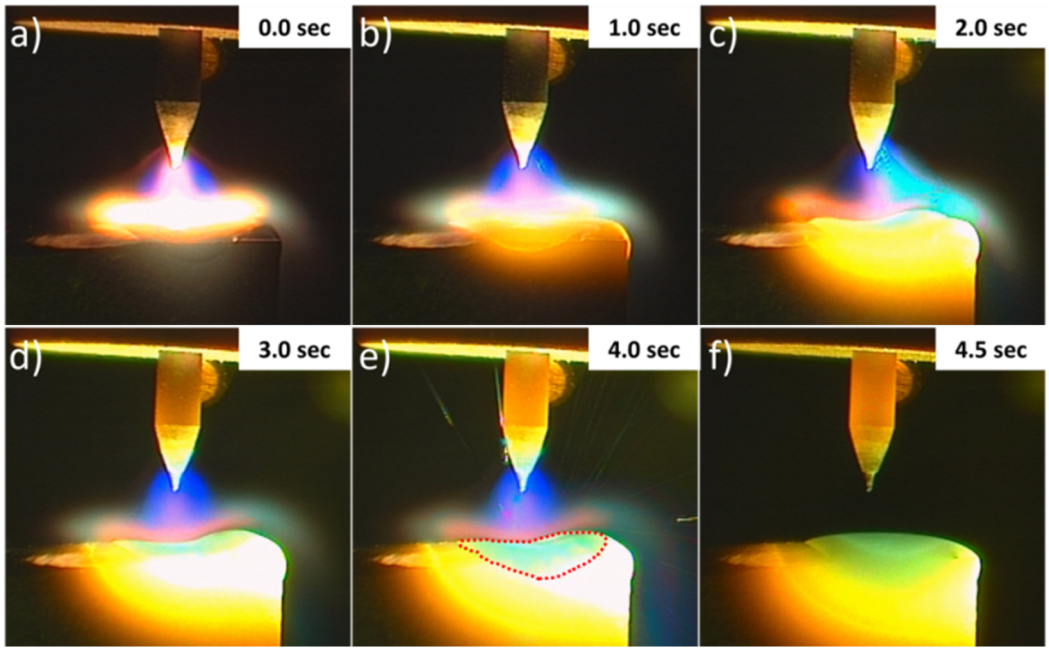

Figure 3.7: Time-resolved images of the weld pool evolution under stationary arc for 4.0 seconds.

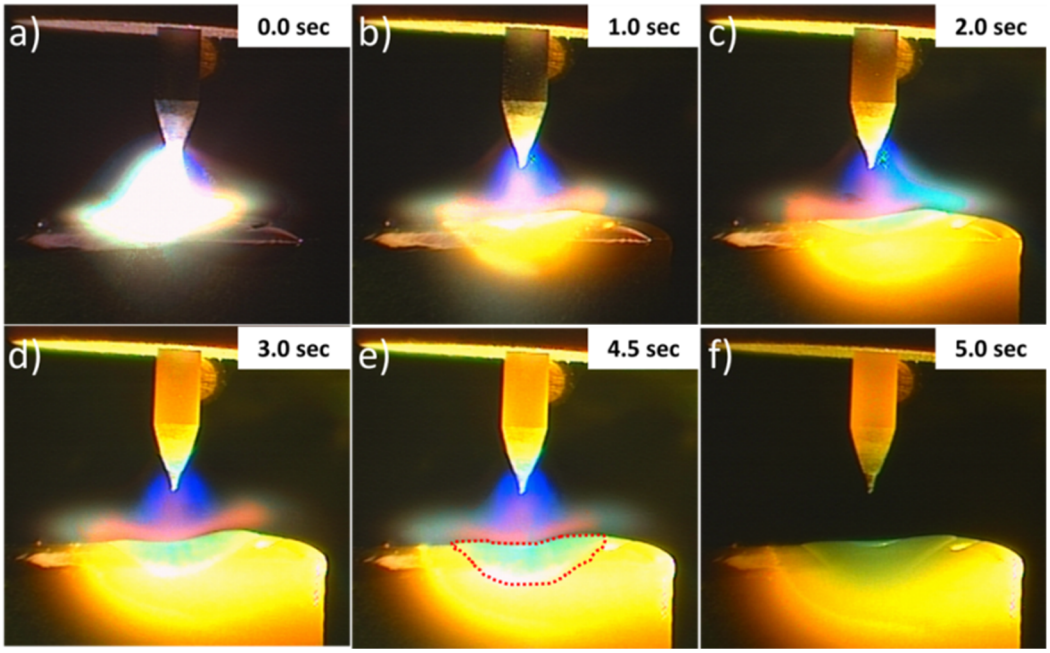

Figure 3.8: Time-resolved images of the weld pool evolution under stationary arc for 4.5 seconds.

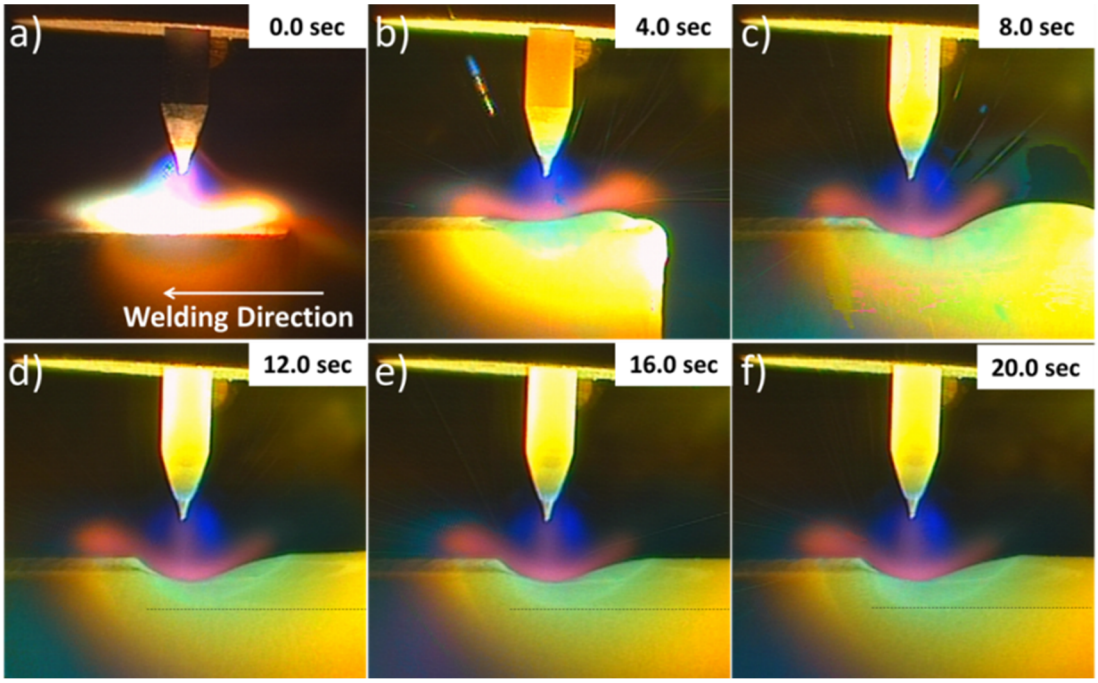

Figure 3.9: Time-resolved images of the steady welding process of unalloyed tungsten using an arc current of 400 Amps, a travel speed of 2 mm/s and a stationary arc for 4.0 seconds.

Figure 3.9 shows the time-resolved images of the autogenous weld performed combining an arc current of 400 Amps, a travel speed of 2 mm/s and a stationary arc for 4.0 seconds. It is clear that the weld pool depth was constant since the beginning of the process. In particular, the weld pool depth was stabilised around 2.75 mm between 4.0 and 8.0 seconds for the beginning of the process.

3.3.3 Metal transfer from the wire to the weld pool

The addition of the feedstock, wire in this case, to the weld pool was the natural following step for the development of the AM process. The effect of the wire feeding orientation on the deposited structure was studied using side feeding and front feeding configurations (**Figure 3.2a** and **Figure 3.2b**). In particular, the side feeding was obtained delivering the wire in the direction orthogonal to the deposition direction, while, for the front feeding, the wire feeding direction and the deposition direction were parallel. The study on the orientation of feeding was fundamental in order to understand the potential and the flexibility of the process developed.

3.3.3.1 Wire side feeding

Figure 3.10 shows a sequence of time-resolved images of the tungsten WAAM process when using the side-feeding configuration. It is important to note the time frame length. A continuous liquid metal transfer from the wire to the weld pool was kept constant for the whole layer deposition. The process was characterised by the ejection of small particles for the entire deposition. In particular, it seemed that these spattered particles were caused by two main ejection mechanisms.

In **Figure 3.10a**, an arrow has been used to point out an ejection stream, which was assumed to be caused by spattered particles coming directly from the liquid pool. Contrarily, in **Figure 3.10c** the spattered particles seemed to have been ejected from the liquid metal at the end of the wire. Spattered particles were already seen for tungsten tiles exposed to helium plasma. Coenen et al. [32] suggested that tungsten erosion may occur during high-temperature exposures by evaporation and macroscopic mass losses from the melt, such as spraying or splashing.

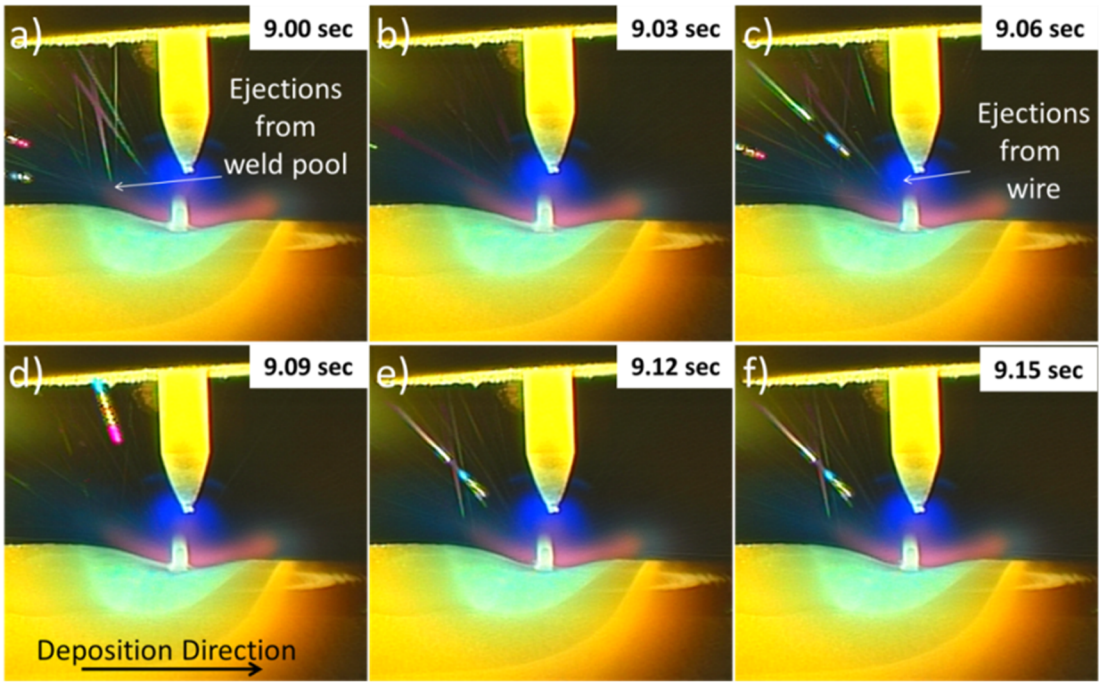

Figure 3.10: Time-resolved images of the deposition performed using side-feeding configuration.

The droplets or macroscopic mass losses, localised predominantly along the melted surface, were indicated to arise because of the Kelvin–Helmholtz instability [32–34]. This phenomenon occurs when there is a difference in velocity across the interface between two fluids. In the case of tungsten WAAM deposition, the ejection of particles occurred due to the Kelvin–Helmholtz instability caused by the different relative speeds and different densities of the liquid tungsten and the helium plasma which created a velocity shear at their interface. Furthermore, it has been reported that the Kelvin–Helmholtz instability can also lead to the evolution of shock waves along the surface of the fluid causing a breakup of the melt surface into droplets [35].

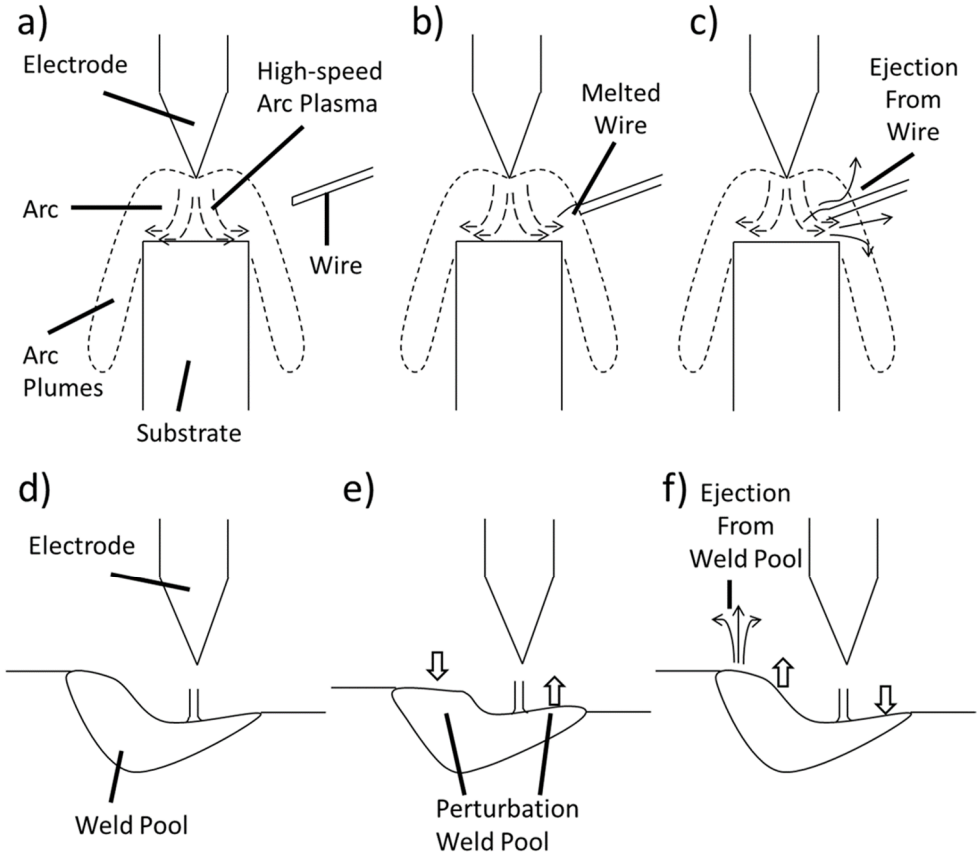

Figure 3.11; Schematisation of different metal particle ejection during the deposition of tungsten using side feeding: ejection from the wire (a-c) and ejection from the weld pool (d-f).

In order to understand the occurrence of the spattered particles, two simple schematics, which describe the two different ejection modes during the deposition of tungsten when using the wire side feeding, are reported in **Figure 3.11.** In

particular, the ejection of the particles from the liquid metal at the end of the wire is schematised from **Figure 3.11a** to **Figure 3.11c**, while, the ejection from the melt pool from **Figure 3.11d** to **Figure 3.11f.**

When the arc welding process is performed on a wall-like workpiece, lateral plasma plumes forms on each side of the workpiece due to the high plasma velocity (**Figure 3.11a**). The effect is more pronounced when using helium instead of argon as shielding gas due to the higher gas velocity at the core of the arc [36]**.** When the wire approaches the arc column from the side, the hot plasma gasses from the arc plumes start to heat up and eventually melt the wire (**Figure 3.11b**). The particle ejections occur when the liquid tungsten at the tip of the wire faces the high-velocity stream of plasma gasses near the centre of the arc, due to the Kevin-Helmotz instability (**Figure 3.11c**).

The particle ejections deriving from the weld pool could be caused by a combined effect of the Kevin-Helmotz instability and a high level of disturbance on the weld pool caused by the wire. This led shock waves to develop within the liquid pool. The impact of the waves could have been high enough to overcome the surface tension, resulting in the ejection of particles from the back of the weld pool (**Figure 3.11f**).

In **Figure 3.12a** is reported the picture of the linear structure deposited using side feeding. The silver surface denoted the complete absence of oxidation. Both sides of the deposited structure using wire side feeding are compared in **Figure 3.12b** and **Figure 3.12c.**

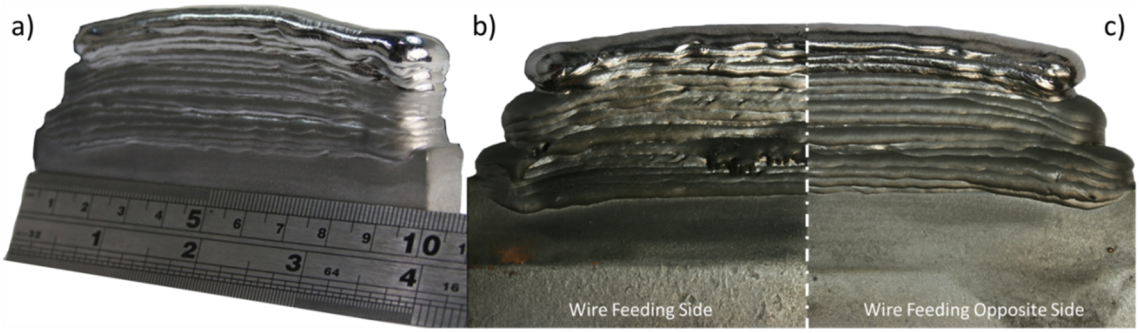

Figure 3.12: Tungsten linear structure deposited using side feeding (a). Comparison of the wire feeding side (b) of the structure and the opposite one (c).

In particular, **Figure 3.12b** shows the wall appearance of the side from which the wire was delivered to the weld pool, while, **Figure 3.12c** shows the wall appearance of the opposite side. A large number of irregularities and small defects were found on the outer surface of the wire feeding side (**Figure 3.12b**). The occurrence of spattered particles, localised on this side of the structure, clearly enhanced the formation of defects like voids and lacks of fusion. Further investigations about the nature and the formation of these defects are reported later within the microstructural analysis section.

3.3.3.2 Wire front feeding

Figure 3.13 reports a time-resolved image sequence of the tungsten WAAM process employing wire front feeding. It can be clearly seen that the process was characterised by a constant bridge transfer of liquid tungsten from the wire to the weld pool. During the bridge transfer, the contact between the weld pool and the tip of the wire was kept constant and this produced a smooth metal transition. There was no presence of spatter or weld pool perturbation during the deposition. The wire was constantly melted and transferred at a controlled rate.

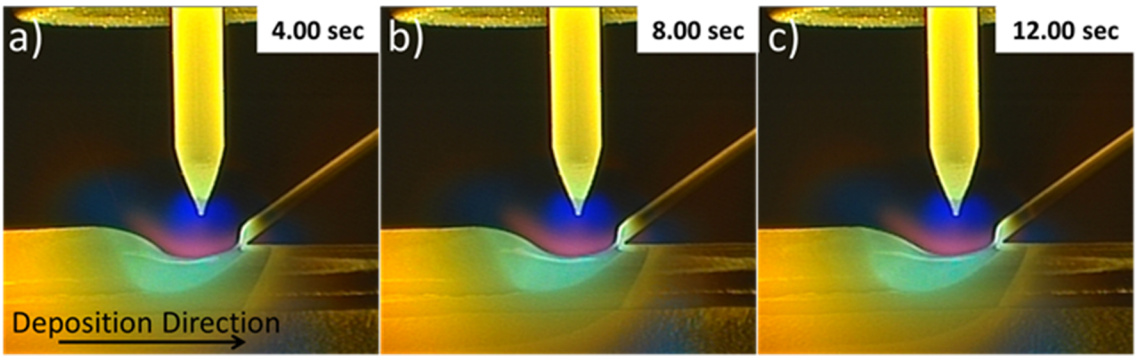

Figure 3.13: Time-resolved images of the front-fed deposition process with a time frame of 4.0 seconds.

The accurate management of all the fundamental parameters and strategy of deposition lead to the full exploitation of the WAAM process potential for the production of tungsten structures. The ejections from the liquid tungsten at the end of the wire were considerably reduced when the front-fed approach was used. This occurred because the wire was promptly transferred to the liquid pool, without interfering with the lateral streams of high-velocity plasma gasses.

3.3.4 Microstructure

The two linear structures deposited respectively by using wire side feeding and wire front feeding were also the objects of microstructural characterisation. The cross-section of the structures parallel to the deposition direction was used to observe the presence of any defects and the crystal structure developed after solidification.

3.3.4.1 Microstructure side-fed deposit

Figure 3.14a shows the microstructural features of the entire deposited structure manufactured using the side feeding. The left-hand side corresponded to the wire feeding side. In general, the absence of large columnar grains, typical of other metal when deposited via WAAM [28,29], can be observed.

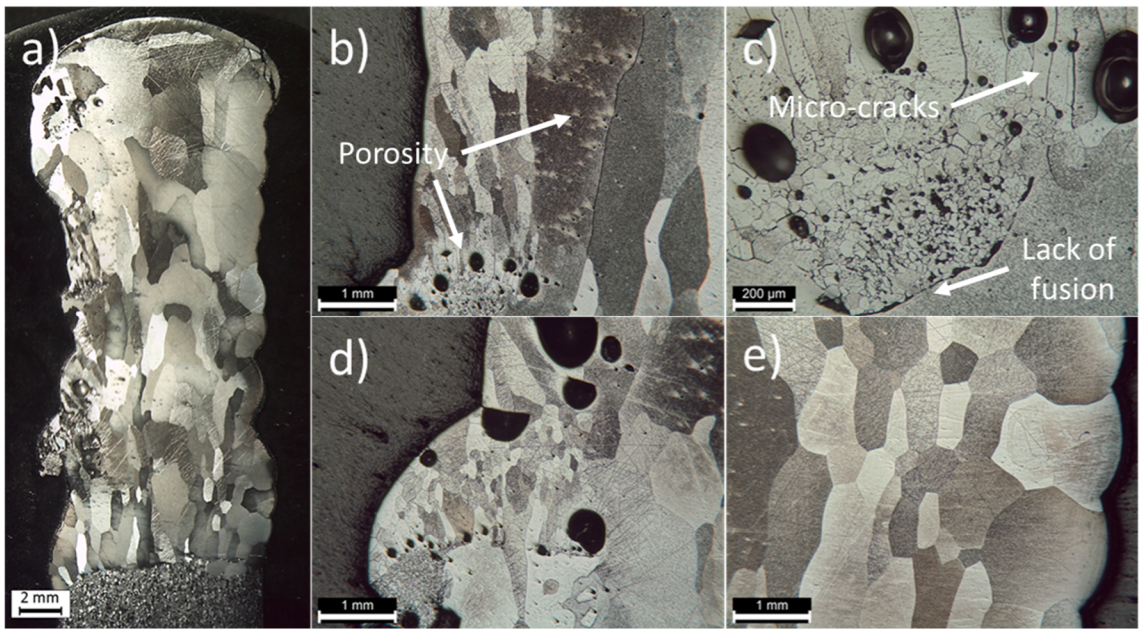

Figure 3.14: Microstructure of the linear structure deposited using wire side feeding (a). Details of the defects located on the side facing the wire feeder (b-d). Detail of the microstructure at the base of the linear structure (e).

The microstructure was composed of equiaxed crystals near the bottom of the structure (**Figure 3.14a** and **Figure 3.14e**) and larger elongated grains on the upper part of the structure (**Figure 3.14a** and **Figure 3.14b**). The left-hand side, the wire feeding side, was characterised by a high presence of defects as: lack of fusion, porosity and micro-cracks among the pores as well as grain with a much finer grain size (**Figure 3.14b** and **Figure 3.14c**).

Starting with a cold substrate and cold clamping system surely enhanced a faster solidification as the thermal conductivity of tungsten is relatively high at room temperature. Furthermore, the rapid solidification rate of tungsten increased the likelihood to form nuclei for the solidification within the liquid and at the surface of the weld pool. These lead to a multidirectional solidification from different nuclei during cooling, instead of epitaxial growth, which resulted in an equiaxed-like microstructure.

As the deposition progressed, the structure gradually became hotter so that it was characterised by a relatively lower value of thermal conductivity and also a lower thermal gradient. Under these conditions, the actual solidification time slightly increased and epitaxial growth occurred for some grains. After the solidification, the heat was retained for a marginally longer time so that some grains experienced grain growth resulting in a coarser grain size. These are the reasons why coarser and elongated grains were formed in the microstructure of the upper layers. The irregular distribution and asymmetry of the grains could be attributed to the disturbance induced by the wire feeding from the side. The grains around the defects on the left side were found to be considerably smaller than the rest of the structure indicating that the wire feeding resulted in a local temperature variation. The liquid metal delivered from the wire to the weld pool also opposed or interfered with the internal flow of the weld pool. The occurrence of porosity and lack of fusion may be addressed to the particles ejected from the liquid tungsten at the wire-weld-pool interface and, also, to pores or voids within the wire feedstock. The presence of these defects and the repetitive process thermal cycles led to the formation of network of micro-cracks among the pores and the lack of fusion.

3.3.4.2 Microstructure front-fed deposit

Figure 3.15a reports the microstructure of the entire deposited structure produced using the front feeding. The crystallisation followed the same trend already seen for the side-fed structure. In particular, finer equiaxed grains (**Figure 3.15a** and **Figure 3.15e**) were found in the initial layers of the structure and coarser elongated grains (**Figure 3.15a** and **Figure 3.15c**) in the upper part of the

deposit. The grains of the upper part seemed to be the result of multiple specular dendritic structures propagating and meeting at the centre of the deposit (**Figure 3.15c**). The complete absence of pores and lacks of fusion within the front-fed structure resulted to be directly correlated to the absence of spattered particles shown in **Figure 3.13**. Thus, avoiding the formation of spatter is required in order to preserve the structural integrity of the tungsten wall deposited via WAAM.

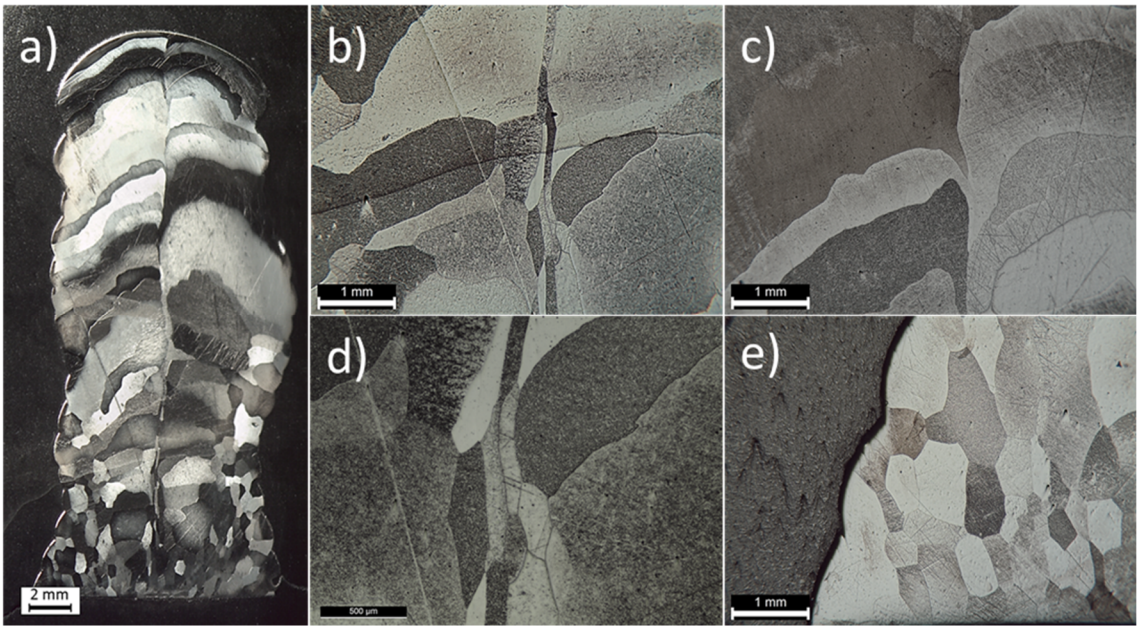

Figure 3.15: Microstructure of the linear structure deposited using wire front feeding (a). Details of the elongated grains found at the centre of the structure (b, d). Detail of the microstructure of the upper part of the structure (c). Detail of the microstructure at the base of the linear structure (e).

3.3.5 Deposition of large-scale tungsten wall

Figure 3.16a and **Figure 3.16b** show the large-scale tungsten structure produced via WAAM using the parameters reported in **Table 3.4** and the wire front feeding approach. The wall reported represents one of the first large-scale structures deposited in unalloyed tungsten using complete fusion by an additive manufacturing technique. The unique aspects of this structure were the absence of any large network of grain boundary cracks within the volume deposited, almost absence of discolouration and oxidation from the fusion process and the constant layer geometry achieved. **Figure 3.16c** shows the detail of the surface of the linear structure with a crack in the middle. In particular, this crack is also visible in **Figure 3.16b** in the middle of the structure's length extending from the baseplate

to one-third of the deposit's height. The crack was characterised by an intergranular fractured surface and no additional intra-layer micro-cracks were observed (**Figure 3.16d**). The occurrence of this single large crack was connected to the deposition procedure. In particular, this structure was deposited on two consecutive days, leaving the structure to completely cool down to room temperature overnight. When the deposition process was restarted, severe thermal shock developed within the already deposited part. Thus, the crack might have been caused by the thermal shock of the first deposition of the second day.

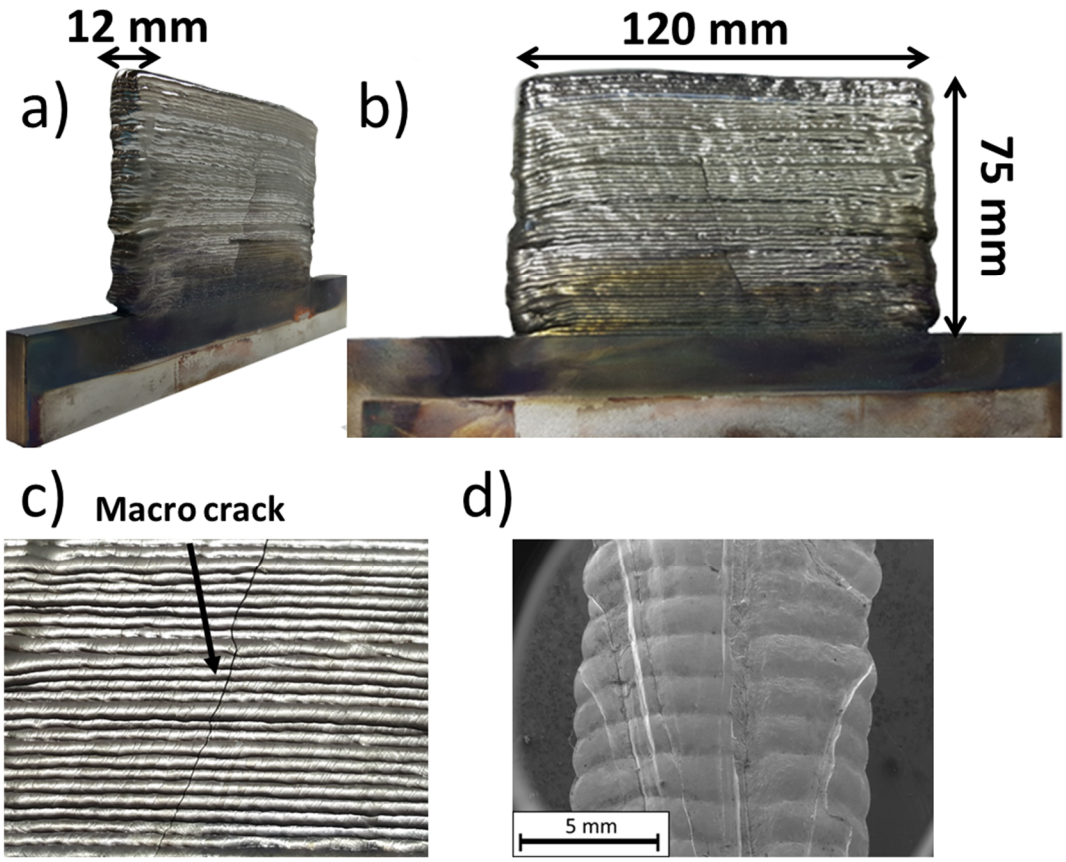

Figure 3.16: Large-scale unalloyed tungsten linear structure deposited via Wire + Arc Additive Manufacturing process (a-b). Picture of the fracture from the outer surface (c) and SEM picture of the fractured surface (d).

3.4 Conclusions

In this study, it has been proven that the Wire + Arc Additive Manufacturing process is suitable and able to produce large-scale refractory metal components by complete fusion. In particular, high-purity tungsten walls have been successfully deposited without oxidation and with a high structural integrity and density. The

design of a proper heat source allowed overcoming some limits of manufacturing typical of unalloyed tungsten as its brittleness at room temperature and its high melting point. The main finding of this study can be summarised as:

- A controlled steady-state heat flow was required in order to obtain constant and predictable weld pool dimensions. This has been achieved using a stationary arc for 4.0 seconds which allowed the weld pool to fully develop before starting the deposition;

- The orientation of the wire feeding has a severe impact on the occurrence of spatter and structural defects, such as pores and lacks fusion. In particular, a defect-free tungsten structure was deposited when using the wire front feeding approach;

- The microstructure of the deposit was also influenced by the orientation of wire feeding. A symmetrical and regular grain distribution has been observed for the structure deposited using wire front feeding, unlike, the structure produced using wire side feeding;

- The Wire + Arc additive Manufacturing technology could be considered a real candidate to replace the current method of manufacturing of tungsten, ensuring the possibility to produce fully-dense large-scale components.

3.5 Bibliography

1. Rieth M., Dudarev SL., Gonzalez De Vicente SM., Aktaa J., Ahlgren T., Antusch S., et al. Recent progress in research on tungsten materials for nuclear fusion applications in Europe. Journal of Nuclear Materials. 2013; 432(August 2012): 482–500. Available at: DOI:10.1016/j.jnucmat.2012.08.018
2. Causet R a., Venhaus TJ. The Use of Tungsten in Fusion Reactors: A Review of the Hydrogen Retention and Migration Properties. Physica Scripta. 2001; T94: 9. Available at: DOI:10.1238/Physica.Topical.094a00009
3. Zhang Y., Galloway A., Wood J., Olsson Robbie MB., Easton D., Zhu W. Interfacial metallurgy study of brazed joints between tungsten and fusion related materials for divertor design. Journal of Nuclear Materials. Elsevier B.V.; 2014; 454(1–3): 207–216. Available at: DOI:10.1016/j.jnucmat.2014.07.058

4. Sheng H., Sun Z., Uytdenhouwen I., Van Oost G., Vleugels J. Temperature and deformation effect on the low and high angle grain boundary structure of a double forged pure tungsten. International Journal of Refractory Metals and Hard Materials. Elsevier Ltd; 2015; 50: 184–190. Available at: DOI:10.1016/j.ijrmhm.2015.01.008
5. Piotter V., Zeep B., Norajitra P., Ruprecht R., von der Weth A., Hausselt J. Development of a powder metallurgy process for tungsten components. Fusion Engineering and Design. 2008; 83: 1517–1520. Available at: DOI:10.1016/j.fusengdes.2008.06.022
6. Németh A a. N., Reiser J., Armstrong DEJ., Rieth M. The nature of the brittle-to-ductile transition of ultra fine grained tungsten (W) foil. International Journal of Refractory Metals and Hard Materials. Elsevier Ltd; 2015; 50: 9–15. Available at: DOI:10.1016/j.ijrmhm.2014.11.005
7. Gaganidze E., Rupp D., Aktaa J. Fracture behaviour of polycrystalline tungsten. Journal of Nuclear Materials. Elsevier B.V.; 2014; 446(1–3): 240–245. Available at: DOI:10.1016/j.jnucmat.2013.11.001
8. Wong K V., Hernandez A. A Review of Additive Manufacturing. ISRN Mechanical Engineering. 2012; 2012: 1–10. Available at: DOI:10.5402/2012/208760
9. Herderick ED. Progress in Additive Manufacturing. JOM. 2015; 67(3): 580–581. Available at: DOI:10.1007/s11837-015-1323-x
10. Guo N., Leu MC. Additive manufacturing: Technology, applications and research needs. Frontiers of Mechanical Engineering. 2013; 8(3): 215–243. Available at: DOI:10.1007/s11465-013-0248-8
11. Frazier WE. Metal additive manufacturing: A review. Journal of Materials Engineering and Performance. 2014; 23(6): 1917–1928. Available at: DOI:10.1007/s11665-014-0958-z
12. Herderick E. Additive manufacturing of metals: A review. Materials Science and Technology Conference and Exhibition 2011, MS and T'11. 2011; 2(176252): 1413–1425. Available at: http://www.scopus.com/inward/record.url?eid=2-s2.0-84856301323&partnerID=40&md5=e02018d10b2ca37a7e2ae1773e4fcaec
13. Cole NC., Gilliland RG., Slaughter GM. Weldability of Tungsten and Its Alloys. Welding research supplement. Chicago; 1971; : 419–426.
14. Scott M., Knowlson P. The welding and brazing of the refractory metals niobium, tantalum, molybdenum and tungsten — a review. Journal of the Less Common Metals. 1963; 5: 205–244. Available at: DOI:10.1016/0022-5088(63)90029-8
15. Lessmannt GG., Gold RE. WELDABILITY OF TUNGSTEN BASE ALLOYS. 1970.
16. Farrell K., Houston JT., Chumley JW. Hot Cracking in Fusion Welds in Tungsten. 1st International AWS-WRC Brazing Conference. Cleveland; 1970. pp. 132–137.
17. Olson DL., Mishra B., Wenman DW. Welding , Brazing and Joining of Refractory Metals and Alloys. Min. Pro. Exi. Met. Rev. 2001; 22: 1–23. Available at: DOI:10.1080/08827509808962487
18. Yap CY., Chua CK., Dong ZL., Liu ZH., Zhang DQ., Loh LE., et al. Review of

selective laser melting: Materials and applications. Applied Physics Reviews. 2015; 2(4). Available at: DOI:10.1063/1.4935926

19. Nie B., Yang L., Huang H., Bai S., Wan P., Liu J. Femtosecond laser additive manufacturing of iron and tungsten parts. Applied Physics A: Materials Science and Processing. Springer Berlin Heidelberg; 2015; 119(3): 1075–1080. Available at: DOI:10.1007/s00339-015-9070-y
20. Wang D., Yu C., Zhou X., Ma J., Liu W., Shen Z. Dense Pure Tungsten Fabricated by Selective Laser Melting. Applied Sciences. 2017; 7(4): 430. Available at: DOI:10.3390/app7040430
21. Iveković A., Omidvari N., Vrancken B., Lietaert K., Thijs L., Vanmeensel K., et al. Selective laser melting of tungsten and tungsten alloys. International Journal of Refractory Metals and Hard Materials. 2018; 72(December 2017): 27–32. Available at: DOI:10.1016/j.ijrmhm.2017.12.005
22. Zhou X., Liu X., Zhang D., Shen Z., Liu W. Balling phenomena in selective laser melted tungsten. Journal of Materials Processing Technology. Elsevier B.V.; 2015; 222: 33–42. Available at: DOI:10.1016/j.jmatprotec.2015.02.032
23. Ding D., Pan Z., Cuiuri D., Li H. Wire-feed additive manufacturing of metal components: technologies, developments and future interests. International Journal of Advanced Manufacturing Technology. 2015; 81(1–4): 465–481. Available at: DOI:10.1007/s00170-015-7077-3
24. Baufeld B., Brandl E., Van Der Biest O. Wire based additive layer manufacturing: Comparison of microstructure and mechanical properties of Ti-6Al-4V components fabricated by laser-beam deposition and shaped metal deposition. Journal of Materials Processing Technology. Elsevier B.V.; 2011; 211(6): 1146–1158. Available at: DOI:10.1016/j.jmatprotec.2011.01.018
25. Williams SW., Martina F., Addison AC., Ding J., Pardal G., Colegrove P. Wire + Arc Additive Manufacturing. Materials Science and Technology. 2016; 32(7): 641–647. Available at: DOI:10.1179/1743284715Y.0000000073
26. Yilmaz O., Ugla AA. Microstructure characterization of SS308LSi components manufactured by GTAW-based additive manufacturing: shaped metal deposition using pulsed current arc. International Journal of Advanced Manufacturing Technology. The International Journal of Advanced Manufacturing Technology; 2017; 89(1–4): 13–25. Available at: DOI:10.1007/s00170-016-9053-y
27. Asala G., Khan AK., Andersson J., Ojo OA. Microstructural Analyses of ATI 718Plus® Produced by Wire-ARC Additive Manufacturing Process. Metallurgical and Materials Transactions A: Physical Metallurgy and Materials Science. Springer US; 2017; 48(9): 4211–4228. Available at: DOI:10.1007/s11661-017-4162-2
28. Wang F., Williams S., Colegrove P., Antonysamy A a. Microstructure and mechanical properties of wire and arc additive manufactured Ti-6Al-4V. Metallurgical and Materials Transactions A: Physical Metallurgy and Materials Science. 2013; 44: 968–977. Available at: DOI:10.1007/s11661-012-1444-6

29. Gu J., Ding J., Williams SW., Gu H., Ma P., Zhai Y. The strengthening effect of inter-layer cold working and post-deposition heat treatment on the additively manufactured Al– 6.3Cu alloy. Journal of Materials Processing Technology. Elsevier; 2016; 230: 26–34. Available at: DOI:10.1016/j.jmatprotec.2015.11.006

30. Lockett H., Ding J., Williams S., Martina F. Design for Wire + Arc Additive Manufacture: design rules and build orientation selection. Journal of Engineering Design. 2017; 4828(December): 1–31. Available at: DOI:10.1080/09544828.2017.1365826

31. Zinov'yev VY., Taluts SG. Thermal Diffusivity and Thermal conductivity of Tungsten in Solid and Liquid States. Physics of Metals and Metallography. 1985; 59(1): 70–76.

32. Coenen JW., Philipps V., Brezinsek S., Bazylev B., Kreter A., Hirai T., et al. Analysis of tungsten melt-layer motion and splashing under tokamak conditions at TEXTOR. Nuclear Fusion. 2011; 51(8). Available at: DOI:10.1088/0029-5515/51/8/083008

33. Klimov N., Podkovyrov V., Zhitlukhin A., Kovalenko D., Bazylev B., Janeschitz G., et al. Experimental study of PFCs erosion under ITER-like transient loads at plasma gun facility QSPA. Journal of Nuclear Materials. Elsevier B.V.; 2009; 390–391(1): 721–726. Available at: DOI:10.1016/j.jnucmat.2009.01.197

34. Garkusha IE., Makhlaj VA., Chebotarev V V., Landman I., Tereshin VI., Aksenov NN., et al. Experimental study of plasma energy transfer and material erosion under ELM-like heat loads. Journal of Nuclear Materials. Elsevier B.V.; 2009; 390–391(1): 814–817. Available at: DOI:10.1016/j.jnucmat.2009.01.215

35. Bazylev B., Landman I., Loarte A., Klimov NS., Podkovyrov VL., Safronov VM. Experiments and modeling of droplet emission from tungsten under transient heat loads. Physica Scripta. 2009; T138. Available at: DOI:10.1088/0031-8949/2009/T138/014061

36. Murphy AB., Tanaka M., Tashiro S., Sato T., Lowke JJ. A computational investigation of the effectiveness of different shielding gas mixtures for arc welding. Journal of Physics D: Applied Physics. 2009; 42: 115205. Available at: DOI:10.1088/0022-3727/42/11/115205

Chapter 4

Paper C

"Wire + Arc Additive Manufacturing process of unalloyed tungsten components and the correlation between microstructure and thermal properties"

G. Marinelli*, [a], F. Martina*, S. Ganguly*, S. Williams*, H. Lewtas**, D. Hancock**, S. Mehraban***, N.Lavery***

*Welding Engineering and Laser Processing Centre (WELPC), Cranfield University, Cranfield, MK43 0AL, United Kingdom

**Culham Centre for Fusion Energy (CCFE), Culham Science Centre, Abingdon, OX14 3DB, United Kingdom

***Department of Materials Engineering, Singleton Abbey, Singleton Park Campus, Swansea, SA2 8PP, United Kingdom

Abstract

Tungsten is considered one of the most promising materials for the utilisation in a fusion nuclear reactor chamber. A controlled production of large-scale tungsten components could be beneficial to produce parts able to withstand irradiation in a nuclear chamber as long as the integrity of the material is preserved during the deposition process. Wire + Arc Additive Manufacture has been demonstrated to be able to deposit defect-free large-scale tungsten structures, with considerable deposition rate. In this study, the microstructure of the as-deposited and annealed deposited material was characterised. Furthermore, the linear coefficient of thermal expansion, the thermal diffusivity and the heat capacity were measured for two orthogonal directions using dilatometry and laser flash analysis under inert atmosphere. The thermal conductivity was also calculated. The annealing process resulted in having a negligible effect on the microstructure. However, the annealing step seemed to have reduced the residual stresses of the tungsten structures. Thus, the heat treatment of the unalloyed tungsten structures after deposition could be greatly beneficial. The results showed that Wire + Arc Additive Manufacturing can be considered as a suitable technology for the production of tungsten components for the nuclear sector.

4.1 Introduction

The development of innovative sources of energy has always been accompanied by an improvement with regards to the material fabrication and material properties in order to ensure optimal energy conversion rates. The controlled extraction of energy from the fusion nuclear reaction is one of the major challenges of the time within the energy sector [1]. Considering this critical and aversive environment of operation, the selection and production of advanced materials play a crucial role in the final application of the new fusion reactors [1,2]. In this sense, tungsten has been considered for several years as the major candidate to be used for both structural and confinement components [2–4]. In particular, the helium-cooled divertor and helium-cooled first wall of the future fusion reactors [1,2,5]. A suitable material for these specific applications should be characterised by excellent mechanical properties over a wide range of temperature, adequate heat resistance and high neutron load capacity [1,6].

The reason why tungsten is considered so valuable for nuclear applications lies in its unique properties. In fact, it is characterised by the highest melting point among metals, high density, relatively high thermal conductivity at room temperature, low coefficient of thermal expansion and excellent mechanical properties at elevated temperatures. Nonetheless, tungsten is also characterised by a high resistance to sputtering or erosion and low tritium retention [7,8].

Nowadays, tungsten is almost exclusively manufactured via powder metallurgy route and hot forming processes because casting would be difficult to accomplish due to the extremely high melting point [9]. Coupling sintering and hot or cold working with these manufacturing technologies, the powder consolidation and the microstructure of the tungsten products can be finely controlled [9]. However, some physical properties of this metal, as the high ductile-to-brittle-transition temperature (DBTT) and the high recrystallization temperature, can represent a limiting factor and can also increase the cost of the production. Furthermore, machining is necessary for the production of complex-shaped parts [1]. This can also restrict the applications of tungsten components due to its hardness and brittleness.

An innovative way of manufacturing components is by using Additive Manufacturing (AM), which can revolutionise the sector [10,11]. Building a component layer after layer can give substantial results on the cost reduction, the freedom of design and the control of mechanical properties [12,13]. Numerous researches have already reported the potential of the AM of metallic materials, some of them are summarised in [14,15]. Within the range of potential technologies developed for AM, wire-feed technologies are strongly characterised by the ability to produce large-scale components [16].

In particular, Wire + Arc additive Manufacture (WAAM) is a novel AM process which employs an electric arc as the heat source and high-quality metal wire as the feedstock [17]. WAAM can directly fabricate fully-dense large 3-D near-net-shape components with a much higher deposition rate, within the order of several kg/h, than most other metal additive manufacture processes [16,17]. The WAAM process has been demonstrated to successfully produce large-scale parts in stainless steel [18], Inconel [19], titanium [20] and aluminium [21] achieving even complex geometries of deposition. Thus, a new way of designing and manufacturing tungsten parts can be achieved by exploiting the benefit of the WAAM process applied to unalloyed tungsten.

Rieth at al. [1] illustrated in their review the fabrication and the joining approaches of tungsten components for nuclear fusion applications. The problem of the mass production of large-scale components and the utilisation of brazing were indicated as main points of improvement. The production of defect-free fully-dense tungsten components on a large scale could favour the production and the testing of prototypes in the nuclear reactor environment, decreasing the timeframe for implementation. In particular, the main parts of the nuclear fusion divertor could be entirely and promptly built in relatively short time. They could also be assembled with the surrounding components possibly eliminating brazing through the utilisation of controlled gradients in compositions.

Lastly, projecting this technology to the complete operating system of the nuclear reactor, a flexible AM technology could be used to repair in-situ large areas of the consumed tungsten armours without the necessity to disable and take out

each of them from the main reaction chamber. The nuclear sector can definitely benefit from a new modular and flexible manufacturing technology for tungsten components.

The requirements for the best application in the nuclear fusion environment of tungsten structural components are the following [1]: high thermal conductivity; high-temperature stability; high recrystallization temperature; sufficient ductility to operate under constant neutron irradiation. Furthermore, isotropy of the microstructure and, in particular, the alignment of the grain can greatly influence the behaviour of the tungsten tiles under high-heat fluxes [22].

The control of these microstructural features can possibly lead to the optimum stress distribution and so the best operating condition avoiding failures [1,22]. Heat flux tests reported that the maximum operating temperature of the helium-cooled divertor should be around 1000 K – 1200 K for the lowest armour temperature, above 2000 K for the armour surface and 800 K for the blanket first wall [1]. Furthermore, the analytical expressions for some tungsten thermos-physical properties relevant for fusion application have been reviewed in the work of Tolias et al. [23]. Some of the thermal properties of tungsten manufactured via different route are reported in **Table 4.1**.

Manufacturing Route	ρ [g cm^{-3}]	α [mm s^{-2}]	k [W m^{-1} K^{-1}]	CTE [µm m^{-1} K^{-1}]	C_P [J g^{-1} K^{-1}]
Theoretical [24]	19.30	--	174	4.5	0.14
P-S [25]	Variable	34 - 88	--	--	--
CVD [26]	19.23	55	163	4.1	0.14
Forged [26]	--	52.5	154	--	0.15
VPS [27]	17.03	48	110	--	--
Sintered [28]	18.60	--	130	--	--
PM [29]	17.27	--	135	--	--
PM + Rolling 60% def. [29]	19.01	--	175	--	--

Table 4.1: Values of density (ρ), thermal diffusivity (α), thermal conductivity (k), coefficient of linear thermal expansion (CTE) and specific heat capacity (C_P) for different manufacturing routes of tungsten components. Every value refers to 293 K.

From **Table 4.1**, it can be seen that a strong relation lies between the thermal properties and the density of tungsten components, particularly with the thermal conductivity and diffusivity. The values of both thermal conductivity and

thermal diffusivity at 293 K decrease when the density decrease. The relation between linear thermal expansions and density is not clearly shown in **Table 4.1.**

None of the investigations available in the literature discusses the employment of WAAM for the production of unalloyed tungsten or the thermal properties of tungsten after deposition using an AM technology. In this study, the microstructure and the thermal properties of unalloyed tungsten structures were characterised in the as-deposited and annealed conditions. In particular, the microstructure along three principal directions was analysed in order to obtain a three-dimensional profile of the grains. The coefficient of linear thermal expansion, the thermal diffusivity and the heat capacity were measured over temperature using respectively dilatometry and laser flash analysis under an inert atmosphere. The thermal conductivity was calculated from the diffusivity, heat capacity and density, measured with hydrostatic weighing. The ultimate scope of this study was to prove that the Wire + Arc Additive Manufacturing process is able to manufacture large-scale unalloyed tungsten components for nuclear applications.

4.2 Experimental Procedure

Unalloyed tungsten wire with a diameter of 1.0 mm was used for the Wire + Arc Additive Manufacturing process. An unalloyed tungsten plate, with dimensions of 210.0 mm in length, 10.0 mm in width and 30.0 mm in height, produced by powder metallurgy was used as substrate for the deposition. The surfaces of the plate were ground and rinsed with acetone prior to deposition in order to remove most of the contaminants. The analyses of the composition of all the materials used in addition to the linear structure deposited were commissioned externally. In particular, X-ray fluorescence (XRF) spectroscopy was used for the detection of the major metallic atoms (W, Mo, Ta, Ti, V, Cr and Fe). LECO combustion analysis was used for the measurement of the concentration of carbon, nitrogen and oxygen. Finally, inductively coupled plasma optical emission spectroscopy (ICP-OES) was used for the detection of potassium.

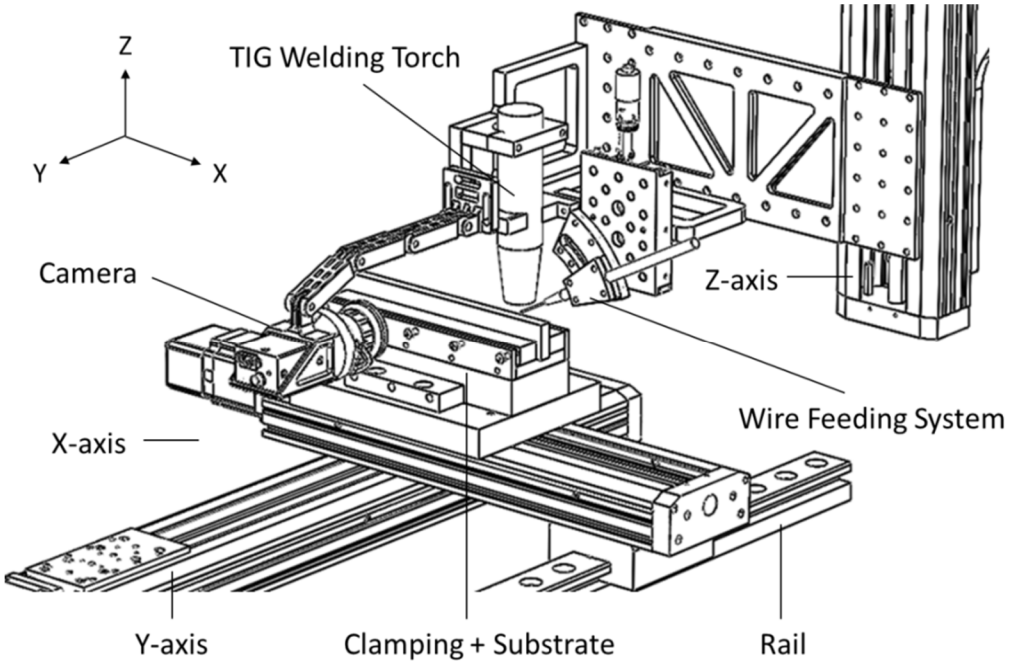

Figure 4.1: Set-up used for the deposition of the tungsten structure via Wire + Arc Additive Manufacture.

Figure 4.1 shows the layout of the apparatus used for the deposition. The substrate was firmly held by a clamping system connected to the X-axis and the Y-axis motorised linear stages. In particular, a lateral force on the substrate was applied by two copper bars, using a series of screws. The wire was fed from the front of the weld pool and deposited layer by layer onto the substrate using a single bead. The direction of deposition was always kept constant for each successive layer. A conventional tungsten inert gas (TIG) welding torch, a power supply and a controlled wire feeder were used for the deposition. The heat source, the wire delivery system and the substrate were attached to three linear motorized high-load stages assembled in XYZ configuration. The apparatus was completely surrounded by a heavy-duty enclosure used to ensure a low level of oxygen when purged with high-purity argon.

The parameters of deposition were kept constant throughout the entire process. They are reported in **Table 4.2.** The acronym TS refers to the travel speed instead, WFS refers to wire feed speed. A large straight structure in tungsten was produced with the dimensions of around 120.0 mm in length, 75.0 mm in height and 12.0 mm in average thickness (**Figure 4.5**).

TS [mm/s]	2
I [A]	400
WFS [mm/s]	35
Electrode-workpiece Distance [mm]	3.5
Electrode angle [°]	45
Electrode Diameter [mm]	3.2
Shielding gas composition [%]	100 He
Gas flow rate [L/min]	15
Oxygen Atmosphere [ppm]	≈100

Table 4.2: Wire + Arc Additive Manufacturing process parameters used for the deposition of unalloyed tungsten.

Different coupons for the measurement of thermal properties were extracted from the structure. In particular, twelve samples for laser flash analysis (LFA), twelve samples for dilatometry (DIL) and six samples for microstructural analysis**.** The geometry and the main dimensions of the LFA and DIL coupons are reported in **Figure 4.2.** The DIL coupons had a cylindrical shape with a total length of 20.0 mm and a radius of 2.5 mm (**Figure 4.2a**). The coupons used for the LFA tests were small tiles of 10.0 mm in height, 10.0 mm in width and 3.0 mm in thickness (**Figure 4.2b**).

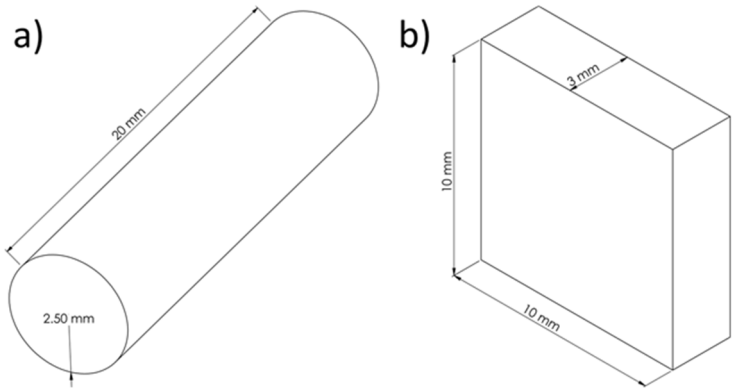

Figure 4.2: Geometry and main dimensions of the coupon used for dilatometry (a) and the coupon used for laser flash analysis (b).

The extraction plan of the coupons from the structure deposited and their denomination is reported in **Figure 4.3a.** Additionally, **Figure 4.3b** shows their position with respect to the deposition direction**.** The extraction of the samples was conducted using electrical discharge machining (EDM). Half of the coupons were tested in the as-deposited condition (As-Dep), while the other half was tested after a thermal treatment (Annealed). In particular, after being cut by EDM, six LFA

coupons, six DIL coupons and one microstructural sample were annealed to 1273 K for 6 hours under vacuum with a heating rate of 5 K per minute as stress-relief annealing [30]. The temperature was constantly measured using two N-type thermocouples. This temperature was chosen in order to simulate the annealing step for defect recovery and aggregation of the tungsten tiles, after being exposed to the nuclear fusion reaction[31,32]. In fact, a previous study showed that dislocation density was decreased and voids were recovered by annealing the tungsten samples at 1173 K [31–33]. In particular, Markina et al. [32] suggested that higher annealing temperature than 1173 K could possibly be more beneficial.

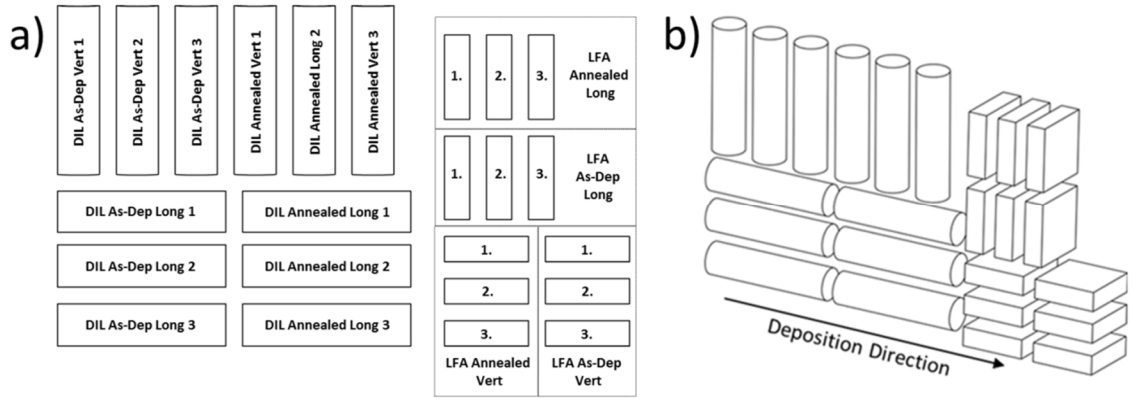

Figure 4.3: Denomination and location of the coupons (a); Arrangement and extraction plan of the coupon with respect to the deposition direction (b).

The microstructure of the component in the as-deposited and annealed condition was examined using three different cross-sections. In **Figure 4.4**, the Z-axis is oriented parallel to the building direction, the X-axis parallel to the deposition direction and the Y-axis perpendicular to the deposition direction.

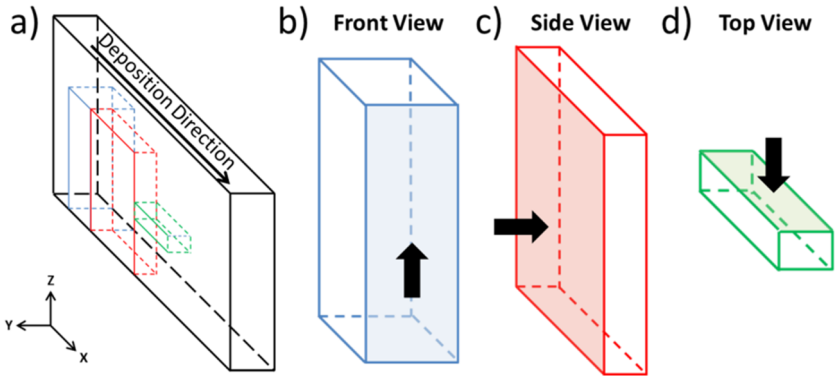

Figure 4.4: Location of the samples within the deposited structure (a). Plane analysed for the *Front View* (b), *Side View* (c) and *Top View* (d).

Figure 4.4 also reports explicitly the cross-sections used for the analysis. They were called respectively *Front View*, *Side View* and *Top View*. The *Front View* showed the microstructural features of the YZ plane (**Figure 4.4b**), the *Side View* of the XZ plane (**Figure 4.4c**) and the *Top View* of the XY plane (**Figure 4.4d**).

The thermal analysis was performed by Swansea University. The linear thermal expansion of the DIL samples was measured using a Netzsch DIL 402 dilatometer. The initial length of each sample was measured using a micrometre and then, each sample was heated from 293 K to 1473 K at a rate of 10 K/min under an argon atmosphere. Then, each sample was cooled at a rate of 10 K/min back to room temperature at 293 K. The variations in length during the expansion and the contraction cycles were recorded using the NETZSCH Proteus software. A known alumina standard was used as a correction sample to remove the effective thermal expansion of the sample carrier. The change in length with the temperature with respect to the original length was indicated as dL/L_o and these values were directly measured by the testing machine. The true coefficient of the linear thermal expansion (α_t) was calculated by using the derivative dL/dT at a single temperature according to **Eq. (4.1)**. This is the slope of the tangent to the curve of length against temperature. The calculations were performed using the specific function of the Netzsch Proteus software.

$$\alpha_t(T) = \frac{1}{L_0}\left(\frac{\partial L}{\partial T}\right)_p \qquad \textbf{(4.1)}$$

Where L_0 is the length at 300 K, T is the single temperature analysed and L is the length of the specimen at that temperature.

The thermal diffusivity of each sample was measured using a Netzsch LFA 457. The thickness of each sample was measured using a micrometre and then coated with a layer of graphite to increase the absorption of the laser radiation and reduce reflection. Each sample was placed in a sample holder made of aluminium titanate with a silicon carbide cap. In particular, a three position sample holder was used and it was filled with two tungsten samples and a Pyroceram 9606 reference standard. Successively, the sample holder was inserted in the high-temperature furnace chamber which was evacuated and backfilled with argon. A

sustained flow of 100 ml per minute of argon was used throughout the experiment. The temperature change of the sample was detected using an InSn IR detector cooled by liquid nitrogen. Temperature steps of 50 K were taken within the temperature range from 293 K to 1273 K. Five shots were performed at each temperature step and the individual diffusivity results measured and then averaged as well as the standard deviation. The thermal diffusivity of each shot was calculated using the Cowon method with pulse correction applied [34]. This model takes into account heat loss from all surfaces of the sample. The values of thermal diffusivity for different temperature were calculated using the NETZSCH Proteus software. From the thermal diffusivity data, the specific heat capacity was also calculated using the Pyroceram reference and the ratio method. In particular, the Netzsch Proteus software analysed the infinite time extrapolated, heat loss corrected voltage of the detector signal corrected by the amplification factors and calculated the heat capacity according to the following relation (**Eq. (4.2)**):

$$C_p^{Sample} = \frac{T_\infty^{Ref.}}{T_\infty^{Sample}} \cdot \frac{Q^{Sample}}{Q^{Ref.}} \cdot \frac{V^{Sample}}{V^{Ref.}} \cdot \frac{\rho^{Ref.} \cdot D^{Ref.}}{\rho^{Sample} \cdot D^{Sample}} \cdot \frac{d^{2,sample\ Orifice}}{d^{2,Ref.Orifice}} \cdot C_p^{Ref.}(T) \qquad \textbf{(4.2)}$$

The bulk density of each sample was measured using the method of hydrostatic weighing, employing Archimedes' principle [35]. A tensiometer was used to determine the weight of the sample in air and in distilled water. From the Δweight, the density can be calculated using the **Eq. (4.3)**:

$$\rho_{samp} = \mathrm{Z} * \frac{W}{\Delta W} \qquad \textbf{(4.3)}$$

Where ρ_{sample} is the density sample, Z is the water density, W is the sample weight in air, ΔM is the difference between weight in air and weight in water. The air and water density values at 300 K were used for calculation. The change in density during heating was also taken into account by using the thermal expansion data from the DIL measurements. The temperature-dependent density was calculated using the **Eq. (4.4)**:

$$\rho(\mathrm{T}) = \frac{\rho_0}{\left(1+\frac{\Delta L}{L_0}(\mathrm{T})\right)3} \qquad \textbf{(4.4)}$$

Thermal conductivity was calculated from the thermal diffusivity, the specific heat and the bulk density as measured and calculated, according to the Laplace relation (**Eq. (4.5)**):

$$k(T) = \alpha(T).\rho(T).C_p(T) \quad \textbf{(4.5)}$$

Where k is the thermal conductivity, α is the thermal diffusivity, ρ is the density and C_p is the specific heat capacity.

4.3 Results and Discussion

4.3.1 Appearance and chemical analysis

Figure 4.5 shows the tungsten structure built for the study. The layers were regular and smooth. Despite a marked propensity of tungsten to the oxidation at high temperature, the effectiveness of the inert argon atmosphere to prevent contamination and oxidation can be assessed by the shiny silver surface of the deposit.

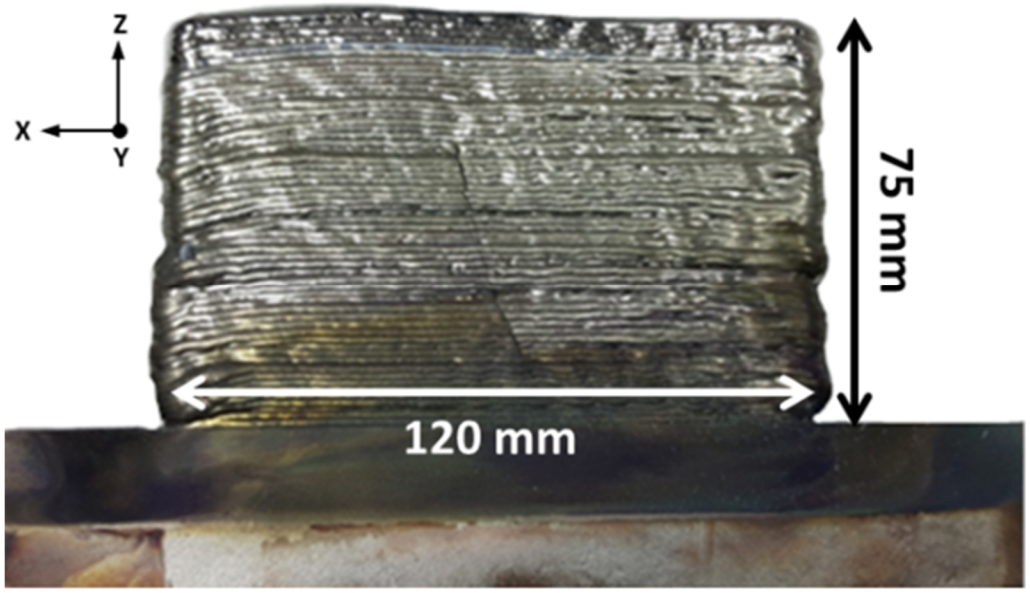

Figure 4.5: Large-scale unalloyed tungsten linear structure deposited via WAAM process.

The composition of the materials used and of the linear structure deposited is reported in **Table 4.3**. The data reported refers to the bulk composition of the material analysed. The results of the chemical analysis clearly assessed that the tungsten structure manufactured via Wire + Arc Additive Manufacturing has a

high-purity of 99.99 wt.%. Comparing the composition of the wire and the wall, it is possible to assess that no additional contamination was registered due to the deposition process.

	W	Mo	Ta	Ti	V	Cr	Fe	C	N	O	K
Substrate	99.99	<0.05	<0.05	<0.05	<0.05	<0.05	<0.05	11 ppm	<10 ppm	<50 ppm	<10 ppm
Wire	99.99	<0.05	<0.05	<0.05	<0.05	<0.05	<0.05	33 ppm	<10 ppm	<50 ppm	<10 ppm
Wall	99.99	<0.05	<0.05	<0.05	<0.05	<0.05	<0.05	<10 ppm	<10 ppm	<50 ppm	<10 ppm

Table 4.3: Elemental composition (wt%) of tungsten substrate, wire and wall used in this study.

4.3.2 Microstructure

Figure 4.6 reports the microstructure of both as-deposited and annealed structure in the YZ plane (*Front View*). The bottom of both samples presented was located around 10.0 mm away from the substrate. The two samples were extracted from the same structure and only one of them (**Figure 4.6b**) was successively subjected to thermal treatment. It can be seen that the annealing process at 1273 K for 6 hours did not have any significant effect on the microstructure. The shape, the size and the orientation of the grains are similar for both cross-sections. Furthermore, it is possible to underline a marked symmetry with regards to the grain shape and orientation respect to the centre of the structure. In particular, two specular arrays of columnar grains inclined at around 45° both pointing toward the centre of the structure were formed during the solidification. The presence of these grains was more predominant on the upper part of both samples. A few conglomerates of finer equiaxed grains were also found and located close to the lower part of the samples.

To fully understand the development of the microstructure of tungsten after deposition, two other additional planes of the only as-deposited structure are reported due to the negligible effect of the heat treatments on the microstructure seen in the annealed sample. In particular, the plane XY (*Top View*) and the plane XZ (*Side View*) have been polished and etched in order to reveal the microstructure, which is reported in **Figure 4.7.**

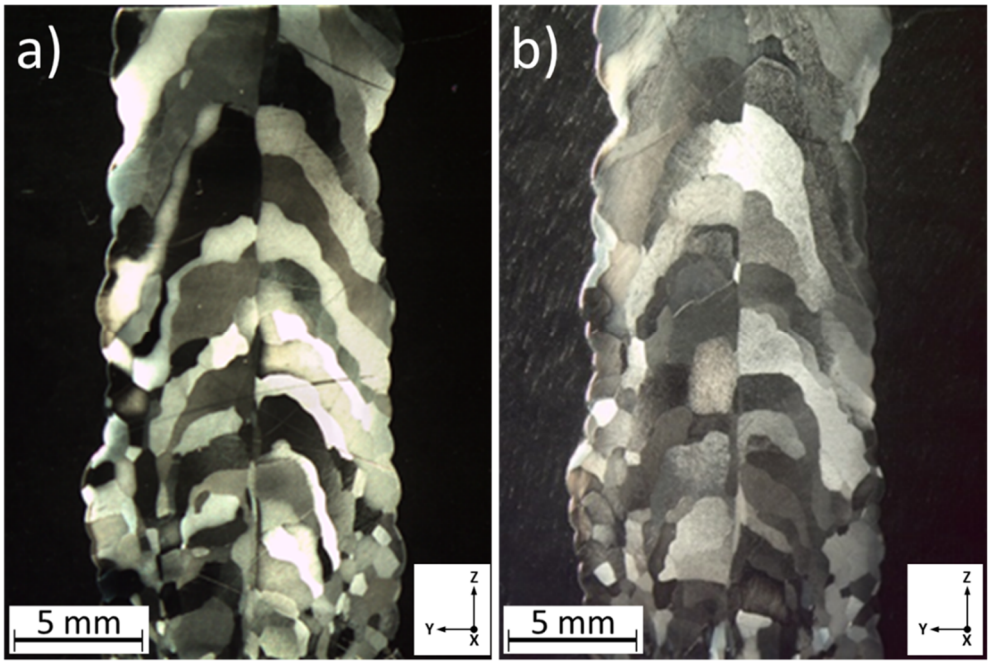

Figure 4.6: Microstructure of the *Front View* of the as-deposited (a) and the annealed structure (b).

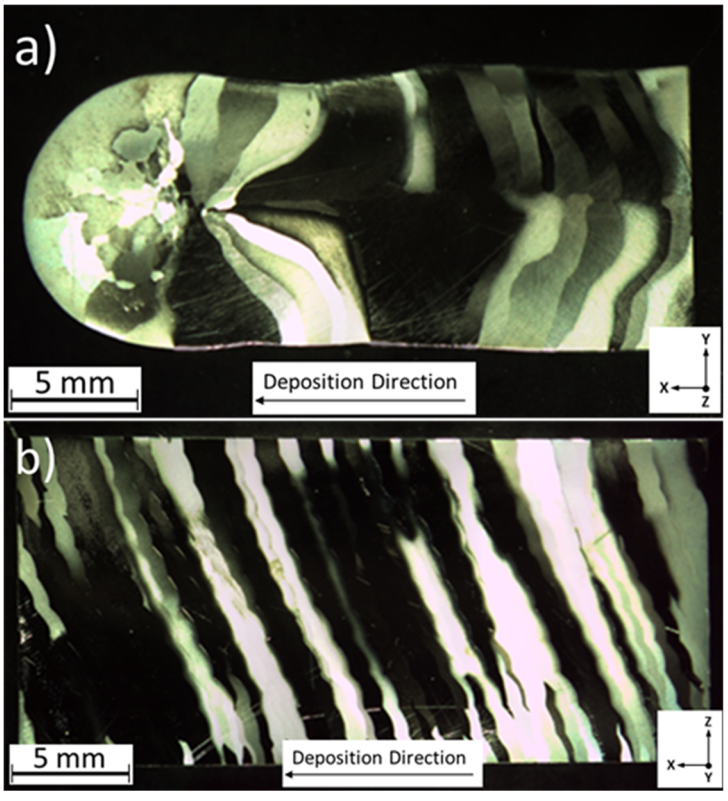

Figure 4.7: Microstructure of the (a) *Top View* and (b) *Side View* of the as-deposited structure.

Figure 4.7a shows the shape and orientation of the grains for the *Top View* and, in particular, the visible region is represented by the last 27.0 mm of the layer

located at 60.0 mm from the substrate. Once again, two specular arrays of grains appeared to have developed during the solidification. The grain observed seemed to be part of a regular pattern in which each grain elongated from the side toward the centre of the layer. Furthermore, each grain seemed to be slightly inclined with respect to the deposition direction. Toward the very end of the deposit, the elongated grain progressively changed the orientation and the presence of few finer grains was also observed. **Figure 4.7b** reports the microstructure of the *Side View*. A consistent array of long and parallel columnar grains has been observed. In particular, each grain was also inclined to around 45°, pointing toward the direction of deposition.

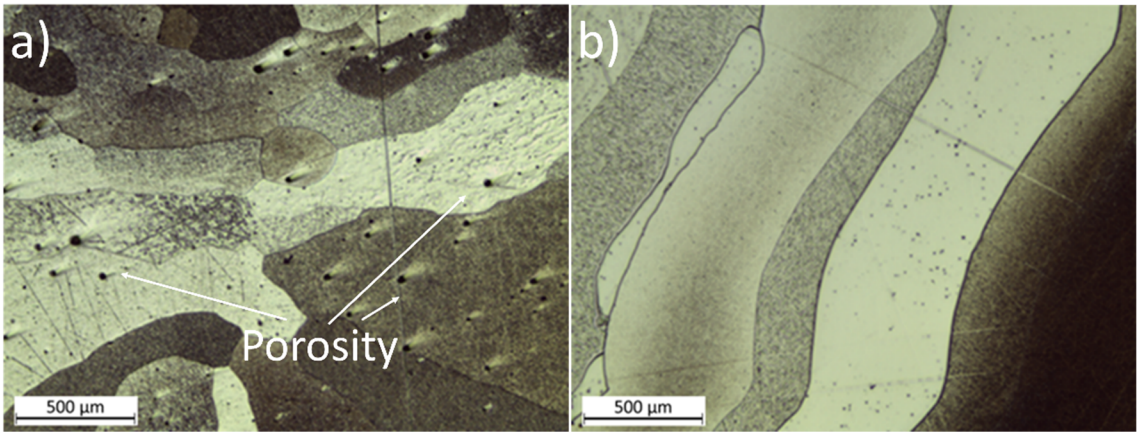

Figure 4.8: Microstructural detail from the *Top View* showing porosity at the end of the deposition (a); Microstructural details from the *Side View* showing wavy grain boundaries (b).

Figure 4.8 reports details of the microstructure found respectively on the etched surface for the *Top View* (**Figure 4.8a**) and the *Side View* (**Figure 4.8b**). A few localised pores were found around the very end of the deposit also accompanied by few finer grains. Furthermore, wavy grain edges were observed (**Figure 4.8b**) which was possibly caused by the progressive remelting of various layers' deposition.

Based on the observation of the grains shape and orientation from the different views already reported (**Figure 4.6** and **Figure 4.7**), the microstructure of unalloyed tungsten after the deposition has been reconstructed and schematised in **Figure 4.9**. In particular, the shape and volume of a single grain have been initially reconstructed in three dimensions in order to resemble the appearance

shown on the different planes reported and successively, a complete assembly has been constructed using two specular arrays of the single grain. The full schematic of the microstructure has been reported in **Figure 4.9c**. A strong similarity exists among the three views of the real sample (**Figure 4.6a**, **Figure 4.7a** and **Figure 4.7b**) and the corresponding schematic (**Figure 4.9b**, **Figure 4.9a** and **Figure 4.9c**). Thus, the microstructure of the unalloyed tungsten after deposition using WAAM can be described as composed of two main series of large columnar grains related by a specular symmetry with respect to the structure centreline.

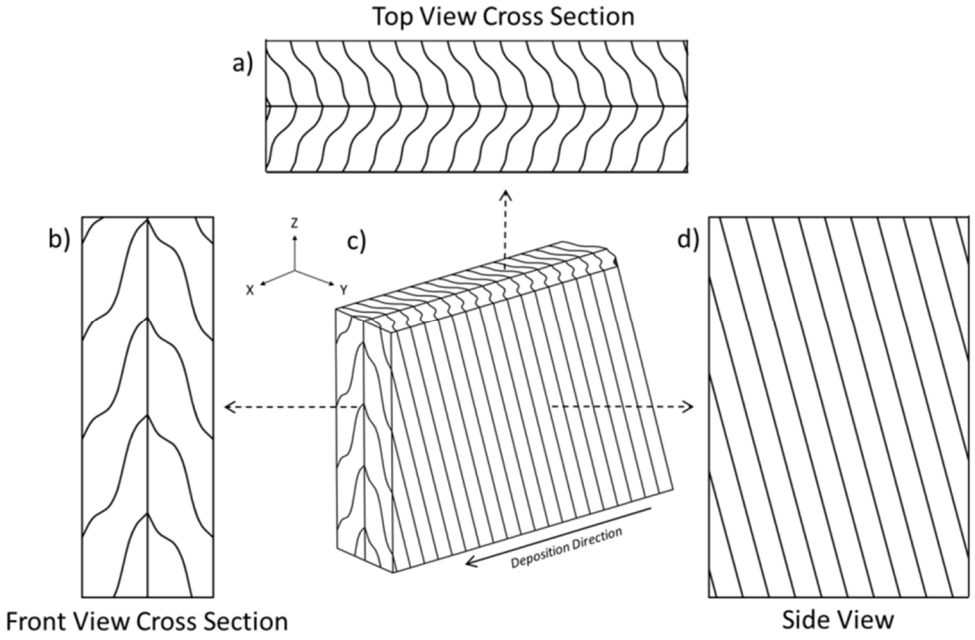

Figure 4.9: Reconstructed microstructural schematic for the *Top View* (a), the *Front View* (b) and *Side View* (d). Three-dimensional schematic representing the microstructure of unalloyed tungsten structure produced via WAAM (c).

The recrystallization temperature of metals typically ranges between 50% and 70% of their melting temperature. The recrystallization temperature of tungsten is reported to be above 1500 K [36]**.** In this study, the annealed sample was heat-treated at a lower temperature so that neither crystal reorientations nor grain boundary migrations occurred during the treatment. The temperature and time of the post-deposition heat treatment have been chosen in order to accomplish a stress relieving treatment. For this reason, a negligible effect of the heat treatment on the microstructure was expected (**Figure 4.6a** and **Figure 4.6b**). The change in size and the distribution of the grains showed along the

height of both as-deposited and annealed structures has been mainly caused by a progressive change of both the thermal properties of the material and substrate temperature (T_s) before the deposition of each layer. **Figure 4.10** illustrates four schematics in order to correlate these variations with the formation of the microstructure. In particular, the schematics from **Figure 4.10a** to **Figure 4.10c** represent how the solidification mode changes with the temperature of the substrate and the concurrence of conduction and radiation to the total heat flux through the structure. These three schematics refer to the plane YZ (*Front View*), the heat fluxes are indicated as $\overrightarrow{\phi_G}$ and their direction with a dashed arrow. Furthermore, **Figure 4.10d** shows the *Side View* of a weld pool during the process and the solidification of the grains starting from the back of the weld pool.

The scenario reported in **Figure 4.10a** refers to the deposition of one of the initial layers when the substrate is cold with a temperature around room temperature ($T_s \approx$ RT). The heat is greatly dissipated from the weld pool bottom toward the bottom of the substrate due to the high thermal gradient and the relatively high thermal conductivity of tungsten at around room temperature. This leads to obtain an increased amount of nucleation sites within the weld pool. Furthermore, the flow of the plasma arc slightly cools the surface of the weld pool enhancing the formation of additional solidification nuclei due to the fast solidification rate of tungsten. For these reasons, the entire liquid volume was pervaded by numerous nucleation sites which promoted the heterogeneous nucleation and multidirectional solidification. This is the reason why finer equiaxed grains have been found near the interface between the substrate and the deposited structure.

In **Figure 4.10b** reports the situation in which a few layers have already been deposited and so that the heat starts to accumulate, increasing the temperature of the substrate ($T_s >$ RT). The major heat flow is pointing predominantly in the same direction of the previous case, but it is characterised by a slower heat flow rate. This is caused by the smaller temperature gradient between weld pool and substrate, and the lower thermal conductivity of tungsten at that temperature. In fact, it is already known that the thermal conductivity of

tungsten decreases with increasing the temperature [25–27]. The thermal conductivity has been also measured in the current study and it is reported in the next section about the results of the LFA analysis. Under these conditions, the front of solidification advances linearly and parallel to the main heat flow direction. Columnar grains start to grow epitaxially onto the partially-melted grains at the bottom of the weld pool.

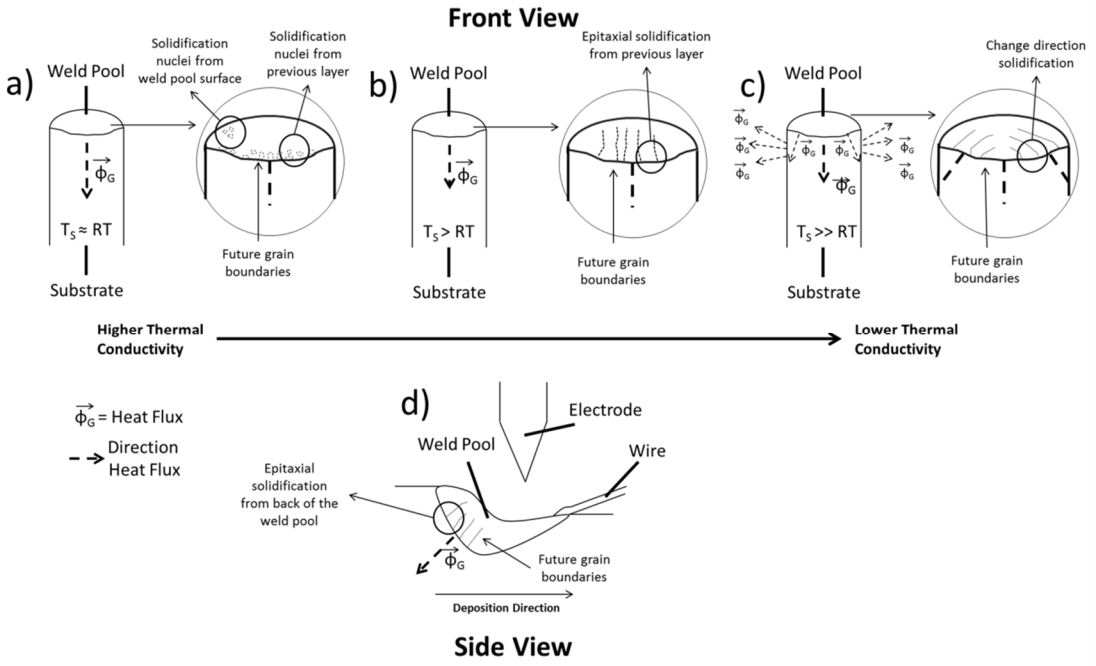

Figure 4.10: Schematics of the main heat flow components and of the formation the future gran boundaries for the *Front View* scenario when $T_s \approx RT$ (a), $T_s > RT$ (b) and $T_s >> RT$ (c), and for the *Side View* scenario (d). (T_s = substrate temperature)

Figure 4.10c reports the schematic relative to the evolution of the case in **Figure 4.10b** when an "N" number of layers have been deposited and the substrate reached a temperature largely higher than room temperature ($T_s >> RT$). The thermal conductivity of the material located below the weld pool is interested in a significant drop and the thermal gradient resulted to be additionally decreased. At very high temperatures, radiation starts to play a considerable role in the dissipation of the heat from the weld pool. In particular, the radiation heat transfer effectiveness increases with increasing temperature according to the Stefan-Boltzmann Law and also tungsten is characterised by a relatively high emissivity [37]. During the deposition, only the material around the weld pool reaches an enough high temperature in order to consider radiation effective. Thus,

the sides of the structure close to the weld pool are cooled slightly more than the bulk of the material below the weld pool so that locally higher-thermal-conductivity regions establish on the side of the weld pool. For this reason, lateral additional heat flows compete with the main flow through the bulk causing the heat to be extracted slightly more efficiently toward the side of the structure. As the front of solidification usually advances following the direction of the heat extraction, the columnar grains start to solidify with a different orientation with respect to the case in **Figure 4.10b**.

Figure 4.10d reports the usual shape of the weld pool during deposition from the *Side View*. As the deposition process involved a moving heat source, the back of the weld pool usually results to be inclined. Under these conditions, the main heat flow points toward the "coldest" part of the structure, the substrate. The inclination of the columnar grains clearly visible in **Figure 4.7b** has been caused by the direction of heat flow of a process involving a moving heat source. The deposition of tungsten via WAAM with a short and constant time interval between the deposition of each layer led to the formation of a microstructure characterised by the crystal structure reported due to the changes in heat transfer. This was mainly caused by the heat accumulation and the variation of the thermal conductivity of tungsten with temperature.

4.3.3 Dilatometry

The typical thermal expansion curves from 300 K to 1473 K for the as-deposited and annealed samples are reported respectively in **Figure 4.11a** and **Figure 4.11b**. For both graphs, the black curve is associated with the longitudinal samples (Long) and the red curve to the vertical samples (Vert). Furthermore, the solid line refers to the heating phase of the measurement cycle instead the dotted line refers to the cooling phase. Both as-deposited and annealed material expanded almost linearly with increasing temperature.

Figure 4.11a reports the typical thermal expansion of the samples tested in the as-deposited condition in vertical and longitudinal direction. It is possible to observe a marked difference between the testing cycles for the two directions. The samples extracted in the vertical direction (Vert As-Dep) presented a narrow

hysteresis loop unlike the samples extracted in the longitudinal direction (Long As-Dep), which presented a much wider hysteresis loop. Furthermore, the heating curve of the Long As-Dep sample recorded a change in slope at around 1050 K. This also led to a residual strain of 4.55 mStrain at around 450 K after cooling.

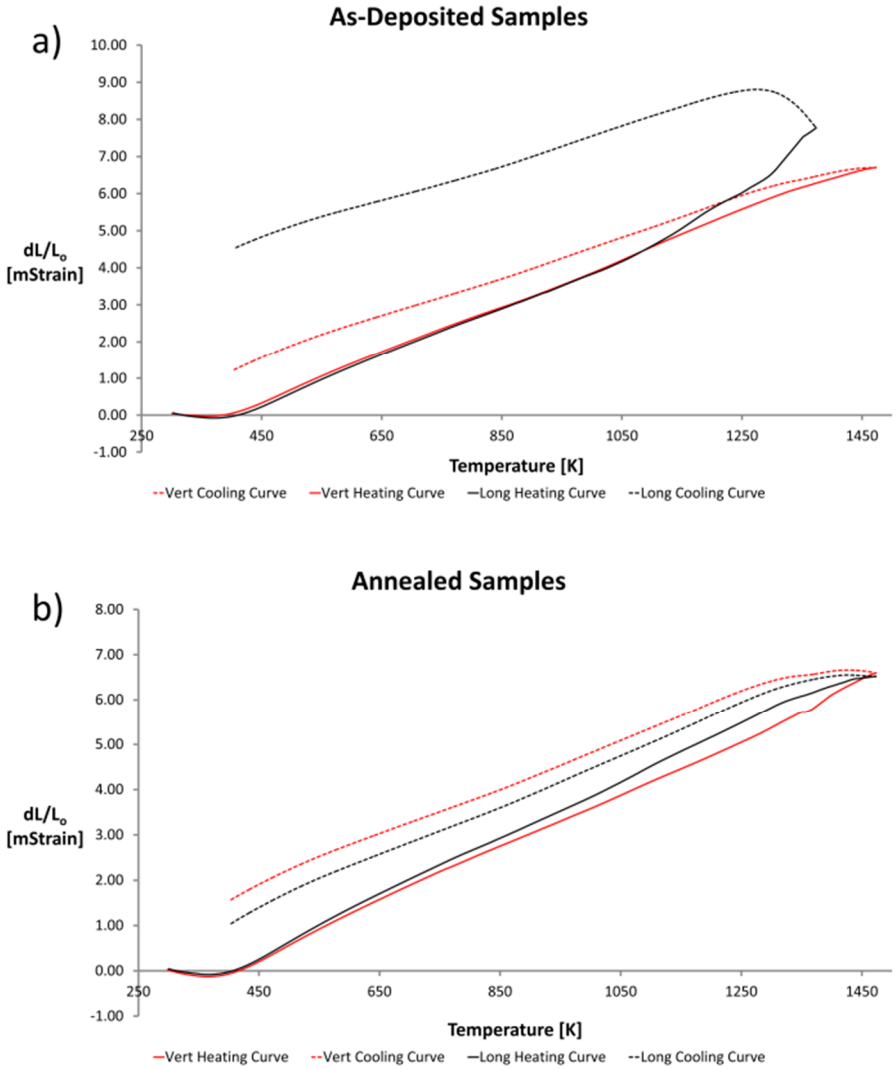

Figure 4.11: Typical thermal expansion curves of the tested samples in the as-deposited condition (a) and the annealed condition (b).

Figure 4.11b reports the typical thermal expansion curves of the samples tested in the annealed condition in both vertical and longitudinal direction. A marked consistency and similarity can be promptly highlighted in term of hysteresis width, maximum levels of strain at 1470 K and the average slope of both heating and cooling curves. Furthermore, the maximum strain at 1470 K recorded for the annealed samples was similar to the maximum strain achieved for the Vert As-Dep samples.

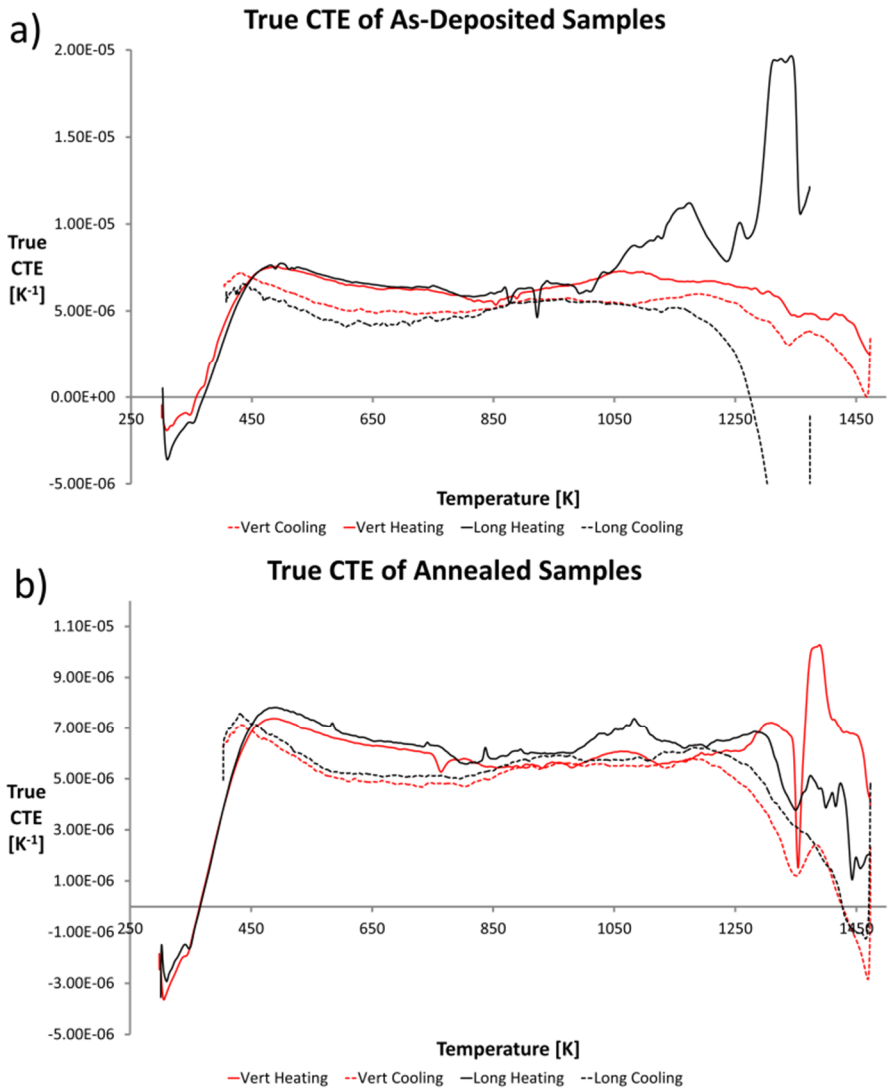

Figure 4.12: The variation of the α_t over temperature for the heating and cooling phase of the as-deposited samples (a) and annealed samples (b).

The variation of the true coefficient of thermal expansion (α_t) between 300 K and 1473 K is reported in **Figure 4.12** for the as-deposited and annealed samples. It can be seen that all samples were characterised by a negative true coefficient of thermal expansion at the beginning of the test. This is due to the initial heating stage within the instrument where the sample carrier is heated before the sample due to the radial furnace. This is measured as the sample effectively shrinking. Then, the α_t started to stabilise at around 450 K. On the other end of the temperature spectrum, between 1050 K and 1473 K, pronounced variations were recorded, especially for the Long As-Dep samples. On average, the

linear coefficient of thermal expansion resulted to be between $4.5x10^{-6}$ μm m^{-1} K^{-1} and $6.8x10^{-6}$ μm m^{-1} K^{-1}.

In general, no major or sudden changes with regards to the slope of the thermal expansion curves have been recorded within the temperature range examined a part of the Long As-Dep samples. The higher maximum strain on heating and the higher residual strain on cooling of the Long As-Dep samples with compared to the Vert As-Dep samples could have been caused by the formation of cracks within the volume of the longitudinal samples.

Tungsten is characterised by a ductile-to-brittle temperature transition (DBTT) which depend on the manufacturing route and it lies in broad temperature intervals [38]. It is known that the utilisation of an additive manufacturing technique almost inevitably leaves some degrees of residual stresses within the volume of the deposited structure [39]. Typically type II residual stresses remain also after cutting as they particularly refer to intergranular stresses [40]. Furthermore, the grain boundaries are known to be the preferred sites of crack nucleation in tungsten [38,41]. Thus, three main factors that could have had contributed to the development of cracks during testing mainly for the Long As-Dep samples are: the brittleness of tungsten at relatively low temperature, the presence of residual stresses due to the deposition process and the orientation and density of the grain boundaries with respect to the direction of expansion.

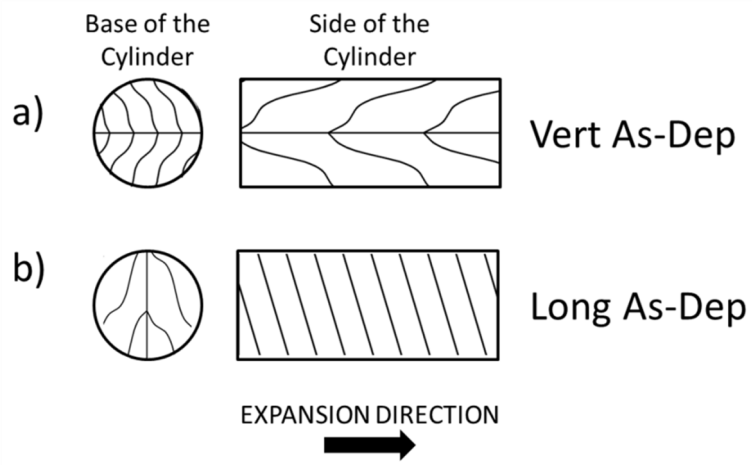

Figure 4.13: Grain structure of the base and the side of the cylindrical DIL sample indicated with respect to the expansion direction for the Vert As-Dep samples (a) and the Long As-dep samples (b).

The reconstruction of the microstructure of the longitudinal and vertical samples with respect to the expansion direction is reported respectively in **Figure 4.13a** and **Figure 4.13b**. Referring to the orientation of the microstructural planes already analysed, for the Vert As-Dep samples the side of the DIL cylindrical coupon corresponding to the *Front View* (**Figure 4.6a**) instead, for the Long As-Dep, the side of the coupon corresponded to the *Side View* (**Figure 4.7b**).

It is possible to notice that the Long As-Dep samples were characterised by a series of long and parallel grain boundaries oriented at around 45° with respect to the expansion direction unlike the Vert As-Dep samples, which presented two series of grains in specular symmetry. The as-deposited samples were likely to have higher residual stresses from the deposition compared to the annealed samples. For this reason, the additional level of strain applied during the dilatometry could have led to the formation of micro-cracks. The presence of these volumetric features could have abruptly increased the length of the specimen registering a pseudo increase in the level of strain. The cracks and the voids may have started to develop and successively grow around 1050 K when the change in slope occurred for the Long As-Dep samples. This has occurred only for the longitudinal samples and not for the vertical samples due to a marked difference in microstructure in these two directions. The cooling curve of the as-deposited samples was not affected by these phenomena because the residual stresses of the samples were redistributed during heating due to the formation of the cracks and voids.

The absence of abrupt changes in strain for the annealed samples has been addressed to the heat treatment. In particular, the annealing process seemed to have eliminated a significant part of the residual stresses decreasing the risk of cracks development during expansion. Additionally, the heat treatment could have promoted the dissolution of interstitial from the grain boundaries to the tungsten bulk.

The eventual occurrence of micro-cracks was clearly visible from the trend of the true coefficient of linear thermal expansion. In the Long As-Dep samples, the curve started to be heavily affected by high-amplitude fluctuation after 1050 K.

The occurrence of micro-cracks upon heating recorded for all the samples needs to be investigated in depth. Based on the characterisation presented in this study, these aspects were not clearly understood.

4.3.4 Laser Flash Analysis

Figure 4.14 reports the trend of thermal diffusivity over temperature ranging from 300 K to 1300 K. The red line refers to the vertical samples (Vert) and the black line refers to the longitudinal (Long) samples for both as-deposited (**Figure 4.14a**) and annealed (**Figure 4.14b**) coupons.

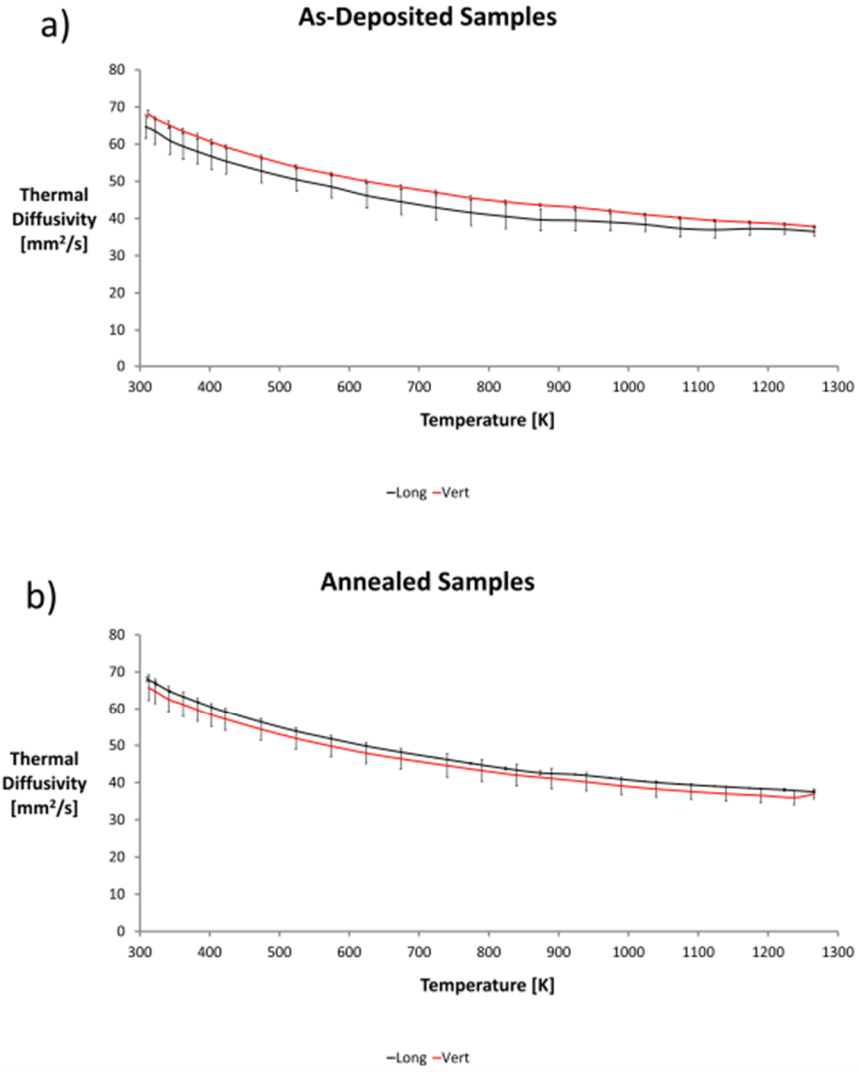

Figure 4.14: Thermal diffusivity curves against temperate of the tested samples in the as-deposited condition (a) and the annealed condition (b) with the associated error bars.

A decrease in thermal diffusivity of around 44% from 300 K to 1300 K has been registered for all the testing conditions. The measured values of thermal conductivity at room temperature and their variation over temperature seemed to be unaffected by the annealing process. Furthermore, the thermal diffusivity values of the two main directions tested were relatively close so that the material exhibited a marked isotropy. It is also noticeable that the two curves associated with the Annealed samples were characterised by an appreciably smaller gap between themselves when compared to the as-deposited samples.

Table 4.4 reports the values of the average density (ρ) corresponded to the sample tested for the LFA measurements. The theoretical density of tungsten at 300 K is 19.3 g/cm^3 and the difference in percentage between this value and the measured ones (ρ_R) are also reported in **Table 4.4**. In **Table 4.4** are also reported some of the calculated values of density, in particular, at 800 K and 1300 K. The values of each condition over temperature were calculated starting from the density at room temperature and taking in account the data from the dilatometry using **Eq. (4.4)**. As result of the calculation, a global reduction of around 2.0% from 300 K to 1300 K was registered for all testing condition.

Samples Set	Ave. ρ at 293 K [g/cm^3]	Standard Dev.	Calc. ρ at 800 K [g/cm^3]	Calc. ρ at 1300 K [g/cm^3]	ρ_R [%]
Long As-Dep	18.82	0.20	18.67	18.53	97.5
Vert As-Dep	19.1	0.05	18.94	18.77	98.9
Long Annealed	19.17	0.03	19.01	18.83	99.3
Vert Annealed	19.18	0.07	19.04	18.86	99.4

Table 4.4: Average density at 293 K for each sample set, the standard deviation of the measurements; the calculated density at 800 K and 1300 K; the density in percentage respect to the theoretical value.

The error associated with the measurements of the density using the Archimedes' principle is usually around ± 1 g/cm^3 and for this reason the values recorded can be considered within the error limit [42]. **Figure 4.15** reports the variation of the specific heat capacity at constant pressure (C_p) over the range of temperatures from 300 K to 1300 K. Once again, the red line refers to the vertical samples (Vert) and the black line refers to the longitudinal (Long) samples for both as-deposited (**Figure 4.15a**) and annealed (**Figure 4.15b**) coupons. In general, for

all of the conditions tested, the heat capacity tended to increase as the temperature increased. Furthermore, the curves of the heat capacity over temperature for the samples extracted in the vertical direction increased progressively with no abrupt variations unlike the curves obtained from the longitudinal samples. The abrupt increment in heat capacity occurred at around 873 K for both as-deposited and annealed. Considering the values of heat capacity at 300 K and at 1300 K, a total increment of around 14% has been registered in the vertical direction and an increment of around 25% has been registered in the longitudinal direction for both as-deposited and annealed.

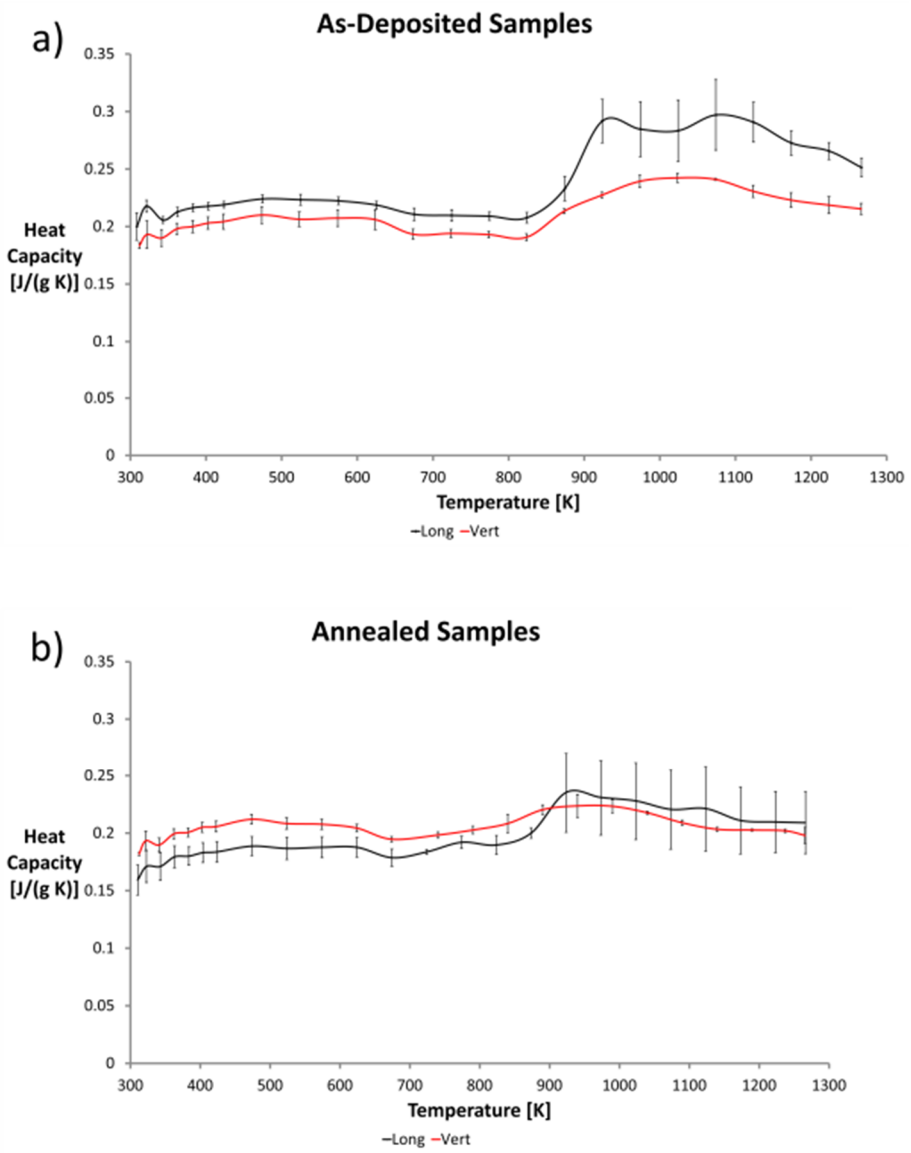

Figure 4.15: Specific heat capacity curves against temperate of the tested samples in the as-deposited condition (a) and the annealed condition (b) with the associated error bars.

Figure 4.16 reports the thermal conductivity (k) calculated over the range of temperature from 300 K to 1300 K using **Eq. (4.5)**. The colour code used in the previous graphs has also been applied to the graphs in **Figure 4.16.** In general, a decreasing trend was registered for the thermal conductivity when the testing temperature increased for all the condition tested. Thus, there was a reduction of around 35% for both as-deposited and annealed samples within the range from 300 K to 1300 K. The abrupt variations measured with respect to the heat capacity were obviously found in the thermal conductivity trends as the last ones were calculated directly from the heat capacity data.

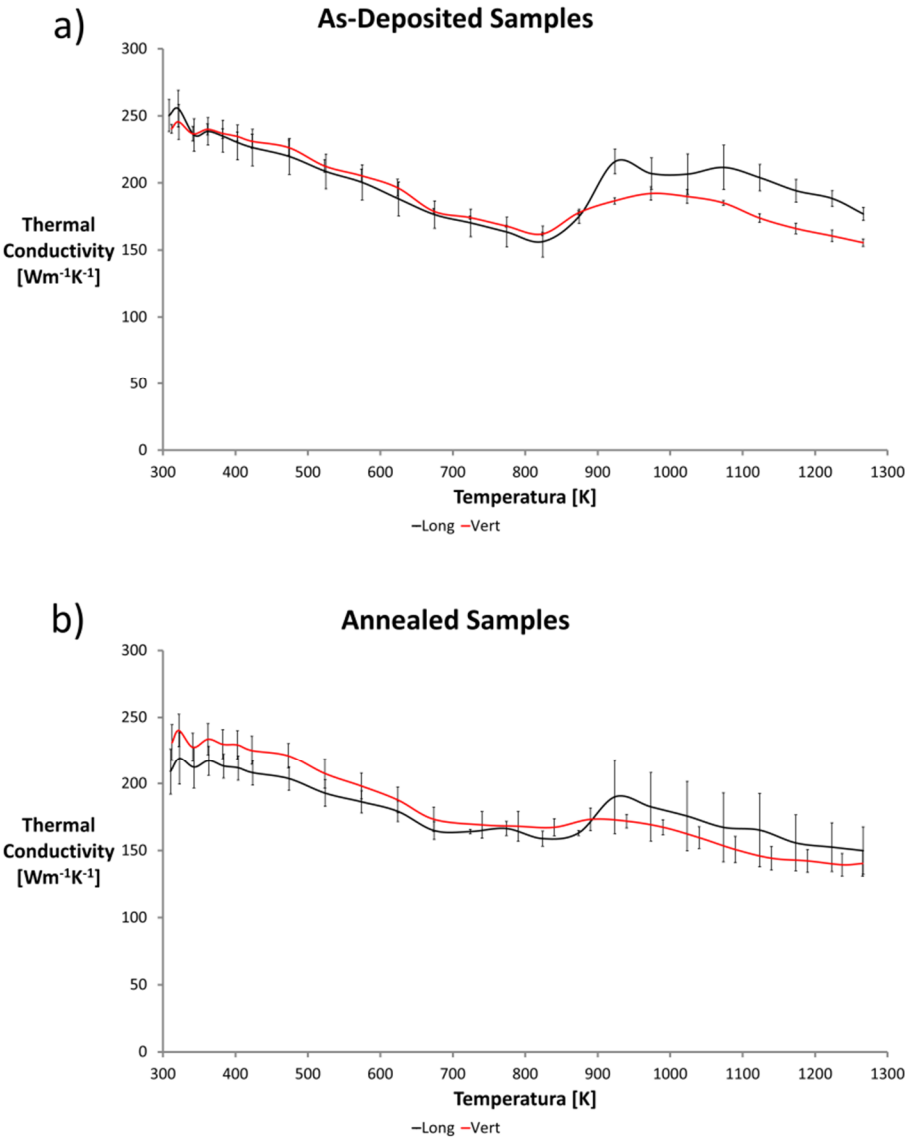

Figure 4.16: Thermal conductivity curves against temperate of the tested samples in the as-deposited condition (a) and the annealed condition (b) with the associated error bars.

The microstructural planes facing the laser during the analysis were the *Top View* (**Figure 4.6**) for the samples in the vertical direction and the *Front View* (**Figure 4.7a**) for the samples in the longitudinal direction. From the data shown in **Figure 4.16**, the microstructure resulted to have a negligible effect of on the thermal properties measured. In particular, the effect of the grain boundaries density and the grain orientation was not appreciable.

The annealing heat treatment had not greatly affected the actual values of thermal diffusivity measured over temperature. The absolute value of thermal diffusivity at room temperature resulted to be similar for all cases analysed with around 66.5 mm/s^2. The slightly large gap between the curves relative to the as-deposited samples is mainly due to the differences in density between the two set of samples so that it is not associated with the heat treatment. Overall, the trends reported resulted to be in accordance with other measurements of thermal diffusivity for unalloyed tungsten [25–27].

The average density of these samples was greatly affected by a localisation of small process defects and should not be considered as densification due to the annealing process. Nonetheless, the difference in density relative to the as-deposited samples and the annealed samples is considered significant. During the heat treatment, the annihilation of volume defects or the desorption of some gaseous means could have possibly promoted a modest densification. Certainly, these aspects need to be accurately investigated in further work.

The abrupt change with regards to the heat capacity registered for the as-deposited samples could have possibly been caused by some physical changes occurred after 873 K. On average, the change was smaller for the annealed samples. The variation in the trend could have been possibly caused by the recovery of the crystal defects. The rearrangement of the atoms to eliminate point or line defects, as a thermally activated process, could have required energy without increasing the total temperature of the metal. Thus, an increment in heat capacity was registered. Regarding the annealed samples, the fluctuation was relatively smaller than the as-deposited ones because a pronounced recovery could have already occurred during the thermal treatment.

The results of the heat capacity measurements directly affected the calculation of the thermal conductivity over the temperature range analysed. The reduction in thermal conductivity has been registered in trend with the data reported in the literature [26,27]. The relatively higher values of thermal conductivity registered for the as-deposited sample were directly affected by the higher heat capacity of the same samples respect to the annealed samples. In both cases analysed, the thermal conductivity resulted to be characterised by a small anisotropy.

From the data reported in **Table 4.1**, the thermal diffusivity and the thermal conductivity greatly depend on the density of the tungsten components. In particular, a higher sample density corresponds to a higher thermal conductivity. In fact, it has been already reported that thermal conductivity can be influenced by volume defects [43,44]. It has also been reported that a high number of dislocation and/or grain boundaries can decrease the thermal conductivity [29]. All of these features increase the interfacial area of tungsten. In this study, it is unexpectedly shown that as-deposited samples are characterised by a slightly lower density and a higher thermal conductivity when compared to the annealed samples. Furthermore, the thermal conductivity of the WAAM deposited tungsten structure resulted to be higher than other manufacturing methods (**Table 4.1**). The high purity, the high density, and the lower number of grains boundaries could have represented the main factor which influenced the thermal conductivity. This also requires further clarifications.

4.4 Conclusions

In this research, the microstructure and its correlation with the thermal properties of tungsten WAAM deposits were characterised. The microstructure in the as-deposited condition has been schematised using a three-dimensional model and the variation over temperature of the linear coefficient of thermal expansion, thermal diffusivity and thermal conductivity have been measured for both as-deposited and annealed conditions. The main results can be summarised as:

- The deposition strategy and the variation in thermal conductivity of the tungsten substrate promoted the formation of a microstructure formed by two specular arrays of columnar grains;

- The annealing process resulted to have a negligible effect on the microstructure but effectively relieve the residual stress of the structure from the deposition process or promote the dissolution of interstitial elements;

- The annealing process did not majorly influence the values and the variation over temperature of the thermal diffusivity;

This study demonstrated that the WAAM process can produce good quality tungsten components for the nuclear industry. Further characterisation of the effect of post-deposition heat treatments on the residual stresses will be needed in order to understand the best production route of tungsten components. Additional metallographic tests are needed in order to understand the recovery of the structure deposited after heat treatment.

4.5 Bibliography

1. Rieth M., Dudarev SL., Gonzalez De Vicente SM., Aktaa J., Ahlgren T., Antusch S., et al. Recent progress in research on tungsten materials for nuclear fusion applications in Europe. Journal of Nuclear Materials. 2013; 432(August 2012): 482–500. Available at: DOI:10.1016/j.jnucmat.2012.08.018
2. Norajitra P., Abdel-Khalik SI., Giancarli LM., Ihli T., Janeschitz G., Malang S., et al. Divertor conceptual designs for a fusion power plant. Fusion Engineering and Design. 2008; 83(7–9): 893–902. Available at: DOI:10.1016/j.fusengdes.2008.05.022
3. Janeschitz G. Plasma-wall interaction issues in ITER. Journal of Nuclear Materials. 2001; 290–293: 1–11. Available at: DOI:10.1016/S0022-3115(00)00623-1
4. Pamela J., Bécoulet A., Borba D., Boutard JL., Horton L., Maisonnier D. Efficiency and availability driven R&D issues for DEMO. Fusion Engineering and Design. 2009; 84(2–6): 194–204. Available at: DOI:10.1016/j.fusengdes.2009.02.028
5. Causet R a., Venhaus TJ. The Use of Tungsten in Fusion Reactors: A Review of the Hydrogen Retention and Migration Properties. Physica Scripta. 2001; T94: 9.

Available at: DOI:10.1238/Physica.Topical.094a00009

6. Bolt H., Barabash V., Federici G., Linke J., Loarte A., Roth J., et al. Plasma facing and high heat flux materials - Needs for ITER and beyond. Journal of Nuclear Materials. 2002; 307–311: 43–52. Available at: DOI:10.1016/S0022-3115(02)01175-3
7. Zhang Y., Galloway A., Wood J., Olsson Robbie MB., Easton D., Zhu W. Interfacial metallurgy study of brazed joints between tungsten and fusion related materials for divertor design. Journal of Nuclear Materials. Elsevier B.V.; 2014; 454(1–3): 207–216. Available at: DOI:10.1016/j.jnucmat.2014.07.058
8. Sheng H., Sun Z., Uytdenhouwen I., Van Oost G., Vleugels J. Temperature and deformation effect on the low and high angle grain boundary structure of a double forged pure tungsten. International Journal of Refractory Metals and Hard Materials. Elsevier Ltd; 2015; 50: 184–190. Available at: DOI:10.1016/j.ijrmhm.2015.01.008
9. Piotter V., Zeep B., Norajitra P., Ruprecht R., von der Weth A., Hausselt J. Development of a powder metallurgy process for tungsten components. Fusion Engineering and Design. 2008; 83: 1517–1520. Available at: DOI:10.1016/j.fusengdes.2008.06.022
10. Wong K V., Hernandez A. A Review of Additive Manufacturing. ISRN Mechanical Engineering. 2012; 2012: 1–10. Available at: DOI:10.5402/2012/208760
11. Herderick ED. Progress in Additive Manufacturing. JOM. 2015; 67(3): 580–581. Available at: DOI:10.1007/s11837-015-1323-x
12. Guo N., Leu MC. Additive manufacturing: Technology, applications and research needs. Frontiers of Mechanical Engineering. 2013; 8(3): 215–243. Available at: DOI:10.1007/s11465-013-0248-8
13. Baufeld B., Brandl E., Van Der Biest O. Wire based additive layer manufacturing: Comparison of microstructure and mechanical properties of Ti-6Al-4V components fabricated by laser-beam deposition and shaped metal deposition. Journal of Materials Processing Technology. Elsevier B.V.; 2011; 211(6): 1146–1158. Available at: DOI:10.1016/j.jmatprotec.2011.01.018
14. Frazier WE. Metal additive manufacturing: A review. Journal of Materials Engineering and Performance. 2014; 23(6): 1917–1928. Available at: DOI:10.1007/s11665-014-0958-z
15. Herderick E. Additive manufacturing of metals: A review. Materials Science and Technology Conference and Exhibition 2011, MS and T'11. 2011; 2(176252): 1413–1425. Available at: http://www.scopus.com/inward/record.url?eid=2-s2.0-84856301323&partnerID=40&md5=e02018d10b2ca37a7e2ae1773e4fcaec
16. Ding D., Pan Z., Cuiuri D., Li H. Wire-feed additive manufacturing of metal components: technologies, developments and future interests. International Journal of Advanced Manufacturing Technology. 2015; 81(1–4): 465–481. Available at: DOI:10.1007/s00170-015-7077-3
17. Williams SW., Martina F., Addison AC., Ding J., Pardal G., Colegrove P. Wire + Arc

Additive Manufacturing. Materials Science and Technology. 2016; 32(7): 641–647. Available at: DOI:10.1179/1743284715Y.0000000073

18. Yilmaz O., Ugla AA. Microstructure characterization of SS308LSi components manufactured by GTAW-based additive manufacturing: shaped metal deposition using pulsed current arc. International Journal of Advanced Manufacturing Technology. The International Journal of Advanced Manufacturing Technology; 2017; 89(1–4): 13–25. Available at: DOI:10.1007/s00170-016-9053-y
19. Asala G., Khan AK., Andersson J., Ojo OA. Microstructural Analyses of ATI 718Plus® Produced by Wire-ARC Additive Manufacturing Process. Metallurgical and Materials Transactions A: Physical Metallurgy and Materials Science. Springer US; 2017; 48(9): 4211–4228. Available at: DOI:10.1007/s11661-017-4162-2
20. Wang F., Williams S., Colegrove P., Antonysamy A a. Microstructure and mechanical properties of wire and arc additive manufactured Ti-6Al-4V. Metallurgical and Materials Transactions A: Physical Metallurgy and Materials Science. 2013; 44: 968–977. Available at: DOI:10.1007/s11661-012-1444-6
21. Gu J., Ding J., Williams SW., Gu H., Ma P., Zhai Y. The strengthening effect of inter-layer cold working and post-deposition heat treatment on the additively manufactured Al– 6.3Cu alloy. Journal of Materials Processing Technology. Elsevier; 2016; 230: 26–34. Available at: DOI:10.1016/j.jmatprotec.2015.11.006
22. Rieth M., Hoffmann A. Influence of microstructure and notch fabrication on impact bending properties of tungsten materials. International Journal of Refractory Metals and Hard Materials. Elsevier Ltd; 2010; 28(6): 679–686. Available at: DOI:10.1016/j.ijrmhm.2010.04.010
23. Tolias P. Analytical expressions for thermophysical properties of solid and liquid tungsten relevant for fusion applications. Nuclear Materials and Energy. Elsevier Ltd; 2017; 13: 42–57. Available at: DOI:10.1016/j.nme.2017.08.002
24. Brandes EA., Brook GB. Smithells Metals Reference Book. Seventh Ed. Butterworth-Heinemann. Butterworth-Heinemann; 1992. 1-534 p. Available at: DOI:10.1016/B978-075067509-3/50014-2
25. Moreau C., Fargier-Richard P., Saint-Jacques RG., Cielo P. Thermal diffusivity of plasma-sprayed tungsten coatings. Surface and Coatings Technology. 1993; 61(1–3): 67–71. Available at: DOI:10.1016/0257-8972(93)90204-2
26. Lv Y., Song J., Lian Y., Yu Y., Liu X., Zhuang Z. The thermal properties of high purity and fully dense tungsten produced by chemical vapor deposition. Journal of Nuclear Materials. Elsevier B.V.; 2015; 457: 317–323. Available at: DOI:10.1016/j.jnucmat.2014.11.095
27. Niu Y., Zheng X., Ji H., Qi L., Ding C., Chen J., et al. Microstructure and thermal property of tungsten coatings prepared by vacuum plasma spraying technology. Fusion Engineering and Design. Elsevier B.V.; 2010; 85(7–9): 1521–1526. Available at: DOI:10.1016/j.fusengdes.2010.04.032
28. Kanpara S., Khirwadkar S., Belsare S., Bhope K., Swamy R., Patil Y., et al.

Fabrication of Tungsten & Tungsten Alloy and its High Heat Load Testing for Fusion Applications. Materials Today: Proceedings. Elsevier Ltd; 2016. pp. 3055–3063. Available at: DOI:10.1016/j.matpr.2016.09.020

29. Zhang X., Yan Q., Lang S., Xia M., Ge C. Texture evolution and basic thermal-mechanical properties of pure tungsten under various rolling reductions. Journal of Nuclear Materials. Elsevier B.V; 2016; 468: 339–347. Available at: DOI:10.1016/j.jnucmat.2015.04.001

30. Zhu XL., Cheng L., De Temmerman G., Shi LQ., Yuan Y., Wang BY., et al. Effects of stress-relief pre-annealing on deuterium trapping and diffusion in tungsten. Fusion Engineering and Design. Elsevier B.V.; 2017; 125: 526–530. Available at: DOI:10.1016/j.fusengdes.2017.05.007

31. Sakurada S., Yuyama K., Uemura Y., Fujita H., Hu C., Toyama T., et al. Annealing effects on deuterium retention behavior in damaged tungsten. Nuclear Materials and Energy. 2016; 9: 141–144. Available at: DOI:10.1016/j.nme.2016.06.012

32. Markina E., Mayer M., Manhard A., Schwarz-Selinger T. Recovery temperatures of defects in tungsten created by self-implantation. Journal of Nuclear Materials. Elsevier B.V.; 2015; 463: 329–332. Available at: DOI:10.1016/j.jnucmat.2014.12.005

33. Ferroni F., Yi X., Arakawa K., Fitzgerald SP., Edmondson PD., Roberts SG. High temperature annealing of ion irradiated tungsten. Acta Materialia. Acta Materialia Inc.; 2015; 90: 380–393. Available at: DOI:10.1016/j.actamat.2015.01.067

34. Cowan RD. Pulse Method of Measuring Thermal Diffusivity at High Temperatures. Journal of applied physics. 1963; 34(4): 926.

35. Sils V., Smakula A. Precision Density Determination of Large Single Crystals by Hydrostatic Weighing. Phys. Rev. Journal. 1955; 99(6).

36. Uytdenhouwen I., Decréton M., Hirai T., Linke J., Pintsuk G., Van Oost G. Influence of recrystallization on thermal shock resistance of various tungsten grades. Journal of Nuclear Materials. 2007; 363–365: 1099–1103. Available at: DOI:10.1016/j.jnucmat.2007.01.146

37. Cagran C., Pottlacher G., Rink M., Bauer W. Spectral emissivities and emissivity X-points of pure molybdenum and tungsten. International Journal of Thermophysics. 2005; 26(4): 1001–1015. Available at: DOI:10.1007/s10765-005-6680-1

38. Gaganidze E., Rupp D., Aktaa J. Fracture behaviour of polycrystalline tungsten. Journal of Nuclear Materials. Elsevier B.V.; 2014; 446(1–3): 240–245. Available at: DOI:10.1016/j.jnucmat.2013.11.001

39. Szost BA., Terzi S., Martina F., Boisselier D., Prytuliak A., Pirling T., et al. A comparative study of additive manufacturing techniques: Residual stress and microstructural analysis of CLAD and WAAM printed Ti-6Al-4V components. Materials and Design. 2016; 89: 559–567. Available at:

DOI:10.1016/j.matdes.2015.09.115

40. Salvati E., Korsunsky AM. An analysis of macro- and micro-scale residual stresses of Type I, II and III using FIB-DIC micro-ring-core milling and crystal plasticity FE modelling. International Journal of Plasticity. 2017; 98: 123–138. Available at: DOI:10.1016/j.ijplas.2017.07.004
41. Gludovatz B., Wurster S., Hoffmann a., Pippan R. Fracture toughness of polycrystalline tungsten alloys. International Journal of Refractory Metals and Hard Materials. Elsevier Ltd; 2010; 28(6): 674–678. Available at: DOI:10.1016/j.ijrmhm.2010.04.007
42. ASTM International. Standard Test Methods for Density of Compacted or Sintered Powder Metallurgy (PM) Products Using Archimedes' Principle. Astm B962-13. 2013; i: 1–7. Available at: DOI:10.1520/B0962-13.2
43. D. P. H. Hasselman. Effect of Cracks on Thermal Conductivity. J. Composite Materials. 1978; 12: 403–407.
44. Francl J., Kingery W. Thermal Conductivity: IX, Experimental Investigation of Effect of Porosity on Thermal Conductivity. Journal of the American Ceramic Society. 1954; 37(2). Available at: http://onlinelibrary.wiley.com/doi/10.1111/j.1551-2916.1954.tb20108.x/abstract

Chapter 5

Paper D

"Process development, microstructure and mechanical properties of two different unalloyed tantalum wires deposited via Wire + Arc Additive Manufacture"

G. Marinelli*, [a], F. Martina*, S. Ganguly*, S. Williams*, G. Shrimpton**, T. Rogers**

*Welding Engineering and Laser Processing Centre (WELPC), Cranfield University, Cranfield, MK43 0AL, United Kingdom

**AWE Aldermaston, Reading, Berkshire, RG7 4PR, United Kingdom.

Abstract

In this study, an innovative way of producing large-scale unalloyed tantalum parts has been developed by using Wire + Arc Additive Manufacture. Two different unalloyed tantalum wires have been used to deposit 200-mm-long structures in tantalum and the effect of the wire chemistry on microstructure, porosity and mechanical properties has been investigated. Furthermore, the effect of the deposition process on surface discolouration and on the mechanical properties has been discussed. The as-deposited structures were characterised by a stable layer geometry during the whole process. Tantalum structures have been deposited with high integrity and excellent mechanical properties. Improved yield strength has been achieved for the deposited structures when compared to commercially available tantalum, even though the grains within the deposited materials were large and had a high aspect ratio. Wire + Arc Additive Manufacture has clearly shown the potential to produce tantalum components with relatively low cost, exploiting the characteristic freedom of design, offering a robust alternative manufacturing route.

5.1 Introduction

Additive Manufacturing (AM) has been identified as a very promising technology with the capability to reinvigorate and remodel the manufacturing sector [1,2]. The technology is based on the simple concept of depositing three-dimensional structures using a layer-by-layer approach [3]. Cost and time reduction, design freedom and engineered materials properties are the main fundamental principles on which AM is based [3].

Among the different AM techniques known today, wire-feed technologies are emerging for the possibility to produce large-scale components [4]. Wire + Arc additive Manufacture (WAAM) is a novel AM process which employs an electric arc as the heat source and high-quality metal wire as the feedstock [5]. WAAM can directly fabricate fully-dense large 3-D near-net-shape components with a much higher deposition rate, typically kg/h, than most other metal additive manufacture processes [4,5]. The WAAM process has been demonstrated to successfully produce large-scale parts in stainless steel [6], Inconel [7], titanium [8] and aluminium [9], achieving even complex geometries of deposition. WAAM is considered a technique suitable for the manufacture of large components because of its high deposition rate, relatively low cost and high flexibility in the design [5,10].

With a melting point of 3017°C and a density of 16.69 g cm^{-3} [11], tantalum is a useful material for specialised applications because of its stability at high temperature, high corrosion resistance and high melting point [12]. Unlike other refractory metals, such as tungsten and molybdenum, tantalum is characterised by a high ductility at room temperature [13,14]. For these reasons, tantalum finds its utilisation within a large range of applications when a combination of all these particular properties is required. For example, tantalum finds major utilisation within the defence sector as well as the electronics, aerospace and chemical industry sector [11–13].

The employment of tantalum has been restrained by some difficulties related to metallurgical, fabrication and cost-related issues [15]. For this reason, investigations of the development of additive manufacturing of unalloyed tantalum

could lead to an improvement and a larger demand for components within many industries. Different studies of AM for tantalum have already been reported which were using, a laser as the heat source and tantalum powder as the feedstock.

A complete study of the selective laser melting (SLM) process, microstructure and mechanical properties of tantalum powder has been conducted by Zhou et al. [16]. Micro-pores and micro-cracks were found within the build when the laser power was not optimised and a high hardness and tensile properties were observed after the deposition. A large loss in ductility was also reported accompanied by a brittle-like fracture. It is important to note that the raw materials used in this study had a concentration of 0.18 wt.% of oxygen. These oxygen levels are considered considerably high so that oxygen lead to a strengthening of the tantalum components [17].

In the work of Thijs et al. [18], the SLM process was studied for pure tantalum, focusing mainly on the microstructural evolution and mechanical properties. Epitaxial grain growth through the layers was observed and led to the formation of large columnar grains and the development of a strong texture. The anisotropy within the microstructure was also found to be reflected on the mechanical properties.

Furthermore, a tantalum coating has been successfully deposited onto titanium using engineered net shaping (LENS) in order to produce controlled porous components with enhanced bio-properties [19]. A further study on porous tantalum parts is reported in the study of Wauthle et al. [20], in which SLM was used effectively to produce porous tantalum implants with fully-interconnected open pores.

Unlike other bcc metals, tantalum shows a high solubility for interstitials, which hardly segregate at the grain boundaries. This is one of the main causes of its improved ductility at room temperature [12,14]. Despite this aspect, the mechanical properties of tantalum are highly influenced by the purity, the temperature and the strain rate [11,14,21]. In particular, interstitials such as nitrogen and oxygen have a strong effect on hardness and yield strength. The manufacturing route has also a large effect. In **Table 5.1**, mechanical properties of

unalloyed tantalum are compared for various production techniques. These data have been taken from the comparison reported in [18] and integrated with the results of [16].

Ta Grade	Commercial pure EB*	Commercial pure P/M**	Soft annealed	Cold-worked	Selective Laser Melting
Modulus Elasticity [GPa]	185	185	186	186	na
Yield Strength [Mpa]	165	220	na	na	450
Ultimate Tensile Strength [MPa]	205	310	200-390	220-1400	739
Elongation [%]	40	30	20-50	2-20	2
Vickers Hardness [Hv]	110	120	60-120	105-200	425

*EB: electron beam melted; **P/M: powder metallurgy.

Table 5.1: Overview of mechanical properties of pure Ta obtained via different manufacturing routes.

Commercially pure tantalum components produced using electron beam melting and powder metallurgy have similar mechanical properties which are mainly influenced by the grain size. It is also clear that cold work impacts predominantly the hardness and the elongation (**Table 5.1**). The data reported for selective laser melting depict unusual properties that are predominantly influenced by the content of oxygen, up to date.

Most of the research reported aimed to develop small-size complex tantalum structures for medical applications. There are currently no studies on the production of large-scale unalloyed tantalum components using additive manufacturing. Furthermore, no studies have been reported on the WAAM process for tantalum and the mechanical properties of the structure obtained. In this study, optimal manufacturing parameters were found showing a great repeatability and consistency for the main geometrical parameters. The impact of the chemistry of two different wires on the evolution of porosity, the microstructure, the hardness and the mechanical properties of the deposited structures has been analysed.

5.2 Experimental Procedure

Two different unalloyed tantalum wires with a diameter of 1.2 mm were used for the WAAM process. Cold-rolled tantalum plates with dimensions of 210 x 50 x 4 mm were used for the initial trials of deposition and for the production of

two twenty-layer walls (**Table 5.2**), used for the investigation of the microstructure and hardness. Larger plates, 400 x 60 x 8 mm-plates, were used for the deposition of two large structures (**Table 5.2**), from which the tensile coupons have been extracted. The surface of the plate was ground and rinsed with acetone prior deposition in order to remove most of the contaminants. **Figure 5.1** shows the layout of the apparatus used in this study.

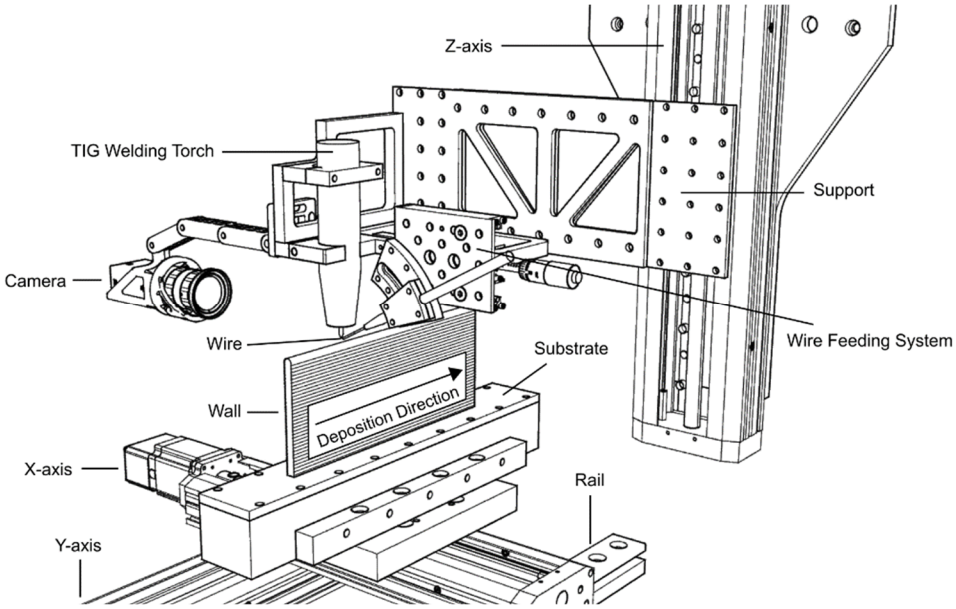

Figure 5.1: Set-up used for the development of the WAAM process for unalloyed tantalum.

A conventional tungsten inert gas (TIG) welding torch, a power supply and a controlled wire feeder were used for the deposition. The heat source, the wire delivery system and the substrate were attached to three linear motorized high-load stages assembled in XYZ configuration. The tantalum wires were deposited layer by layer onto the substrate using a single bead. The direction of deposition was always kept constant for each successive layer and the wire was fed from the side of the weld pool. The apparatus was surrounded by an enclosure used to ensure a low level of oxygen when purged with argon. A MC500S welding camera was used to study and monitor the process during the deposition of each layer. The camera was located opposite to the direction of wire feeding as shown schematically in **Figure 5.1**.

Table 5.2 reports a summary of all the samples produced and analysed within this study. In particular, four straight walls were produced and analysed. They were labelled as Wall1S, Wall2S, Wall1 and Wall2. The first two were walls

made of twenty layers each. The last two walls were produced with the dimensions of 230 mm in length, 110 mm in height and 10 mm in thickness. Each structure was deposited using the same wire within the entire build (**Table 5.2**). The walls were produced using the parameters shown in **Table 5.3.** The parameters were kept constant throughout the entire process.

Sample Name	Number of Layers	Wire used	Analysis
Wall1S	20	Wire1	• Hardness interface substrate/wall; • Geometrical control; • Microstructure.
Wall2S	20	Wire2	
Wall1	90	Wire1	• Chemical analysis; • Oxide Layer; • Porosity; • Microstructure; • Tensile Tests.
Wall2	90	Wire2	

Table 5.2: Summary of the samples produced and their domination.

TS [mm/s]	WFS [mm/s]	I [A]	Electrode-workpiece Distance [mm]	Electrode angle [°]	Electrode Diameter [mm]	Shielding gas composition [%]	Gas flow rate [L/min]	Oxygen Atmosphere [ppm]
4.0	40	300	3.5	45	3.6	100 He	15	≈100

Table 5.3: WAAM process parameters used for the deposition of unalloyed tantalum.

The microstructure was examined using a cross-section perpendicular to the deposition direction (extracted from the region reported in purple in **Figure 5.2a**). The samples were polished using the procedure shown in **Table 5.4**. The composition of the etchant used for this investigation was under nondisclosure agreement being proprietary of H.C. Starck. The presence and thickness of the oxide layer on the outer surface of the walls were measured using a scanning electron microscope (SEM) operating at 20 kV electron beam power. The same instrument was used for the analysis of the fractured surfaces of selected tensile coupons. Vickers microhardness was measured using an automatic hardness testing machine. The main parameters for the hardness acquisition were 500g load

and 10 seconds indentation time for each testing point. A three-line scan with 0.5 mm spacing and thirteen points each was performed through the height of each wall and they have been averaged for Wall1 Wall2 and Substrate. Furthermore, an analysis of the hardness at the interface between substrate and wall was conducted only for Wall1S and Wall 2S.

Grinding and Polishing means	Time [min]
SiC Paper 240 grid	2
SiC Paper 1200 grid	6
SiC Paper 2500 grid	6
Alpha alumina 0.3 μm suspension	15
Alumina and silica 0.05 μm suspension	15
Colloidal silica 0.02 μm suspension	15

Table 5.4: Grinding and polishing procedure used for the microstructural preparation.

Tensile coupons were extracted parallel and perpendicular to the build direction (**Figure 5.2a**), according to the requirements of BS EN ISO 6892-1-2009 standard.

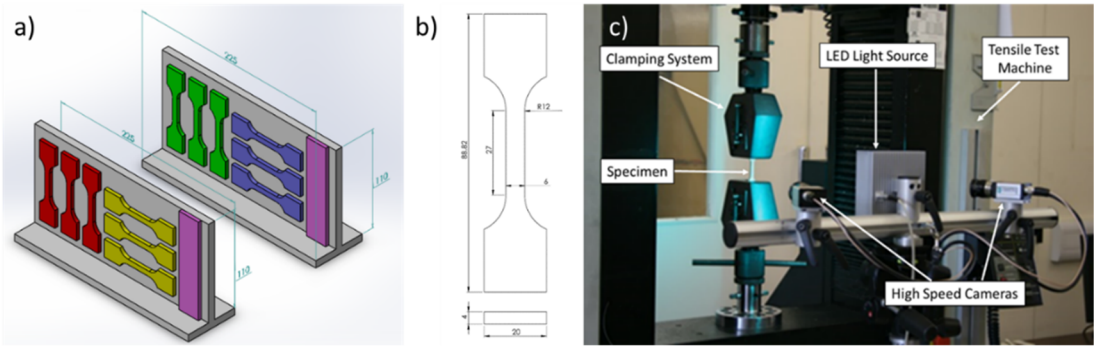

Figure 5.2: (a) Extraction position and direction of the tensile coupons for each wall; (b) Main dimensions of the tensile coupon used for the tests; (c) Apparatus used for tensile tests and DIC recording.

The tensile specimens (**Figure 5.2b**) had a dogbone shape with a gauge length of 27 mm, a gauge width of 6 mm and a thickness of 4 mm, resulting in a cross-sectional area of 24 mm^2. The overall length of the specimen was 88.82 mm and the radius of the fillet was 12.0 mm. Length and width of the grip section were both equal to 20 mm. Four control specimens were also extracted from a commercially available tantalum plate, the same as used as the substrate material, and tested in order to provide a baseline for comparison. Six samples were extracted and tested from each of the two builds as shown in **Figure 5.2a**. Each

tensile coupon was painted in order to create a speckle pattern for the digital image correlation (DIC).

Tensile tests were carried out with an Instron 5500R electromechanical machine equipped with a 20kN load cell. No extensometer has been used during testing. The cross-head displacement speed was 1.0 mm/min. Two high-speed cameras were set up in the front of the sample on a stable tripod, as shown in **Figure 5.2c**, coupled with a LED light source. LED illumination was used to overcome interference from surrounding light. The cameras were equipped with a filter in order to capture and analyse only the reflected green light. The distance between the camera and the specimen was adjusted to the area to be measured. The random speckle pattern was sprayed on the coupon surface using, first, a white paint and, secondly, a black paint for the displacement measurements. The cameras were connected to a computer and the data was recorded using the software ISTRA 4D from Dantec Dynamics.

The same software has been used for the post-processing of the digital image correlation and for the calculation of the yield strength, ultimate tensile strength and elongation. Oxygen and nitrogen levels, as well as other main metallic and non-metallic contaminants, within the deposited wall materials, the parent welding wires and the substrates were determined via chemical analysis.

5.3 Results and Discussion

5.3.1 Chemical analysis

6	W	Mo	Ta	Ti	V	Cr	Fe	C	N	O	K
Substrate	<0.05	<0.05	99.99	<0.05	<0.05	<0.05	<0.05	33 ppm	<10 ppm	60 ppm	<10 ppm
Wire1	<0.05	<0.05	99.98	<0.05	<0.05	<0.05	<0.05	36 ppm	11 ppm	190 ppm	<10 ppm
Wire2	<0.05	<0.05	99.87	<0.05	<0.05	<0.05	<0.05	20 ppm	<10 ppm	86 ppm	<10 ppm
Wall1	<0.05	<0.05	99.97	<0.05	<0.05	<0.05	<0.05	48 ppm	13 ppm	226 ppm	<10 ppm
Wall2	<0.05	<0.05	99.73	<0.05	<0.05	<0.05	<0.05	29 ppm	<10 ppm	164 ppm	<10 ppm

Table 5.5: Elemental composition (wt%) of tantalum Substrate, Wire1, Wire2, Wall1 and Wall2.

Table 5.5 shows the results of the chemical analysis of the substrate, the two wires and the two walls used for mechanical testing. These analyses were commissioned externally. X-ray fluorescence (XRF) spectroscopy was used for the detection of the major metallic atoms (W, Mo, Ta, Ti, V, Cr and Fe). LECO combustion analysis was used for the measurement of the concentration of carbon, nitrogen and oxygen. Finally, inductively coupled plasma optical emission spectroscopy (ICP-OES) was used for potassium. All the materials used were high-purity unalloyed tantalum products. The substrate had the lowest content of nitrogen and oxygen respectively with a concentration of <10 ppm and 60 ppm. The two wires mainly differ in the oxygen level. This is reflected directly in the composition of the two walls built. The content of oxygen in the atmosphere of deposition was constantly monitored and kept around 100 ppm so the content of oxygen slightly increases in both cases. This is an indication of the high solubility and affinity of oxygen with tantalum [17]. More relevant is the difference of 62 ppm of oxygen between the two walls. The effect on the hardness and on the porosity is reported later.

5.3.2 Bead appearance and outer oxide layer

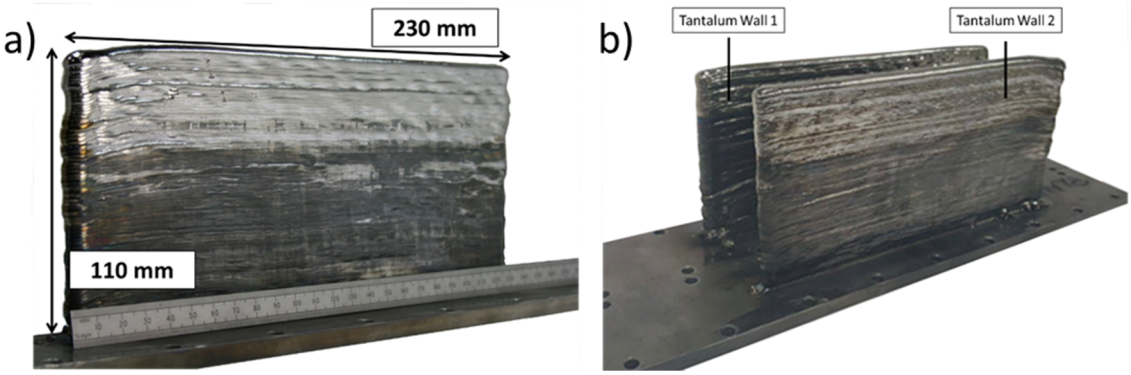

Figure 5.3: (a) Linear structure made of unalloyed tantalum with the main dimensions; (b) Picture of the two linear structures deposited and studied in this investigation.

Figure 5.3 shows the two walls deposited for the mechanical testing and their main dimensions. Noteworthy is the complete absence of distortion after unclamping the substrate, clearly visible in **Figure 5.3b**. This is mainly due to two factors: a high geometrical stiffness of the wall-plus-substrate component and to a localised plastic deformation of both substrate and the lower part of the wall material while still clamped. From **Figure 5.3a** and **Figure 5.3b,** it can also be seen

that both structures exhibit a more pronounced opacity on the lower part with respect to their top. In particular, this layer developed for the lower layers, always leaving the top layers of a shiny silver appearance. This region of the outer surface has been characterised using scanning electron microscope in order to verify the nature of this opaque layer.

Figure 5.4a and **Figure 5.4b** show the different appearances of the structure outer surface at the top and the bottom respectively, underlying a marked darkening of the bottom surface. **Figure 5.4c** and **Figure 5.4d** show the investigation of the cross-section of the structure after polishing for both top and bottom. The bottom part of the wall presents a layer with an average thickness of around 1.7 μm unlike the top part. During the deposition of each wall, the top layers have always presented a silver surface despite lower layers began to darken. This is likely to be an oxide accumulation on the surface but it is not clear the reason why this occurs. In general, this feature is not considered detrimental because it will be machined away after the deposition.

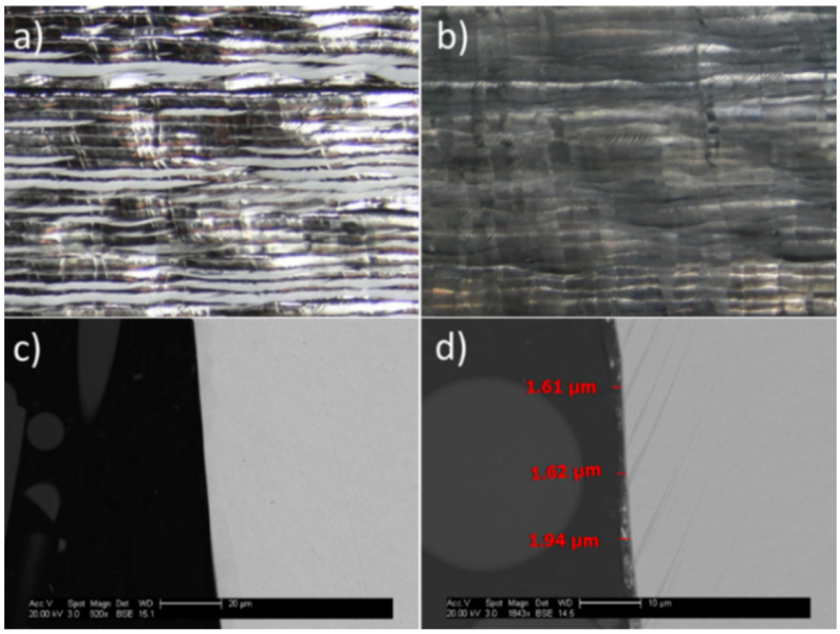

Figure 5.4: Detail of the outer surface of the top (a) and the bottom (b) of the tantalum structure; Scanning electron microscope picture of the cross-section of the top (c) and the bottom (c) of the structure.

5.3.3 WAAM process and geometrical control

The geometry of each deposited layer characterises the WAAM process for unalloyed tantalum. In particular, layer height and the layer width have been used

as the main parameters of evaluation [22]. Four measurements were taken along the length of the wall after every layer, averaging the small-scale discrepancies. **Figure 5.5** shows the variation of the increment of layer height and layer width during the initial ten layers for both Wall1S and Wall2S. The geometrical values for the successive layers are not reported because a permanent geometrical stability in height was observed. Generally, as the number of layers increases, there is a decrease in layer height accompanied by an increase in the layer width for the initial layers. A constant layer height of around 1.2 mm was recorded for both walls after the fifth layer. The average constant width was measured to be around 10.0 mm for both structures, also after the fifth layer.

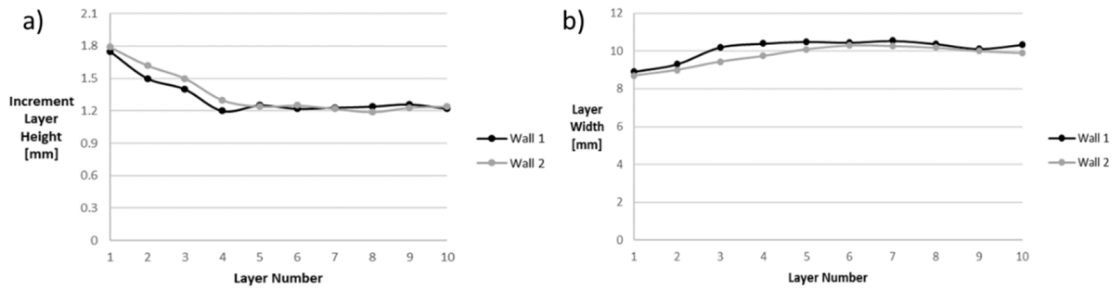

Figure 5.5: (a) Increment of the layer height against the layer number; (b) Total layer width against the layer number.

A transient condition with regards to the heat sink dimensions faced by each layer was the main factor influencing the geometry of the initial layers [22]. When stability was reached with respect to the size of the heat sink and the corresponding heat transfer, the same stability was reported for the geometrical features.

5.3.4 Porosity

Figure 5.6 shows the cross-section of Wall1 and Wall2 after polishing. The surface of Wall1 presented some scattered porosity throughout its height (**Figure 5.6a**). In contrast, the porosity within Wall2 was completely absent (**Figure 5.6b**). The largest pores had an average diameter of 200 µm instead, the scatter porosity had the average diameter of 80-100 µm. Referring to **Table 5.5**, the wire used for the deposition of Wall1 had a higher concentration of oxygen with respect to the wire used to produce Wall2. The content of oxygen can possibly be directly linked to the

presence of porosity. The occurrence and formation of the porosity are discussed later.

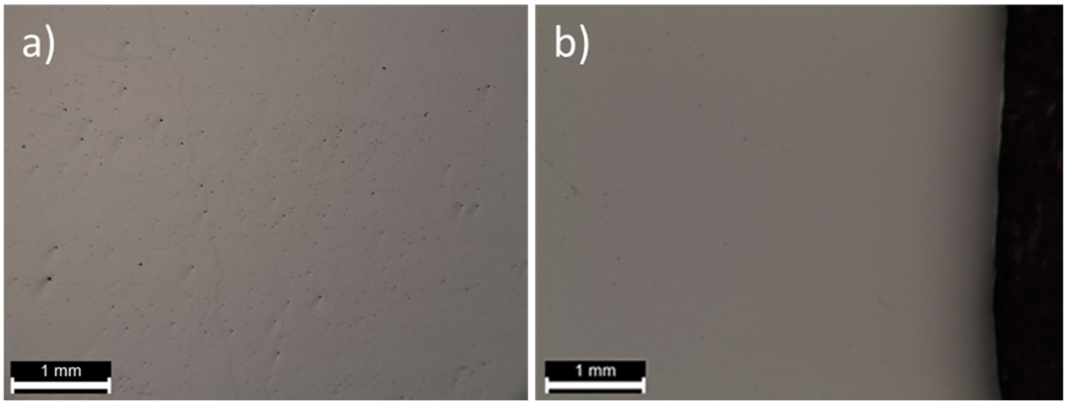

Figure 5.6: Optical microscope picture of a section of the Wall1 (a) and Wall2 (b) after polishing.

5.3.5 Microstructure and banding occurrence

Figure 5.7 shows the typical microstructure of the as-deposited tantalum structures produced using WAAM. **Figure 5.7a** shows the microstructure of Wall1S, used to show the interface between substrate and wall. The grain structure of Wall1 and Wall2 along the structure is shown in **Figure 5.7b** and **Figure 5.7c**. It can be seen that columnar grains developed during the solidification and grew in the direction parallel to the building direction for all the structures deposited. This is typical epitaxial growth along the building direction that some materials develop when processed with an AM process. Thijs et al. reported the evolution of columnar grain for tantalum processed by SLM [18] and the same grain development can be found for Ti-6Al-4V structures processed using WAAM [22]. In particular, the columnar grains increased in size with the height of the wall. The peculiar columnar grains can be seen for both Wall1 and Wall2 so that the different chemistry of the wires has not influenced the solidification mode of the crystals. Furthermore, all structures present an unusual macroscopic banding between each deposited layer. Similar cases have been seen for Ti-6Al-4V [8]. In the case of titanium, the banding is due to a localised change of the α-grains due to the re-heating when depositing the successive layer [8,23]. In the case of unalloyed tantalum, secondary phases or sub-grain structures did not develop when exposed to cyclical re-heating.

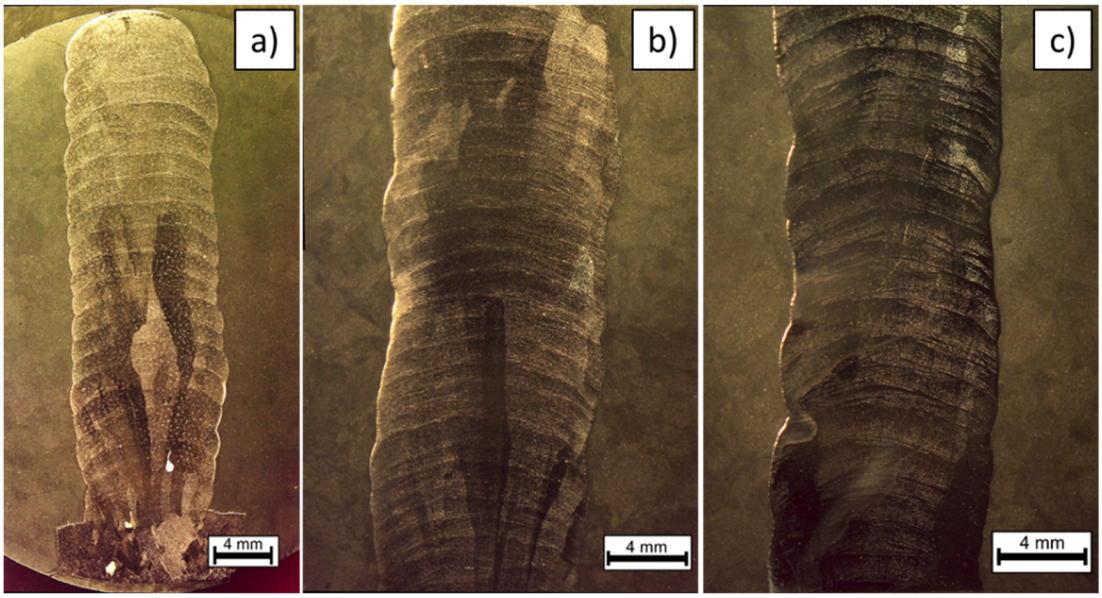

Figure 5.7: Microstructure of Wall1S (a), Wall1 (b) and Wall2 (c).

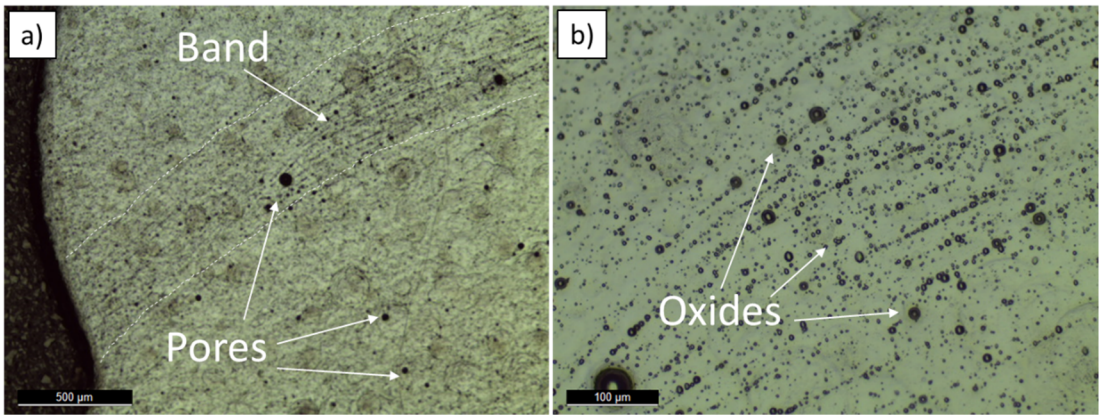

Figure 5.8: Banding between the layers in Wall1 and pores (a) and oxides within the band (b).

Figure 5.8 shows the nature of the banding in Wall1 between two consecutive layers, which was also observed in Wall2. Scattered void-like structures were distributed along a line (band) across the interface between two successive layers (**Figure 5.8a**). These voids were remarkably smaller than the porosity in Wall1 (**Figure 5.6a**). **Figure 5.8b** shows how these features were lined up on successive and almost equidistant line. Additionally, few larger pores were also found within the banding regions. Noteworthy is also the appearance of the banding regions only after etching. As **Figure 5.6** shows, none of these regions was observed after polishing only. A reasonable hypothesis is that these void-like features forming the bands are caused by the detachment, caused by the etching, of fine oxide particles, which possibly formed during the solidification of the liquid

pool. The average banding distance resulted to be similar to the layer height for all the structures. Thus, this phenomenon seemed to be directly connected to the solidification of each layer.

Oxygen may be present in two chemical states within a tantalum component, oxygen in solid-solution or oxide precipitate [24], and their occurrence depends on process temperature, cooling rate and oxygen concentration [24]. The oxygen in solid-solution mainly impacts the average hardness of the material, as it has also been reported later in this study. The oxide precipitates are volatile above 1600°C [25] and some studies reported the formation of these particles even at a very low concentration of oxygen [26]. Furthermore, they are strongly attacked by the etchant leaving surface features similar to a void-like feature [24]. In fact, Stecura et al. [26] also found these voids not only at the grain boundaries but also within the grains with the same morphology and features of the voids in **Figure 5.8b**.

This sustains the hypothesis of the formation of oxide particles for the concentration of oxygen within the walls and the wires. Thus, the bands could be possibly caused by the presence of a regular dispersion of tantalum oxides particles, in particular, Ta_2O_5 as most stable compound [27], and they were visible due to the strong attack by the etchant because of the high reactivity of these regions. Furthermore, the disperse porosity seen in **Figure 5.6** could have been caused by the vaporization of a large accumulation of oxide particles when temperatures as high as 3000°C have been seen at the bottom of the weld pool while depositing the successive layer. In general, the complete understanding of this phenomenon would require further investigations.

5.3.6 Hardness

The average hardness was evaluated for the Substrate, Wall1 and Wall2; instead, Wall1S and Wall2S have been used to evaluate the hardness at the substrate-wall interface. For all the measurements, hardness values have been measured along the centreline of the structure. **Table 5.6** reports the average hardness values for each condition associated with the oxygen composition in

ppm. In particular, the values for Wall1 and Wall2 have been measured along their height between 60.0 mm and 70.0 mm from the substrate.

	Hardness [Hv]	Standard Deviation	Oxygen content [ppm]
Substrate	96.0	1.3	60
Wall 1	114	0.8	226
Wall 2	99.0	1.0	164

Table 5.6: The average hardness value of the Substrate, Wall 1 and Wall 2 with the associated standard deviation and the oxygen content in ppm.

The hardness shows a trend when compared to the oxygen content of the three samples. Higher was the content of oxygen and higher resulted to be the average hardness value. This is a common trend in the literature [17], particularly, nitrogen and oxygen are strong hardeners of unalloyed polycrystalline tantalum. In the work of Stecura [26] is shown that the hardness of tantalum increased almost linearly when increasing oxygen content in solid solution. Furthermore, it has been reported that the hardness of unalloyed tantalum is mostly governed by the content of oxygen in solid solution and, contrarily, the oxide precipitates have no considerable effect due to their incoherence with the crystals [24]. Spitzig et al. [28] reported about the solid solution hardening due to oxygen as interstitial for vanadium, niobium and tantalum. The effect has been associated with the misfit between the oxygen and the metal atoms. The different average hardness values for the deposited walls, Wall1 and Wall2, can be attributed mainly to the oxygen content in solid solution because the grain structure was almost identical, and no large variation of hardness has been measured at the band regions.

Figure 5.9 represents the variation of the hardness from the bottom of the substrate to the top of Wall1S and Wall2S. The origin of the X-axis has been chosen as the top surface of the substrate. From **Figure 5.9**, it is possible to underline three different regions of interest: Substrate, Zone1 and Zone2. The average hardness values for each region and for both Wall1S and Wall2S are reported in **Table 5.7.**

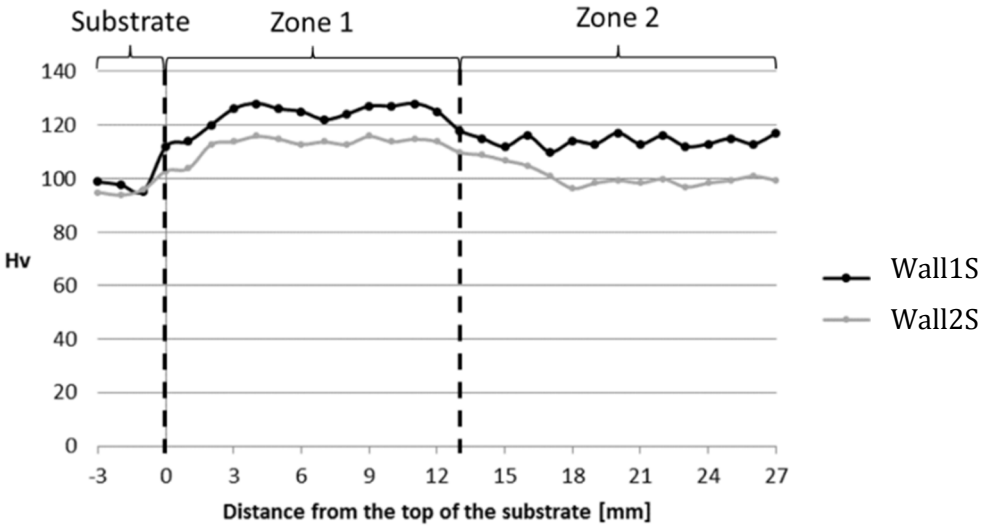

Figure 5.9: Hardness values of the tantalum Wall1S and Wall2S with respect to the distance from the top of the substrate.

	Substrate	Wall1S Zone1	Wall1S Zone2	Wall2S Zone1	Wall2S Zone2
Average	96	123	114	112	100
Stand. Dev.	1.15	5	2	4	3.5

Table 5.7: Statistical study of the distributions of tantalum hardness values.

The average hardness of Zone1 was measured to be always higher than the hardness of Zone2 for both Wall1S and Wall2S. This difference can be possibly addressed to the considerable effect of thermal straining, which induced strain hardening. Unalloyed polycrystalline tantalum is known to be subject to great work hardening when a consistent amount of stress is applied [29]. When pure materials are subjected to cyclical deformation, they exhibit an initial hardening which stabilises for any further deformations [30]. In general, for a soft pure metal, the dislocation density is low but, after cyclic plastic straining, the dislocation density increases rapidly which causes a strengthening. This effect is defined cycling hardening. This is confirmed by comparing the values of the average hardness in **Table 5.6** and the hardness of Zone2 in **Table 5.7** for both walls.

5.3.7 Tensile properties

In **Table 5.8** are summarised the main tensile properties for Substrate, Wall1 and Wall2 in both vertical (V) and horizontal (H) direction. **Figure 5.10** shows the representative stress-strain curves for these conditions. It is evident

that for both deposited structures and direction of testing, a higher yield strength compared to the Substrate has been measured. Contrarily, a clear reduction in total elongation can be seen for both Wall1 and Wall2 with respect to the Substrate. Additionally, an evident anisotropy has been observed for both walls.

Coupon Name	YS [MPa]	St. Dev.	UTS [MPa]	St. Dev.	Elongation [%]	St. Dev.
Substrate	182	3.7	265	7.8	62	2.5
Wall1 V	216	10.0	241	10.0	27	1.0
Wall1 H	234	7.0	261	3.0	36	6.0
Wall2 V	194	1.9	218	8.2	35	3.0
Wall2 H	208	14	226	9.8	32	7.0

Table 5.8: Tensile properties of the Substrate, Wall1 and Wall 2 in both vertical and horizontal direction.

DIC usually over-estimates the elongation of the material [31], which is evident when comparing **Table 5.1** and **Table 5.8.** The major contributions to the high yield strength of the deposited structures were the higher content of oxygen. As already reported in the literature, the yield stress has been seen to increase linearly with increasing amounts of nitrogen or oxygen [17]. This can also be seen when comparing the yield strength of Wall1 over Wall2 in both testing directions.

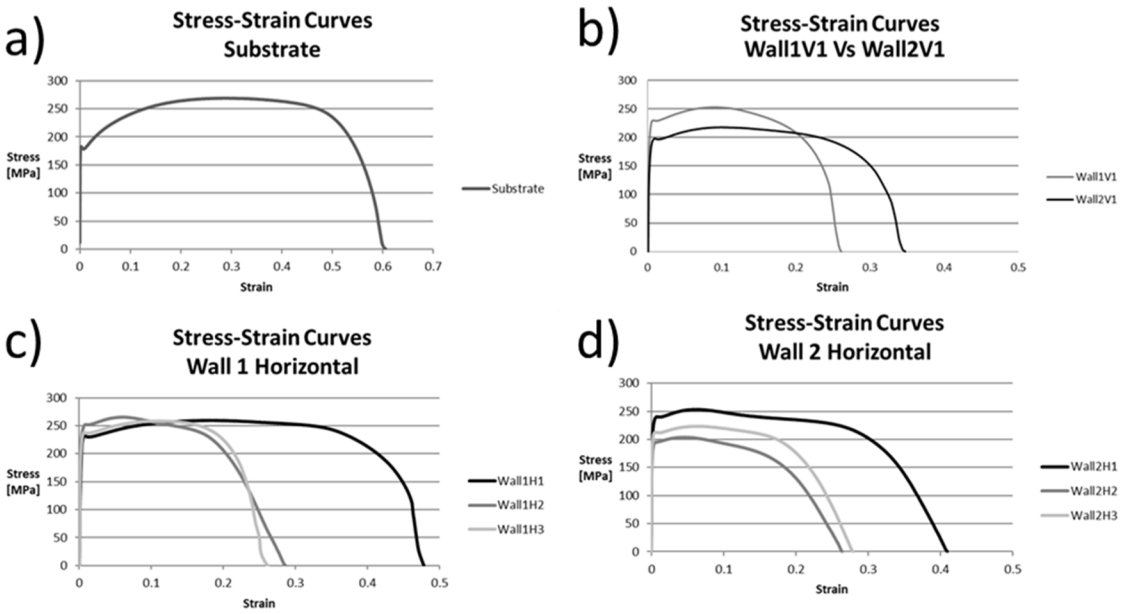

Figure 5.10: Representative stress-strain curves of Substrate (a), Wall1 and Wall2 in the vertical direction (b), Wall1 (c) and Wall2 (d) in the horizontal direction.

The impurity level in tantalum can have a much higher influence on the mechanical strength compared to the grain size [16,32]. The interstitial atoms obstacle the movement of the dislocations, increasing the absolute stress for plastic deformation [32]. The large reduction in elongation has been addressed mainly to the differences in grain size and shape between substrate and walls. The substrate was characterised by fine equiaxed microstructure, unlike the deposited structures, which was formed by large columnar grains. For a relatively small grain size under uniaxial load, grain rotation and grain sliding become likely [33,34]. The high mobility of the fine equiaxed grains has possibly confined or stopped the formation and growth of the voids within the gauge volume. The strain accumulation and the features of the fractured surfaces are reported later.

The yield strength and the ultimate tensile strength were higher for the vertical samples compared to the horizontal ones for both structures. A similar scenario has been reported by Fude et al. [8] and Brandl et al. [23] for Ti-6Al-4V deposited using Wire + Arc and Wire + Laser Additive Manufacture. Baufeld et al. [35] also reported a consistent anisotropy when testing vertical and horizontal samples extracted from an AM component. Thijs et al. [18] reported a marked anisotropy with regards the mechanical properties for tantalum structure deposited using SLM. The anisotropy has been directly connected to crystallographic texture, grain shape and size developed during the deposition of the directional columnar growth. In particular, considering the long columnar grains with high aspect ratio, the grain size within the gauge volume for the horizontal direction was smaller on average than in the vertical direction. The higher amount of grain boundaries influenced considerably the tensile properties [35].

From **Figure 5.10c** and **Figure 5.10d**, it is possible to see that the horizontal coupons extracted from the top of the structures (Wall1H1 and Wall2H1) presented a larger elongation with respect to the coupons extracted from the root of the deposits (Wall1H3 and Wall2H3). The effect related to the location of the coupon within the structure has been attributed to the thermal straining, already reported for the hardness.

5.3.8 Strain Localisation

Figure 5.11 shows the strain maps under tensile load recorded using digital image correlation (DIC) for different samples. A scale between 0 mStrain and 500 mStrain was used for all the cases to facilitate the comparison. The distance covered after a specific time by the cross-head of the tensile machine was used as global displacement and it is reported in millimetres. The strain maps shown represent the evolution of the strain from the beginning of the test until about uniform elongation. After this point, the speckle pattern was damaged by the heavy necking and the values of the strain were not acquirable. Comparing the strain maps, it is possible to see that the tensile coupons extracted from the walls presented a faster strain localisation when compared to the substrate coupons. This has been attributed to their different microstructure.

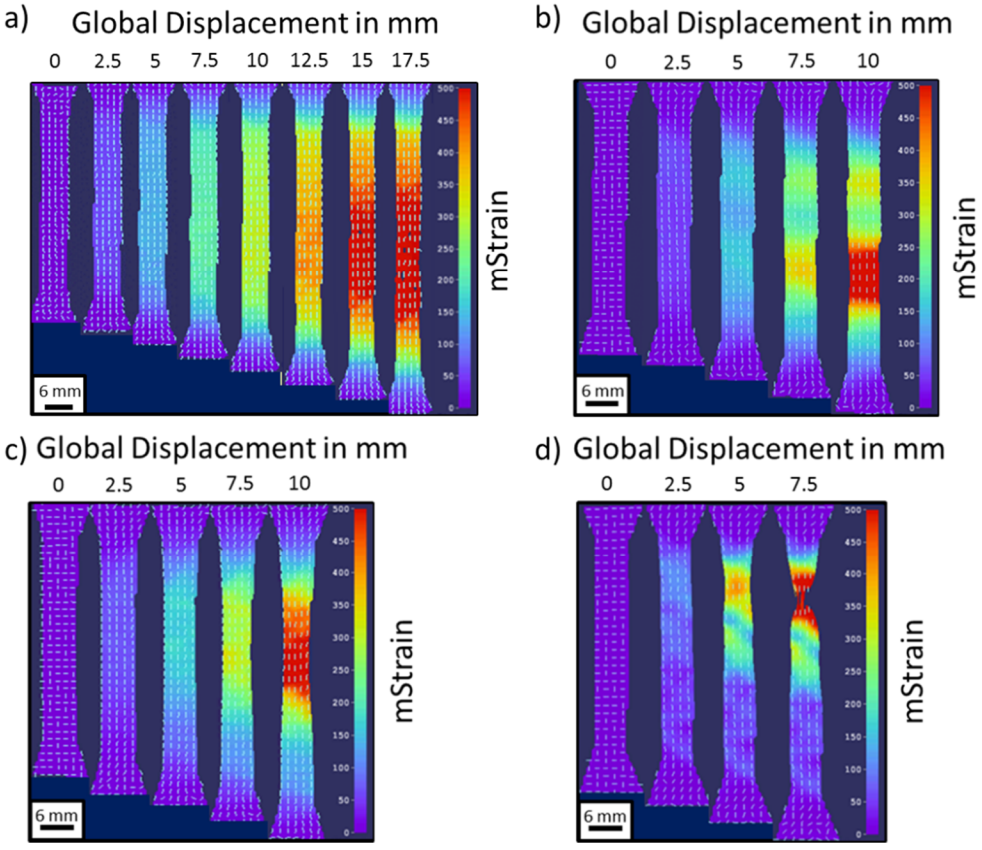

Figure 5.11: Strain maps produced with digital image correlation for (a) substrate, (b) vertical coupon Wall 1, (c) horizontal coupon close to the top of the Wall 2 (Wall2H1) and (d) horizontal coupon close to the bottom of Wall 2 (Wall2H2).

As discussed previously, for fine microstructure the mobility of the grains under uniaxial load is high. The re-orientation and sliding of the grains within the

substrate led to a much more uniform distribution of the strain through the all gauge length. For the vertical specimen from Wall1, the formation of voids happened predominantly within the large grains leading to a high concentration of strain and a much smaller uniform elongation. Furthermore, the fracture and the formation of micro-voids have possibly been enhanced by the presence of the oxide particles forming the bands. As already reported, the coupon in **Figure 5.11c** and **Figure 5.11d** had similar values of yield strength and ultimate tensile strength but a large difference in elongation. The sudden localisation of the strain for the sample Wall2H2 (**Figure 5.11d**) corroborates the explanation reported before for the discrepancies in elongation. It appears that the abrupt strain localisation has been enhanced by a percentage of strain already present before the test for the cyclic straining effect.

5.3.9 Fractography

Figure 5.12 reports the typical surface features found on the fractured surfaces of the coupons used for the tensile tests. The fracture of a specimen from Wall1 is reported in **Figure 5.12a** and **Figure 5.12b**, a specimen from Wall2 in **Figure 5.12c** and **Figure 5.12d** and the fracture of the Substrate specimen in **Figure 5.12e** and **Figure 5.12f**. Parabolic-like (**Figure 5.12b**) and spherical (**Figure 5.12d**) dimples have been found for samples from the walls. In contrast, the analysis of the fractured surface of the substrate (**Figure 5.12e-f**) has not revealed a dominant presence of dimples, unlike for the deposited structures. **Figure 5.12a**, **Figure 5.12c** and **Figure 5.12e** report the all area of the coupon which comprehends the fracture surface and the lateral side from the necking. The coupons from the deposited structures experienced a necking along the only gauge thickness unlike the substrate, which presented necking along both gauge thickness and width. It can be deduced that the grains size of the substrate allowed the grains to slide on each other during the testing leading to a reduction for both gauge thickness and width and the almost absence of micro-voids and dimples.

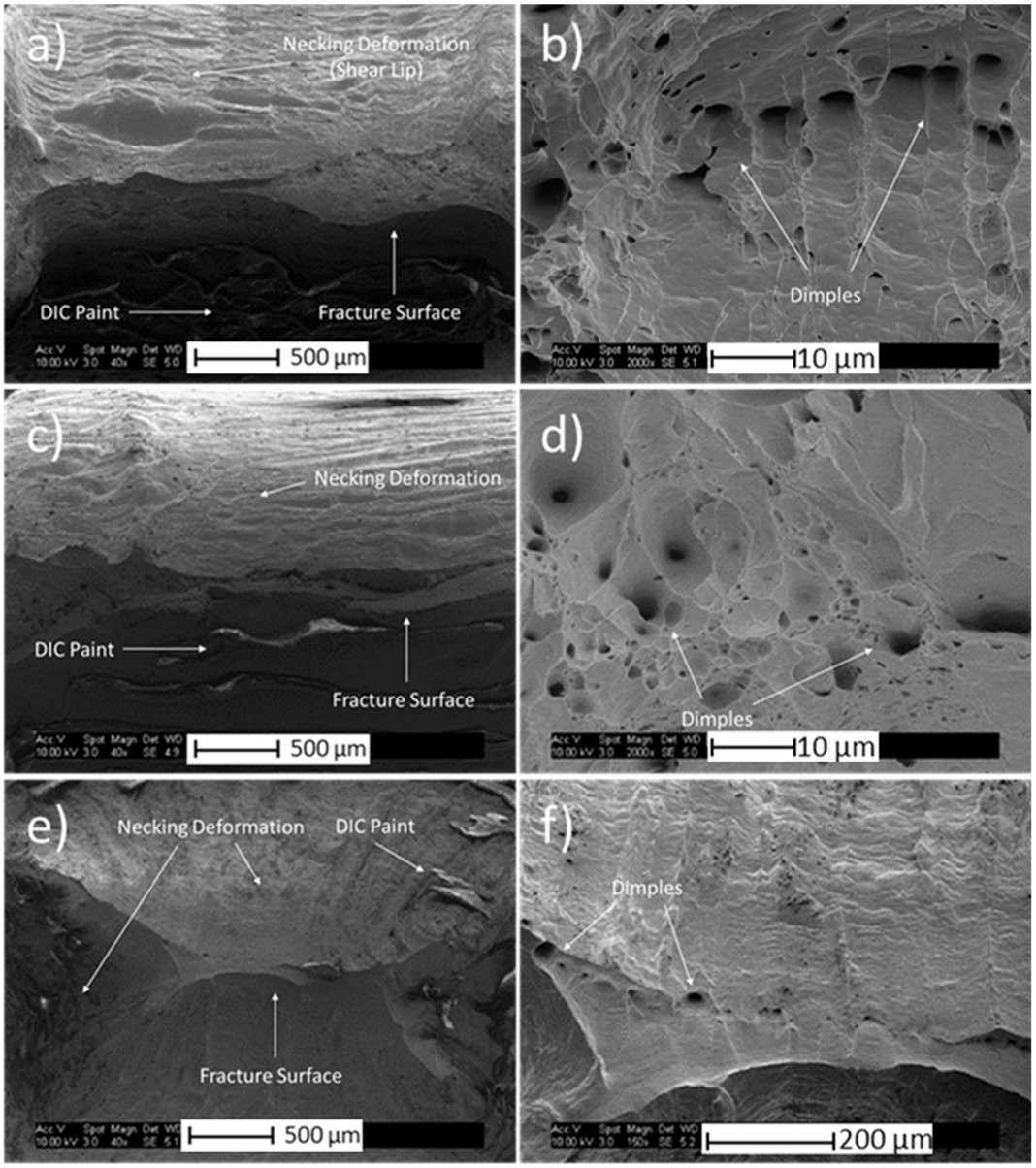

Figure 5.12: Fracture surface of a coupon from Wall 1 (a-b), Wall 2 (c-d) and the substrate (e-f).

5.4 Conclusions

In this research, the Wire + Arc Additive Manufacturing process for tantalum has been studied and proven. The chemistry of two different unalloyed tantalum wires has been correlated to the microstructure, porosity and mechanical properties of the as-deposited structure. The main findings of this study can be summarised as follows:

- The high flowability of unalloyed tantalum, the high ductility and good thermal conductivity gave a high processability via Wire + Arc Additive

Manufacturing. Furthermore, the control of the process parameters has led to the development of a robust deposition process with an average layer height of 1.2 mm and an average layer width of 10.0 mm;

- An anisotropic microstructure has been found for the tantalum deposited via WAAM. Large columnar grains grew epitaxially from the substrate through the entire height of the deposit. The presence of macroscopic bands associated with the deposition of each pass was also observed and associated with small craters caused by the removal of dispersed fine oxide particles;

- The content of oxygen within the two different wires has been found one of the main causes to influence the porosity and the average total hardness. Particularly, a larger content of oxygen led to the development of micron-size porosity and higher hardness values;

- The tensile properties of the deposited walls were comparable to the substrate material, unlike the total elongation. The high yield strength of the walls has been addressed to the material chemistry, in particular, to the content of oxygen. The loss in elongation has mainly been addressed to the shape and size of the grains;

- Thermal straining due to the deposition of the successive layers and so the cyclic thermal cycles have been seen to markedly influence the deposited structures. A cyclic hardening effect has been seen using the hardness profile at the substrate-wall interface. A cyclic plastic strain has also influenced the mechanical properties along the height of the structure for the horizontal samples.

5.5 Bibliography

1. Wong K V., Hernandez A. A Review of Additive Manufacturing. ISRN Mechanical Engineering. 2012; 2012: 1–10. Available at: DOI:10.5402/2012/208760

2. Herderick ED. Progress in Additive Manufacturing. JOM. 2015; 67(3): 580–581. Available at: DOI:10.1007/s11837-015-1323-x

3. Guo N., Leu MC. Additive manufacturing: Technology, applications and research needs. Frontiers of Mechanical Engineering. 2013; 8(3): 215–243. Available at: DOI:10.1007/s11465-013-0248-8

4. Ding D., Pan Z., Cuiuri D., Li H. Wire-feed additive manufacturing of metal components: technologies, developments and future interests. International Journal of Advanced Manufacturing Technology. 2015; 81(1–4): 465–481. Available at: DOI:10.1007/s00170-015-7077-3

5. Williams SW., Martina F., Addison AC., Ding J., Pardal G., Colegrove P. Wire + Arc Additive Manufacturing. Materials Science and Technology. 2016; 32(7): 641–647. Available at: DOI:10.1179/1743284715Y.0000000073

6. Yilmaz O., Ugla AA. Microstructure characterization of SS308LSi components manufactured by GTAW-based additive manufacturing: shaped metal deposition using pulsed current arc. International Journal of Advanced Manufacturing Technology. The International Journal of Advanced Manufacturing Technology; 2017; 89(1–4): 13–25. Available at: DOI:10.1007/s00170-016-9053-y

7. Asala G., Khan AK., Andersson J., Ojo OA. Microstructural Analyses of ATI 718Plus® Produced by Wire-ARC Additive Manufacturing Process. Metallurgical and Materials Transactions A: Physical Metallurgy and Materials Science. Springer US; 2017; 48(9): 4211–4228. Available at: DOI:10.1007/s11661-017-4162-2

8. Wang F., Williams S., Colegrove P., Antonysamy A a. Microstructure and mechanical properties of wire and arc additive manufactured Ti-6Al-4V. Metallurgical and Materials Transactions A: Physical Metallurgy and Materials Science. 2013; 44: 968–977. Available at: DOI:10.1007/s11661-012-1444-6

9. Gu J., Ding J., Williams SW., Gu H., Ma P., Zhai Y. The strengthening effect of inter-layer cold working and post-deposition heat treatment on the additively manufactured Al– 6.3Cu alloy. Journal of Materials Processing Technology. Elsevier; 2016; 230: 26–34. Available at: DOI:10.1016/j.jmatprotec.2015.11.006

10. Lockett H., Ding J., Williams S., Martina F. Design for Wire + Arc Additive Manufacture: design rules and build orientation selection. Journal of Engineering Design. 2017; 4828(December): 1–31. Available at: DOI:10.1080/09544828.2017.1365826

11. Cardonne SM., Kumar P., Michaluk CA., Schwartz HD. Tantalum and its alloys. International Journal of Refractory Metals and Hard Materials. 1995; 13(4). Available at: DOI:10.1016/0263-4368(95)94023-R

12. Köck W., Paschen P. Tantalum-processing, properties and applications. Jom. 1989; 41(10): 33–39. Available at: DOI:10.1007/BF03220360

13. Buckman RW. New Applications for Tantalum and Tantalum Alloys. Jom. 2000; (March): 40–41. Available at: DOI:10.1007/s11837-000-0100-6

14. Bechtold J. Tensile properties of annealed tantalum at low temperatures. Acta

Metallurgica. 1955; 3: 249–254. Available at: DOI:10.1016/0001-6160(55)90060-2

15. Kim Y., Lee D., Hwang J., Ryu HJ., Hong SH. Fabrication and characterization of powder metallurgy tantalum components prepared by high compaction pressure technique. Materials Characterization. Elsevier Inc.; 2016; 114: 225–233. Available at: DOI:10.1016/j.matchar.2016.03.005
16. Zhou L., Yuan T., Li R., Tang J., Wang G., Guo K. Selective laser melting of pure tantalum: Densification, microstructure and mechanical behaviors. Materials Science and Engineering A. 2017; 707(September): 443–451. Available at: DOI:10.1016/j.msea.2017.09.083
17. Puhr-Westerheide J., Elssner G. On the solid solution hardening of tantalum by nitrogen and oxygen. Journal of The Less-Common Metals. 1970; 20(4): 371–374. Available at: DOI:10.1016/0022-5088(70)90013-5
18. Thijs L., Montero Sistiaga ML., Wauthle R., Xie Q., Kruth JP., Van Humbeeck J. Strong morphological and crystallographic texture and resulting yield strength anisotropy in selective laser melted tantalum. Acta Materialia. Acta Materialia Inc.; 2013; 61(12): 4657–4668. Available at: DOI:10.1016/j.actamat.2013.04.036
19. Balla VK., Banerjee S., Bose S., Bandyopadhyay A. Direct laser processing of a tantalum coating on titanium for bone replacement structures. Acta Biomaterialia. Acta Materialia Inc.; 2010; 6(6): 2329–2334. Available at: DOI:10.1016/j.actbio.2009.11.021
20. Wauthle R., Van Der Stok J., Yavari SA., Van Humbeeck J., Kruth JP., Zadpoor AA., et al. Additively manufactured porous tantalum implants. Acta Biomaterialia. Acta Materialia Inc.; 2015; 14: 217–225. Available at: DOI:10.1016/j.actbio.2014.12.003
21. Nemat-Nasser S., J. B. Isaacs., M. Liu. Microstructure of high-Strain, High-Strain-Rate Deformed Tantalum. Acta Materialia. 1998; 46(4): 1307–1325.
22. Martina F., Mehnen J., Williams SW., Colegrove P., Wang F. Investigation of the benefits of plasma deposition for the additive layer manufacture of Ti-6Al-4V. Journal of Materials Processing Technology. Elsevier B.V.; 2012; 212(6): 1377–1386. Available at: DOI:10.1016/j.jmatprotec.2012.02.002
23. Brandl E., Baufeld B., Leyens C., Gault R. Additive manufactured Ti-6A1-4V using welding wire: Comparison of laser and arc beam deposition and evaluation with respect to aerospace material specifications. Physics Procedia. 2010; 5(PART 2): 595–606. Available at: DOI:10.1016/j.phpro.2010.08.087
24. Efe M., Kim HJ., Chandrasekar S., Trumble KP. The chemical state and control of oxygen in powder metallurgy tantalum. Materials Science and Engineering A. Elsevier B.V.; 2012; 544: 1–9. Available at: DOI:10.1016/j.msea.2012.01.100
25. Jehn H., Olzi E. High temperature solid-solubility and phase studies in the system tantalum-oxygen. Journal of The Less-Common Metals. 1971; 27(1972): 297–309.
26. Stecura S. Observation of oxide particles below the apparent oxygen solubility

limit in tantalum. Metallurgical Transactions. 1974; 5(6): 1337–1340. Available at: DOI:10.1007/BF02646617

27. Garg SP., Krishnamurthy N., Awasthi A., Venkatraman M. The O-Ta (Oxygen-Tantalum) system. Journal of Phase Equilibria. 1996; 18(1): 63–77. Available at: DOI:10.1007/s11669-997-0076-9

28. Spitzig W a., Owen C V., Scott TE. Effects of Oxygen on the mechanical behavior of hydrogenated V, Nb, and Ta. Metallurgical Transactions A. 1986; 17(3): 527–535. Available at: DOI:10.1007/BF02643960

29. Papakyriacou M., Mayer H., Plenk H., Stanzl-Tschegg S. Cyclic plastic deformation of tantalum and niobium at very high numbers of cycles. Materials Science and Engineering A. 2002; 325(1–2): 520–524. Available at: DOI:10.1016/S0921-5093(01)01446-0

30. Mughrabi H. The cyclic hardening and saturation behaviour of copper single crystals. Materials Science and Engineering. 1978; 33(2): 207–223. Available at: DOI:10.1016/0025-5416(78)90174-X

31. Quinta da Fonseca J., Preuss M., Ryan P., Withers PJ., Quinta da Fonseca J. Ryan P. , Withers P.J. PM. Mechanical Property Mapping using Image Correlation and Electronic Speckle Interferometry. Applied Mechanics and Materials. 2004; 1–2: 147–152. Available at: DOI:10.4028/www.scientific.net/AMM.1-2.147

32. Kim Y., Kim E-P., Noh J-W., Lee SH., Kwon Y-S., Oh IS. Fabrication and mechanical properties of powder metallurgy tantalum prepared by hot isostatic pressing. International Journal of Refractory Metals and Hard Materials. Elsevier Ltd; 2015; 48: 211–216. Available at: DOI:10.1016/j.ijrmhm.2014.09.012

33. Tang Y., Bringa EM., Meyers MA. Inverse Hall-Petch relationship in nanocrystalline tantalum. Materials Science and Engineering A. Elsevier; 2013; 580: 414–426. Available at: DOI:10.1016/j.msea.2013.05.024

34. Jarmakani HN., Bringa EM., Erhart P., Remington BA., Wang YM., Vo NQ., et al. Molecular dynamics simulations of shock compression of nickel: From monocrystals to nanocrystals. Acta Materialia. Acta Materialia Inc.; 2008; 56(19): 5584–5604. Available at: DOI:10.1016/j.actamat.2008.07.052

35. Baufeld B., Van Der Biest O., Gault R. Microstructure of Ti-6Al-4V specimens produced by shaped metal deposition. International Journal of Materials Research. 2009; 100(11): 1536–1542. Available at: DOI:10.3139/146.110217

Chapter 6

Paper E

"Grain refinement in unalloyed tantalum structure deposited using Wire + Arc Additive Manufacture and vertical cold rolling"

G. Marinelli*, [a], F. Martina*, S. Ganguly*, S. Williams*, G. Shrimpton**, T. Rogers**

*Welding Engineering and Laser Processing Centre (WELPC), Cranfield University, Cranfield, MK43 0AL, United Kingdom

**AWE Aldermaston, Reading, Berkshire, RG7 4PR, United Kingdom

Abstract

Components manufactured via Wire + Arc Additive Manufacturing are usually characterised by large columnar grains. Vertical cold rolling is a known technique used to induce local plastic deformations which can lead to a reduction of distortion, reduction of residual stresses and refinement of the microstructure in additively manufactured parts. The refinement usually occurs with the subsequent layer deposition, which is used as heat treatment. Inter-pass rolling was applied with a load of 50 kN to a tantalum linear structure to understand its effectiveness in refining the grains structure, obtaining a transition from columnar to equiaxed grains. An average grain size of 650 μm has been obtained after five cycles of rolling and deposition. When the rolled layer was reheated during the subsequent deposition, recrystallisation occurred leading to the growth of new strain-free fine equiaxed grains. The depth of the refined region has been characterised and correlated to the hardness profile developed after rolling. A reduction of porosity was also registered. Furthermore, a random texture was formed after rolling, which would result in generating isotropic mechanical properties. Wire + Arc Additive Manufacturing process demonstrated the ability to deposit sound refractory metal components and the possibility to improve the microstructure when coupled with cold inter-pass rolling.

6.1 Introduction

One of the most promising manufacturing technologies is Additive Manufacturing (AM) [1,2]. Three-dimensional structures can be promptly deposited starting from 3D-model designs using a layer-by-layer approach [3]. The practical advantages are the cost reduction, freedom of design and engineered mechanical properties [3]. Numerous rewarding researches have already reported the potential of the AM of metallic materials, some of them are summarised in [4].

Wire-feed technologies are emerging among the vast AM technologies mainly because of their ability to produce large-scale components [5]. Wire + Arc additive Manufacture (WAAM) is a novel AM process which employs an electric arc as the heat source and high-quality metal wire as the feedstock [6]. WAAM can directly fabricate fully-dense large 3-D near-net-shape components with a much higher deposition rate, in the order of several kg/h, than most other metal additive manufacture processes [5,6]. The WAAM process has been demonstrated to successfully produce large-scale parts in stainless steel [7], Inconel [8], titanium [9] and aluminium [10] achieving even complex geometries of deposition. WAAM is considered to be a technique suitable for the manufacture of large and engineered components because of its high deposition rate, relatively low cost and its potential disruptive capability in bringing significant changes in the design philosophy [6,11].

Tantalum represents one of the most promising materials for high-temperature applications due to its high melting point and its inertness at high temperatures [12]. The stable oxide layer that immediately covers tantalum components is the main reason for its chemical stability against corrosion [13]. Furthermore, tantalum is characterised by a large ductility at room temperature unlike other refractory metals as tungsten and molybdenum [14,15]. These peculiar properties made tantalum a great candidate for the production of components for the aerospace sector as well as the defence, the electronics and chemical industry sector [12,14,16].

A few studies have been reported with regards to the development of an additive manufacturing process for unalloyed tantalum, mainly employing a laser

as the heat source and tantalum powder as the feedstock. Selective laser melting (SLM) has been used by Zhou et al. [17] to produce one of the first additively manufactured structures of unalloyed tantalum. In the work of Thijs et al. [18], the SLM process was studied for unalloyed tantalum focusing mainly on the microstructural evolution and mechanical properties. Furthermore, tantalum coating has been successfully deposited on titanium using engineered net shaping (LENS) in order to produce controlled porous components with enhanced bio-properties [19]. A further study on porous tantalum parts is reported in the study of Wauthle et al. [20], in which SLM was used effectively to produce porous tantalum implants with fully-interconnected open pores.

Most of the metallic materials processed using an additive manufacturing technique present unique microstructural features that can lead to marked anisotropy, such as the formation of columnar grains [3]. Different researchers have reported a clear connection between the columnar grain structure and the anisotropy of mechanical properties [18,21]. Usually, when the processing speed is relatively low or the thermal conductivity of the material is relatively low, the solidification of the weld pool slows down [22]. In such case, long columnar grains form because of a positive thermal gradient is seen at the solidification front and an epitaxial growth onto the partially-melted grains of the previous layer occurs [22]. For most alloys and AM processes, this is the preferred and predominant mode of solidification.

Evolution of columnar grains was regularly seen for Ti-6Al-4V when processed using directed energy deposition (DED) [23], electron beam melting (EBM) [24] and WAAM [9]. Large columnar grains were also observed for the deposition of graded structures between iron and aluminium using WAAM [25]. In the work of Thij et al. [18], epitaxial grain growth through the layers was observed in SLM of tantalum components. This led to the formation of large columnar grains with the development of a strong texture and a marked anisotropy with regards to the yield strength. The presence of the epitaxially-grown columnar grains has also been observed for nickel-based superalloys [26,27].

The refinement of the microstructure of AM as-deposited materials can be achieved through modification of the solidification regime or altering the alloy chemistry with the addition of specific elements [28]. These methods are not suitable when the stability of the process must be controlled constantly, and the purity of the alloys used must be preserved. The operative process window may need continuous modifications to keep the intrinsic variables, which control the final product properties, constant. The addition of further elements for grain refining can also enhance the segregation and the formation of brittle second phases, which would lead to detrimental effect.

However, refining can be obtained using successive steps of high-level deformation and successive heat treatment at controlled temperatures [21]. For tantalum components, investigations regarding the effect of rolling, high-pressure torsion and equal-channel angular pressing on the microstructural refinement have already been reported [29–33]. In particular, ultrafine and nanostructured tantalum components can be produced by applying severe plastic deformation steps to conventional coarse-grained metals achieving from micron- to nanometre-size grains [31,34].

The effectiveness of cold working coupled with the additive manufacturing deposition has been already proven. In particular, cold rolling has been used for Ti-6Al-4V for the improvement of the large columnar β-phase microstructure and decrease the strong texture typically seen after deposition using wire-based AM processes [21]. With the application of cold rolling, small deformation steps are introduced between the deposition process leading to an induced refining due to the combination of the rolling strain and thermal energy from the successive deposition [21].

The properties of a metal at room temperature are usually influenced by the grain size and shape. Thus, the achievement of a fine equiaxed microstructure with, possibly, the random texture is vital for some application of tantalum. If tantalum is used as structural material for high-temperature applications, small grain size and isotropy in mechanical properties would be needed in order to achieve the optimal performances. If tantalum is used as a sputtering target, a

strong texture would lead to an inconsistent erosion rate through the surface of the target [35,36].

In this paper, the eventual refinement of the microstructure of tantalum linear structures has been investigated. In, particular, the aim of the study was to verify whether sufficient plastic strain could be induced by inter-pass rolling and reformation of the deformed grains occur during successive deposition. The impact of the rolling load on the depth of refining and grain size has been evaluated and correlated with different hardness profiles of the structures. The influence of the recrystallisation on the crystallographic texture developed was also characterised.

6.2 Experimental Procedure

Unalloyed tantalum wire with a diameter of 1.2 mm was used for the Wire + Arc Additive Manufacturing process. Cold-rolled tantalum plate with dimensions of 210 x 50 x 4 mm was used for the deposition of the linear structure. The surface of the plate was ground and rinsed with acetone prior to deposition in order to remove most of the contaminants. The composition of the materials used and of the linear structure deposited is shown reported in **Table 6.1**.

	W	Mo	Ta	Ti	V	Cr	Fe	C	N	O	K
Substrate	<0.05	<0.05	99.99	<0.05	<0.05	<0.05	<0.05	33 ppm	<10 ppm	60 ppm	<10 ppm
Wire	<0.05	<0.05	99.98	<0.05	<0.05	<0.05	<0.05	36 ppm	11 ppm	190 ppm	<10 ppm
Wall	<0.05	<0.05	99.97	<0.05	<0.05	<0.05	<0.05	48 ppm	13 ppm	226 ppm	<10 ppm

Table 6.1: Elemental composition (wt%) of tantalum substrate, wire and wall used in this study.

Figure 6.1 shows the layout of the apparatus used for the deposition. The principal axes of coordinates have been kept constant for all the schematics reported. In particular, the Z-axis was oriented parallel to the building direction, the Y-axis parallel to the deposition direction and the X-axis parallel to the substrate width. A conventional tungsten inert gas (TIG) welding torch, a power supply and a controlled wire feeder were used for the deposition. The heat source,

the wire delivery system and the substrate were attached to three linear motorized high-load stages assembled in XYZ configuration.

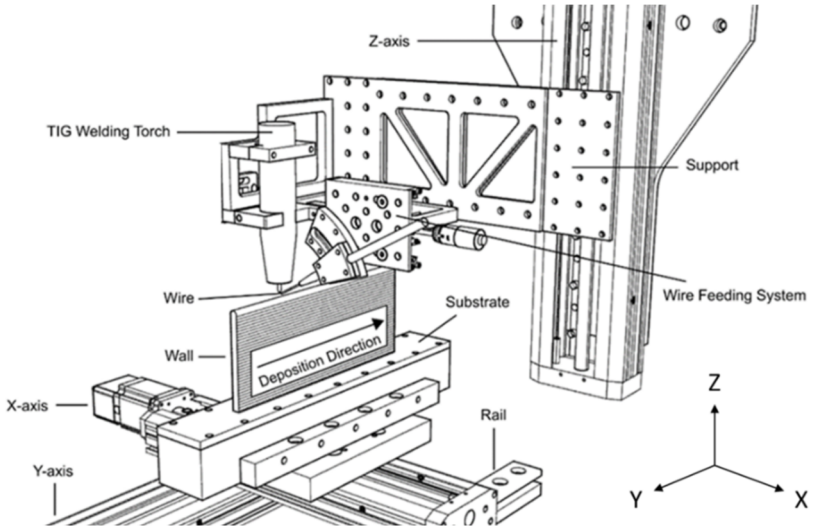

Figure 6.1: Set-up used for the deposition of unalloyed tantalum using the WAAM process.

The direction of deposition was always kept constant for each successive layer and the wire was fed from the side of the weld pool. The apparatus was surrounded by a heavy-duty enclosure used to ensure a low level of oxygen when purged with high-purity argon. The linear structure was produced using the parameters shown in **Table 6.2.** TS refers to the travel speed and WFS to the wire feed speed.

TS [mm/s]	WFS [mm/s]	I [A]	Electrode-workpiece Distance [mm]	Electrode angle [°]	Electrode Diameter [mm]	Shielding gas composition [%]	Gas flow rate [L/min]	Oxygen Atmosphere [ppm]
4	40	300	3.5	45	3.6	100 He	15	≈100

Table 6.2: WAAM process parameters used for the deposition of unalloyed tantalum.

For the application of inter-layer cold working, a rolling rig was used to load and move the roller at a constant travel speed onto the structure deposited. A schematic diagram of the rolling equipment is shown in **Figure 6.2.** The actual force applied by the roller was calibrated with a load cell before the experiments. The roller was lowered until it touched the sample and, as the load was built up, moved onto the desired part of the structure. Every rolling step has been

conducted when the material was cooled down to room temperature. The main rolling parameters are reported in **Table 6.3.**

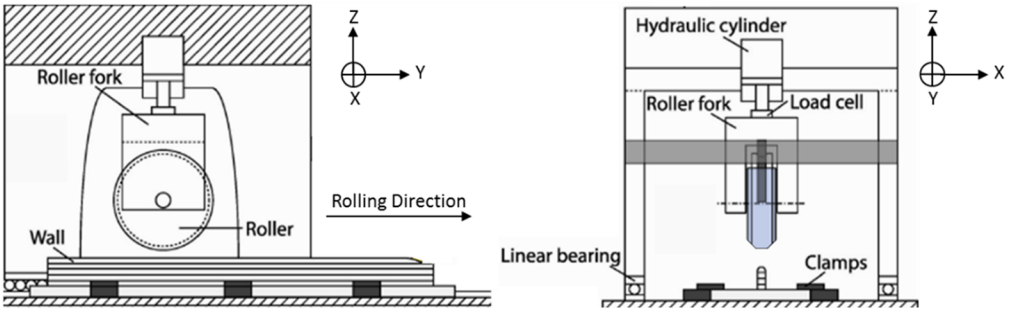

Figure 6.2: Schematic of the rolling rig used for the application of cold working between each successive layer.

Load [kN]	Roller Diameter [mm]	Rolling Speed [mm/s]	Rolling Temperature
50	100	10	RT

Table 6.3: Rolling parameters used for this study.

The structure was deposited within an inert atmospheric chamber and then placed on the rolling rig after the deposition of each layer, in order to perform the cold rolling step. The deposition of the next layer started inside the atmospheric chamber only after the oxygen content was below 100 ppm. These two set-ups were used as two separate machines because of the difficulties related to the building of an inert atmosphere chamber around the entire rolling rig keeping the low level of oxygen and, also, avoiding any contamination from the oil of the hydraulic system. The substrate and the wall were always kept clamped for the all process of deposition and rolling and they were unclamped only after the deposition of the last layer, which was not rolled. A straight wall was produced with the dimensions of 190 mm in length. All the samples analysed within this study were extracted from the same build.

The location and the manufacturing route for each sample are shown in **Figure 6.3.** Four main samples were produced using a different combination of deposition and rolling. The sample called 1R was manufactured only after the deposition of fifteen layers of unalloyed tantalum without the application of any rolling steps. The sample 2R was extracted from the portion of the wall that was normally deposited for fifteen layers and just rolled once. The sample 3R had the same history of samples 2R but with an additional single layer deposited on top,

right after rolling. The sample 4R was produced with fifteen layers of the deposited structure without rolling plus five layers between which inter-pass rolling was applied. The regions from which sample 1R, sample 2R and sample 3R were extracted were 40 mm long and the sample 4R was extracted from the remaining 70-mm-long structure. The structure was produced gradually decreasing the deposition and the rolling path length.

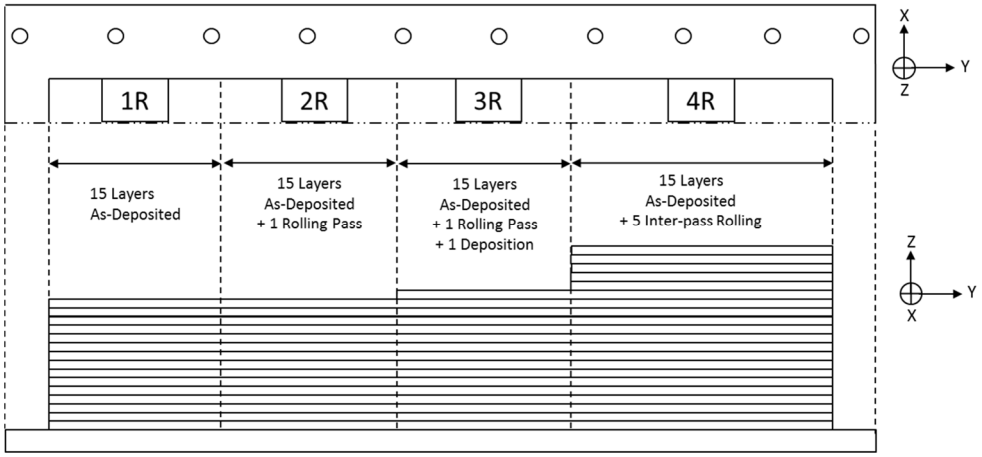

Figure 6.3: Schematic of the manufacturing route used to produce each sample analysed. The name of the samples extracted per each region is also reported.

The four samples from the structure were characterised for porosity, hardness, grain size and texture. The microstructure was examined using the cross-section perpendicular to the deposition direction. The samples were polished using the procedure in **Table 6.4**. The composition of the etchant used for this investigation was under nondisclosure agreement being proprietary of H.C. Starck. The presence and distribution of porosity were characterised before etching. Vickers hardness contour maps were produced using the measurements collected using an automatic hardness testing machine. The main parameters for the hardness acquisition were 500g load and 10 seconds dwell time for each testing point.

Grinding and Polishing means	Time [min]
SiC Paper 240 grid	2
SiC Paper 1200 grid	6
SiC Paper 2500 grid	6
Alpha alumina 0.3 μm suspension	15
Alumina and silica 0.05 μm suspension	15
Colloidal silica 0.02 μm suspension	15

Table 6.4: Grinding and polishing procedures used for the microstructural preparation.

Several line-scans with 1 mm spacing were performed through the height and width of each portion of the wall in order to obtain the relative contour maps. The microstructure of the sample 4R was characterised by using a scanning electron microscope (SEM) operating at 20 kV electron beam power. In particular, the grain size and grain orientation were measured using an electron backscatter diffraction (EBSD) detector within the SEM. Polar contour maps were used to analyse the texture of the local microstructure. The sample 4R was chosen as it was the sample that showed the most evident contrast in microstructure within the same build. The root and the top of the samples were measured to understand the variations within the microstructure.

6.3 Results

6.3.1 Contour profiles

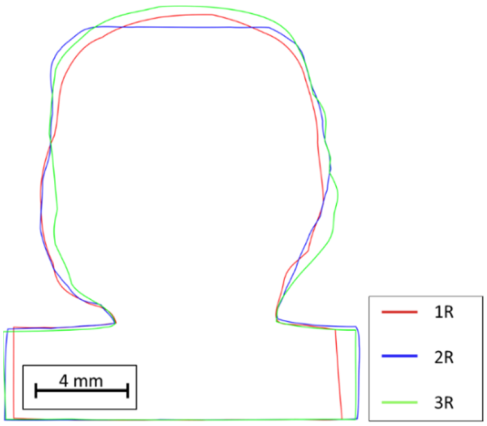

Figure 6.4: Overlap of the total contour of the cross-section of sample 1R, 2R and 3R.

Figure 6.4 shows the overlap of the cross-sectional contour profiles for the sample 1R with fifteen as-deposited layers (red), the sample 2R with fifteen as-deposited layers plus one rolling pass on top (blue) and the sample 3R with fifteen as-deposited layers plus one rolling pass and one deposited layer on top (green). It can be clearly seen that rolling with the load of 50 kN had a great effect on deforming the upper part of the sample 1R both in vertical and lateral direction. The variation in the total height and width due to the rolling was measured using the main dimensions of sample 1R and 2R. The noise in the dimensional data associated with the deposition process and the surface roughness of the structure was reduced by averaging four measurements along the same samples for both the

height and width. The total height reduced from 14.6 mm of sample 1R to 14.0 mm of sample 2R with a reduction of 0.6 mm. The total width increased from 10.0 mm in sample 1R to 11.0 mm of sample 2R, with an increment of 1.0 mm. When a further layer was deposited (sample 3R), the total width remained almost constant, with only an increment in the total height by 0.95 mm.

6.3.2 Microstructure

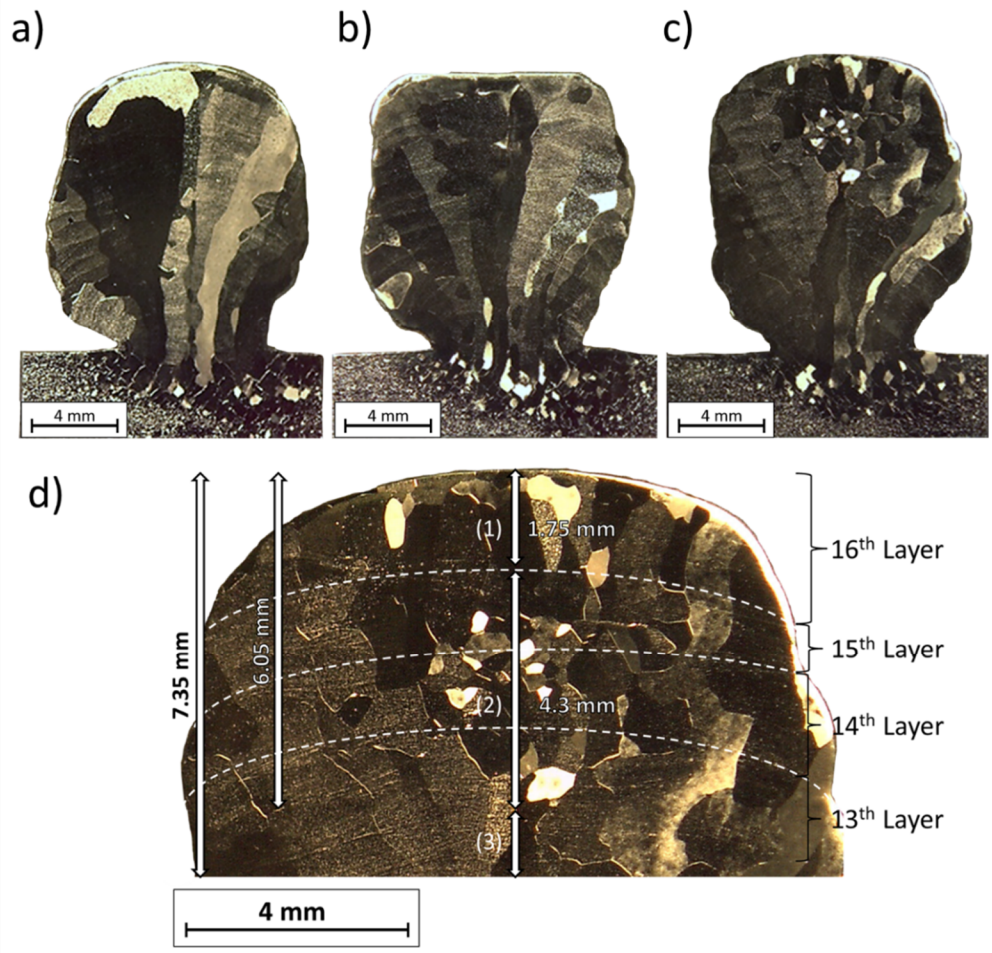

Figure 6.5: Optical micrograph images of sample 1R (a), 2R (b) and 3R (c). High magnification of the recrystallised top part of sample 3R (d).

The microstructure of the three samples as called 1R, 2R and 3R are reported in **Figure 6.5a**, **Figure 6.5b** and **Figure 6.5c** respectively. All the samples produced presented a smaller total width near the baseplate due to a transient heat flow condition, which stabilised for the upper layers as reflected in the almost consistent total width. The sample 1R (**Figure 6.5a**) demonstrated large columnar grains, which grew epitaxially from the base plate toward the top of the sample

parallel to the building direction. It can be reported that the dendrites were in average 1.0 mm wide and extended from the base plate to the top of the deposit. The size and the morphology of the grains appeared to be almost identical for the sample 2R as the only rolling pass just flattened the upper surface, plastically deforming the structure (**Figure 6.5b**). The sample 3R (**Figure 6.5c**) presented a significant reduction of the grain size and a change in morphology localised to the upper region. It can be indicated that the majority of the refined equiaxed grains had a grain size between 250 μm and 350 μm, unlike few larger grains which were found to have a size between 600 μm and 850 μm.

Figure 6.5d shows a higher magnification micrograph of the refined region of sample 3R. The borderline indicated in **Figure 6.5d** were individuated following the geometrical features of the outer surfaces. The last four layers were chosen to illustrate the depth and the width of the refined region. In particular, the top 7.35 mm of the structure were reported, and three different zones of the microstructure can be distinguished: the last deposited layer (1) which is in the as-deposited conditions, the refined region (2) and the layers (3) where was not visible the effect of rolling. Near the top of the structure, fine columnar grains were found to compose the microstructure of the last deposited layer, growing epitaxially onto the refined grains. The refined region extended from 1.75 mm in depth until 6.05 mm in depth, which protracted across three layers below the last one (from the fifteenth to the thirteenth layer) and was localised at the middle of the structure. From 6.05 mm in depth until the baseplate, large columnar grains were left unchanged, typical of the as-deposited material.

The microstructural features of the sample 4R have been reported in **Figure 6.6**. The sample 4R represents the evolution of sample 3R as it was produced coupling fifteen as-deposited layers and, on top of them, five additional inter-pass rolled layers leaving the last layer unrolled (sample 3R + four inter-pass layers). **Figure 6.6a** shows the global microstructure of the sample 4R pointing out the marked change in microstructure for the upper layers. The boundaries of each layer were not clear due to the considerable lateral and vertical deformation occurred during the inter-pass rolling. This also resulted in an average larger

width for the upper layers. The large columnar grains typical of the as-deposited condition extended from the substrate until 7.25 mm in height.

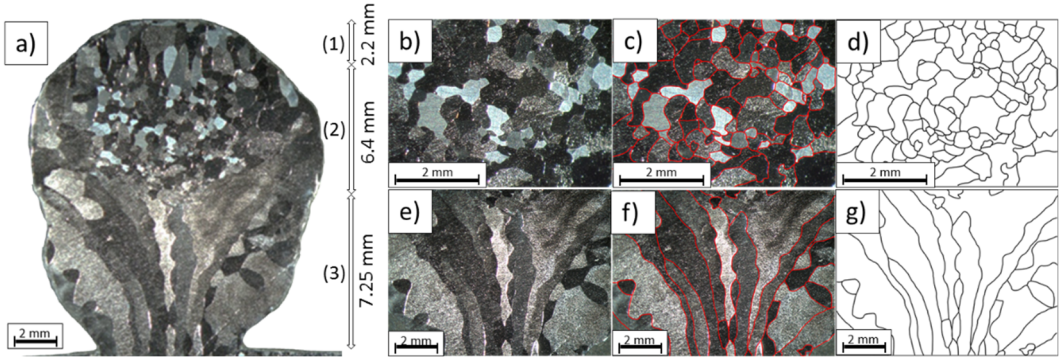

Figure 6.6: Optical micrograph of sample 4R (a). Detail of the microstructure from the recrystallised zone (b) with highlighted grain boundaries (c) and schematisation (d). Detail of the microstructure from the columnar as-deposited region (e) with highlighted grain boundaries (f) and schematisation (g).

The refined region extended for around 6.4 mm in height and it had a total width of around 7.6 mm. The average grain size has been measured according to standard ASTM E112-96 (2004) and resulted to be around 650 μm. The top 2.2 mm presented a typical microstructure of the as-deposited layer without any rolling after deposition, similar to the top of sample 3R. The images reported from **Figure 6.6b** to **Figure 6.6g** reports details of the microstructure of the refined region and columnar region. It is important to note the change in scale. These figures have been used to highlight the grain boundaries and report a schematisation of the structure in order to have a much more comprehensible perception of the grain structures analysed.

6.3.3 Porosity and deformation bands

Figure 6.7 reports the optical images of the polished surface for samples 1R, 2R and 3R focusing the attention on the presence of porosity within the samples. **Figure 6.7a** shows some micron-size pores in sample 1R. A similar distribution of porosities was found in sample 2R near the top and bottom of the structure (**Figure 6.7b** and **Figure 6.7c**). In the upper part of samples 2R, some pores resulted to be elongated due to the rolling (**Figure 6.8a**). **Figure 6.7e** shows the porosity found in the bottom part of sample 3R and it resulted to be similar to sample 1R and sample 2R. **Figure 6.7d** reports, in particular, the boundary

between the 16th layer as deposited and the 15th layer of sample 3R, which has been deposited, rolled and refined. It is clear that the refined region had smaller and fewer pores that the last as-deposited layer, which was characterised by the presence of larger porosity as for samples 1R and 2R.

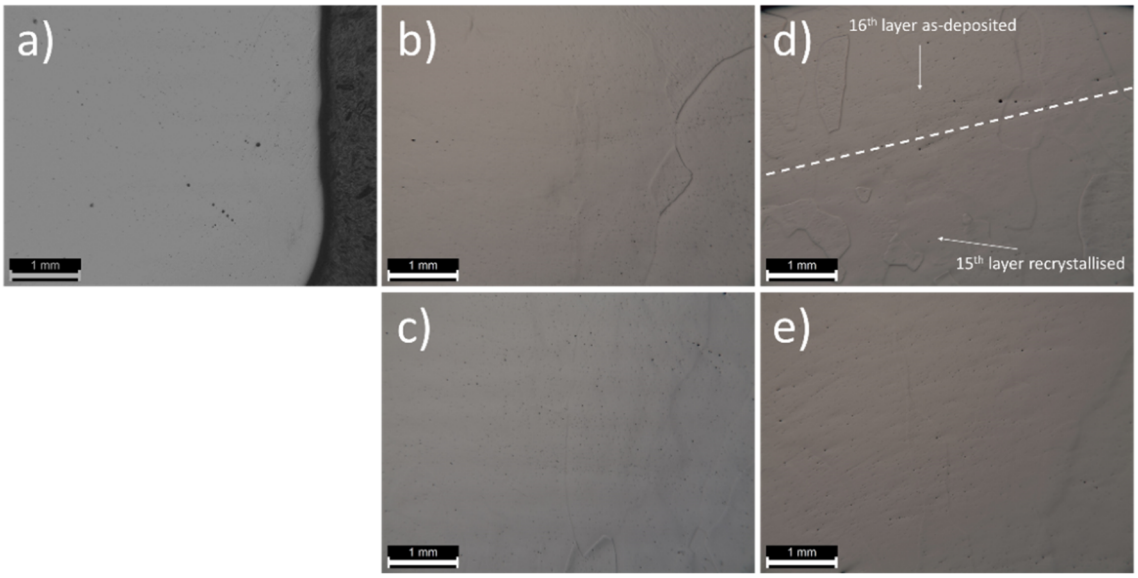

Figure 6.7: Polished cross-sections showing the porosity within the sample 1R (a), the top of the sample 2R (b), the bottom of the sample 2R (c), the top of the sample 3R (d) and the bottom of the sample 3R (e).

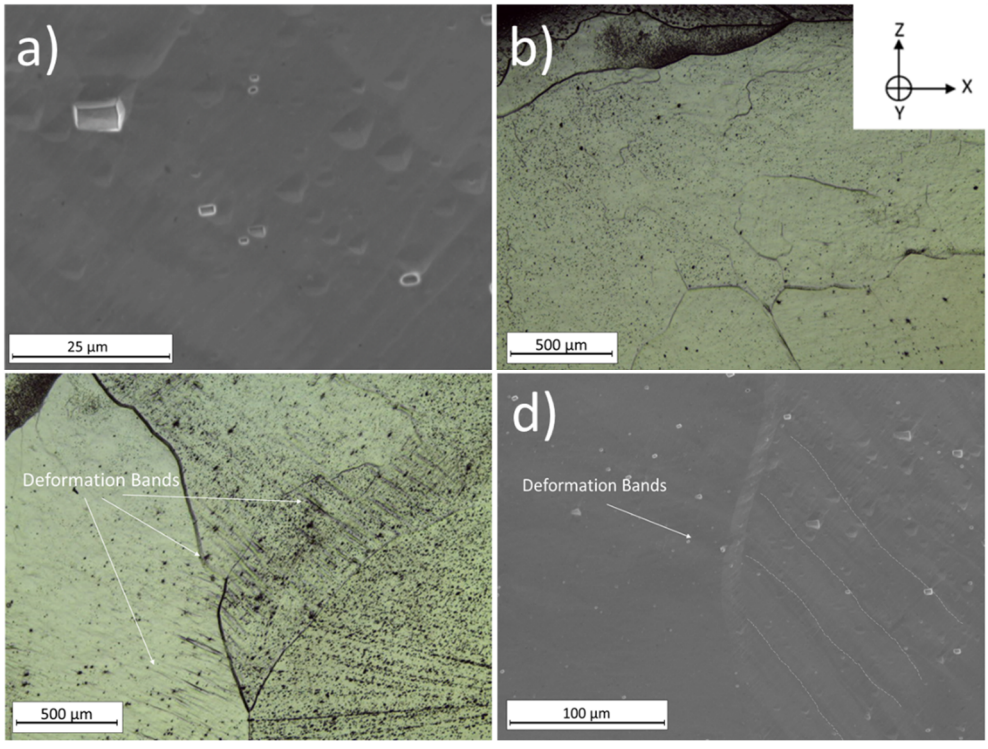

Figure 6.8: Flattened pores found at the top of the sample 2R (a); Microscopic bands across grains in sample 2R (b-d).

Figure 6.8b, **Figure 6.8c** and **Figure 6.8d** show some distinctive features found on the surface of sample 2R within the same grain and across multiple grains. In particular, in **Figure 6.8c** and **Figure 6.8d** is shown an unusual banding seen across some grain boundaries. Each line of the bands was pointing in the direction of around 30° to 45° compared to the Z-axis. These deformation bands were associated with the high degree of lateral deformation.

6.3.4 Hardness

The hardness contour maps for the three fundamental samples (sample 1R, sample 2R and sample 3R) were constructed from the Vickers hardness measurements in order to visualise the strain localisation and its magnitude due to the rolling (**Figure 6.9).** A scale between 100 Hv and 210 Hv was used for all the samples to facilitate the comparison. The lower and the upper limits in the scale have been chosen considering the hardness of the as-deposited material and the maximum value of hardness found. The fundamental unit of the X-axis and the Y-axis is reported to be equal to 1 mm. The origin of the X-axis has been placed at the width centerline of each sample, while the origin of the Y-axis has been set at the top for each sample.

Figure 6.9a reports the hardness distribution for the sample 1R, which represents the control as-deposited material. The hardness was found to be consistent with small fluctuation around a mean value of 114 Hv across the width and height**. Figure 6.9b** reports the hardness map for the sample 2R, after the single rolling pass. The impact of rolling on the hardness values and distribution can be clearly seen.

The application of the load increased the hardness of the whole structure up to 10.0 mm in depth from the top. A predominant high-hardness region developed from 1.0 mm to 6.5 mm in depth and its width was around 4.0mm. The hardness almost doubled reaching the value of 205 Hv at its peak. **Figure 6.9c** shows the hardness distribution of the sample 3R. The overall hardness of the structure was reduced compared to the rolled structure. From the top up to a depth of 1.75 mm, the hardness reduced and returned similar to the average hardness of 1R, the as-deposited material. The region between 1.75 mm and 6.0

mm in depth is characterised by slightly higher average hardness around 118 Hv. The lower region going from 6.0 mm to 9.0 mm in depth was characterised by the highest hardness with an average hardness of 125 Hv.

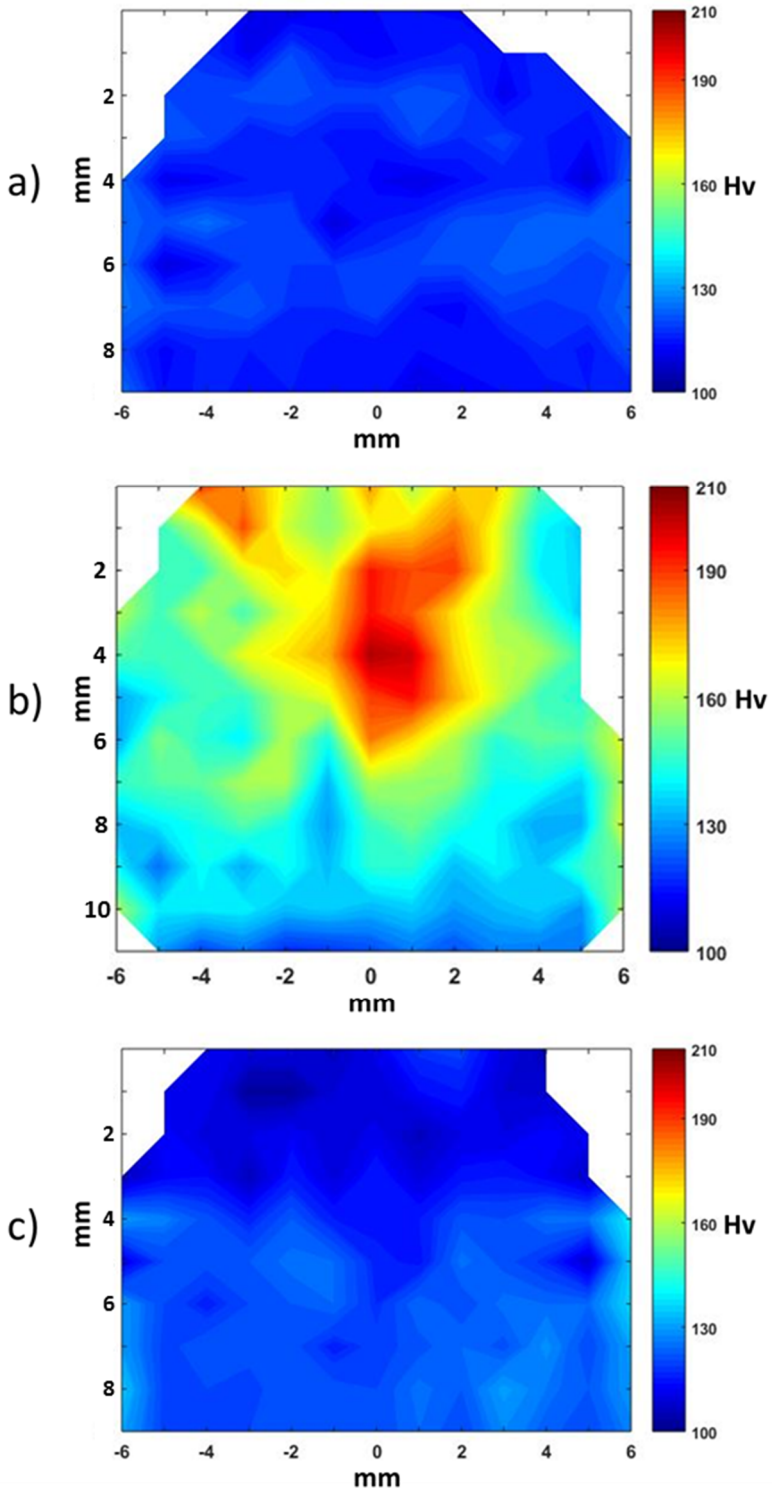

Figure 6.9: Contour maps relative to the Vickers hardness measurements for sample 1R (a), 2R (b) and 3R (c).

6.3.5 Texture

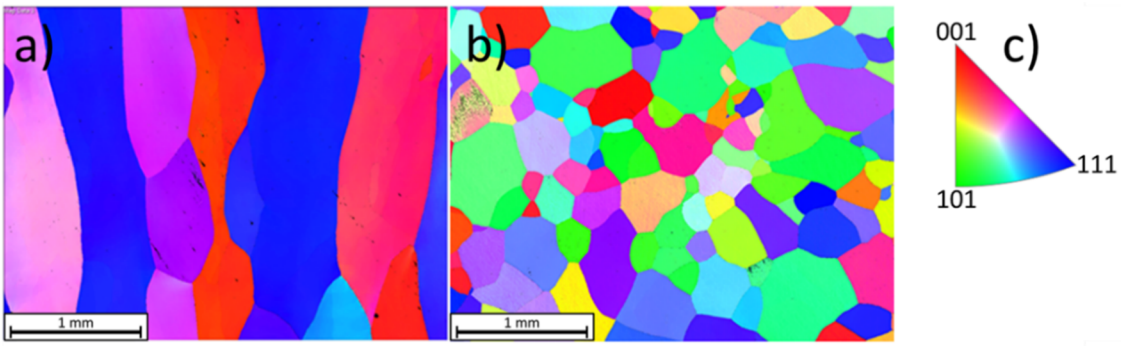

Figure 6.10: EBSD images of the columnar as-deposited region (a) and the recrystallised grains (b) of sample 4R. Legend with regards to colour and orientation (c).

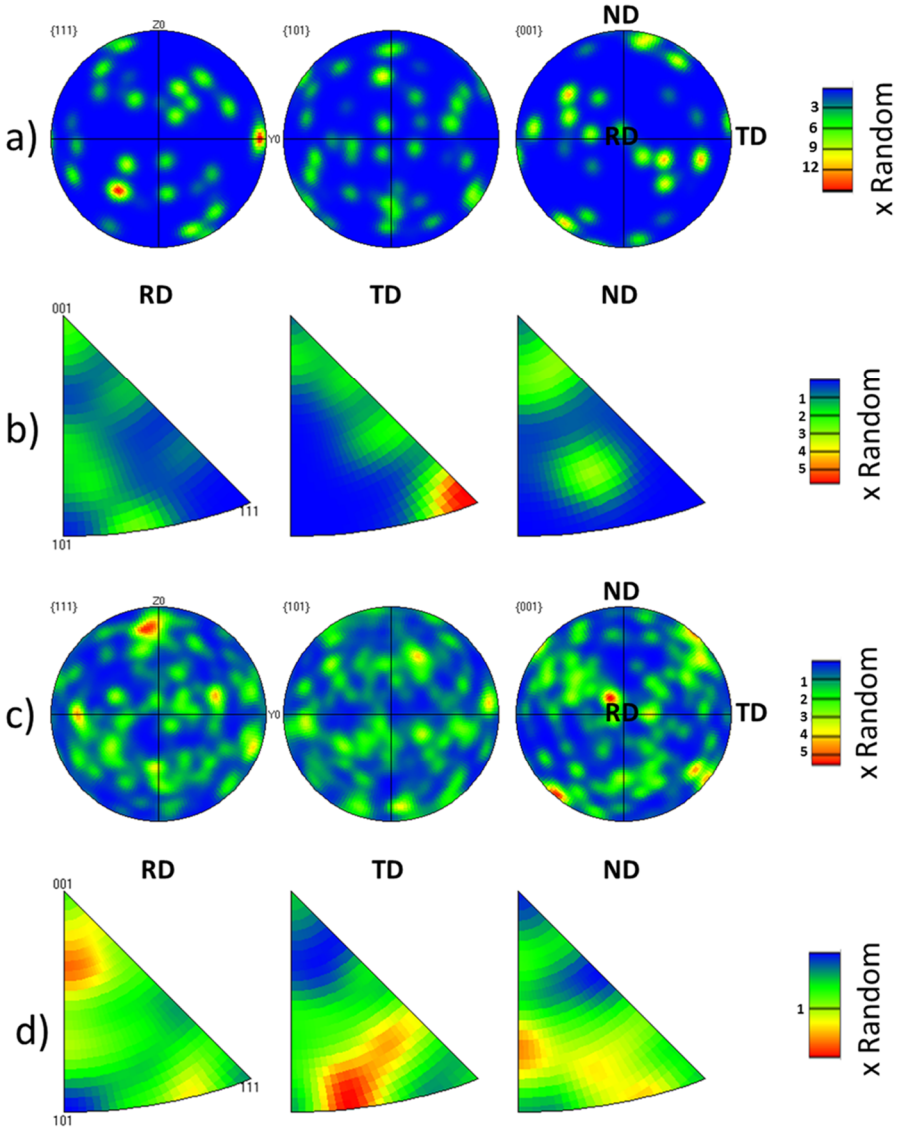

Figure 6.11: Pole figures and inverse pole figures obtained from EBSD maps for the columnar as-deposited region (a-b) and the recrystallised grains (c-d) of sample 4R.

In order to analyse the change in texture from the columnar structures to the refined equiaxed grains, electron backscattered diffraction (EBSD) images were analysed. The images reported in **Figure 6.10** are maps of tantalum acquired at the columnar and refined grain structure region of sample 4R. The orientation of the crystals is indicated in the direction parallel to the building direction (Z-axis). The columnar region (**Figure 6.10a**) was characterised by the absence of columnar grains oriented in the <101> direction, showing some preferential directions of crystallisation. The EBSD map for the refined region (**Figure 6.10b**) presents much more refined grains with random orientation. The columnar grains were completely refined to equiaxed grains, and the preferred orientation of crystals developed during deposition was eliminated.

The change in texture is shown in **Figure 6.11.** When comparing **Figure 6.11a** and **Figure 6.11c**, the change in texture when rolling was applied is evident. The columnar as-deposited region showed pole intensities peaking at 12 x random, while for finer equiaxed grains the peak intensities were around 5 x random. A marked scatter of the signal from different crystallographic planes was also clear for the refined region. It is important to note that the columnar grains were not characterised by a strong texture but showed a preferred orientation in the <111> direction (**Figure 6.11b**). In order to have a much more precise estimation of the texture, a larger amount of grains should be taken in the analysis. The main aim of this analysis was to verify whether cold rolling and the resulting plastic straining followed by the heat from successive deposition are also effective in reducing the texture. The pole figures represent microtextures rather than macro-textures.

6.4 Discussion

All the industrial sectors which employ tantalum components aim to obtain fine equiaxed microstructure with the reduction or elimination of the crystallographic texture so that they can benefit from improved mechanical properties and complete isotropy. The results showed above surely prove that deformation, by using rolling in this case, at room temperature applied in between the deposition of each layer lead to a large refinement of the grain structure as well

as reduction of porosity and texture. In the samples studied, the rolling load applied caused a compressive strain within the previously-deposited layers and the thermal field of the subsequent deposition allowed new recrystallised grains to form and grow. The recrystallisation occurred within the centre of the deposited structure, where the peak of strain was located and was extended as deep as three layers below the last deposited one. Successive steps of rolling and deposition led to a progressively larger area of fine equiaxed grains with an average grain size of 650 μm after five inter-pass rolling steps.

6.4.1 Induced strain and the depth of recrystallisation

6.4.1.1 Recrystallisation of unalloyed tantalum

The process that leads to the formation of new strain-free grains, which nucleate from deformed parent grains, is defined as recrystallisation. The formation of these new grains is driven mainly by the energy stored within the metal from the deformation, and the temperature, as it is a thermally activated mechanism. In general, the deformation increases the density of crystal imperfections, as for instance dislocations, which act as nucleation sites for new grains when the recrystallisation temperature is reached. Thus, temperature and strain regulate the nucleation rate and the grain growth rate.

Unalloyed polycrystalline tantalum is characterised by a recrystallisation temperature that varies within the range from 900°C to 1450°C, depending on the level of impurities and, predominantly, on the level of strain/deformation [29]. Usually, a high content of impurities increases the recrystallisation temperature. Köck et al. [12] reported that the deformation of arc-melted tantalum components can be pronouncedly influenced by metalloids, as carbon, nitrogen and oxygen. In the work of Mathaudhu et al. [37], the reported recrystallization curves showed that all tantalum specimens were fully-recrystallize at 1100°C but some of the samples recrystallised between 900°C and 1000°C according to the degree of deformation applied. A typical range of strain level in unalloyed tantalum, in order to obtain recrystallisation, was indicated to range from 1.2 to 4.6 [38]. The recrystallisation temperature associated to different strain levels was also

indicated: samples with a strain of 1.2 recrystallised at 1100°C, with a strain of 2.32 recrystallised at 1000°C, instead, with a strain of 3.48 recrystallised at 900°C [38].

6.4.1.2 The relation between hardness and strain

As the application of strain gauges on the external surfaces of the wall was not possible due to the surface roughness and the extremely high thermal fields from the deposition, the hardness profile was used to evaluate the strain distribution within the bulk of the structure. This because it is well known that tantalum components are subjected to considerable strain hardening when cold working is applied due to a high dislocations density formed by the plastic deformation [38,39]. Thus, the change in hardness after rolling can be directly associated with the strain.

In the work of Aditya et al. [30] about cold rolling of tantalum sheets, a trend between cold reduction (strain) and Vickers hardness was clearly shown. An increasing of average hardness was seen until cold reduction superior to 65%, where the hardness stabilised around 200 Hv. In the work of Mathaudhu et al. [37], the hardness of an arc-melted tantalum ingot was reported to increase after rolling. In particular, a hardness of 170 Hv was reached after one rolling cycle and a hardness of 210 Hv after two rolling cycles. In other studies on rolling of tantalum plates, micro-hardness values reached maximum levels around 230 Hv after only two rolling cycles with a strain of 2.3 [33]. In general, a plateau of hardness was always seen around 210 Hv - 220 Hv for the studies already reported, even for a high level of deformation. This saturation in formability and hardness was reported to be associated with the high density of dislocation which obstacle the further motion of themselves [30].

6.4.1.3 The relation between hardness and dislocation density

An empirical relation has been proposed in the literature [40] which correlated dislocation density (ρ) to the variation of Vickers hardness for cold worked tantalum. The equation is reported as following (**Eq. 6.1**):

$$\rho = 1.6\ x\ 10^{9}(m^{-2})\left(\frac{H - H_{ing}}{M\ Pa}\right)^{2} \qquad \textbf{(6.1)}$$

Where H is the Vickers hardness after cold working and H_{ing} is the hardness of the as-received material prior to deformation. Stuwe et al. [40] also proposed a minimum critical dislocation density in order to have spontaneous nucleation, which was indicated to be equal to $3x10^{14}$ m^{-2}. From the equation reported, the corresponding Vickers hardness to the critical dislocation density is equal to 130 Hv [30,40]. When considering the hardness distributions reported in **Figure 6.9**, it is possible to assess that the rolling step clearly induced a certain amount of strain within the bulk material associated with an increase in hardness to values as high as 210 Hv. The deformation localised around the hardness maximum should also be considered characterised by a considerable dislocation density, enough to induce recrystallisation. Furthermore, the hardness contour map reported in **Figure 6.9b** for samples 2R can be clearly considered a representation of the prior history of plastic deformation within the height and the width of the sample.

6.4.1.4 Effect of the thermal field on the hardness

The measurements of the thermal field evolution during and after the deposition have not been recorded with the use of thermocouples. The difficulties faced during the preparation of the experiments were the selection of thermocouples able to record a range of temperatures as high as 3000°C and also capable of being attached to the tantalum surface. The oxide layer on the tantalum surface made the attachment of the thermocouples difficult. Temperature measurements and thermal 3D-modelling would be needed for further developments of the study. This would help to understand if the depth of recrystallisation was mainly influenced by the strain or by the temperature. Although the lack of thermal data, the grain refinement achieved in sample 3R shows that the thermal field developed after the deposition clearly covered the range of recrystallisation temperature of tantalum.

The contour map of sample 3R (**Figure 6.9c**) shows how the thermal field developed from the deposition affected the hardness of the entire structure. There were particularly three main regions characterised by the hardness and the location. These regions corresponded precisely with the three regions of microstructure reported in sample 3R (**Figure 6.5c** and **Figure 6.5d**). The region

at the top extended from the top until 1.75 mm in depth which corresponded precisely to the fusion boundary location of the last layer (**Figure 6.5d**). The hardness was found to be very close to the as-deposited material and it was influenced only by the content of oxygen within the wire material. In fact, it is known that nitrogen and oxygen are strong hardeners of unalloyed polycrystalline tantalum [41]. In the work of Stecura [42], it is shown that the hardness of tantalum increased almost linearly when increasing oxygen content in solid solution. Samples with a different concentration of oxygen have been tested finding a hardness value of around 120 Hv for a tantalum specimen with a purity of 99.95 wt.% and a hardness value of around 500 Hv at about 1000 ppm of oxygen. The hardness of 114 Hv for the as-deposited differs from the typical hardness of a tantalum structure of 90 Hv mainly due to the 226 ppm of oxygen within the wire (**Table 6.1**). The region below this one corresponded entirely to the recrystallised region. The hardness was explained by the size and shape of the new recrystallised grains. Even if the strain was almost totally relieved by the formation of these new defect-free grains, the density of grain boundaries locally increased when compared to the parent columnar grains. The grain boundaries impeded the dislocation movements. This has led to a local strengthening effect according to the Hall-Petch relation.

Successively, the lower part of the sample 3R was characterised by a general decreasing in hardness when compared with the same portion of sample 2R but showing a visible retention of strain. The change in strain concentration and the dislocation density induced by the rolling was not sufficiently high to induce recrystallisation so that recovery occurred. The small driving force, in terms of strain and temperature, led to a general softening without the formation of new grains.

6.4.1.5 Dislocations density and oxygen content

The critical hardness value of 130 Hv obtained by the relation indicated by Stuwe et al. (**Eq. 6.1**) has been achieved for the top 7.0/8.0 mm of the sample 2R. Despite the dislocation density of $3x10^{14}$ m^{-2} associated with this hardness value and the assertion that this is the minimum value to obtain nucleation of new

grains, the recrystallization occurred only within a region characterised by a hardness ranging between 170 Hv to 205 Hv. The dislocation densities associated with these values of hardness should result to be respectively $5x10^{14}m^{-2}$ and $1.2x10^{15}m^{-2}$ using the relation of Stuwe et al. (**Eq. 6.1**). This equation does not take into account the effect of interstitials on the hardness in tantalum. As already reported, oxygen increases the total hardness of tantalum when present in solid solution, even in small quantities. The small amount of oxygen within the material used in this study could have led to a more pronounced strain hardening so that a higher nominal value of hardness was measured after cold working. Thus, the dislocation density for each region of sample 2R should be considered slightly lower than the over-estimation from the **Eq. 6.1**.

6.4.2 Recrystallisation mechanism

In the current study, the rolling load was applied in the direction parallel to the major axis of the columnar grains of the tantalum structure (**Figure 6.5**). Under the compressive stress, the columnar grains were deformed not only in the vertical direction but also laterally. This led to the formation of deformation bands among multiple grains with an angle close to 45° compared to the direction of the load applied (**Figure 6.8c** and **Figure 6.8d**). These bands could have been formed by a large number of crystal planes sliding, in blocks, along preferred slip planes. These features have been considered as slips mainly because the crystal axis and the crystal orientation remained the same without the formation of sub-grain boundaries as it is seen in twinning [43]. This need to be further investigated as no evidence is shown in this study.

Similar features have been seen from Mathaudhu et al. [33] and they have been addressed to the occurrence of slip. Nemat-Nasser et al. [44] affirmed that the slip of the screw dislocations on {110} planes was the dominant deformation mechanism observed in tantalum. Furthermore, elongated dislocations cells with small misorientations were found to form bands which were defined as the predominant microstructural characteristic of the shear-localization region. Micro-bands have also been reported in tantalum and their existence was mainly associated with the primary slip system in a <111> crystal direction [45]. For bcc

metals, such as tantalum, commonly slip occurs in the <111> direction on the planes {110}, {112} and {123}, which are the planes with largest interplanar spacing [31]. The Burgers vector is a/2<111> [46] and these particular screw dislocations control the most of the deformation properties of bcc metals so that in tantalum. In the study of Liu et al. [45], it has been seen that grains in <111> direction stored a higher amount of energy compared to the other directions and also <111> grains were the preferential place for nucleation of recrystallised grains after application of thermal energy. They have also seen that the dislocations were distributed uniformly only in <111> grains with a deformed matrix and concluded that this evenly stored energy represented the strong driving force for the growth of new crystals [45]. In the current study, the columnar grains seemed to have crystallised on a preferred <111> direction. The deformation applied by the roller led to the development of deformation bands, potentially series of slips, which have acted as nucleation sites for recrystallisation. The investigation needs further analysis in order to understand which family of crystal imperfections actually acted as a nucleation site for the new strain-free grains.

6.4.3 Porosity

Scattered pores were distributed across the bulk of samples 1R and 2R (**Figure 6.7a** and **Figure 6.7c**) with some flattened oval pores found on the upper part of sample 2R (**Figure 6.8a**). The aim of this section is not to discuss the formation of porosity, as it has been done elsewhere (**Chapter 5**). The presence of porosity was particularly reduced within the recrystallised region of sample 3R (**Figure 6.7d**). This phenomenon has been already reported in aluminium structures deposited via WAAM and rolled with a load of 45 kN [47]. The pore closure was also reported by Toda et al. [48] and Chaijaruwanich et al. [49] respectively for the cold and hot rolling of aluminium structures. The gas entrapped within the pore was considered to be mainly dissociated atomic oxygen. When the load was applied to the material, the pores slightly changed their shapes and the surrounding material was characterised by a higher dislocation density. This could have led to an entrapment of atomic gas in dislocation and vacancies

induced by the rolling step. Additionally, the elimination of the porosity could have been promoted by the dissolution of the gaseous atoms within the bulk of the new recrystallised grains during their growth.

6.4.4 Texture

When using Wire + Arc Additive Manufacture to deposit unalloyed tantalum, columnar grains develop during the solidification and grow in the direction perpendicular to the deposition direction. This is a typical example of epitaxial growth along the building direction that some materials develop when processed with an additive manufacturing process as seen by Thijs et al. for unalloyed tantalum [18] and by Martina et al. for Ti-6Al-4V [50]. Although this value should be treated with caution as the mapped area was relatively small and the grain size was large, the as-deposited columnar grains shown in this work presented some preferred orientation in the direction <111> (**Figure 6.10a**, **Figure 6.11a** and **Figure 6.11b**). **Figure 6.11b** clearly shows the high intensity of {111} planes. The randomisation of the texture after recrystallisation was clear when analysing **Figure 6.10b**, **Figure 6.11c** and **Figure 6.11d.** The main factor influencing the grains texture developed from recrystallization is definitely the nucleation mechanism. The shear bands found within and across the columnar grains after rolling represent a strong conglomeration of crystals defects which could act as nucleation sites. Nucleation of strain-free grains at shear bands has been observed in many metals including copper and its alloys [51,52] and aluminium[53]. Furthermore, in the case analysed, the new recrystallized grains have a completely different orientation when compared to the deformed parent metal. The recrystallization orientation may correspond to the randomly orientated defects/nuclei placed within the slip bands.

6.5 Conclusions

The impact of cold vertical rolling with a load of 50 kN on the porosity, the microstructure and the texture of an additively-manufactured tantalum component has been studied. A fundamental study has been performed in order to understand the change in microstructure and hardness that occurred after every

step of the process. Three main samples corresponding to three sequential steps were used in this study. In particular, the as-deposited material (sample 1R), as-deposited + rolling (sample 2R), as-deposited + rolling + deposition (sample 3R). The sample 3R promptly showed an improved microstructure already with only one rolling pass and one subsequent deposition. Sample 4R was used for the evaluation of the texture of the refined microstructure. The main finding of the study are summarised as follows:

- Combining the effect of cold rolling with a load of 50 kN and the successive layer deposition, it is possible to achieve recrystallisation in tantalum additively manufactured components;

- The refined region found in sample 3R exactly corresponded to the peak in hardness of sample 2R. Thus, the evaluation of strain distribution using hardness map resulted valuable to understand the depth of the wall affected by one single rolling step;

- The elimination of pores due to rolling has been observed and addressed to the entrapment of oxygen atomic gas within dislocation and vacancies, and or to the dissolution of the oxygen within the bulk of the new recrystallised grains during their growth;

- The new strain-free grains presented an equiaxed microstructure and a complete random texture.

6.6 Bibliography

1. Wong K V., Hernandez A. A Review of Additive Manufacturing. ISRN Mechanical Engineering. 2012; 2012: 1–10. Available at: DOI:10.5402/2012/208760
2. Herderick ED. Progress in Additive Manufacturing. JOM. 2015; 67(3): 580–581. Available at: DOI:10.1007/s11837-015-1323-x
3. Guo N., Leu MC. Additive manufacturing: Technology, applications and research needs. Frontiers of Mechanical Engineering. 2013; 8(3): 215–243. Available at: DOI:10.1007/s11465-013-0248-8
4. Frazier WE. Metal additive manufacturing: A review. Journal of Materials

Engineering and Performance. 2014; 23(6): 1917–1928. Available at: DOI:10.1007/s11665-014-0958-z

5. Ding D., Pan Z., Cuiuri D., Li H. Wire-feed additive manufacturing of metal components: technologies, developments and future interests. International Journal of Advanced Manufacturing Technology. 2015; 81(1–4): 465–481. Available at: DOI:10.1007/s00170-015-7077-3
6. Williams SW., Martina F., Addison AC., Ding J., Pardal G., Colegrove P. Wire + Arc Additive Manufacturing. Materials Science and Technology. 2016; 32(7): 641–647. Available at: DOI:10.1179/1743284715Y.0000000073
7. Yilmaz O., Ugla AA. Microstructure characterization of SS308LSi components manufactured by GTAW-based additive manufacturing: shaped metal deposition using pulsed current arc. International Journal of Advanced Manufacturing Technology. The International Journal of Advanced Manufacturing Technology; 2017; 89(1–4): 13–25. Available at: DOI:10.1007/s00170-016-9053-y
8. Asala G., Khan AK., Andersson J., Ojo OA. Microstructural Analyses of ATI 718Plus® Produced by Wire-ARC Additive Manufacturing Process. Metallurgical and Materials Transactions A: Physical Metallurgy and Materials Science. Springer US; 2017; 48(9): 4211–4228. Available at: DOI:10.1007/s11661-017-4162-2
9. Wang F., Williams S., Colegrove P., Antonysamy A a. Microstructure and mechanical properties of wire and arc additive manufactured Ti-6Al-4V. Metallurgical and Materials Transactions A: Physical Metallurgy and Materials Science. 2013; 44: 968–977. Available at: DOI:10.1007/s11661-012-1444-6
10. Gu J., Ding J., Williams SW., Gu H., Ma P., Zhai Y. The strengthening effect of inter-layer cold working and post-deposition heat treatment on the additively manufactured Al– 6.3Cu alloy. Journal of Materials Processing Technology. Elsevier; 2016; 230: 26–34. Available at: DOI:10.1016/j.jmatprotec.2015.11.006
11. Lockett H., Ding J., Williams S., Martina F. Design for Wire + Arc Additive Manufacture: design rules and build orientation selection. Journal of Engineering Design. 2017; 4828(December): 1–31. Available at: DOI:10.1080/09544828.2017.1365826
12. Köck W., Paschen P. Tantalum-processing, properties and applications. Jom. 1989; 41(10): 33–39. Available at: DOI:10.1007/BF03220360
13. Bischof M., Mayer S., Leitner H., Clemens H., Pranzas K., Staron P., et al. Microstructure and Mechanical Properties of Si and Y Doped Tantalum. 16th International Plansee Seminar. 2005; : 489–503.
14. Buckman RW. New Applications for Tantalum and Tantalum Alloys. Jom. 2000; (March): 40–41. Available at: DOI:10.1007/s11837-000-0100-6
15. Bechtold J. Tensile properties of annealed tantalum at low temperatures. Acta Metallurgica. 1955; 3: 249–254. Available at: DOI:10.1016/0001-6160(55)90060-2
16. Cardonne SM., Kumar P., Michaluk CA., Schwartz HD. Tantalum and its alloys.

International Journal of Refractory Metals and Hard Materials. 1995; 13(4). Available at: DOI:10.1016/0263-4368(95)94023-R

17. Zhou L., Yuan T., Li R., Tang J., Wang G., Guo K. Selective laser melting of pure tantalum: Densification, microstructure and mechanical behaviors. Materials Science and Engineering A. 2017; 707(September): 443–451. Available at: DOI:10.1016/j.msea.2017.09.083
18. Thijs L., Montero Sistiaga ML., Wauthle R., Xie Q., Kruth JP., Van Humbeeck J. Strong morphological and crystallographic texture and resulting yield strength anisotropy in selective laser melted tantalum. Acta Materialia. Acta Materialia Inc.; 2013; 61(12): 4657–4668. Available at: DOI:10.1016/j.actamat.2013.04.036
19. Balla VK., Banerjee S., Bose S., Bandyopadhyay A. Direct laser processing of a tantalum coating on titanium for bone replacement structures. Acta Biomaterialia. Acta Materialia Inc.; 2010; 6(6): 2329–2334. Available at: DOI:10.1016/j.actbio.2009.11.021
20. Wauthle R., Van Der Stok J., Yavari SA., Van Humbeeck J., Kruth JP., Zadpoor AA., et al. Additively manufactured porous tantalum implants. Acta Biomaterialia. Acta Materialia Inc.; 2015; 14: 217–225. Available at: DOI:10.1016/j.actbio.2014.12.003
21. Martina F., Colegrove PA., Williams SW., Meyer J. Microstructure of Interpass Rolled Wire + Arc Additive Manufacturing Ti-6Al-4V Components. Metallurgical and Materials Transactions A: Physical Metallurgy and Materials Science. Springer US; 2015; 46(12): 6103–6118. Available at: DOI:10.1007/s11661-015-3172-1
22. David SA., Babu SS., Vitek JM. Welding : Solidification and Microstructure. JOM. 2003; (June).
23. Carroll BE., Palmer TA., Beese AM. Anisotropic tensile behavior of Ti-6Al-4V components fabricated with directed energy deposition additive manufacturing. Acta Materialia. Acta Materialia Inc.; 2015; 87: 309–320. Available at: DOI:10.1016/j.actamat.2014.12.054
24. Antonysamy AA., Meyer J., Prangnell PB. Effect of build geometry on the beta-grain structure and texture in additive manufacture of Ti6Al4V by selective electron beam melting. Materials Characterization. The Authors; 2013; 84: 153–168. Available at: DOI:10.1016/j.matchar.2013.07.012
25. Shen C., Pan Z., Cuiuri D., Roberts JON., Li H. Fabrication of Fe-FeAl Functionally Graded Material Using the Wire-Arc Additive Manufacturing Process. Metallurgical and Materials Transactions B. Springer US; 2016; 47(1): 763–772. Available at: DOI:10.1007/s11663-015-0509-5
26. Vilaro T., Colin C., Bartout JD., Nazé L., Sennour M. Microstructural and mechanical approaches of the selective laser melting process applied to a nickel-base superalloy. Materials Science and Engineering A. Elsevier B.V.; 2012; 534: 446–451. Available at: DOI:10.1016/j.msea.2011.11.092
27. Li S., Wei Q., Shi Y., Zhu Z., Zhang D. Microstructure Characteristics of Inconel

625 Superalloy Manufactured by Selective Laser Melting. Journal of Materials Science and Technology. 2015; 31(9): 946–952. Available at: DOI:10.1016/j.jmst.2014.09.020

28. Yan F., Xiong W., Faierson E. Grain Structure Control of Additively Manufactured Metallic Materials. Materials. 2017; 10(11): 1260. Available at: DOI:10.3390/ma10111260
29. Sandim HRZ., Martins JP., Pinto AL., Padilha AF. Recrystallization of oligocrystalline tantalum deformed by cold rolling. Materials Science and Engineering A. 2005; 392(1–2): 209–221. Available at: DOI:10.1016/j.msea.2004.09.032
30. Aditya A V., Subramanian PK., Gopala Krishna V., Chinta Babu U. Influence of rolling path on microstructure and mechanical properties in EB refined tantalum. Transactions of the Indian Institute of Metals. 2012; 65(5): 435–442. Available at: DOI:10.1007/s12666-012-0148-3
31. Huang Y., Maury N., Zhang NX., Langdon TG. Microstructures and mechanical properties of pure tantalum processed by high-pressure torsion. Materials Science and Engineering. 2014; 63: 012100. Available at: DOI:10.1088/1757-899X/63/1/012100
32. Renk O., Ghosh P., Pippan R. Generation of extreme grain aspect ratios in severely deformed tantalum at elevated temperatures. Scripta Materialia. Acta Materialia Inc.; 2017; 137: 60–63. Available at: DOI:10.1016/j.scriptamat.2017.04.024
33. Mathaudhu SN., Hartwig KT. Processing microstructure property relationships in severely deformed tantalum. Materials Science and Engineering A. 2007; 463(1–2): 94–100. Available at: DOI:10.1016/j.msea.2006.08.120
34. Maury N., Xian N., Huang Y., Zhilyaev AP., Langdon TG. A critical examination of pure tantalum processed by high-pressure torsion. Materials Science & Engineering A. Elsevier; 2015; 638: 174–182. Available at: DOI:10.1016/j.msea.2015.04.053
35. Lee SL., Doxbeck M., Mueller J., Cipollo M., Cote P. Texture, structure and phase transformation in sputter beta tantalum coating. Surface and Coatings Technology. 2004; 177–178: 44–51. Available at: DOI:10.1016/j.surfcoat.2003.06.008
36. Ellis EAI., Chmielus M., Baker SP. Effect of sputter pressure on Ta thin films: Beta phase formation, texture, and stresses. Acta Materialia. 2018; 150: 317–326. Available at: DOI:10.1016/j.actamat.2018.02.050
37. Mathaudhu SN., Ted Hartwig K. Grain refinement and recrystallization of heavily worked tantalum. Materials Science and Engineering A. 2006; 426(1–2): 128–142. Available at: DOI:10.1016/j.msea.2006.03.089
38. Hartwig K t., Mathaudhu SN., Maier HJ., Karaman I. HARDNESS AND MICROSTRUCTURE CHANGES IN SEVERELY DEFORMED AND RECRYSTALLIZED TANTALUM. Ultrafine Grained Materials II. 2002; 11: 151–160.

39. Pan Z., Li Y., Wei Q. Tensile properties of nanocrystalline tantalum from molecular dynamics simulations. Acta Materialia. 2008; 56(14): 3470–3480. Available at: DOI:10.1016/j.actamat.2008.03.025

40. Stüwe HP., Padilha AF., Siciliano F. Competition between recovery and recrystallization. Materials Science and Engineering A. 2002; 333(1–2): 361–367. Available at: DOI:10.1016/S0921-5093(01)01860-3

41. Puhr-Westerheide J., Elssner G. On the solid solution hardening of tantalum by nitrogen and oxygen. Journal of The Less-Common Metals. 1970; 20(4): 371–374. Available at: DOI:10.1016/0022-5088(70)90013-5

42. Stecura S. Observation of oxide particles below the apparent oxygen solubility limit in tantalum. Metallurgical Transactions. 1974; 5(6): 1337–1340. Available at: DOI:10.1007/BF02646617

43. Murr LE., Meyers MA., Niou C-S., Chen YJ., S. Pappu., C. Kennedy. SHOCK-INDUCED DEFORMATION TWINNING IN TANTALUM. Acta Materialia. 1997; 45(1): 157–175.

44. Nemat-Nasser S., J. B. Isaacs., M. Liu. Microstructure of high-Strain, High-Strain-Rate Deformed Tantalum. Acta Materialia. 1998; 46(4): 1307–1325.

45. Y. H. Liu., S. F. Liu., J. L. Zhu., C. Deng., H. Y. Fan., L. F. Cao., et al. Strain path dependence of microstructure and annealing behavior in high purity tantalum. Materials Science and Engineering A. Elsevier B.V.; 2017; 707(August): 518–530. Available at: DOI:10.1016/j.msea.2017.09.097

46. Yang LH., Soderlind P., Moriarty JA. Atomistic simulation of pressure-dependent screw dislocation properties in bcc tantalum. Materials Science and Engineering A. 2001; 309–310: 102–107. Available at: DOI:10.1016/S0921-5093(00)01618-X

47. Gu J., Ding J., Williams SW., Gu H., Ma P., Zhai Y. The effect of inter-layer cold working and post-deposition heat treatment on porosity in additively manufactured aluminum alloys. Journal of Materials Processing Technology. Elsevier B.V.; 2016; 230: 26–34. Available at: DOI:10.1016/j.jmatprotec.2015.11.006

48. Toda H., Yamaguchi T., Nakazawa M., AOKI Y., UESUGI K., SUZUKI Y., et al. Four-Dimensional Annihilation Behaviors of Micro Pores during Surface Cold Working. Materials transactions. 2010; 51(7): 1288–1295. Available at: DOI:10.2320/matertrans.M2010069

49. Chaijaruwanich A., Dashwood RJ., Lee PD., Nagaumi H. Pore evolution in a direct chill cast Al-6 wt.% Mg alloy during hot rolling. Acta Materialia. 2006; 54(19): 5185–5194. Available at: DOI:10.1016/j.actamat.2006.06.029

50. Martina F., Mehnen J., Williams SW., Colegrove P., Wang F. Investigation of the benefits of plasma deposition for the additive layer manufacture of Ti-6Al-4V. Journal of Materials Processing Technology. Elsevier B.V.; 2012; 212(6): 1377–1386. Available at: DOI:10.1016/j.jmatprotec.2012.02.002

51. Duggan BJ., Hatherly M., Hutchinson WB., Wakefield PT. Deformation structures and textures in cold-rolled 70:30 brass. Metal Science. 1978; 12(8): 343–351.

52. Ridha AA., Hutchinson WB. Recrystallisation mechanisms and the origin of cube texture in copper. Acta Metallurgica. 1982; 30(10): 1929–1939. Available at: DOI:10.1016/0001-6160(82)90033-5

53. Hjelen J., Orsund R., Nes E. On the Origin of Recrystallization Textures in Aluminum. Acta Metall. Mater. 1991; 39(7): 1377–1404. Available at: DOI:Doi 10.1016/0956-7151(91)90225-P

Chapter 7

Paper F

"Investigation of Wire + Arc Additive Manufacture for the production of functionally graded structures by refractory and its characterisation"

G. Marinelli*, [a], F. Martina*, S. Ganguly*, S. Williams*, H. Lewtas**, D. Hancock**
*Welding Engineering and Laser Processing Centre (WELPC), Cranfield University, Cranfield, MK43 0AL, United Kingdom
**Culham Centre for Fusion Energy (CCFE), Culham Science Centre, Abingdon, OX14 3DB, United Kingdom

Abstract

Components employing functionally graded structures are usually preferred when used for severe and critical service conditions due to the possibility to take advantage of the controlled variation of the material properties within the same structure. Wire + Arc Additive Manufacturing (WAAM) is an emerging manufacturing technology which has the design flexibility of producing sound graded structures simply by adjusting the power and the composition of the feedstock. In this study, a single structure made out of two functional gradations, respectively between tantalum and molybdenum and between molybdenum and tungsten, were successfully deposited with a linear gradient in both composition and hardness. The microstructure, the elemental composition and the hardness as a function of position were characterised and discussed. The analysis of the microstructure was used to verify the structural integrity of the deposit while the analysis of chemical composition and hardness were used to evaluate the gradation dimensions. The study demonstrates that WAAM has the potential to successfully deposit refractory-metal functionally graded structures, obtaining controlled properties.

7.1 Introduction

Functionally graded structures, commonly named with the acronym FGSs, are advanced and highly-functional parts of a component that present a localised continuous variation of chemical composition and, usually, microstructure which leads to innovative mechanical or thermal responses [1]. This spatial gradation can be completely custom-made for specific performances or functions [2].

The term "functionally graded material" has been originally introduced in Japan in 1984 when the development of thermal barrier coating was studied [3]. The need of graded material arises in order to replace the sharp transition, when two materials are interfaced, with a gradation which produces smooth changeover from one material to the next [4]. Extreme-environment applications require components that can provide exceptional performances when, for instance, different stress fields are localized at different positions within the same part. For this reason, these critical components need graded properties and microstructural features complemented by different alloys.

A very specific example of an extreme environment is represented by the nuclear fusion reactor, in which components are affected by substantially different thermal gradients [5,6]. Other applications can be, for instance, spacecraft heat shields, heat exchanger tubes, biomedical implants and flywheels [7]. The manufacture of FGSs also allows new structures made of ordinarily incompatible materials to be implemented in one structure in order to create new material solutions for other sectors [7]. Typically, materials that have marked differences with regard to physical and chemical properties can be embedded in a single structure [7].

In recent years, a great attention has been given to a specific class of graded structures, in particular, metal-based functionally graded materials [8]. Metal-based graded structures can be built not only taking into account the compositional gradient but also using a microstructural or geometrical gradient of a single-material component. In particular, there have been reported studies aiming to obtain a gradual change in microstructure [9] produced with local

functionalities in crystallographic texture and grain size [10] and others which implement geometrical gradient in functional mesh density [11].

Naebe [12] published a review of different techniques for FGSs production and their impact on the final properties. Other basic production techniques specifically for metal-based structures can be found in the work of Sobczak et al. [8]. In general, there are several manufacturing approaches that allow obtaining the required compositional gradient and these include gas phase, liquid phase and solid phase methods [13]. In addition to these techniques, additive manufacturing (AM) processes have been extensively presented in the literature as promising and flexible approaches able to modulate and control the gradient within multi-material structures.

The study and the implementation of these manufacturing techniques will certainly bring a step forward the entire development of next-generation graded structures [12]. The characteristic high accuracy and process controllability of AM allows coupling of graded composition with geometrical and microstructural features achieving the production, as for instance, of biocompatible high-technology prosthesis [12].

Different additive manufacturing processes and materials have been already studied and characterised aiming at the production of controlled and innovative metal-based functional gradients. In the work of Domack and Baughman [14], three different manufacturing routes were used to produce a graded structure between Inconel 718 and Ti-6Al-4V. In particular, they studied laser metal powder deposition, flat wire welding, and ultrasonic foil consolidation. The structures manufactured in this study presented macroscopic cracking due to the formation of brittle phases. Moreover, FGSs between iron and aluminium have also been produced by Wire + Arc Additive Manufacturing (WAAM) in the study of Shen et al. [15] showing a regular chemical gradient and acceptable mechanical properties. Additional work on the experimental characterization and computational analysis has been conducted for structures with a gradient from Ti-6Al-4V to Invar 36 [16] and from 304L stainless steel incrementally graded to Inconel 625 [17]. Niendorf et al. [9] proved the feasibility of producing stainless steel components with different local functionalities by using selective laser

melting (SLM). This was achieved through the manipulation and the control of the microstructure at different build positions. The production of a gradient with regards to the mesh density for high strength and high energy absorption Ti-6Al-4V components has also been studied and produced using electron beam melting (EBM) [11]. Furthermore, some studies on residual stress evolution for graded structures were reported in the work of Dao et al. [18] and Cannillo et al. [19].

When analysing these studies, it is possible to asses that the main challenges for the production of graded structures using additive manufacturing are the concentration of residual stresses, the mismatch of thermo-mechanical properties of the deposited metals and the formation of intermetallics or other brittle phases during the deposition process. Thus, inaccuracy with regards to the process calculation and design specifications can drive to unwanted failures [20].

As already mentioned, an increasing interest with regards to innovative manufacturing techniques of high-performance refractory metal components has been registered within the nuclear sector. This because these metals are primarily characterised by the high melting point and density so that they are able to withstand the reactor's high temperatures. In fact, molybdenum thermal blankets have been proposed as functional materials for piping of nuclear systems in the work of Rizakhanov et al. [21]. Additionally, tungsten and its alloys are considered to be the best candidate as plasma-facing materials [22]. However, their brittleness at low temperatures presents a limitation for their use as a structural material [23]. Weber and Aktaa [24] conducted a numerical assessment for graded tungsten-to-steel joints. They estimated that a controlled graded structure between the two metals is necessary for the divertor application in order to overcome their remarkable difference in thermal expansion. They proposed vacuum plasma spraying (VPS) and resistance sintering under ultra-high pressure (RSUHP) as suitable methods for the production of sound functionally graded tungsten-to-steel joints [24]. For all these reasons, the production of components for the high-temperature applications using additive manufacturing is becoming one of the most ambitious objectives of the nuclear industry.

Until now, very few investigations have been reported with regards to the possibility of producing parts in unalloyed tungsten, tantalum and molybdenum

using additive manufacturing methods. Moreover, investigations referring to functional gradations of such materials, within the same components, have been reported to be almost absent. In the present work, graded structures comprising of three dissimilar alloys, in particular tantalum, molybdenum and tungsten, were fabricated within the same structure using Wire + Arc Additive Manufacture. These metals were deposited in their unalloyed form using a wire feedstock. Fundamental characteristics that are common for the three metals used are the high melting point and their complete miscibility without the formation of secondary phases amongst each other. The aspects for which they differentiate are physical properties such as the coefficient of thermal expansion, thermal conductivity and ductile-to-brittle transition temperature. A unique and robust way of manufacturing controlled gradients between different refractory metals using a WAAM process is presented. The goal of the current study was to investigate the manufacturing of refractory metal graded structures and analyse the quality of the formed joints by hardness and chemical composition evaluations.

7.2 Experimental Procedure

The functionally graded structures analysed in this study were deposited within the same deposit, which had total dimensions of 10.5 mm in height and 8.5 mm in average width. Starting from a tantalum plate, a linear structure was deposited initially using molybdenum wire and, successively, adding tungsten wire. The materials used in the study were high-purity unalloyed tungsten, tantalum and molybdenum, as shown in **Table 7.1.** Some mechanical properties and thermo-physical properties of these metals are also summarised in **Table 7.2.**

	W	Mo	Ta	Ti	V	Cr	Fe	C	N	O	K
W wire	99.99	<0.05	<0.05	<0.05	<0.05	<0.05	<0.05	33 ppm	<10 ppm	<50 ppm	<10 ppm
Mo wire	99.99	<0.05	<0.05	<0.05	<0.05	<0.05	<0.05	33 ppm	<10 ppm	59 ppm	<10 ppm
Ta sub	99.99	<0.05	<0.05	<0.05	<0.05	<0.05	<0.05	33 ppm	<10 ppm	60 ppm	<10 ppm

Table 7.1: Elemental composition (wt%) of tungsten wire (W wire), molybdenum wire (Mo wire) and tantalum substrate (Ta sub).

	K [$Wm^{-1}K^{-1}$]	T_f [°C]	α [$\mu m\ m^{-1}K^{-1}$]	E [GPa]
W	174	3422	4.5	411
Mo	138	2623	4.8	330
Ta	57.5	3017	6.3	185

Table 7.2: Typical values of thermal conductivity (K), melting point (T_f), the coefficient of thermal expansion (α) and elastic modulus (E) for tungsten, molybdenum and tantalum from [25].

The tantalum plate was 4.0 mm in thickness and it was polished and rinsed with acetone in order to remove the oxide layer and other residues of contaminants. The molybdenum and tungsten wires used had both a wire diameter of 1.0 mm. **Figure 7.1** shows the layout of the welding apparatus used in this study. In particular, a conventional tungsten inert gas (TIG) torch, a power supply and a controlled wire feeder were used for the deposition. The heat source, the wire delivery system and the substrate were attached to three linear motorized high-load stages assembled in XYZ configuration. The apparatus was surrounded by a heavy-duty enclosure used to ensure a low level of oxygen when purged with argon.

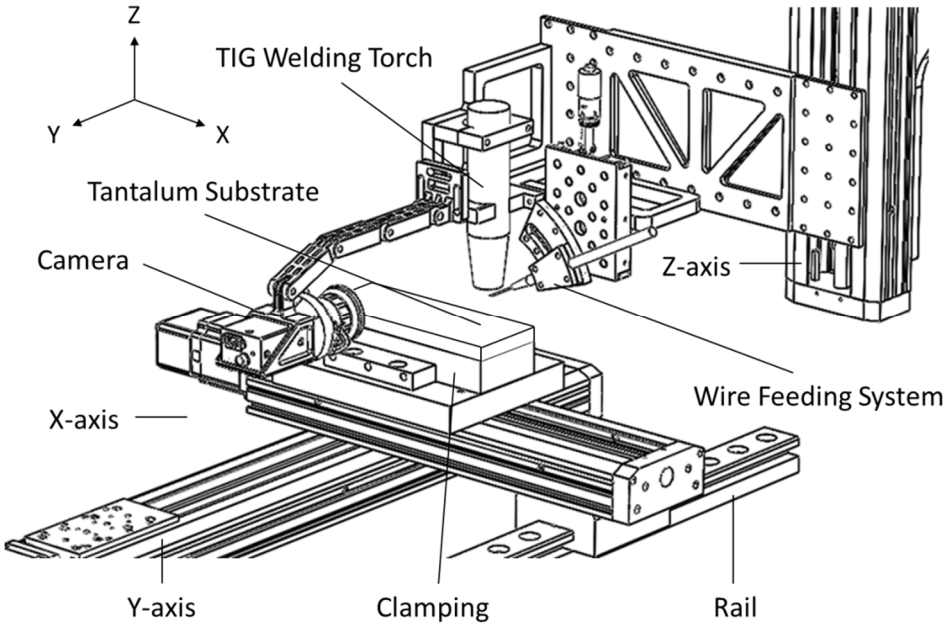

Figure 7.1: Set-up used for the deposition of refractory metal FGS using the WAAM process.

Table 7.3 lists the process parameters which were kept constant during the deposition in order to decrease the process variables. The procedure and the process parameters used for the deposition of each layer are reported in **Table 7.4**.

Electrode-to-workpiece distance	3.5 mm
Tungsten electrode tip angle	45°
Diameter of the electrode	3.6 mm
Torch shielding gas composition	100% He
Shielding gas flow rate	15 L min^{-1}
Oxygen Atmosphere of Deposition	<100 ppm

Table 7.3: Values for the process parameters excluded from the factorization.

Layer Num.	TS [mm/s]	WFS [mm/s]	I [A]	
1	4	20	300	Molybdenum Wire
2	4	20	300	
3	4	20	300	
4	4	20	300	
5	4	20	300	
6	4	20	300	
7	4	20	300	
8	4	20	300	
9	4	15	300	Tungsten Wire
10	4	15	300	
11	4	15	300	
12	4	20	300	
13	3	20	300	
14	3	20	300	

Table 7.4: Procedure of deposition of the functionally graded structures.

The deposition of each successive layer was performed once the substrate was cooled down to room temperature. The cross-section, perpendicular to the deposition direction, was selected for the characterisation. The samples were polished and chemically etched to reveal the microstructural features developed during the deposition. Murakami's Reagents were used as etchant solution for the investigation of all three alloys. The hardness of the structure was measured using

an automatic hardness testing machine. The main parameters for the hardness acquisition were 1000g load, a step size of 100µm step and an indentation time of 15 seconds for each testing point. The chemical composition of the structure deposited was measured using a scanning electron microscope (SEM) equipped with an energy-dispersive spectrometer (EDS) operating at 20 kV.

7.3 Results and Discussion

7.3.1 Microstructure

Figure 7.2 reveals the microstructure of the two functional gradations within the structure deposited. In specific, a graded structure between tantalum (Ta) and molybdenum (Mo) was located at the bottom whereas a graded structure between molybdenum and tungsten (W) was located at the middle-height of the sample.

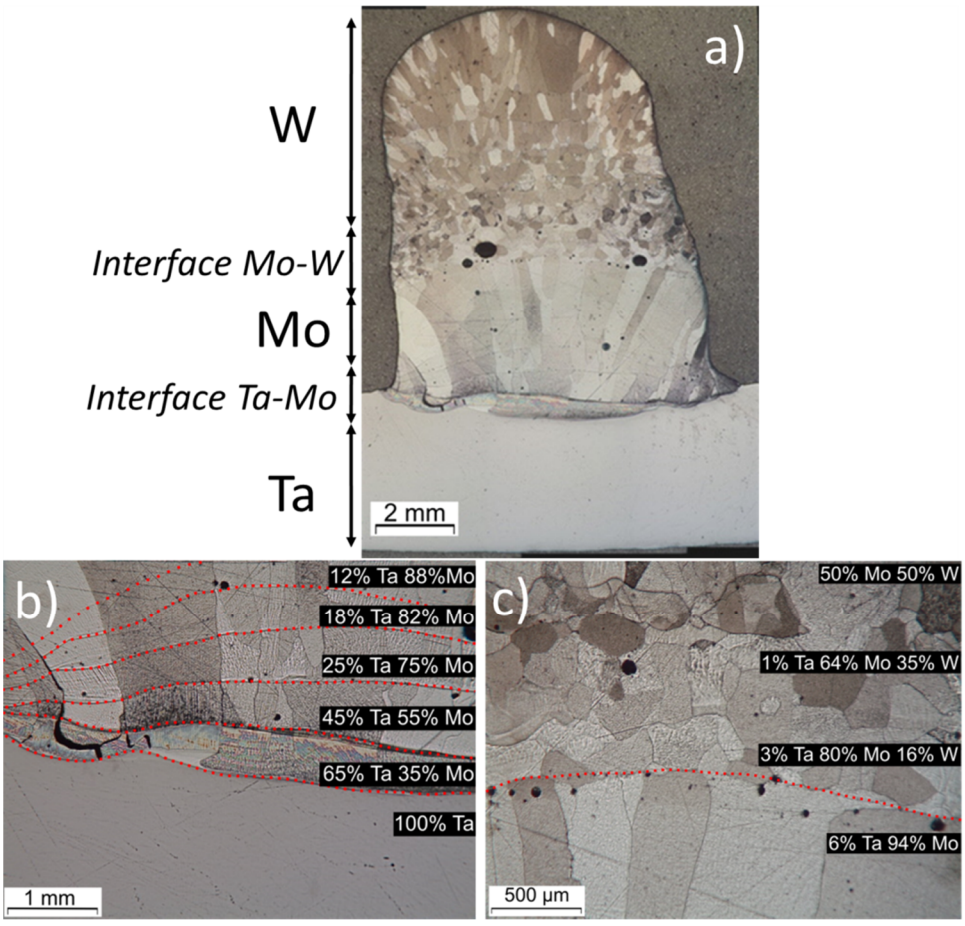

Figure 7.2: Microstructure of the entire deposited structure (a); Higher magnification micrographs of the tantalum to molybdenum interface (b) and the molybdenum to tungsten interface (c).

Figure 7.2 shows the higher-magnification micrographs of some microstructural features present at different spatial positions of the deposited structure, in particular at the interface between of the deposition of two refractory metals. **Figure 7.2a** reports the microstructure of the whole deposited structure and its characteristic features. In particular, large columnar grains were visible within Mo-rich regions while finer equiaxed grains were forming the prevalent microstructure of W-rich regions. Furthermore, the existence of cracks at the interface between Ta and Mo was also reported as well as the presence of porosity localized mainly at the interface between Mo and W. Additionally, an impressive absence of cracks at the interface between Mo and W was reported. The microstructural evolution and the distribution of the defects throughout the layers can be directly correlated to the material composition characterising the different regions.

Figure 7.2b shows the microstructural features at the tantalum-molybdenum interface, which consisted of columnar grain with a marked presence of cracks across the grain boundaries. The average non-stoichiometric composition of the first deposited layer of Mo resulted to be around 65 wt.% of Ta and 35 wt.% of Mo. With the successive layer depositions of molybdenum, the columnar grains developed parallel to the building direction with an increased presence of porosity but a decreased presence of cracks. This characteristic columnar-like microstructure was seen within the range in composition from about 55 wt% to 94 wt% of Mo. When W was introduced in the deposition, the second gradation started to form and a noticeable a reduction of the porosity and the change in microstructure from columnar to equiaxed were seen with a content of W equal to 15 wt.% (**Figure 7.2c**).

The causes of the cracks evolution between Ta and Mo can be addressed to the intense stress fields developed at this particular interface during the deposition or to the critical mechanical mismatch between the two metals due to their difference in plasticity (**Table 7.2**). Further investigations were carried out in order to verify the presence of compositional or microstructural fluctuations and are reported within the following sections.

Columnar grains in components produced by additive manufacturing has been already reported for tantalum, titanium and nickel alloys [26–30]. These grains usually forms onto previous partially melted ones, which act as nucleation sites, and grow epitaxially, parallel to the building direction, across multiple layers. This resulted to be the typical solidification process of Mo-rich regions. Typically, a finer microstructure can be produced by a faster solidification rate or by employing a lower process heat input. This could possibly lead to a change in the solidification regime from columnar to equiaxed grains.

In the case reported, the addition of W to Mo produced a metallic solution with an increased melting point and thermal conductivity with respect to unalloyed Mo. As a consequence, the liquid solution started to solidify at a higher rate, as well as the heat was extracted from the liquid pool at a higher rate. Under these conditions, the epitaxial grain growth was not anymore the preferred mechanism that dominates the solidification but it was outclassed by heterogeneous nucleation caused by a faster cooling rate. Thus, within the weld pool, numerous nuclei started to form which, then, initialised the crystallisation. The continuous increasing of tungsten content promoted this effect leading to the formation and growth of fine equiaxed grains within the melt pool. Furthermore, each layer was deposited when the entire structure was cooled at room temperature and this could have enhanced or ensured the heterogeneous nucleation conditions.

A similar phenomenon has been seen in the study of Shen et al. [15] in which FGSs between iron and aluminium were deposited. With respect to the work of Shen et al. [15], the major similarity is in the fact that, a metal with higher thermal conductivity was deposited on a metal with lower thermal conductivity. In fact, the thermal conductivities of iron and aluminium are respectively 80.4 W $m^{-1}K^{-1}$ and 205 W $m^{-1}K^{-1}$ [15]. The values for molybdenum and tungsten are respectively 138 W $m^{-1}K^{-1}$ and 174 W $m^{-1}K^{-1}$ (**Table 7.2**). For this reason, depositing aluminium on iron can be compared to the deposition of tungsten on molybdenum and, in fact, a similar effect was observed with regards to the solidification and the resulting microstructural pattern. Furthermore, in the work of Reichardt et al. [31], a sharp change from columnar to finer equiaxed grains

have been reported when depositing vanadium-rich alloy onto titanium-rich alloy. The authors addressed the occurrence of this phenomenon to the insufficient process heat input, as vanadium has a higher melting point than titanium. **Table 7.4** reports the procedure used in the current study for the deposition of the structure. From the Mo deposition to the W deposition, the progressive heat input for every layer has been kept constant, excluding the last two tungsten layers, while the increasing tungsten content progressively raised the melting point of the weld pool alloy.

It can be deduced that the finer microstructure of the W-rich regions could have been possibly produced by the progressively higher melting point of the alloys and the enhanced extraction of the heat, which promoted heterogeneous nucleation against the epitaxial growth.

7.3.2 Correlation between hardness and chemical composition

Figure 7.3 reports the elemental composition and the Vickers hardness profile of the structure as a function of the position relative to the top of the substrate. In particular, the hardness curve is represented in black while, the composition of Ta, Mo and W are represented respectively in blue, red and green. All the measurements were performed at the centreline of the structure.

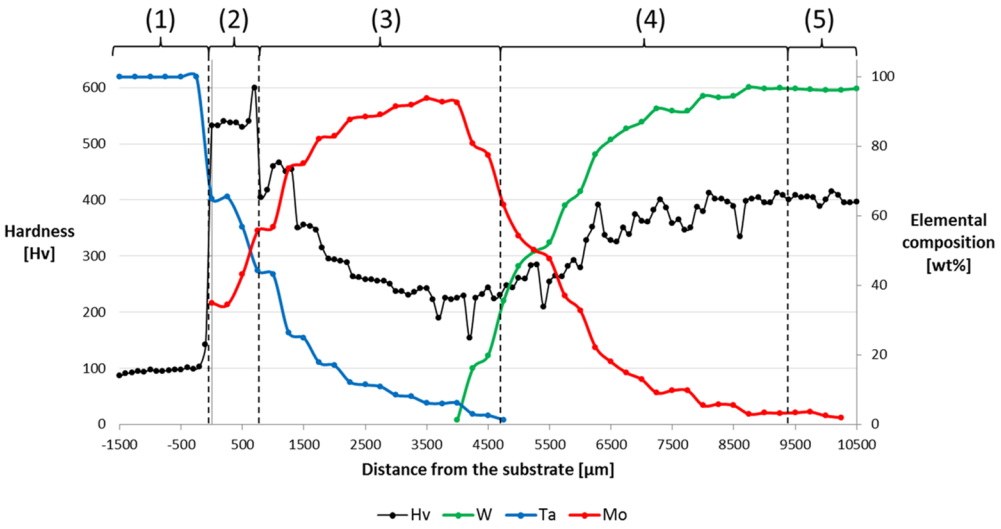

Figure 7.3: Microhardness (black) of the graded alloys overlaid on W (green), Ta (blue) and Mo (red) composition versus the distance from the substrate top.

The average measured composition was precisely reflecting the hardness profile along the structure. In particular, the hardness and the composition of each layer can be seen from the trends. Small progressive plateaus were observed for both composition and hardness, which resembled the dimensions of each deposited layer. The first FGS, between Ta and Mo, extended for about 4000.0 μm while the second, between Mo and W, extended for about 5500.0 μm.

When depositing one layer, the previously deposited one was only partially melted and, with the addition of the wire feedstock, an alloy with a new composition was formed. The reiteration of this process created a smooth gradient in composition, which can be designed and controlled by varying the process parameters. The re-melting and the quantity of the material added are the main factors to consider and monitor in order to control the gradient slope and dimension. In fact, the re-melting of the layer is directly connected to the melting point of the local alloy and to the heat input. High re-melting leads to a low dilution of the melted layer composition. The quantity of the material added for the WAAM process is directly connected to the WFS to TS ratio and wire diameter. High WFS to TS ratio leads to a high dilution of the melted layer composition. Thus, the dilution of each layer is directly proportional to the WFS to TS ratio and inversely proportional to the process heat input.

The hardness trend along the entire structure did accurately overlie the compositional gradients. In particular, five main regions of interest can be recognised with regards to the hardness profile (**Figure 7.3**): (1) Ta substrate, (2) interface Ta to Mo, (3) FGS Ta to Mo, (4) FGS Mo to W and (5) almost unalloyed W. The hardness of the Ta substrate remained constant to an average of 95 Hv along the entire substrate thickness. The interface between Ta and Mo was characterised by a hardness of around 550-600 Hv. Successively, the hardness constantly decreased within the first FGS until stabilising at around 240 Hv for Mo-rich regions. With the addition of W, the hardness gradually increased within the FGS between Mo and W until it stabilised at around 400 Hv on average of W-rich regions at the top of the structure.

It can be surely reported a pronounced sharp increasing in hardness with the addition of Mo to the unalloyed Ta. No intermetallic phases were formed

during the deposition due to their complete solid solubility. Typically, Ta vigorously decreases its plasticity and increases its hardness when alloyed with a relatively large quantity of tungsten, as reported in the study of Chen and Gray [32]. A similar effect could have verified when the first two layers of Mo were deposited. For this reason, the presence of numerous cracks is also justified by the marked brittleness of this intermediate metallic solution.

Various excursions were observed for the hardness profile as soon as tungsten was introduced in the built. Further investigations by using EDS maps and elemental analysis of the graded structure between molybdenum and tungsten have been performed in order to explain these variations.

7.3.3 EDS maps and chemical analysis

7.3.3.1 Interface between tantalum and molybdenum

Figure 7.4a-c reports the back-scattered electron images and the energy-dispersive spectrometer (EDS) elemental maps for the interface between Ta and Mo. **Figure 7.4d-f** refers to higher magnification region within the mixing zone located on the first layer.

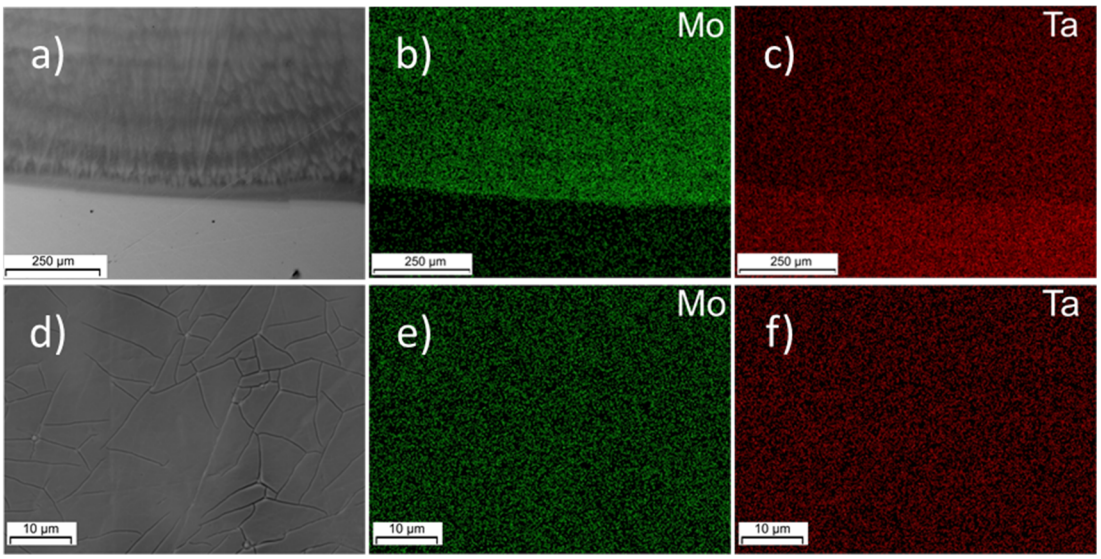

Figure 7.4: Back-scattered electron images (a)(d) and EDS elemental maps (b-c)(e-f) of the Ta-Mo interface.

A sudden change in contrast is reported in **Figure 7.4a,** which represents the compositional layer boundary between the first layer of Mo and the Ta substrate. The EDS maps reported in **Figure 7.4b** and **Figure 7.4c** show

respectively the distribution of Mo and Ta across the interface. This region was characterised by the presence of cracks and a considerably high hardness. When analysing this region at higher magnification, a dense network of several hundred-micron-long cracks was found, as shown in **Figure 7.4d**. From the elemental maps in **Figure 7.4e** and **Figure 7.4f**, the cracked area was not showing any enriched regions or inconsistent compositional variations around the cracked zones, remarking the absence of inhomogeneities.

Some of the physical and thermal properties of both Ta and Mo are reported in **Table 7.2.** From these data, it is possible to notice the considerable differences with regards the coefficient of linear thermal expansion (α) and the elastic modulus (E). In particular, they are respectively 6 μm $m^{-1}K^{-1}$ and 170 GPa for Ta and 4 μm $m^{-1}K^{-1}$ and 329 GPa for Mo. Weber and Aktaa [24] assessed that the difference in mechanical properties is one of the most critical problems when joining dissimilar metals. Bobbio et al. [16] argued that one of the causes of the development of severe cracking for their investigation on the graded structures between Ti-6Al-4V and Invar was possibly associated with the marked difference in the coefficient of thermal expansion of the two metals which can lead to a high concentration of stresses, after multiple thermal cycles. For these reasons, the large mismatch of thermal and mechanical properties of Ta and Mo can be identified as the principal cause for the occurrence of cracks within the interface between these two metals.

The magnitude of the residual stresses for components deposited via WAAM is usually reported to be considerably high due to the intrinsic nature of the process. In particular, the interface between deposit and baseplate resulted to be characterised by a larger concentration of residual stresses with compared to the upper layers [33]. At this specific location of the deposit, both longitudinal and transverse components of the residual stress are summed increasing the local loading of the part [34].

With regards to the case analysed in this study, the development of the dense network of cracks seen at the interface between Ta and Mo was caused by a combined effect of the considerable mismatch between physical and mechanical properties of the metals and the concentration of residual stress at the root of the

structure due to the deposition process. Besides these factors, the increased hardness and brittleness of the alloy 35Mo65Ta also played a crucial role.

7.3.3.2 Molybdenum to tungsten interface

Back-scattered electron images and EDS elemental maps relative to the FGS between Mo and W are shown in **Figure 7.5.** The characterisation of variations in composition was conducted for the initially deposited layers of W, in particular, where the average non-stoichiometric composition measured at this position was 80 wt% in Mo, 16 wt% in W and 4 wt% in Ta.

The differences in contrast in the back-scattered electron images are due to a compositional gradient or zoning instead of surface or grain morphology. Mo-rich zones are shown as darker regions than W-rich, which are shown as brighter regions. The contrast reflects the average composition at every point. Therefore, it is possible to notice W enriched zones located across the layer surrounded by a Mo-W matrix, as shown in the elemental maps reported in **Figure 7.5b** and **Figure 7.5c.** This phenomenon was observed only for the initial W layers.

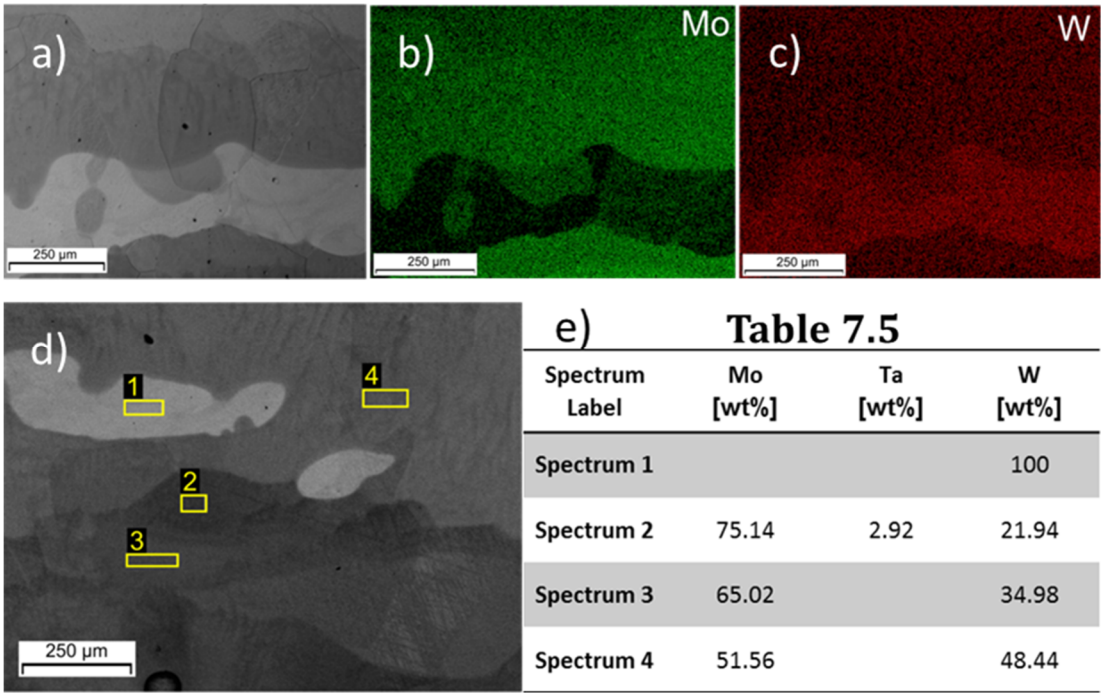

e) **Table 7.5**

Spectrum Label	Mo [wt%]	Ta [wt%]	W [wt%]
Spectrum 1			100
Spectrum 2	75.14	2.92	21.94
Spectrum 3	65.02		34.98
Spectrum 4	51.56		48.44

Figure 7.5: Back-scattered electron image (a) and EDS elemental maps (b-c) for the FGS between Mo and W; Back-scattered electron image (d) of the FGS between Mo and W and **Table 7.5** with the elemental composition of the local chemical analysis (e).

In order to quantify and characterise these variations in composition, EDS elemental analysis at multiple zones characterised with different contrast was performed. The location of each acquisition is indicated in **Figure 7.5d**. In **Figure 7.6e** is reported **Table 7.5**, which lists the values of the elemental composition of the four regions examined. It can be seen that the brightest regions were characterised by a composition of 100 wt.% of W while some surrounding regions were characterised by a W composition as low as 22.0 wt.%.

During the deposition of the initial layer using W wire, W-rich regions formed within the structure mainly because of the difference with regards to the melting point and the thermal conductivity of the two metals. In particular, W is characterised by a much higher melting point and thermal conductivity than Mo (**Table 7.2**) so that faster solidification occurred for the W-rich regions. Usually, the deposition of each layer by an additive manufacturing process can be considered to be inherently a non-equilibrium state because of the rapid solidification of the liquid pool. For this reason, the optimal mixing condition of the two liquid metals, within the weld pool, was not reached and the distribution of the alloying element was not uniform for the initial layers. These localised variations in composition had a noticeable impact on the hardness trend, as shown in **Figure 7.3**. The features described were not observed in the successive layer mainly due to the increased content of W which facilitated the alloying with Mo.

The absence of cracks observed between W and Mo was one of the most important features to be highlighted. Contrarily to the FGS between Ta and Mo, the Mo-W FGS was not presenting either micro- or macro-cracks within its volume. The two metals are characterised by similar elastic modulus and coefficient of linear thermal expansion (**Table 7.2**), which can be considered to be the main reason for the high integrity of the structure, a part of the complete solid solubility.

7.4 Conclusions

In the present work, the deposition of multiple graded structures between tantalum, molybdenum and tungsten was studied. This represents one of the first process studies with regards to the deposition of controlled gradations for large-scale refractory metal structures. The Wire + Arc Additive Manufacturing process

proved to be characterised by a great flexibility and potential with regards to the creation of advanced components through controlled deposition. The microstructure, hardness profile and elemental composition were characterised along the height of the structure. The main findings can be summarised as:

- A dense network of cracks has been reported to populate the interface between tantalum and molybdenum. This has been mainly caused by the mismatch in coefficient of thermal expansion between the two parent metals and by the increased brittleness of the alloy in a non-stoichiometric 35Mo-65Ta combination;

- A sharp change in the microstructural evolution was observed when depositing tungsten onto molybdenum. The main reason is to be found in the heterogeneous solidification from several nuclei with the weld pool due to the fast solidification of the weld pool;

- Variations in both composition and hardness were observed within the initial layers of the FGS between molybdenum and tungsten. It was caused by the substantial difference in melting point of the two metals and the rapid solidification characteristic of the AM processes, which did not favour the formation of a homogeneous alloy;

- The absence of cracks within the molybdenum-tungsten functionally graded structure has been reported. This has been promoted by the similarity with regard to the coefficient of thermal expansion of the two metals. This led the intermediate alloys to accommodate the stresses and the cyclical expansion with the minimum localization of strain.

This study proved that investigations on the influence of the process parameters as heat input and quantity of added material and on the development of a computational model would lead to allow building any controlled gradations in composition using Wire + Arc Additive Manufacture. Furthermore, when depositing FGSs using an additive manufacturing technique, not the only the

miscibility of the alloys and the eventual formation of intermetallic or other brittle phases have to be considered but also the possible mismatch in both thermal and mechanical properties. In particular, a pronounced mismatch with regards to the thermal properties could lead to a sudden change in the solidification regime, which can affect the microstructure, while a mismatch in mechanical properties could lead to failure, such as cracks, also enhanced by the residual stresses that develop when manufacturing components with an AM process.

7.5 Bibliography

1. Reddy JN. Analysis of functionally graded plates. Int. J. Numer. Meth. Engn. 2000; 47: 663–684. Available at: DOI:10.1002/(SICI)1097-0207(20000110/30)47:1/3<663::AID-NME787>3.0.CO;2-8
2. Kawasaki A., Watanabe R. Concept and P/M fabrication of functionally gradient materials. Ceramics International. 1997; 23(1): 73–83. Available at: DOI:10.1016/0272-8842(95)00143-3
3. Koizumi M. FGM activities in Japan. Composites Part B: Engineering. 1997; 28(1–2): 1–4. Available at: DOI:10.1016/S1359-8368(96)00016-9
4. Niino M., Hirai T., Watanabe R. The functionally gradient materials. Journal of the Japan Society for Composite Materials. 1987; 13: 257–264.
5. Pareige P., Russell KF., Stoller RE., Miller MK. Influence of long-term thermal aging on the microstructural evolution of nuclear reactor pressure vessel materials: an atom probe study. Journal of Nuclear Materials. 1997; 250(2–3): 176–183. Available at: DOI:10.1016/S0022-3115(97)00264-X
6. Bernstein A., Bowden NS., Misner A., Palmer T. Monitoring the thermal power of nuclear reactors with a prototype cubic meter antineutrino detector. Journal of Applied Physics. 2008; 103(7). Available at: DOI:10.1063/1.2899178
7. Bohidar SK., Sharma R., Mishra PR. Functionally Graded Materials : A Critical Review. International journal of Scientific Footprints. 2014; : 8–29.
8. Sobczak JJ., Drenchev L. Metallic Functionally Graded Materials : A Specific Class of Advanced Composites. Journal of Materials Science & Technology. Elsevier Ltd; 2013; 29(4): 297–316. Available at: DOI:10.1016/j.jmst.2013.02.006
9. Niendorf BT., Leuders S., Riemer A., Brenne F., Tr T., Richard HA., et al. Functionally Graded Alloys Obtained by Additive Manufacturing. Advanced Engineering Materials. 2014; 16: 857–861. Available at: DOI:10.1002/adem.201300579
10. Popovich VA., Borisov E V., Popovich AA., Su VS., Masaylo D V., Alzina L. Functionally graded Inconel 718 processed by additive manufacturing : Crystallographic texture , anisotropy of microstructure and mechanical properties. Materials and Design. 2017; 114: 441–449. Available at:

DOI:10.1016/j.matdes.2016.10.075

11. Li BS., Zhao S., Hou W., Teng C., Hao Y., Li Y., et al. Functionally Graded Ti-6Al-4V Meshes with High Strength and Energy Absorption. Advanced Engineering Materials. 2016; Available at: DOI:10.1002/adem.201500086
12. Naebe M., Shirvanimoghaddam K. Functionally graded materials : A review of fabrication and properties. Applied Materials Today. Elsevier Ltd; 2016; 5: 223–245. Available at: DOI:10.1016/j.apmt.2016.10.001
13. Sasaki M., Hirai T. Fabrication and Properties of Functionally Gradient Materials. The Centennial Memorial Issue of The Ceramic Society of Japan. 1991; 99(10): 1002–1013. Available at: https://www.jstage.jst.go.jp/article/jcersj1988/99/1154/99_1154_1002/_pdf
14. Domack MS., Baughman JM. Development of nickel-titanium graded composition components. Rapid Prototyping Journal. 2005; 11(1): 41–51. Available at: DOI:10.1108/13552540510573383
15. Shen C., Pan Z., Cuiuri D., Roberts JON., Li H. Fabrication of Fe-FeAl Functionally Graded Material Using the Wire-Arc Additive Manufacturing Process. Metallurgical and Materials Transactions B. Springer US; 2016; 47(1): 763–772. Available at: DOI:10.1007/s11663-015-0509-5
16. Bobbio LD., Otis RA., Paul J., Dillon RP., Shapiro AA., Liu Z., et al. Additive manufacturing of a functionally graded material from Ti-6Al-4V to Invar : Experimental characterization and thermodynamic calculations. Acta Materialia. Elsevier Ltd; 2017; 127: 133–142. Available at: DOI:10.1016/j.actamat.2016.12.070
17. Carroll BE., Otis RA., Paul J., Suh J., Dillon RP., Shapiro AA., et al. Functionally graded material of 304L stainless steel and inconel 625 fabricated by directed energy deposition : Characterization and thermodynamic modeling. Acta Materialia. Elsevier Ltd; 2016; 108: 46–54. Available at: DOI:10.1016/j.actamat.2016.02.019
18. M. Dao., Gu P., Maewal A., Asaro RJ. A Micromechanical Study of Residual Stresses in Functionally Graded Materials. Acta Materialia. 1996; 45(8): 3265–3276.
19. Cannillo V., Montorsi M., Siligardi C., Sola A., de Portu G., Micele L., et al. Microscale computational simulation and experimental measurement of thermal residual stresses in glass-alumina functionally graded materials. Journal of the European Ceramic Society. 2006; 26(8): 1411–1419. Available at: DOI:10.1016/j.jeurceramsoc.2005.02.012
20. Soodi M., Masood SH., Brandt M. Thermal expansion of functionally graded and wafer-layered structures produced by laser direct metal deposition. International Journal of Advanced Manufacturing Technology. 2013; : 2011–2018. Available at: DOI:10.1007/s00170-013-5157-9
21. Rizakhanov RN., Polyanskii MN., Barmin a. a., Rudshtein RI. Functional materials for the piping of nuclear propulsion systems. Inorganic Materials: Applied

Research. 2014; 5(2): 124–128. Available at: DOI:10.1134/S2075113314020178

22. Khripunov BI., Koidan VS., Ryazanov AI., Gureev VM., Kornienko SN., Latushkin ST., et al. Study of tungsten as a plasma-facing material for a fusion reactor. Physics Procedia. Elsevier B.V.; 2015; 71(February): 63–67. Available at: DOI:10.1016/j.phpro.2015.08.313

23. Gumbsch P. Brittle fracture and the brittle-to-ductile transition of tungsten. Journal of Nuclear Materials. 2003; 323: 304–312. Available at: DOI:10.1016/j.jnucmat.2003.08.009

24. Weber T., Aktaa J. Numerical assessment of functionally graded tungsten/steel joints for divertor applications. Fusion Engineering and Design. Elsevier B.V.; 2011; 86(2–3): 220–226. Available at: DOI:10.1016/j.fusengdes.2010.12.084

25. Brandes EA., Brook GB. Smithells Metals Reference Book. Seventh Ed. Butterworth-Heinemann. Butterworth-Heinemann; 1992. 1-534 p. Available at: DOI:10.1016/B978-075067509-3/50014-2

26. Segerstark A., Andersson J., Svensson LE. Investigation of laser metal deposited Alloy 718 onto an EN 1.4401 stainless steel substrate. Optics and Laser Technology. Elsevier Ltd; 2017; 97: 144–153. Available at: DOI:10.1016/j.optlastec.2017.05.038

27. Carroll BE., Palmer TA., Beese AM. Anisotropic tensile behavior of Ti-6Al-4V components fabricated with directed energy deposition additive manufacturing. Acta Materialia. Acta Materialia Inc.; 2015; 87: 309–320. Available at: DOI:10.1016/j.actamat.2014.12.054

28. Baufeld B., Biest O Van der., Gault R. Additive manufacturing of Ti-6Al-4V components by shaped metal deposition: Microstructure and mechanical properties. Materials and Design. Elsevier Ltd; 2010; 31(SUPPL. 1): S106–S111. Available at: DOI:10.1016/j.matdes.2009.11.032

29. Vilaro T., Colin C., Bartout JD., Nazé L., Sennour M. Microstructural and mechanical approaches of the selective laser melting process applied to a nickel-base superalloy. Materials Science and Engineering A. Elsevier B.V.; 2012; 534: 446–451. Available at: DOI:10.1016/j.msea.2011.11.092

30. Thijs L., Montero Sistiaga ML., Wauthle R., Xie Q., Kruth JP., Van Humbeeck J. Strong morphological and crystallographic texture and resulting yield strength anisotropy in selective laser melted tantalum. Acta Materialia. Acta Materialia Inc.; 2013; 61(12): 4657–4668. Available at: DOI:10.1016/j.actamat.2013.04.036

31. Reichardt A., Dillon RP., Paul J., Shapiro AA., Mcenerney BW., Momose T., et al. Development and characterization of Ti-6Al-4V to 304L stainless steel gradient components fabricated with laser deposition additive manufacturing. Materials and Design. Elsevier Ltd; 2016; 104: 404–413. Available at: DOI:10.1016/j.matdes.2016.05.016

32. Chen SR., Gray GT. Constitutive behavior of tantalum and tantalum-tungsten alloys. Metallurgical and Materials Transactions A. 1996; 27(10): 2994–3006. Available at: DOI:10.1007/BF02663849

33. Ding J., Colegrove P., Mehnen J., Ganguly S., Almeida PMS., Wang F., et al. Thermo-mechanical analysis of Wire and Arc Additive Layer Manufacturing process on large multi-layer parts. Computational Materials Science. Elsevier B.V.; 2011; 50(12): 3315–3322. Available at: DOI:10.1016/j.commatsci.2011.06.023

34. Szost BA., Terzi S., Martina F., Boisselier D., Prytuliak A., Pirling T., et al. A comparative study of additive manufacturing techniques: Residual stress and microstructural analysis of CLAD and WAAM printed Ti-6Al-4V components. Materials and Design. 2016; 89: 559–567. Available at: DOI:10.1016/j.matdes.2015.09.115

Chapter 8

Conclusions and Future Work

8.1 Introduction

The main aim of this chapter is to determine the actual impact of the research findings on both scientific and industrial point of view. Thus, the significance of the research is discussed considering the perspectives and implications of the findings in a broader context. A proposed optimal design for a Wire + Arc Additive Manufacturing system dedicated to refractory metals is indicated followed by the main conclusions of the study.

8.2 Contribution to knowledge

The development of additive manufacturing technologies specifically for the deposition of tungsten and tantalum presented various gaps since the beginning of the research. The main gaps have been reviewed and listed in **Chapter 1**. For simplicity, some of them are briefly summarised in order to place the discussion in context. In particular:

- A limited number of available investigations focused on the deposition of tungsten and tantalum and a complete absence of investigation of the Wire + Arc Additive Manufacturing process for these metals;

- The investigations available are concentrated on additive manufacturing processes for small-scale components employing a laser as the heat source and powder as the feedstock;

- The absence of procedures for additive manufacturing techniques able to produce defect-free tungsten components;

- The absence of investigations focused on the production of controlled functionally graded structures of dissimilar refractory metals.

The principal research questions identified in **Chapter 1** of the present dissertation have been formulated based on these main gaps and the available knowledge within the literature. The answers to each of these questions have been successfully addressed by the achievement of the research objectives.

The overall study is in strong agreement with the research available in literature with regards to the real feasibility of depositing refractories using AM. Nonetheless, overlapping the combinations of the research chapter results to the literature gaps, it is visible how original knowledge was also produced which extends the comprehension of the additive manufacture for the refractory metals. This has a considerable significance within the field of study and could help other researchers to refine the investigations using processes different than WAAM. Moreover, the entire set of results generally proves that the process developed can be considered as a valid alternative to existing manufacturing techniques. The main contribution to knowledge can be summarised as follows:

- This research represents the first investigations of Wire + Arc Additive Manufacturing process for both tungsten and tantalum;

- The suitable hardware, process parameters and clamping systems have been illustrated;

- An additive manufacturing process has been developed for large-scale refractory metal components;
- Characterisation of the microstructure and the relation with mechanical and thermal properties have been investigated;

- In process cold work was shown to be effective in improving the microstructure of tantalum;

- Defect-free fully-dense components have been successfully deposited;

- It has been demonstrated that functionally graded structures among refractory metals can be manufactured.

8.3 Impact of the research and future work

The presented research summarised a number of benefits and improvements which enlarge the potential and the flexibility of AM processes, in particular WAAM. Furthermore, as an exploratory research, opportunities for further investigations were raised as well as conceptualisations of the technology within different industries.

Generally, the list of materials recognised to be processable using WAAM can now encounter three new metals, such as tungsten, molybdenum and tantalum. This represents a concept of proof for the validity of the deposition process. Additionally, this research showed that alloys characterised by a high Young's modulus and a high melting point can be manufactured without frequent failures, such as cracking.

Moreover, fundamental information can be extracted from this study which would extend and enhance the underpinning science of AM processes for refractory metals other than WAAM. The following section briefly presents which research aspects were recognised as valuable for further development and understanding.

8.3.1 Future work for further development

The results of the research programme on the development of WAAM for the refractory metals open toward the possibility of further process development and material characterisation. In particular, additional research could focus on:

- Determine a complete relationship between deposit dimensions and process heat input in order to the develop a model suitable for the automation of the

of the WAAM process for both tungsten and tantalum;

- Characterise the mechanical properties of tungsten structures over a large temperature range. In particular, Charpy impact test to characterise the ductile-to-brittle temperature transition and three-point bending or tensile test in order to determine the flow stress over the entire temperature range in tension as well as in compression;

- Characterise the mechanical properties of the tantalum structures produced using the combination of WAAM and inter-layer cold rolling. This would be useful to understand if the mechanical anisotropy was eliminated and the strength improved;

- Model the relationship between process parameters and compositional gradient dimensions for functionally graded structure in order to predict the composition of each layer prior deposition;

- Measure and characterise the residual stress distribution of both tungsten and tantalum structure which can lead to further developments of necessary tools for stress mitigation technique for better process flexibility;

- Investigate the feasibility of using alternative heat sources, such as laser or arc-laser hybrid, rather than arc for the deposition of refractory metals because of the possibility to have much more control on the energy density and distribution.

8.3.2 Future work for further understanding

Some aspects presented in the research chapters require further investigations in order to obtain a complete understanding of the phenomena. Some of them are indicated as follow:

- The characteristic banding reported within tantalum structures after etching needs to be further characterised in order to establish and verify if it was caused by the detachment of finely dispersed oxide particles;

- Thermal straining affected the mechanical properties of the tantalum structure based on the location of specimen extraction. This need to be further understood in order achieve a standard deposition process;

- The thermal properties measured for tungsten structure needs to be further corroborated. In particular, additional tests need to be performed on different heat-treated tungsten structure to understand the physical mechanism which led to the specific results reported;

- Further investigations are needed in order to understand which family of crystal imperfections actually acted as a nucleation site for the new strain-free grains when rolling is coupled with WAAM for tantalum.

8.4 Impact on future applications of the research

The full implementation of the additive manufacture for industrial applications is yet to arrive, while, its potential has been clearly shown in the last years. This is the main factor which is leading many industrial sectors to finance high-quality research of AM materials and processes. Each of these sectors is looking for new manufacturing routes for specific components and materials. In particular, aeronautics and aerospace sectors are mainly focused on the AM development for light alloys, such as aluminium, magnesium and titanium alloys. The application of high-melting-point and high-thermal-conductivity materials is of interest for the nuclear sector.

The results of this research would be of benefit for this last sector as well as other sectors which require the application of parts in severe environments. In particular, the important outcome lies in the possibility to produce near-net-shape components in tungsten and tantalum employing a high deposition rate. In fact, the process developed was characterised by a deposition rate of 2.7 kg/h for tungsten

and 2.9 kg/h for tantalum. This will allow manufacturing medium to large scale components achieving total a weight of over 10 kg. The potentially unlimited build volume also differentiated this study when compared to the other investigation on AM of refractory metals. The following sections will be focused on the impact of the research on two specific industrial sectors, such as nuclear and defence.

8.4.1 Nuclear

The nuclear sector would benefit from this study because it opens new possibilities with regards to the material selection. In particular, in the past, the utilisation of refractory metals, such as tungsten, has been considered with precautions due to their limited workability using conventional manufacturing techniques. Thus, the possibility to manufacture high-performance and relatively low-cost tungsten components via WAAM represents a major benefit for this industry. The tungsten armours need to be solidly attached to the other parts of the divertor system which would require joining between dissimilar materials. A proved design proposal for this approach is to use WAAM to create functionally graded structures between tungsten and other metals in order to have gradient not only in composition but also in thermal expansion. This will possibly mitigate the occurrence of cracks due to mismatch in materials' thermal properties. Furthermore, the consumption and erosion of the tungsten armour after many operating cycles can be addressed by the utilisation of WAAM as in-service repairing technique. Tungsten is also a preferred choice for the nuclear sector for its high resistance to irradiation. This represents a considerable progress towards the commercial feasibility.

8.4.2 Defence

The results produced by the study on the WAAM process development and material characterisation of tantalum mainly impact the defence sector. This because the WAAM process developed can lead to large cost reductions and increased production flexibility of tantalum components, such as balance weights for missiles bodies and parts within the rocket propulsion systems. The flexibility associated with the WAAM process developed can lead to continuous design

enhancements due to its digital approach and, also, to set-up production lines directly on the military field. Moreover, the process developed can be used to execute maintenance in-situ of multiple components.

8.5 WAAM system for refractory metals

Part of the merit of the research needs to be attributed to the WAAM machine used to develop the process parameters and to deposit large-scale refractory metal components. In particular, the experimental set-up shown in most of the research chapters was designed and assembled by the author of the present dissertation for the PhD research purposes. The term WAAM machine refers to the entire combination of welding and manipulation hardware components, software interface, wire delivery system, clamping systems and inert atmospheric chamber. Although the WAAM machine was designed for the deposition of refractory metals, multiple improvements would be required to be implemented within a WAAM system fully-dedicated to high-melting-point materials. In particular, the following specific equipment would be needed:

- Specific welding torch designs;
- High-frequency and heat resistant manipulation system;
- Controlled cooling system for both manipulators and clamping system;
- Sealed and heat-resistant inert atmospheric chamber;
- Cooled welding torch with high operational duty cycle;
- Accurate wire positioning system.

Furthermore, the refractory metal wires used for all the investigations reported were commercially available material. These wires are generally fabricated to be used in application other than AM. The commercial availability of specifically designed chemistry of the wires could lead to improvement of the quality and the properties of the deposits when using WAAM.

8.6 Conclusions

The Wire + Arc Additive Manufacturing process for the production of refractory metal components has been investigated in this study, in particular for

tungsten and tantalum. The aim of this dissertation was to investigate the WAAM process for these metals and to understand the underpinning issues of their deposition. The main research conclusions are:

- The Wire + Arc Additive Manufacturing process is a suitable manufacturing route for large-scale components of both tungsten and tantalum;

- A satisfactory deposition regime was obtained for tungsten in order to obtain crack-free deposits;

- The tungsten components are characterised by thermal properties suitable for the application in the nuclear sector;

- Good mechanical properties have been achieved for the tantalum deposited structure;

- Inter-layer cold working is effective in improving the microstructure of tantalum components;

- Functionally graded structure can be successfully deposited using the WAAM process.

The overall research revealed many aspects of useful practical knowledge which helped in building the theoretical knowledge for both research advancements and industrial applications. In particular, the research presented could have a potential impact on the nuclear and the defence sectors for the production of highly functional and structural components.

The existing literature which focuses on the field of additive manufacturing has been expanded with new data, which contributed to a better understanding of the deposition process. In fact, when comparing the knowledge gaps within the current literature with the results reported, it can be seen that they confirm the possibility to deposit refractory metals, but they are distinguished from the literature for the achievable size of the deposits and the absence of internal defects.

Furthermore, the investigations available in the literature are mainly based on the deposition using laser and powder. The results presented in this dissertation also expand the list of suitable and new manufacturing techniques for refractory metals, which can now include Wire + Arc Additive Manufacture.

Additionally, one of the most valuable information from this study is the fundamental hardware requirements to implement on a fully-operating WAAM machine dedicated to the deposition of high-melting-point and highly reactive materials, such as refractory metals. Particular attention needs to be given to the production and utilisation of high-purity wire, as the composition of the feedstock is fundamental for the production of high-quality components.

Although the additive manufacturing process developed is considered far from its maturation, the results presented in this dissertation represent the foundation of a possible disruptive change in the way refractory metal components are manufactured. The next step for this important achievement is left for future research and some of the potential areas of future improvement were indicated within the general discussion in the section dedicated to future research.

Appendix A

Strategies for tungsten deposition

A1 Introduction

In this appendix, further information with regards to the characterisation and the stabilisation of the Wire + Arc Additive Manufacturing process for unalloyed tungsten presented in **Chapter 3** is provided. In particular, the steps toward the development of the correct deposition strategy are illustrated briefly showing the main reason for the advancement of the investigation.

A2 Methodology

A2.1 Experimental Set-up

Different clamping systems were used for the investigations reported in this appendix in order to understand the impact of the clamping force on the occurrence of cracks. Front feeding was employed for all the deposition strategies presented. All the depositions occurred in a high-purity argon atmosphere.

A2.2 Deposition Strategy 1

Table A.1 presents the process parameters used for the Deposition Strategy 1. The substrate used was a tungsten plate with a thickness of 5.0 mm and the diameter of the tungsten wire was 1.0 mm. The deposition occurred on the flat side of the tungsten plate (**Figure A.1**).

TS [mm/s]	I [A]	WFS [mm/s]	AGC [He%]
2	350	23.5	100

Table A.1: Process parameters used for the Deposition Strategy 1.

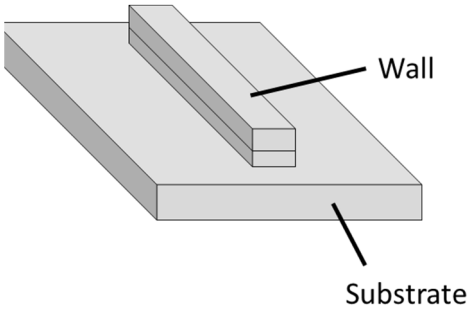

Figure A.1: Substrate orientation with respect to the deposition for Deposition Strategy 1.

A2.3 Deposition Strategy 2

Table A.2 presents the process parameters used for the Deposition Strategy 2. The substrate used was a tungsten plate with a thickness of 5.0 mm and the diameter of the tungsten wire was 1.0 mm. The substrate was placed under the torch in a different configuration. In particular, the deposition occurred on the side of the substrate (**Figure A.2**).

TS [mm/s]	I [A]	WFS [mm/s]	AGC [He%]
2	350	23.5	100

Table A.2: c

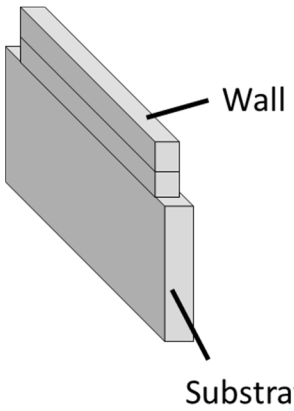

Figure A.2: Substrate orientation with respect to the deposition for Deposition Strategy 2.

A2.4 Deposition Strategy 3

In order to understand if the clamping load combined with the great thermal excursions were the causes of the severe cracking of the tungsten substrate, a lateral force and a new strategy of deposition have been tried. **Figure A.3** shows a model of the clamping system used for the Deposition Strategy 3. In

particular, a lateral force was applied to the substrate (blue part) using two strips of metal (red parts) and five screws. Firstly, copper and, successively, tantalum has been used as lateral stripes. Furthermore, **Figure A.4** helps to schematise the single step of the new strategy of deposition. The approach consists of three main steps:

- Deposition on tungsten substrate;
- Removal of the deposited structure from the substrate;
- Clamping of the structure deposited and successive deposition.

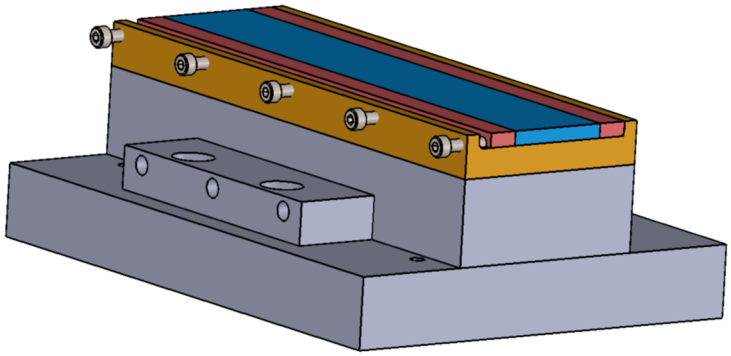

Figure A.3: Model of the clamping system used during the investigation (blue part: tungsten; red parts: copper/tantalum; orange part: copper).

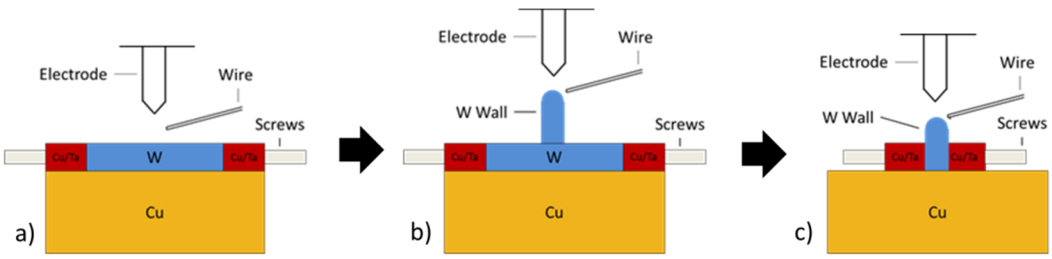

Figure A.4: Description of the steps of the new strategy of deposition for tungsten. a) beginning of deposition onto the substrate; b) deposition of few layers of tungsten; c)deposition on top of the wall without substrate.

Table A.3 presents the process parameters used for the Deposition Strategy 3. The substrate used was a tungsten plate with a thickness of 5.0 mm and the diameter of the tungsten wire was 1.0 mm.

TS [mm/s]	I [A]	WFS [mm/s]	AGC [He%]
2	350	23.5	100

Table A.3: Process parameters used for the Deposition Strategy 3.

A3 Results

A3.1 Deposition Strategy 1

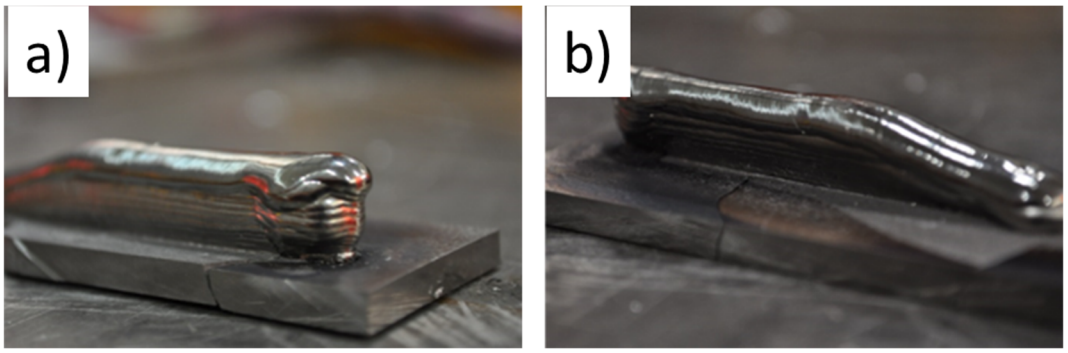

Figure A.5: Tungsten wall deposited using the Deposition Strategy 1.

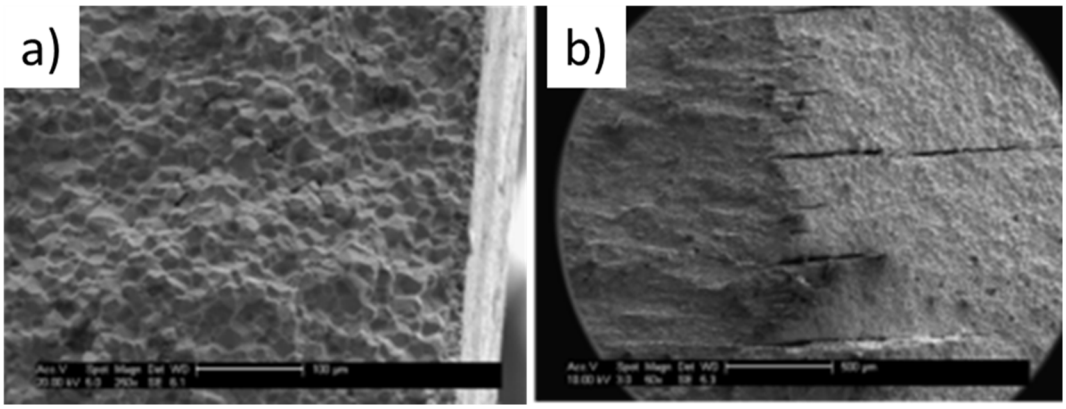

Figure A.6: Different features found on the cracked features.

In **Figure A.5** are reported two pictures of the first deposited structure in unalloyed tungsten via WAAM. The deposition process resulted to be successful although, the development of cracks from the side of the substrate which were affecting the integrity of the entire structure. In particular, upon cooling, cracks developed from the edge of the substrate toward the deposited layer, which presented the higher amount of residual stresses. In the **Figure A.6** are presented different features found on the fractured surface of tungsten substrate. **Figure A.6a** reports the surface of a typical brittle transgranular fracture of tungsten. In

Figure A.6b is reported a failure feature similar to a marked delamination of the tungsten substrate. The repetitive expansions and contractions due to the different thermal cycles after deposition led to the deterioration of the substrate made by powder metallurgy.

A3.2 Deposition Strategy 2

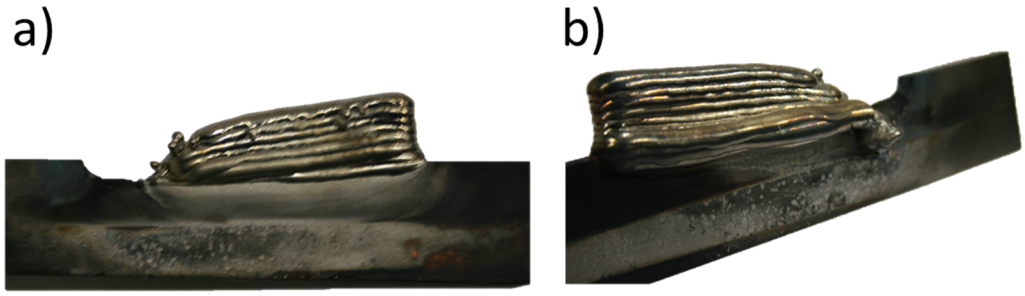

Figure A.7: Tungsten wall deposited using the Deposition Strategy 2.

Figure A.7 reports two pictures of the tungsten structure deposited using the Deposition Strategy 2. It is possible to see that no cracks developed during the process. However, the wall presented a marked slope along its length. In fact, the accumulation of the heat and the decreasing of the thermal conductivity of tungsten led to unfavourable geometrical features.

A3.3 Deposition Strategy 3

Figure A.8a and **Figure A.8b** show the results of a single deposition of tungsten. The copper strips were completely melted around the tungsten substrate. The molten copper reached the bottom of the substrate altering the regular heatsink condition that was present before. Furthermore, the presence of molten copper and copper vapour led to a considerable contamination of the welding electrode. Then, a high melting point material was used for the successive trials. **Figure A.8c** and **FigureA.8d** show the results of the deposition when usinf tantalum lateral strips. Two layers of tungsten were deposited without process-related problems but a pronounced distortion was present, which was affecting the deposition of the successive layers.

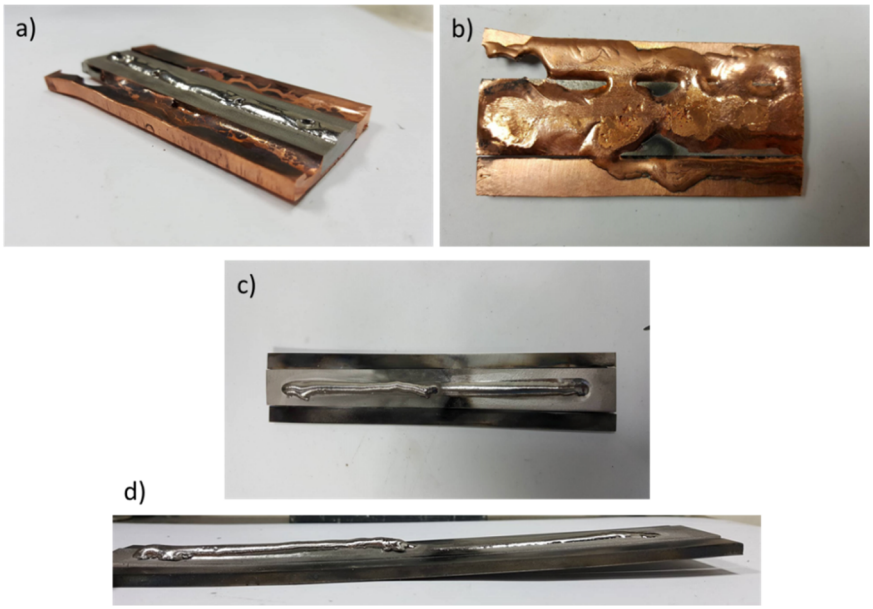

Figure A.8: a) Top view of tungsten plate and copper lateral bars; b) Bottom view of tungsten plate and copper lateral bars; c) Top view of tungsten plate and tantalum lateral bars; d) Side view of tungsten plate and tantalum lateral bars.

Appendix B

Mechanical Testing and Residual Stresses measurements of tungsten

B1 Introduction

In this appendix, further information with regards to the characterisation of mechanical properties and residual stresses of deposited tungsten structures is provided. In particular, the reasons for the unaccomplished investigations have been illustrated.

B2 Methodology

B2.1 Experimental Set-up

The set-up used for the deposition of the tungsten structure has been already reported in **Figure 4.1** of **Chapter 4**.

B2.2 Mechanical Properties

3-point bending test and Small punch test at elevated temperatures were planned to be performed for the characterisation of the mechanical properties of the tungsten structure deposited. The coupons geometry and dimensions are reported in **Figure B.1**. The samples were extracted using electro-discharge machining (EDM).

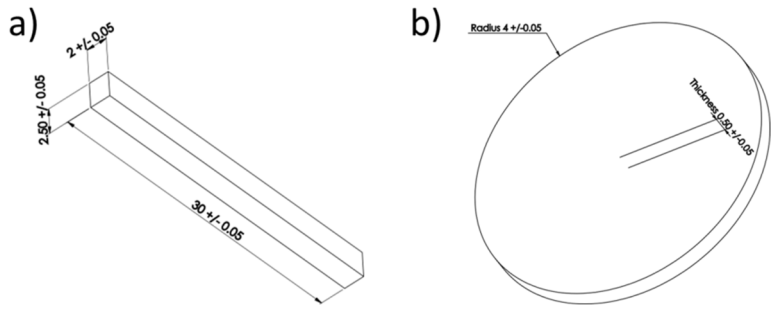

Figure B.1: Geometry and main dimensions of the 3-point bending test (a) and the Small punch test (b).

B2.3 Residual Stresses

The residual stresses of the tungsten structure should have been measured using the SALSA stress imager of the Institut Laue-Langevin (ILL), FRANCE. The submitted and accepted proposal presented the following experimental plan:

"Two samples (similar to the first successful wall shown in **Figure B.2a**)) will be manufactured at Cranfield University using the same deposition parameters, of which one will be thermally stress relieved at 1050 °C in an inert atmosphere. So far only optical microstructural analysis of tungsten WAAM has been produced, as seen in **Figure B.2b**). The production of subsequent walls shows a good repeatability. The next step will be an EBSD analysis of the crystallographic orientation and texture of the grains.

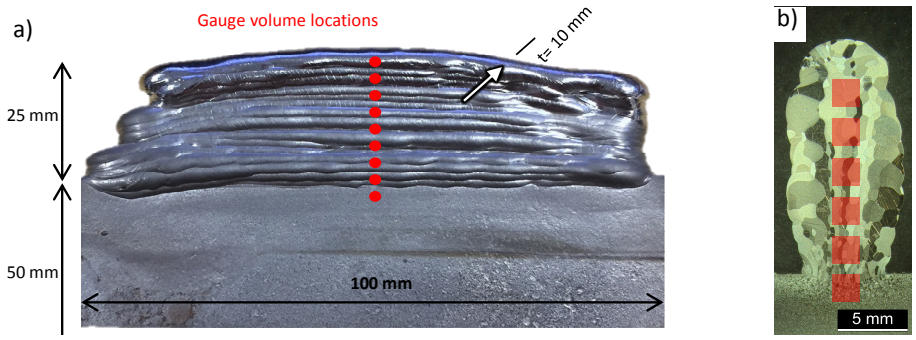

Figure B.2: Wire + Arc Additively Manufactured Tungsten Wall deposited on Tungsten substrate a); Microstructure of a Tungsten wall with suggested dimensioned Gauge Volumes b).

Strain measurements will be carried out using SALSA. Ten equidistant gauge volumes (2 x 2 x 2 mm) will be located in the symmetry axis of each specimen. The high flux of SALSA is required to get a quality signal to achieve good spatial resolution for the given path length in the 10 mm thick tungsten sample. The target plane in the bcc tungsten lattice will be the {211} family with a $d211$ = 1.288 Å. The wavelength of the incident beam will be set close to λ = 1.822 Å in order to produce a cuboid gauge volume. Each gauge volume will be measured in the longitudinal, transverse and normal direction to calculate the three 2 principle residual stresses. **Figure B.2b** shows the large grain size in comparison to the gauge volume. EBSD will be performed beforehand to understand the crystallographic texture. Oscillating of ±5° could also be employed to help getting a

faster result. However, for the given path length 40 min exposure time per gauge volume should generate a quality signal. The sample will be moved along the z-direction in order to place all 10 gauge volumes into the beam consecutively. The total exposure time is [40min x 10 volumes x 3 directions x 2 specimen] = 2400 min. The microstructure along the wall height is homogeneous, so only one d0 measurement is required. 8 h will be enough for d0 measurement and setup, which sums up to 48 h in total. No special environment will be required during the measurement."

B3 Results

B3.1 Mechanical Properties

Figure B.3: Thin slices of tungsten structures cut using electro-discharge machining.

Mainly due to the brittleness of the tungsten structure and also to the small dimensions of the coupons, it was not possible to extract the samples needed due to a predominant occurence of cracks during the cutting process (**Figure B.3**). The samples extracted from the dilatometry and the laser flash analysis (**Chapter 4**) were larger than the one in **Figure B.1** and they were extracted without any major failures.

B3.2 Residual Stresses

The outcome of the experimental proposal was successful and the beam time was allocated for the experiments. Unfortunately, the utilisation of the SALSA equipment at the Institut Laue-Langevin (ILL) was suspended for over one year due to unexpected critical failures of the equipment itself. This inconvenient has markedly limited the possibility to accomplish the measurements.

Appendix C

Development of parameters for tantalum deposition

C1 Introduction

In this appendix, further information with regards to the initials stages of the tantalum deposition development presented in **Chapter 5** is presented. The results of the tantalum autogenous bead-on-plate welds and the single layer deposition will be reported.

C2 Methodology

C2.1 Experimental Set-up

The set-up used for the initial development stages of the tantalum deposition has been already reported in **Figure 5.1** of **Chapter 5**.

C2.2 Autogenous welds

The tantalum autogenous bead-on-plate welds were performed using the set of process parameters listed in **Table C.1.**

C2.3 Single-pass welds

The tantalum single layer depositions were performed using the set of process parameters listed in **Table C.2.**

Sample Name	TS [mm/s]	AGC [He%]	I [A]
1	2	100	250
2	4	100	250
3	6	100	250
4	2	100	200
5	4	100	200
6	6	100	200
7	2	100	150
8	4	100	150
9	6	100	150
10	2	100	300
11	4	100	300
12	6	100	300
13	2	100	100
14	4	100	100
15	6	100	100

Table C.1: Process parameters for the tantalum autogenous bead-on-plate welds.

Sample Name	TS [mm/s]	I [A]	AGC [He%]	WFS [mm/s]
1B	4	250	100	20
2B	4	250	100	40
3B	4	250	100	60
4B	4	200	100	20
5B	4	200	100	40
6B	4	200	100	60
7B	4	300	100	20
8B	4	300	100	40
9B	4	300	100	60

Table C.2: Process parameters for the tantalum single layer depositions.

C3 Results

C3.1 Autogenous welds

Figure C.1 shows the bead-on-plate welds of a tantalum plate. This investigation

was used to define a small operative working window which correlates the travel speed (TS), the welding current (I) and the weld width.

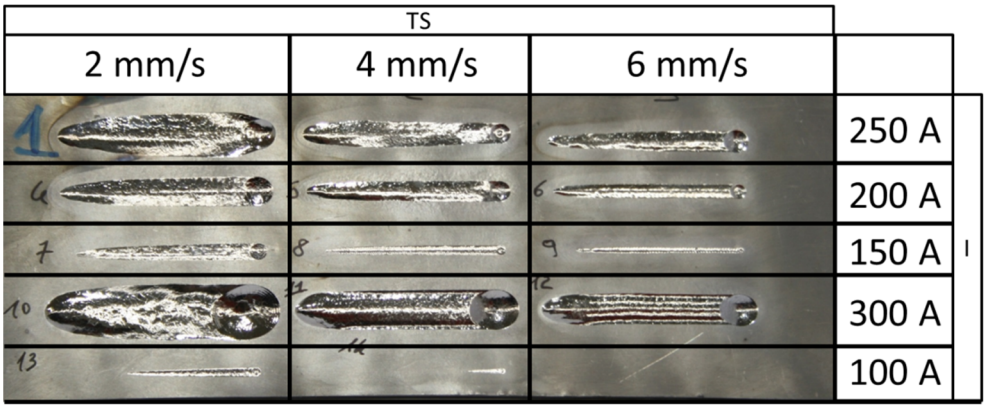

Figure C.1: Bead appearance of the tantalum autogenous bead-on-plates welds.

In particular, the welds performed using a welding current of 100 Amps have been eliminated from further investigations because no regular weld pool developed at this level of power. A weld bead width between 2.3 and 13.0 mm was achieved exploring the range of current and welding speed reported. The set of bead-on-plate performed using 4 mm/s have been used for further process development as the weld bead width were within the range of interest and the welding speed could allow a good deposition rate.

C3.2 Single-pass welds

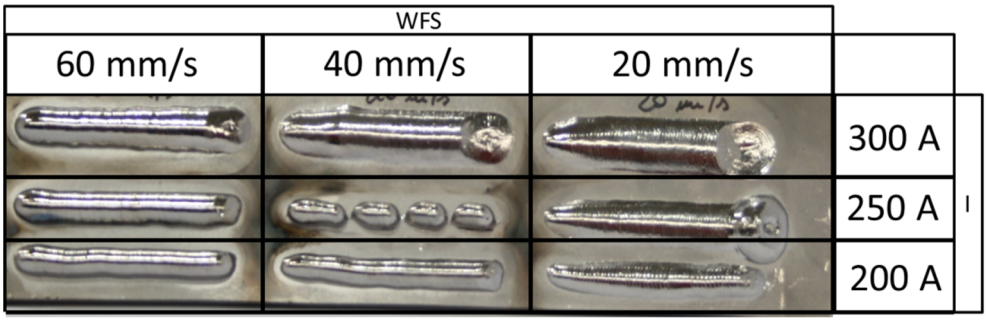

Figure C.2: Bead appearance of the tantalum single layer deposition.

Figure C.2 shows the bead appearance of the single layer deposition using different wire feed speed (WFS) and different welding current (I). The travel speed was kept constant to 4 mm/s as result from the previous experiments. The deposition performed using WFS of 40 mm/s and I of 250 Amps have been affected by an error of communication between the welder and the wire feeder so that this

case presents a discontinuous bead. Layer heights between 0.7 mm and 1.8 mm were achieved. WFS between 60 mm/s and 40 mm/s have been considered for further investigations due to the high productivity and high deposition rate that can be achieved using these parameters.

Appendix D

Refining tantalum microstructure by using pulsing arc current

D1. Introduction

In this appendix, further information with regards to an additional strategy employed to refine the microstructure of tantalum component presented in **Chapter 6** is provided. The methodology and the results of the deposition of tantalum using pulsed arc current are reported.

D2. Methodology

One of the methods to achieve the refinement of the microstructure involves the use of a pulsed current during the deposition process. The main parameters of the current pulsed waveform are indicated in **Figure D.1.**

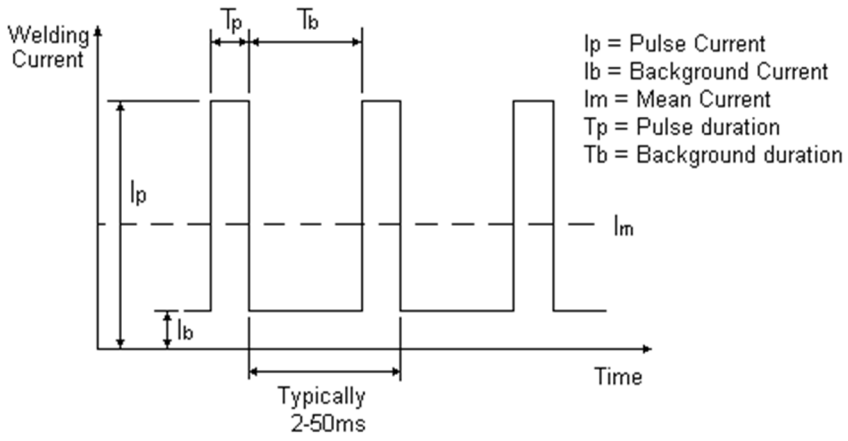

Figure D.1: Scheme of the waveform of the current during pulsed deposition.

In particular, during the deposition, the current follows a characteristic waveform, oscillating between the pulse and the background value. The set of

parameters used for the pulsed deposition are reported in **Table D.1**. In particular, the mean current was kept constant to 300 Amps in order to achieve the same deposition dimensions of the structures presented in **Chapter 5.**

Samples Name	Mean Current [A]	Pulse Current [A]	Background Current [A]	Pulse Duration [s]	Background Duration [s]	Pulse Duty Ratio	Frequency [Hz]	TS [mm/s]	WFS [mm/s]
a	300	350	284	0.1	0.3	25%	2.5	4	60
b	300	350	250	0.2	0.2	50%	2.5	4	60
c	300	350	150	0.3	0.1	75%	2.5	4	60
d	300	350	284	0.2	0.6	25%	1.25	4	60
e	300	350	250	0.4	0.5	50%	1.25	4	60
f	300	350	150	0.6	0.2	75%	1.25	4	60

Table D.1: Process parameters used for the deposition of tantalum using pulsed current

D3 Results

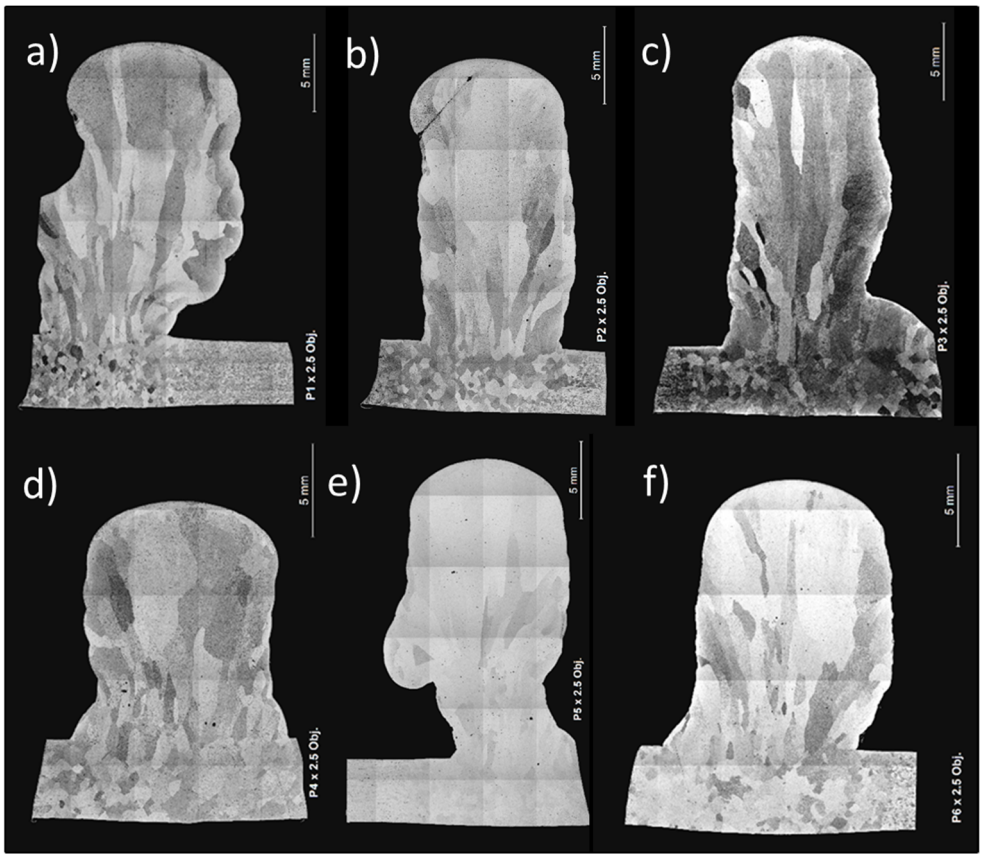

Figure D.2: Comparison of the microstructure of the tantalum deposited structure using pulsed current.

The micrographs of the deposited structures are reported in **Figure D.2.** The microstructure resulted to be unvaried for all the cases when compared to the as-deposited structure using constant current. In particular, large columnar grains evolved from the substrate towards the direction of deposition. A higher frequency would have possibly increased the probability of stimulating the flaking of the mushy zone leading to the refining. This experiment has been considered to have a large number of variables which needed a large number of experiments to explore. This has been considered too costly so that the focus was shifted on the experiments reported in **Chapter 6** for the microstructural refinement.

Appendix E

Development of parameters for dissimilar metal deposition

E1 Introduction

In this appendix, further information with regards to the dissimilar deposition of dissimilar refractory metals (tantalum, molybdenum and tungsten) presented in **Chapter 7** is provided. In particular, the initial stage of deposition of tungsten, firstly, onto molybdenum substrate and, secondly, onto tantalum substrate is reported.

E2 Methodology

E2.1 Experimental Set-up

The set-up used for the deposition of the tungsten has been already reported in **Figure 7.1** of **Chapter 7.** The molybdenum substrate was 5.0 mm thick while the tantalum substrate was 4.0 mm thick. For both substrates, initial tungsten single layer has been deposited using different parameters an, successively, a small tungsten wall has been deposited onto the respective substrate. Furthermore, fractured surfaces located at the junction between the two materials have been analysed using electron scanning microscope.

E2.2 Tungsten on Molybdenum

Table E.1 reports the process parameters used for the tungsten single layer deposition onto molybdenum substrate.

Sample Name	TS [mm/s]	I [A]	WFS [mm/s]	AGC [He%]
1Mo	4	350	10	100
2Mo	4	350	15	100
3Mo	4	350	20	100
4Mo	4	350	25	100

Table E.1: Process parameters used for the tungsten single layer deposition onto molybdenum substrate.

Table E.2 reports the process parameters used for the deposition of tungsten wall onto molybdenum substrate.

Sample Name	TS [mm/s]	I [A]	WFS [mm/s]	AGC [He%]
WMowall	4	350	20	100

Table E.2: Process parameters used for the deposition of tungsten wall onto molybdenum substrate.

E2.3 Tungsten on Tantalum

Table E.3 reports the process parameters used for the tungsten single layer deposition onto tantalum substrate.

Sample Name	TS [mm/s]	I [A]	WFS [mm/s]	AGC [He%]
1Ta	4	300	5	100
2Ta	4	300	10	100
3Ta	4	300	15	100
4Ta	4	300	20	100
5Ta	4	300	25	100
6Ta	4	300	30	100

Table E.3: Process parameters used for the tungsten single layer deposition onto tantalum substrate.

Table E.4 reports the process parameters used for the deposition of tungsten wall onto tantalum substrate.

Sample Name	TS [mm/s]	I [A]	WFS [mm/s]	AGC [He%]
WTawall	4	300	20	100

Table E.4: Process parameters used for the deposition of tungsten wall onto tantalum substrate.

E3 Results

E3.1 Tungsten on Molybdenum

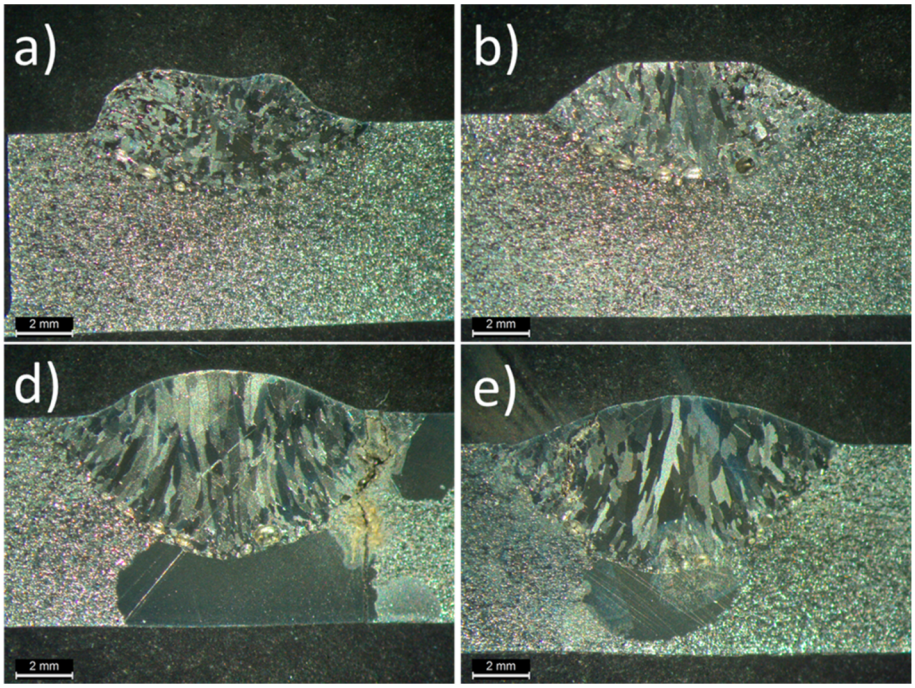

Figure E.1: Micrographs of the tungsten single layer depositions onto molybdenum substrate.

Figure E.1 reports the micrographs of the tungsten single layer depositions onto molybdenum substrate. It could be seen that for all the tests there was the development of porosity at the fusion boundary. **Figure E.2** reports the microstructure of the tungsten wall deposited onto molybdenum substrate. It is possible to see that the wall was characterised by a mixture of small columnar-like and equiaxed grains unlike the substrate under the weld pool which was characterised by large grain growth**. Figure E.3** shows the fracture that developed across the boundaries between the substrate and the wall. The fracture was caused by a combined effect of coalescence of pores and the development of cracks among them. This was confirmed also by the fractured surface reported in **Figure E.4.**

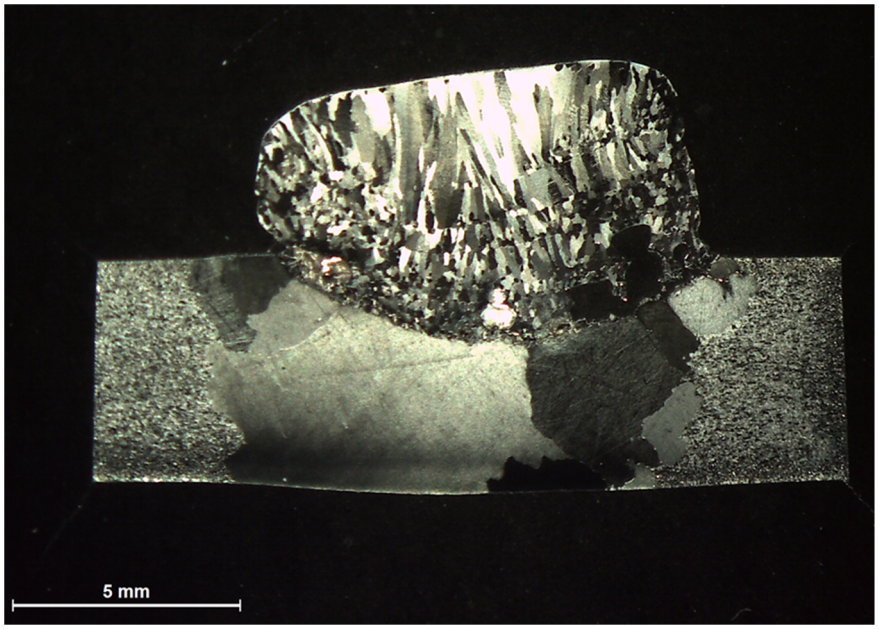

Figure E.2: Micrographs of the tungsten wall onto molybdenum substrate.

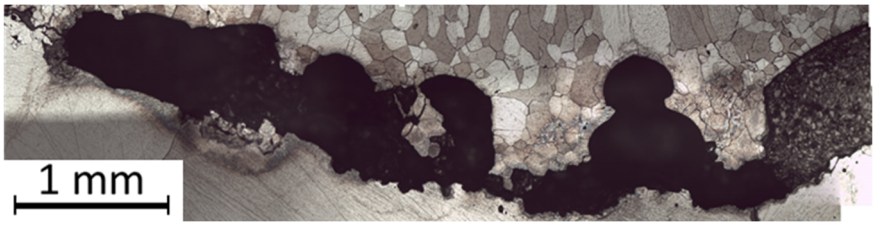

Figure E.3: Micrographs of the fracture located at the fusion boundary of the tungsten wall onto molybdenum substrate.

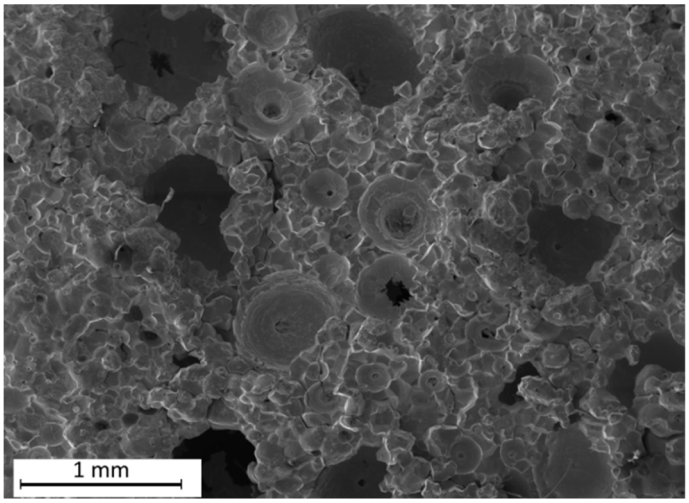

Figure E.4: Electron microscope image of the fractured surface between molybdenum substrate and tungsten wall.

E3.2 Tungsten on Tantalum

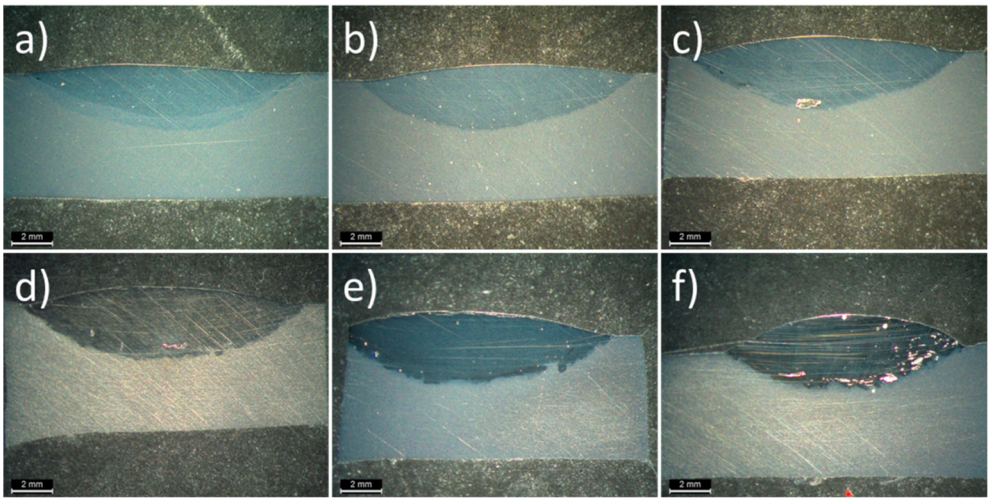

Figure E.5: Micrographs of the tungsten single layer deposition onto tantalum substrate.

Figure E.5 reports the micrographs of the tungsten single layer depositions onto tantalum substrate. It could be seen that only for some was observed the development of some porosity but there was no presence of macro-cracks within the welds.

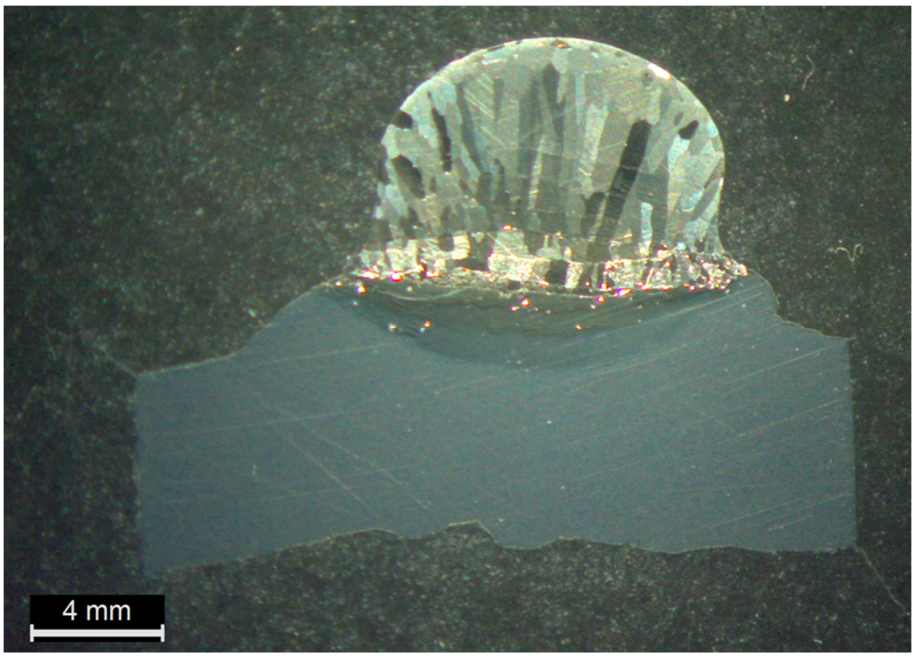

Figure E.6: Micrographs of the tungsten wall onto tantalum substrate.

Figure E.6 reports the microstructure of the tungsten wall deposited onto tantalum substrate. The tungsten wall was characterised by columnar grains. Some pores were localised for the first three layers. **Figure E.7** shows the fracture that

developed across the boundaries between the substrate and the wall. The fracture resulted to be caused mainly by the large difference in thermal expansion of the two metals. Furthermore, the enhanced brittleness caused by the addition of large quantities of tungsten to tantalum also contributed to the devilment of cracks. **Figure E.8** reports an image of the fractured surface which was characterised mainly by a brittle fracture profile.

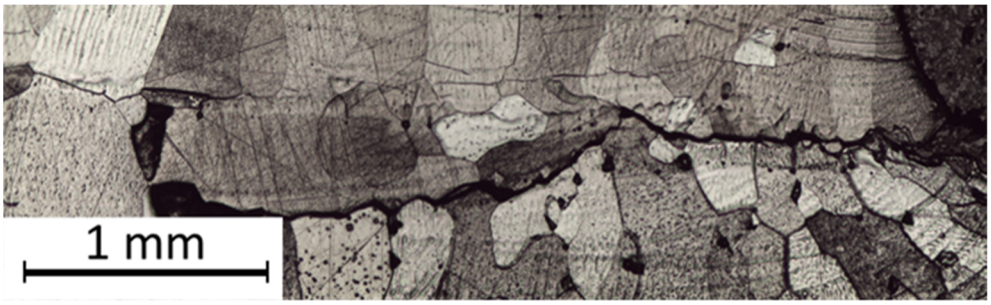

Figure E.7: Micrographs of the fracture located at the fusion boundary of the tungsten wall onto tantalum substrate.

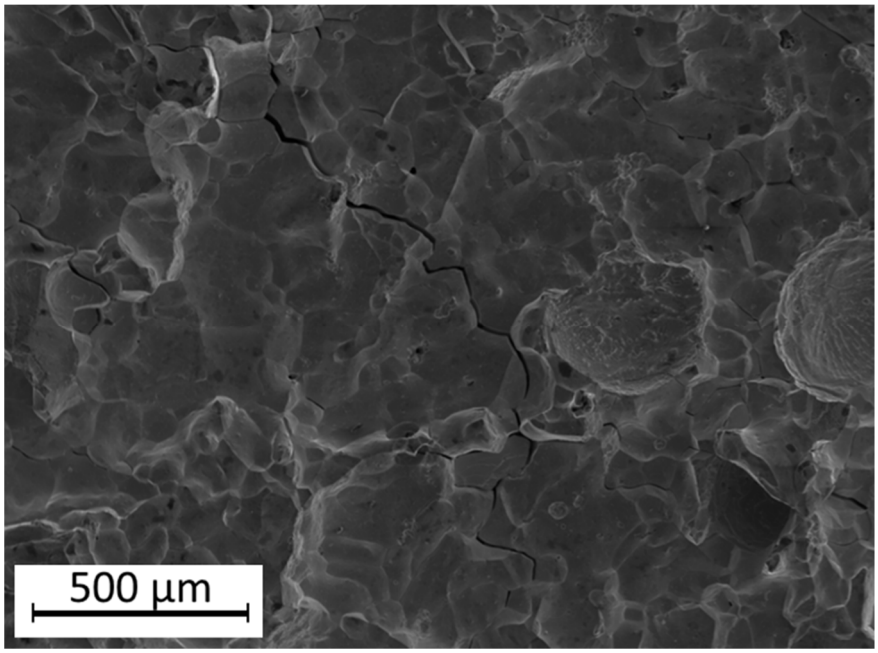

Figure E.8: Electron microscope image of the fractured surface between tantalum substrate and tungsten wall.